ABSTRACT

Title of dissertation: NEXT-GENERATION SUPERCONDUCTING METAMATERIALS: CHARACTERIZATION OF SUPERCONDUCTING RESONATORS AND STUDY OF STRONGLY COUPLED SUPERCONDUCTING QUANTUM INTERFERENCE META-ATOMS

Jingnan Cai
Doctor of Philosophy, 2024

Dissertation directed by: Professor Steven M. Anlage
Department of Physics

Metamaterials are artificial structures consisting of sub-wavelength 'atoms' with engineered electromagnetic properties that create exotic light-matter interactions through the effective medium approximation. Since the early 2000s, superconductors have been incorporated into a variety of structures to achieve tunable, low-loss, and nonlinear metamaterials, and have enabled applications such as negative index of refraction, near zero permittivity, and parametric amplification. We have designed, fabricated and characterized two types of superconducting metamaterials based on the quantum three-junction flux qubits and classical radio frequency superconducting quantum interference devices (rf SQUIDs).

The coplanar waveguide resonators hosting the qubit meta-atoms exhibit anomalous reduction in loss in microwave transmission measurements at low rf excitation levels upon decreasing temperature below 40 mK. In contrast, the well-known standard tunneling model (STM) of the two-level system (TLS), believed to be the

dominant source of loss at low temperatures, predicts a loss increasing then saturating with lowering temperatures. This anomalous loss reduction is attributed to the discrete nature of an ensemble of TLSs in the resonator. As temperature decreases, the individual TLS response bandwidth reduces with their coherence rate $\Gamma_2 \sim T$, creating less overlap between neighboring TLSs in the energy spectrum. This effective reduction in the density of states around the probe frequency is responsible for the observed lower loss at low rf excitation levels and low temperatures as compared to the STM prediction. We also incorporate the discrete TLS ansatz with the generalized tunneling model proposed by Faoro and Ioffe [PRL 2012, 109, 157005 and PRB 2015, 91, 014201] to fit the experimental data over a wide range of temperatures and rf excitation powers. The resulting goodness of fit is better than all common alternative explanations for the observed phenomenon.

Metamaterials made of large arrays of hysteretic ($\beta_{\mathrm{rf}} = L_{\mathrm{geo}}/L_{\mathrm{JJ}} > 1$) classical rf SQUIDs are also designed and characterized in microwave transmission measurements, where we observed the SQUID self-resonances tuning with applied dc and rf magnetic flux, as well as temperature. The resonance features are tuned with dc flux in integers of the flux quantum, as expected. Due to the phenomenon of multistability present in the large system, the resonance bands can cross those from adjacent dc flux periodicities resulting in hysteresis in dc flux sweeps, which is observed in the experiment. Furthermore, we developed a new three-dimensional architecture of rf SQUID metamaterials where the nearest-neighbor SQUID loops overlap. The resulting capacitive coupling dramatically changes the response by introducing many more resonance bands that spread over a broad range of frequencies, the upper limit

of which is much higher than the single-layer counterparts. A resistively and capacitively shunted junction (RCSJ) model with additional capacitive coupling between SQUIDs is proposed and successfully attributes the high frequency bands to the displacement current loops formed between the overlapping wiring of neighboring SQUIDs. The capacitively-coupled rf SQUID metamaterial is relevant to the design of single-flux-quantum-based superconducting digital electronic circuits, which has adopted three-dimensional wiring to reduce the circuit footprint.

NEXT-GENERATION SUPERCONDUCTING METAMATERIALS: CHARACTERIZATION OF SUPERCONDUCTING RESONATORS AND STUDY OF STRONGLY COUPLED SUPERCONDUCTING QUANTUM INTERFERENCE META-ATOMS

by

Jingnan Cai

Dissertation submitted to the Faculty of the Graduate School of the
University of Maryland, College Park in partial fulfillment
of the requirements for the degree of
Doctor of Philosophy
2024

Advisory Committee:
Professor Steven M. Anlage, Chair/Advisor
Dr. Kevin D. Osborn
Dr. Benjamin S. Palmer
Professor Aaron Sternbach
Professor Thomas M. Antonsen
Professor Ichiro Takeuchi, Dean's Representative

Acknowledgments

As a classic joke goes, the best part of the PhD program is the summer before it starts, when the possibilities seem endless and the pressure of the research work is yet to set in. Although the real situation is a bit more complicated, life as a PhD student is indeed challenging. I lost count of how many nights I spent in the lab running experiments, analyzing data, or reading papers. Now that I have finally earned a title before my name, I want to acknowledge all the people who helped me through this journey, without whom this achievement would not have been possible.

First of all, I owe a debt of gratitude to my advisor, Professor Steven M. Anlage, an accomplished scientist and an experienced mentor. I am deeply grateful that Professor Anlage took me in as a research assistant in my first year, a bold move considering the course load for a first-year student. Since then, his trust and support have nurtured my growth from a student into a researcher. I remember that during a major revision of a paper, when I explored an alternative interpretation for the measurement result in the original draft, we were under a lot of pressure to finish this project and start the next one. Professor Anlage was patient through this process. He did not dismiss my idea and allowed me to spend more time developing this new model. That was the first time that I felt like an independent researcher and produced some original research work. In retrospect, I simply cannot ask for a better advisor, who is as knowledgeable, resourceful, open-minded, hard-working and yet lenient to the students.

I thank the committee members: Dr. Kevin D. Osborn, Dr. Benjamin S.

Palmer, Professor Thomas M. Antonsen, Professor Aaron Sternbach, and Professor Ichiro Takeuchi for their time reviewing the thesis and overseeing the defense. Their constructive feedback has improved this dissertation. I would like to acknowledge Dr. Palmer in particular for his generosity to allow us to use the facility in his lab, which has been crucial for this thesis work.

I want to acknowledge my collaborators: Dr. Robin Cantor, who helped me with the SQUID design and provided the high-quality metamaterial sample foundational to this dissertation, Dr. Nikos Lazarides, and Dr. Johanne Hizanidis, who are experts in theoretical modelling of the SQUID metamaterials and had major contributions to the project. They have also guided me and provided critical feedback to the SQUID metamaterial work.

The majority of a PhD student's time is spent in the lab along with their peers. Therefore, I need to thank my labmates for providing a friendly and supportive climate in the group: Dr. Min Zhou, Dr. Seokjin Bae, Dr. Bakhrom Oripov, Dr. Tamin Tai, Dr. Shukai Ma, Dr. Cougar Garcia, Dr. Lei Chen, Chung-Yang Wang, Arthur Carlton-Jones, Jared Erb, Isabella Giovannelli, Nadav Shaibe, Yilin Li, Dr. En-jui Kuo, Ethan Zack, Braden Larsen, and Hemanth Challagulla. In particular, I want to thank Bakhrom, who had been my mentor since I first joined the group and practically saved my life driving me to the hospital when I had an appendicitis; Tamin, who collaborated closely with me and taught me a lot about thin film fabrication and microwave engineering; Jared, who has been an excellent gym buddy since a year ago when I decided to work out to recover from emotional trauma; and Yilin, who, despite being my youngest mentee, is wise beyond their

years and helped me recover emotionally. I have learned a lot from my labmates both in research and in life and hopefully have also taught some of them a thing or two. They will forever be a part of the few and sparse fond memories of my PhD life.

I would like to thank the staff at the Quantum Materials Center: Douglas Bensen, Brian Straughn, John Touart and Bruce Lee Rowley (RIP), whose technical expertise has contributed significantly to my projects. Doug and Brian in particular have been diligently maintaining the facility at the center and often gone out of their way to support our research. I would also like to thank Dr. Sudeep Dutta who shared some lab space with us and kept the aging infrastructure running for the dilution fridges for years. I thank the staff at the Maryland Nanocenter: John Abrahams and Jonathan Hummel, for maintaining the cleanroom and teaching me quite a few fabrication techniques. I also thank Dr. Yizhou Huang from Dr. Palmer's group at the Laboratory of Physical Sciences, who helped us with the thin film evaporation for several superconducting resonator samples.

I thank my friends: Emerald, Abraham, Keagan, Wance, Kungang, Xiuyu, Xi, Yuhua, Jiuyuan and my furry companions: Nelson and Riven for their physical and emotional supports during my PhD years. I was not known for being socially adept. Nonetheless, they have put up with me and influenced me to become slightly more socially acceptable now.

I also want to thank my parents for their support since my college years. They have made many sacrifices for me to continue my education abroad in the past decade. I am also in debt to my grandparents, with whom I have grown up

since the age of a toddler. I have not been able to travel back to visit any of my family since the pandemic, not even to attend the funeral of my grandpa three years ago. I have owed my gratitude to them for letting me purse my passion half a world away.

There are many others that had helped shape me into the current person I am even before my PhD career started: my English tutor Ms. Zhang, my math tutor Mr. Wei, many high school teachers and my undergraduate advisor Martin Greven. However, I simply cannot remember all, and I apologize for inadvertently leaving out anyone.

Table of Contents

List of Tables

List of Figures

Chapter 1

Introduction

1.1 Overview of superconducting metamaterials

Metamaterials are artificial structures consisting of 'atoms' with exotic electromagnetic properties that are designed to create new light-matter interactions. One important tool for understanding and engineering the metamaterial is the effective medium approximation (EMA), which can be dated back to Maxwell's original work on electromagnetic waves [1]. The concept behind EMA is quite intuitive and general. The electromagnetic field amplitude cannot change on a scale much less than its wavelength. Therefore, the details of any structures smaller than that length scale could be omitted, and their effect on the electromagnetic wave could be generalized as some phenomenological parameters (e.g. effective permittivity, permeability) that describe the average response of the microscopic structures. Through careful engineering, effective material properties that do not occur naturally can be achieved. For example, a medium with a negative index of refraction [2, 3, 4] can be used for cloaking, building a superlens with focusing power beyond the Rayleigh limit, and achieving a negative phase velocity. Metamaterials with near zero permittivity [5, 6, 7, 8, 9] possess near-infinite phase velocity and wavelength and can be applied to create near-perfect displacement current shielding [10].

There are three hallmark properties of superconductors: zero dc resistance, the

perfect diamagnetic response under applied magnetic field, known as the Meissner effect, and coherent macroscopic quantum phenomena such as flux quantization and Josephson effects. In the superconducting state, the electrons are bonded with one another to form Cooper pairs with binding energy twice the superconducting gap energy, 2Δ [11]. A macroscopic ensemble of Cooper pairs is described by a coherent wave function: $\Psi = \Psi_0 \exp(i\phi)$. The flux quantization condition, playing an important role in this thesis, can be derived from this wave function as follows.

Consider a closed superconducting loop under an applied magnetic field. The electric current in the loop is related to the probability current of the wave function:

$$\vec{J_p} = \frac{\Psi_0^2}{m}(\hbar\vec{\nabla}\phi + 2e\vec{A}) \tag{1.1}$$

where m is the mass of an electron, $\hbar = h/(2\pi)$ is the reduced Planck constant, and e is the elementary charge. As a consequence of the Meissner effect, the magnetic field is zero deep inside the superconductor and the induced current has to flow in a thin layer near the surface and vanishes in the bulk. The current inside the superconductor is therefore zero, which requires

$$-\frac{\hbar}{2e}\vec{\nabla}\phi = \vec{A}$$

Integrating the above equation over a closed loop deep inside the superconductor, we have:

$$-\frac{\hbar}{2e}\oint \vec{\nabla}\phi \cdot d\vec{l} = \oint \vec{A} \cdot d\vec{l}$$

The left hand side can be evaluated using $\int \vec{\nabla}\phi \cdot d\vec{l} = 2n\pi$, which is a consequence of the single-valued wave function, since the wave function Ψ is invariant under 2π

changes in phase. The right hand side is just the definition of the total flux trapped in the loop. We then have

$$n\frac{h}{2e} = \Phi \tag{1.2}$$

where n is an integer and Φ is the magnetic flux enclosed in the loop. Physically, Eq.(1.2) states that the flux through a superconducting loop has to be quantized in the unit of flux quantum, $\Phi_0 = h/(2e)$.

Superconducting metamaterials take advantage of these three hallmark properties to achieve tunablity, low loss, and nonlinearity that are essential for many applications.

1.2 Different realizations of superconducting metamaterials

The constituent meta-atoms of the superconducting metamaterials can come in a variety of shapes and styles. Here we consider a number of designs relevant to the thesis.

1.2.1 Split ring resonator

A simple split-ring resonator (SRR) consists of a metallic loop with inductance L interrupted by a gap with capacitance C, whose self resonant frequency is dictated by its geometry, $\omega_0 = 1/\sqrt{LC}$. Some typical realizations of the SRR are summarized in Fig.1.1 .

The metamaterial is built from arranging a large one or two dimensional array of identical SRRs on a planar surface, forming a metasurface (e.g. a lithographically

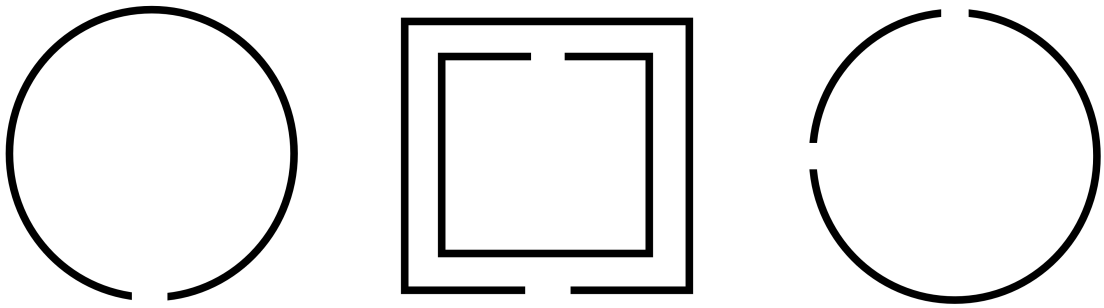

Figure 1.1: Different realizations of split ring resonator meta-atoms, where the black lines represent the metallic structure. All designs feature inductive loops and gap capacitors which give rise to the geometric resonance of the meta-atom, typically in the microwave frequency range.

defined pattern on a chip). These surfaces can also be stacked in the third dimension to achieve three dimensional metamaterials [12]. The metamaterial is operated in the configuration where external rf magnetic field is perpendicular to the metasurface to maximize the coupling between the applied field and the inductive loop in the meta-atom. When an SRR is driven at frequency ω near their resonance ω_0, the real part of the relative permeability of the effective medium can become negative:

$$\mu_{\mathrm{r,eff}} = 1 - \frac{f\omega^2}{\omega^2 - \omega_0^2 + i\Gamma\omega} \tag{1.3}$$

where f is the filling fraction of the meta-atoms, and Γ is the loss parameter [4]. The real part of the effective permeability attains negative real values for $\omega \gtrsim \omega_0$.

To achieve simultaneous negative permittivity, one can construct an array of metallic wires which posses a cut-off frequency analogous to the plasma frequency ω_p in a metal [13]. The effective permittivity of this system is given as [3]:

$$\epsilon_{\text{r,eff}} = 1 - \frac{\omega_p^2}{\omega^2 + i\gamma\omega} \tag{1.4}$$

where γ is the dielectric loss parameter. The real part of the permittivity becomes negative when the system is operated at $\omega < \omega_p$. Therefore, a metamaterial with negative index of refraction can be realized by combining the two systems: the SRR array with resonance ω_0 and the wire array with plasma frequency ω_p, given that $\omega_0 < \omega_p$ [14]. The results depend only on the geometry of the meta-atom but not any superconducting element. In fact, the early work on SRR metamaterials are based on normal lossy metals [15, 16, 17]. However, the loss in the medium is the limiting factor for achieving perfect negative index of refraction: $n = -1 + i0$. The loss can be reduced significantly by building the metamaterial out of superconductors [18, 19]. In addition, the magnetic field and temperature dependent penetration depth λ of the superconductor gives rise to a kinetic inductance L_k that introduces some tunability to the metamaterial [20, 19].

1.2.2 rf SQUID

Similar to the split-ring resonator, the radio frequency (rf) Superconducting QUantum Interference Device (SQUID) is also a self resonant structure containing a loop inductance L_{geo} and a gap capacitance C. What sets them apart from the split ring resonators is the inclusion of a Josephson junction, as illustrated in Fig. 1.2.

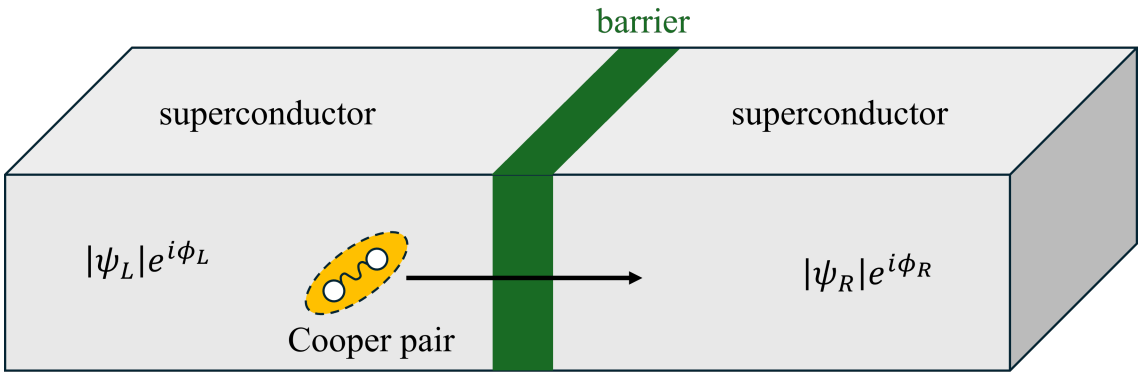

Figure 1.2: Schematic of a Josephson junction between two superconductors, where Cooper pairs can tunnel through the barrier to induce supercurrent even in the absence of a potential difference across the barrier.

The Josephson junction is a barrier made of insulator, normal metal, or a weakly superconducting material connecting two superconducting regions where the Cooper pairs are in a coherent state described by the macroscopic quantum wave function $|\psi|e^{i\phi}$ [21]. These pairs of electrons have finite probabilities of tunneling through the barrier depending on the gauge-invariant phase difference δ across the junction:

$$\delta = \phi_L - \phi_R - \frac{2\pi}{\Phi_0}\int_L^R \vec{A}(\vec{r}) \cdot d\vec{l}, \tag{1.5}$$

where $\vec{A}$ is the magnetic vector potential, $\Phi_0 = h/(2e) \approx 2.07 \times 10^{-15}$Wb is the flux quantum and the integral is taken from the left to the right edge of the barrier. The tunneling of charge carriers can induce a current without an applied potential difference between the two superconductors, as described by the dc Josephson effect:

$$I = I_c \sin\delta \tag{1.6}$$

where I_c is the critical current of the junction which is the maximum supercurrent that the junction can support. I_c depends on the geometry of the junction as well as the superconducting gap in each side, which reduces with increasing temperature [21].

The voltage across the junction is related to the rate of change of the gauge-invariant phase difference in the ac Josephson effect:

$$\frac{d\delta}{dt} = \frac{2\pi}{\Phi_0} V \tag{1.7}$$

If one differentiates Eq.(1.6) in time, the expression for the junction inductance L_{JJ} is obtained:

$$\begin{aligned} \frac{dI}{dt} &= I_c \cos\delta \frac{d\delta}{dt} = \frac{2\pi I_c \cos\delta}{\Phi_0} V \\ V &= \frac{\Phi_0}{2\pi I_c \cos\delta} \frac{dI}{dt} = L_{\mathrm{JJ}} \frac{dI}{dt} \end{aligned} \tag{1.8}$$

The dependence of the Josephson inductance on the gauge-invariant phase difference δ is illustrated in Fig. 1.3.

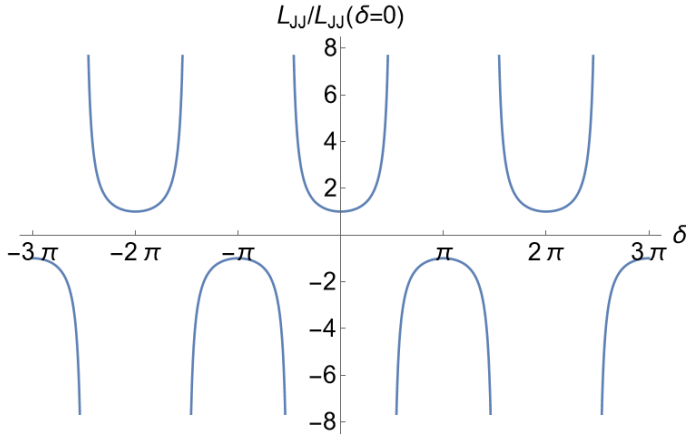

Figure 1.3: Junction inductance L_{JJ} as a function of the gauge-invariant phase difference δ.

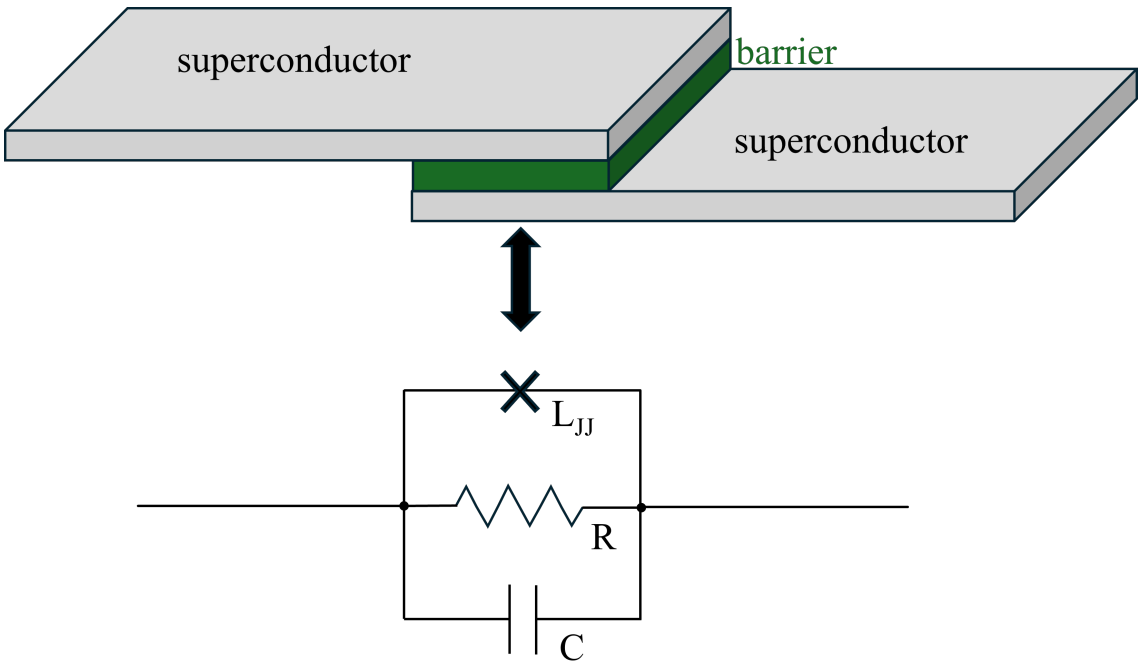

Figure 1.4: Schematic design of a Josephson junction made from two overlapping electrodes separated by a tunnel barrier, and the corresponding resistively and capacitively shunted junction circuit model.

The junction can be modeled as a parallel RLC circuit as shown in Fig. 1.4, where the supercurrent channel is represented by the junction inductance shown as a '$\times$', the normal current channel by the resistance R, and the displacement current channel by the capacitance C.

Using the circuit model where the junction inductance and the loop inductance are in parallel, the self resonance frequency of the rf SQUID can be determined as

$$\omega_0 = \sqrt{\left(\frac{1}{L_{\text{geo}}} + \frac{1}{L_{\text{JJ}}(\delta)}\right) C^{-1}} \,. \tag{1.9}$$

Compared to an SRR, the rf SQUID resonance clearly has enhanced tunability through the gauge-invariant phase difference dependence of L_{JJ}, as illustrated in

Fig. 1.3. A similar negative effective permeability is expected near the resonance of the rf SQUID as in the SRR under the weak excitation limit where linear dynamics of the junction is assumed [22, 23]. However, the key distinct feature of the rf SQUID as a meta-atom is its nonlinearity, which has been thoroughly examined and demonstrated by the two-tone intermodulation distortion (IMD) experimental results on rf SQUID metamaterials [24, 25]. The intrinsic nonlinearity of the Josephson effect, along with the extreme tunability of rf SQUIDs, leads to bistability [26, 27] and multistability [28, 29] in their response to rf and dc driving magnetic fields. This in turn leads to complex and hysteretic behavior, including the phenomenon of transparency [30]. Theory predicts that, under appropriate circumstances, driven rf SQUIDs will display strange nonchaotic attractors [31] and chaos [32, 33]. The rf SQUID metamaterials can also act as nonlinear gain media when immersed in passing electromagnetic waves [34, 35, 36, 37, 38, 39, 40], which is based on the nonlinear processes enabled by the Josephson effect that transfer energy to a signal at frequency f_s from a strong pump signal at frequency f_p.

In early theoretical and experimental works on rf SQUID metamaterials, the rf SQUIDs were packed together side-by-side in either one [41, 23, 42, 43] or two dimensions,[44] with substantial long-range (dipole-dipole) mutual inductance of the SQUID loops due to their close lateral proximity in the plane. Prior work examining collections of Josephson-junction-based devices in two dimensions, not necessarily metamaterials, include the following: superinductors made up of planar ladders of superconducting wires/loops incorporating Josephson junctions [45], and Josephson transmission lines utilizing SQUID arrays to create magneto-inductive waveguides

[46, 47]. Another type of Josephson metamaterial recently realized utilizes a tunable plasma edge created by current-biased linear arrays of Josephson junctions embedded in a three-dimensional waveguide [48], which interacts mainly with high frequency electric fields, rather than magnetic fields.

1.2.3 Qubit

Except for the macroscopic quantum phenomena in the rf SQUIDs (i.e. Josephson effect, and flux quantization), the treatment of these meta-atoms is mostly classical, where the dynamics is governed by classical electromagnetism. However, through careful engineering of the superconducting circuits, quantum mechanical two level systems can be created from the discrete energy levels. These devices are aptly named quantum bits (qubits), which form the building block for quantum computing. There are three different realizations of superconducting qubits that involve three different forms of tuning through an applied flux [49], voltage [50], and bias current [51, 52] as illustrated in Fig.1.5.

The quantum metamaterial created from an ensemble of these qubit meta-atoms is a rich platform for studying collective quantum phenomena, such as a breathing mode with an oscillating band gap [53], and superradiance [54, 55, 56, 57]. More generally, a system of quantum meta-atoms can be naturally employed for quantum simulation [58, 59] where a specific Hamiltonian that is analytically unsolvable can be realized and analyzed experimentally.

The three-junction flux qubit embedded in a coplanar waveguide (CPW) res-

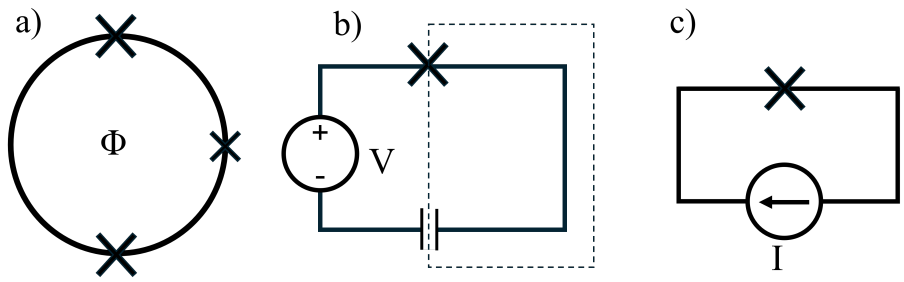

Figure 1.5: Schematics of three different kinds of superconducting qubits: flux, charge and phase qubits. a) A three junction flux qubit is made of a superconducting loop interrupted by three Josephson junctions and is tuned with external flux Φ. b) The Cooper-pair box, a type of charge qubit, is built by connecting a Josephson junction and a capacitor in series, creating a superconducting island between them as outlined by the dashed box. This qubit is controlled by the applied voltage V. c) A phase qubit consists of a Josephson junction and is biased by applied current I.

onator in particular is a good candidate for building a quantum metamaterial since the qubit presents a large anharmonicity, making the effective two level system robust to a large drive which could otherwise promote the system into higher excited states, can be tuned *in situ* with an applied magnetic field, and has a small foot print to enable uniform coupling of a large array to the cavity [42]. However, the low coherence time of these meta-atoms has been a limitation in their application. Although tremendous progress has been made in terms of design, fabrication and measurement techniques, which has led to orders of magnitude increase in coherence time [60, 61, 62], a comprehensive understanding of the responsible loss mechanisms under all operating conditions (e.g. temperature, excitation power, etc.) is still

missing. Therefore, an investigation of these losses in the superconducting circuit remains relevant.

1.3 Outline of Thesis

This thesis is organized as follows. Chapter 2 discusses the work on designing, fabricating, and characterizing the capacitively-coupled coplanar waveguide resonator originally intended for housing the quantum metamaterial consisting of three-junction flux qubits. The characterized loss of the resonator exhibits typical power dependence from saturation of two-level systems. However, the temperature dependence shows an anomalous reduction upon reducing temperature below TLS saturation. This effect is modeled by combining a discrete ensemble of TLS and the generalized tunneling model. This work has been published as [63].

Chapter 3 studies the conventional rf SQUID metamaterial with side-by-side geometry made from individual hysteretic rf SQUIDs whose geometric inductance is much larger than the junction inductance. The meta-atoms are modeled by the resistively and capacitively shunted junction (RCSJ) model. The strong inductive coupling among the SQUID meta-atoms combined with the multistability from the hysteretic SQUIDs gives rise to interesting nonlinear dynamics. In particular, the rf SQUID metamaterial is observed experimentally to undergo two flux quanta periodicity when tuned under the applied dc magnetic flux, contrary to the conventional one flux quantum periodicity.

Chapter 4 introduces the design of overlapping SQUID metamaterials and their

theoretical treatment. We incorporated strong capacitive coupling due to the overlapping capacitors formed between the two overlapping wiring layers from the two neighboring SQUIDs into the RCSJ model. We begin by modeling two overlapping SQUIDs and studying the response in both the linear and nonlinear high-frequency driving limits. By exploring a sequence of more and more complicated arrays, the formalism is eventually extended to the $N \times N \times 2$ overlapping metamaterial array, where we develop an understanding of the many $(8N^2 - 8N + 3)$ resulting resonant modes in terms of three classes of resonances. The capacitive coupling gives rise to qualitatively new self-resonant responses of rf SQUID metamaterials, and is demonstrated through analytical theory, numerical modeling, and experiment in the 10-30 GHz range on capacitively and inductively coupled rf SQUID metamaterials. This work has been published as [64].

Chapter 5 serves as a summary of the thesis and outlines directions for future research based on the results presented in this work.

Chapter 2

Two Level Systems in the Superconducting Coplanar Waveguide Resonator

Two-dimensional (2D) planar high internal quality factor (Q_i) superconducting resonators have been widely fabricated and investigated in recent times for applications such as single photon detectors [65], kinetic inductance detectors [66], and quantum buses in quantum computing technology [60]. A 2D superconducting resonator to house a qubit metamaterial intended for both resonant and dispersive readouts of the qubits, as done in Ref. [67], is designed and fabricated. This chapter discuses the characterization of the 2D resonator and establishes a thorough understanding of the relevant loss mechanisms.

In microwave measurements, although all qubits are operated at an excitation frequency well below the superconducting gap energy, microwave photons can be absorbed by quasiparticles, which in turn interact with the phonon bath, creating non-equilibrium distributions of both quasiparticles and phonons [68, 69, 70, 71]. This process affects the population of quasiparticles, in addition to pair-breaking processes induced by cosmic rays [72] higher order microwave harmonics, and stray infrared radiation [73, 74, 75]. These non-equilibrium quasiparticles are one limiting factor on superconducting resonator Q_i and qubit coherence, which can reduce both the qubit relaxation time (T_1^{Qubit}) and the coherence time (T_2^{Qubit}) [76].

Another comparable loss mechanism ubiquitous in 2D superconducting resonators is the dissipation incurred by the interaction between the resonant electric field and the two-level system (TLS) [77, 78, 79, 80, 81, 82, 83, 84, 85, 86, 87, 88, 89, 90, 27, 91]. Despite the elusive microscopic origin of the TLS (some recent works suggesting hydrogen impurities in alumina as one candidate for the TLS [92, 93]), TLSs can be simply modeled as electric dipoles that couple to the microwave electric field. In general, TLSs are abundant in amorphous solids and can also exist in the local defects of crystalline materials. They are found in three kinds of interfaces in the superconducting resonators: the metal-vacuum interface due to surface oxide or contaminants; the metal-dielectric substrate interface due to residual resist chemicals and buried adsorbates; and the dielectric substrate-vacuum interface with hydroxide dangling bonds, processing residuals, and adsorbates [94]. To address these issues, different kinds of geometry of coplanar waveguide (CPW) structure have been proposed and fabricated, with more care given to the surface treatment to alleviate the TLS losses [95]. For example, a trenched structure in the CPW helps to mitigate the metal-dielectric TLS interaction with the resonator fields [96, 97]. These efforts have improved the 2D resonator intrinsic quality factor to more than 1 million in recent realizations of high-Q_i resonators [96, 98, 99, 100, 97]. Nevertheless, TLSs still exist even in extremely high Q_i 3D superconducting radio frequency cavities used in particle accelerator applications [101]. Recently, other sources of the TLS loss have been proposed based on quasiparticles trapped near the surface of a superconductor [102].

Clearly the TLS loss is a universal issue in superconducting resonators. However, at microwave frequencies, this loss was long thought to be constant under low microwave power and low temperature [78, 103, 104, 80, 79, 90]. Measurements in this regime were limited due to the constraints of noise levels in both electronic equipment and the thermal environment. Therefore, experimental investigation of the TLS at low temperatures and microwave excitation are important, and would assist the superconducting quantum information community to understand its effect on operating quantum devices.

We have designed a 2D half wavelength resonator to host many three-junction flux qubits for the study of the collective behavior of quantum meta-materials. Analogous to cavity quantum electrodynamics, qubits serve as artificial meta-atoms with mutual coupling [105, 53, 106, 107, 108] and can be read out through the dispersive frequency shift of the cavity[109, 42, 110]. Theoretical publications discussing the physics of qubit arrays coupled to the harmonic cavities predict a number of novel collective behaviors of these meta-atoms [111, 112, 113]. In this chapter, we report our finding on the TLS loss in the low power and low temperature limit of this particular design of capacitively-coupled half-wavelength resonator, without the qubits. The technique of very low power microwave measurement with low noise to enhance the signal-to-noise ratio (SNR) is critical for measuring this behavior of TLSs.

2.1 Design and fabrication of the resonator

The CPW resonator in this work is designed with a tapering geometry at the center that gradually shrinks the signal line width w and the spacing between the signal line and ground s as shown in Fig.2.1 (b). The smaller size enhances the coupling to the qubit meta-atoms to be hosted in the center. The CPW resonator chip was mounted on a printed circuit board bolted inside a copper box. Several lumps of indium were pressed between the on-chip ground planes and the copper box ground to achieve a continuous ground contact, which mitigates parasitic resonant microwave modes due to uneven electrical grounding. The indium lumps also secured the chip in the center of the printed circuit board. The on-chip transmission line is wire-bonded to the center conductor of the transmission line on the printed circuit board by gold wires. Finally, the copper box is capped by a copper lid to eliminate stray light illumination. The schematics of the setup are shown in Fig.2.1

The resonator is designed with a center line width $w = 50\ \mu m$ and spacing $s = 30\ \mu m$ (the distance between center conductor line and ground plane as illustrated in Fig. 2.2(b)) to maintain the characteristic impedance near 50 Ω in the meander part. At the center of the resonator a tapering structure narrows the center line width down to $w = 1\ \mu m$ and spacing to $s = 12\ \mu m$, which gradually increases the characteristic impedance to 100 Ω at the resonator center. A model of the CPW microwave resonator was constructed in a microwave simulation software, CST (Computer Simulation Technology) Microwave Studio. The model structure represents the entire CPW resonator and coupling capacitors, both of which repro-

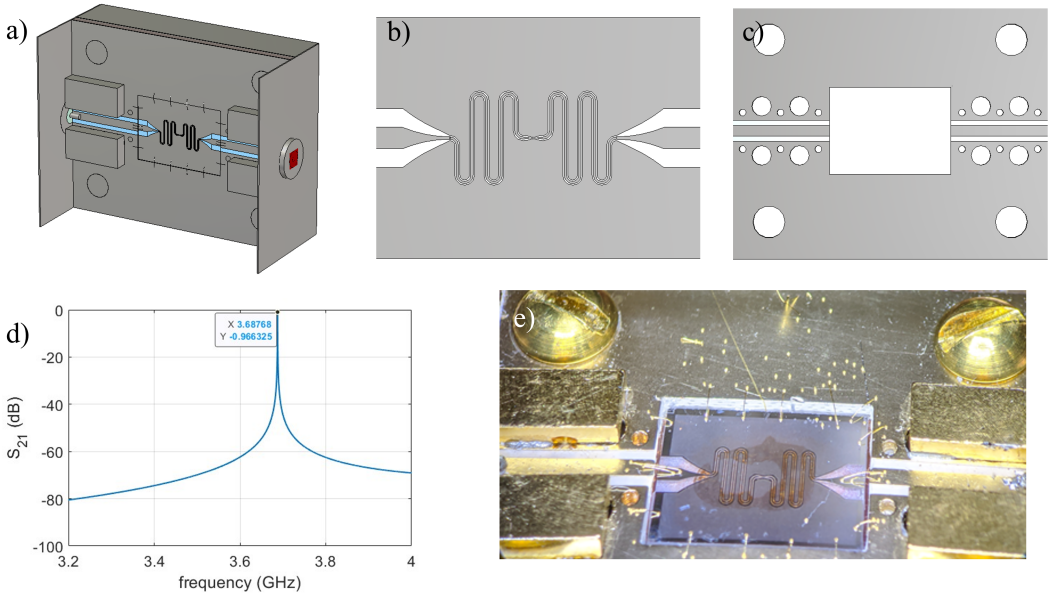

Figure 2.1: [Design and schematics of the CPW resonator sample. a) Model of the CPW resonator sample with its packaging in CST. The design of the CPW resonator chip and the printed circuit board for interfacing the chip and the coaxial connectors in the measurement setup are shown in b) and c). The gray areas in b) are superconductor while the white regions are exposed insulating substrate. d) The simulated transmission through the entire setup determines the fundamental resonance at 3.688 GHz. e) a picture of the sample in its package.

duce the geometrical structure in our superconducting chip. The superconductor is modeled as a perfect electric conductor. The simulation above is obtained from the finite element frequency domain solver in CST and predicts the fundamental resonance at 3.688 GHz.

2.1.1 Fabrication of coplanar waveguide resonator

The aluminum (Al) half-wavelength ($\lambda/2$) CPW resonator was fabricated using standard photo-lithography procedures. First, a 70 nm thick Al film was deposited on a 3-inch diameter sapphire wafer using thermal evaporation technology with a background pressure of $\sim 3 \times 10^{-7}$ mbar. Then a thin SHIPLEY1813 photo-resist was coated on top of the film and exposed to UV through the designed photomask. The UV exposed wafer was developed and then wet etched by commercial Transene Aluminum Etchant. The remaining photoresist was stripped off by acetone and the entire wafer was cleaned by methanol and isopropanol. Finally, the wafer was coated in a protective photo-resist and then diced into many chips. After dicing, the protective photo-resist was removed.

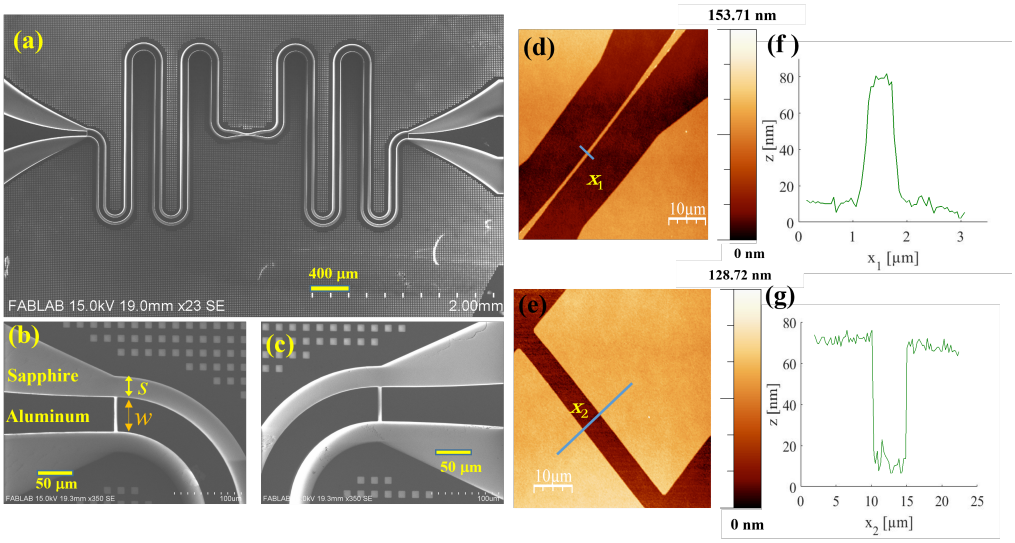

Figure 2.2: Pictures of the CPW resonator. a) An SEM image of the aluminum CPW resonator on a sapphire substrate. b) c) Zoom-in SEM images of the left and right capacitive couplers. d) AFM image highlighting the tapered center conductor with a 1 μm wide center trace near the center of the resonator, and e) AFM topography image highlighting the 5 μm wide capacitive coupler from b) or c). Note that the AFM probe scanning direction is 45 degrees with respect to the center-line direction to reduce AFM scanning artefacts. f) Line scan profile of AFM image to show thickness of the center line in d). g) Line scan profile of the capacitive coupler. Both line scans show an Al film thickness of 70 nm.

The fabricated CPW resonator sample is shown in Fig. 2.2 (a). The entire resonator is surrounded by many 10 μm by 10 μm vortex moats. The resonator is symmetric and capacitively coupled through 5 μm gaps (Fig. 2.2 (b) and 2.2 (c)) in the center conductor. A topographic image of the narrowed resonator center section is shown in Fig. 2.2 (d) with a critical dimension around $w = 1$ μm in width. Line

cuts shown in the atomic force microscopy (AFM) images in Fig. 2.2 (d), (e) show that the Al film is 70 nm thick.

2.2 Transmission measurement on the coplanar waveguide resonator

2.2.1 Resonator transmission measurement setup

The device was placed in a closed Cryoperm cylinder in a BlueFors (BF-XLD 400) croygen-free dilution refrigerator (base temperature 10 mK) to minimize any stray DC magnetic field, and the shield was thermally anchored to the mixing chamber plate. The microwave excitation was attenuated by a series of attenuators in the input line at different cooling stages in the dilution fridge before going into the resonator to reduce the noise. The transmitted signal was amplified twice through a cryogenic amplifier and a room temperature amplifier before being measured by a Keysight N5242A vector network analyzer (VNA). The low power measurements were performed using the smallest intermediate frequency bandwidth (1 Hz) of the VNA, with a 400 kHz span across the resonance, following 5 averages to reduce the random noise. A thru calibration of the setup was performed in a separate cool down to determine the overall loss/gain in the transmission lines leading to the resonator. The schematics of the setup is shown below in Fig.2.3

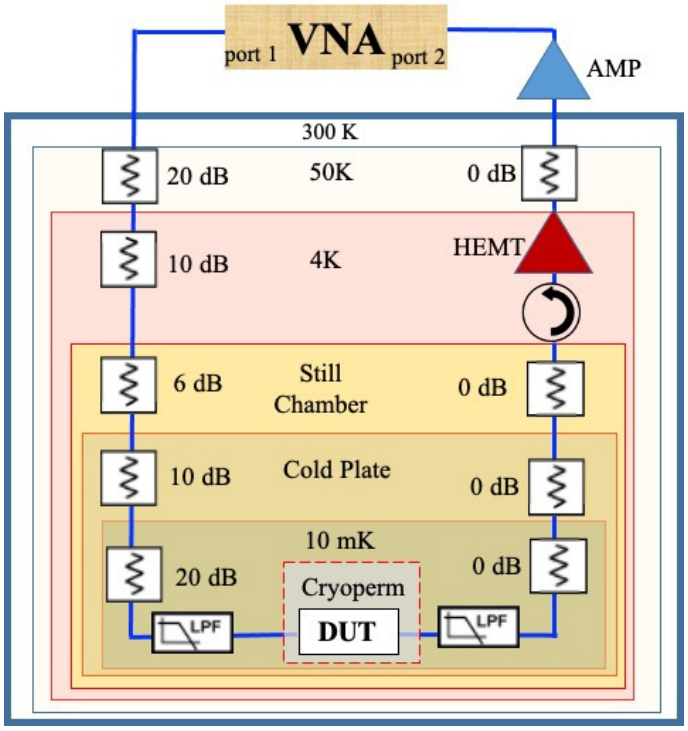

Figure 2.3: Schematic of the microwave measurement setup for the study of the aluminum $\lambda/2$ resonator. The VNA at room temperature sends a signal from port 1 to the cryostat. The signal is attenuated at each stage of the cryostat before passing through the low-pass filter (LPF) and entering the device under test (DUT). The DUT is surrounded by a Cryoperm magnetic shield. The output signal also passes through a low-pass filter before going through 0-dB attenuators that thermalize the coaxial cable center conductor. The signal passes through an isolator and is amplified at the 4 K stage and at room temperature, before entering the VNA in port 2.

A variety of attenuators (produced by XMA) are used on each cryogenic stage to thermalize the center conductors of the coaxial cables. The total attenuation in the input line is -66 dB. Both the input line and output line on either side of

the device are filtered by commercial microwave low-pass filters. The input line has a Marki Microwave low pass filter (`FLP-1460`) with 3-dB cutoff frequency at 14.6 GHz and the output line has another Marki Microwave low pass filter (`FLP-1250`) with 3-dB cutoff frequency at 12.5 GHz. The output line goes through the cryogenic isolator (QUINSTAR Technology `QCI-G0301201AM`) with working frequency band 3-12 GHz. The signal is amplified by 36 dB using a commercial high-electron mobility transistor (HEMT) amplifier (Low Noise Factory `LNF-LNC0.3_14A` with typical noise temperature 4.2 K) at the 4K stage, and then further amplified by 37 dB using another room temperature HEMT amplifier (Low Noise Factory `LNF-LNC2_6A` with typical noise temperature 50 K at ambient temperature).

2.2.2 Experimental Data

The measured transmitted signal ($\hat{S}_{21}(f)$) has a fundamental ($\lambda/2$) resonance peak around $f = 3.644$ GHz at the fridge base temperature when sweeping the frequency, f. The complex $\hat{S}_{21}(f)$ signal is fitted to an equivalent circuit model of a two-port resonator capacitively coupled to external microwave excitation [114, 71].

$$\hat{S}_{21}(f) = |S_{21,\text{in}}||S_{21,\text{out}}| \left(\frac{Q_L/Q_c}{1 + 2iQ_L(\frac{f}{f_0} - 1)} e^{i\phi} \right) + C_0 \tag{2.1}$$

where $|S_{21,\text{in}}|$ and $|S_{21,\text{out}}|$ are the net loss or gain in the transmission of the input and output line, respectively. Q_L is the loaded quality factor. Q_c is the coupling quality factor representing the dissipation to the external circuit, $i = \sqrt{-1}$, f_0 is the resonance frequency of the half-wavelength ($\lambda/2$) CPW resonator, ϕ is the phase

and C_0 is an offset in the complex S_{21} plane due to background contributions[114]. The measured transmission amplitude vs. frequency and the fit to the complex $\hat{S}_{21}$ are shown in Fig. 2.4.

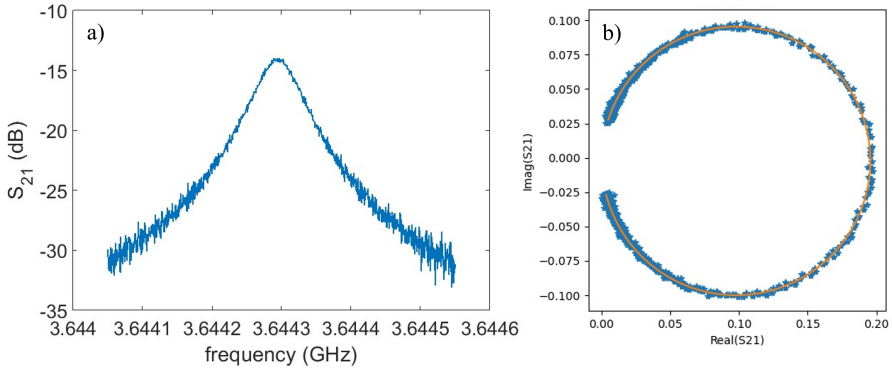

Figure 2.4: Sample S_{21} signal measured at the fundamental mode of the resonator. a) The measured magnitude of transmission $S_{21}(dB)$. b) Fit to the complex transmission $\hat{S}_{21}$ shown as the the orange curve.

The internal quality factor, Q_i, inversely proportional to the the internal loss, $\delta = Q_i^{-1}$, is extracted from the identity $1/Q_L \equiv 1/Q_i + 1/Q_c$. The absorbed power P_{ab} of the resonator is characterized by the average number of circulating microwave photons in the cavity on resonance, which can be estimated using the approximation [71, 115] $\langle n \rangle = \frac{2Q_L^2 P_{in}}{Q_c \hbar \omega_0^2}$ for a two-port device, where $\hbar$ is the reduced Planck constant, and $\omega_0 = 2\pi f_0$ is the angular frequency of the resonance.

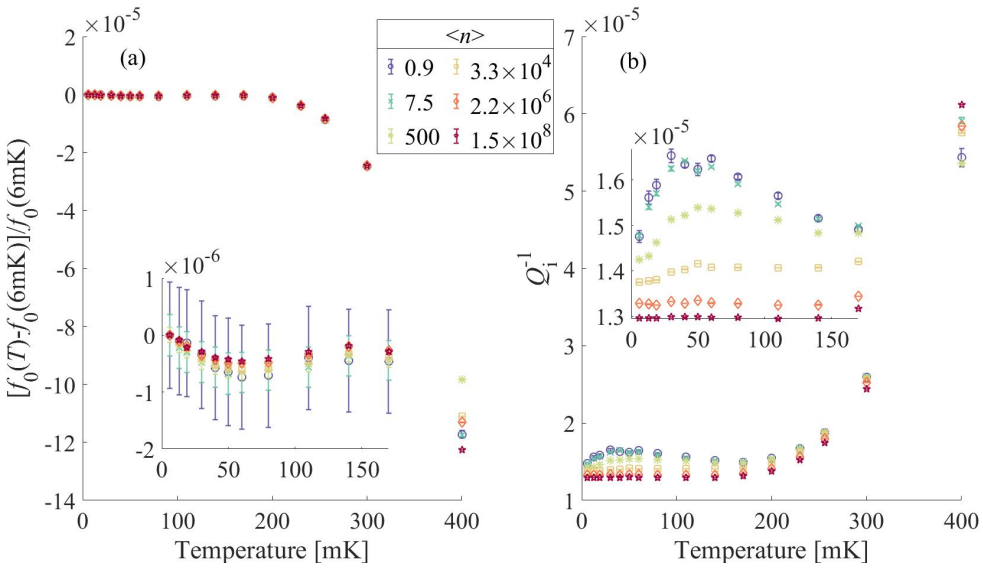

Figure 2.5: a) Temperature dependent first harmonic resonant frequency shift $\Delta f/f_0(6\text{mK})$, with $\Delta f = f_0 - f_0(6\text{mK})$ of the $\lambda/2$ Aluminum co-planar waveguide resonator on sapphire substrate measured at different excitation powers (average photon numbers). Here $f_0(6\text{mK})$ is the resonance frequency measured at the base temperature for each excitation power . b) Temperature dependent loss (inverse of intrinsic quality factor, Q_i^{-1}) at its first harmonic frequency of a Aluminum co-planar waveguide resonator on sapphire substrate measured at different circulating photon numbers $\langle n \rangle$. Some of the error bars are smaller than the data point such as those for the high power and temperature measurements.

Figure 2.5(a) illustrates the temperature dependence of the fractional resonant frequency shift from the resonance frequency at lowest temperature, $(f_0(T) - f_0(6\text{mK}))/f_0(6\text{mK})$, for different circulating microwave photon numbers inside the CPW resonator, where 6 mK is the measured fridge base temperature. The resonance frequencies start at their maxima at the fridge base temperature and then

show local minima around 60 mK. This phenomenon seems to be independent of the average circulating photon number and can be explained by the standard tunneling model (STM) of TLSs [104]. Upon further increasing the temperature above 150 mK, the resonance frequencies quickly decrease due to the thermal quasiparticles, which increases the real and imaginary parts of the surface impedance of the superconducting resonator. The inset focuses on the low temperature regime and shows a very small power dependence that is qualitatively similar to the strong field correction to the frequency shift in the STM proposed by Gao, which predicts smaller frequency shifts for higher power [116].

The temperature dependence of the measured internal loss is shown in Fig. 2.5(b). For high power measurements ($\langle n \rangle > 10^6$), the loss is constant at low temperatures (below 150 mK) which is expected for the typical non-interacting TLSs. At higher temperatures, the loss increases due to thermal quasiparticles. For low power measurements ($\langle n \rangle < 10^6$), starting from the minimum temperature, the loss has an unusual increase at low temperatures, from the base temperature to a peak at 40 mK. The loss then drops with increasing temperature following the equilibrium value of the population difference in TLSs [82, 117]. Similar to the high power measurements, the loss rises again above 150 mK due to thermal quasiparticles. The observed loss decrease with decreasing temperature from 40 mK to 10 mK has not been explicitly acknowledged and discussed in prior work of microwave superconducting resonators until recently [118]. Indications of an upturn in $Q_i(T)$ has otherwise been attributed to poor SNR and therefore treated as not statistically significant[117, 119].

2.3 Model of the frequency shifts in the coplanar waveguide resonator

The power and temperature dependent frequency shifts are explained by the TLS and the dynamics of quasiparticles. These two mechanisms could overlap and become difficult to distinguish in the operation of many superconducting devices, including resonators and qubits, [76]. A simple model that combines both quasiparticles and TLSs contribution in one equation describes the resonance frequency Δf data in Fig. 2.5,[87, 95, 120]

$$\begin{aligned}\frac{f_0(T)-f_0(0)}{f_0(0)} =& \frac{\delta_0}{\pi}\left(Re\left[\Psi(\frac{1}{2}+\frac{\hbar\omega}{2\pi i k_B T})\right]-log(\frac{\hbar\omega}{2\pi k_B T})\right) \\ &- \frac{\alpha}{2}\left(\frac{n_{qp}}{2N_0\Delta_{S0}}\left[1+\sqrt{\frac{2\Delta_{S0}}{\pi k_B T}}\exp(\zeta)I_0(\zeta)\right]\right) \end{aligned} \tag{2.2}$$

where $\zeta = \frac{hf_0}{2k_BT}$, f_0 is the resonance frequency as a function of the temperature, δ_0 is the zero temperature and zero power loss tangent from the TLS, $\Psi(\cdot)$ is the digamma function, $\alpha = L_{kinetic}/L_{total}$ is the kinetic inductance fraction of the CPW resonator, N_0 is the single spin density of states, Δ_{S0} is the aluminum superconducting gap at zero temperature, and $I_0(\cdot)$ is the 0th order modified Bessel function of the first kind. The first term in Eq. 2.2 represents the frequency shift caused by the TLS mechanism [82, 85] and the second term is the frequency shift due to quasiparticles using the Bardeen-Cooper-Schrieffer (BCS) model for $k_BT,\ hf_0 \ll \Delta_{S0}$, and written explicitly in terms of quasiparticle number density n_{qp} [120], including both thermal and non-equilibrium quasiparticles. However, the model with only thermal quasiparticle $n_{th} = 2N_0\sqrt{2\pi k_B T\Delta_{S0}}\exp\left(-\frac{\Delta_{S0}}{k_BT}\right)$ (valid for $T \ll T_c$) seems to match the measurement sufficiently well, where $N_0 = 10^{47}\ J^{-1}\,m^{-3} \approx 1.74\times10^4 \mu eV^{-1}\mu m^{-3}$

is the single spin electronic density of states at the Fermi level [69, 75].

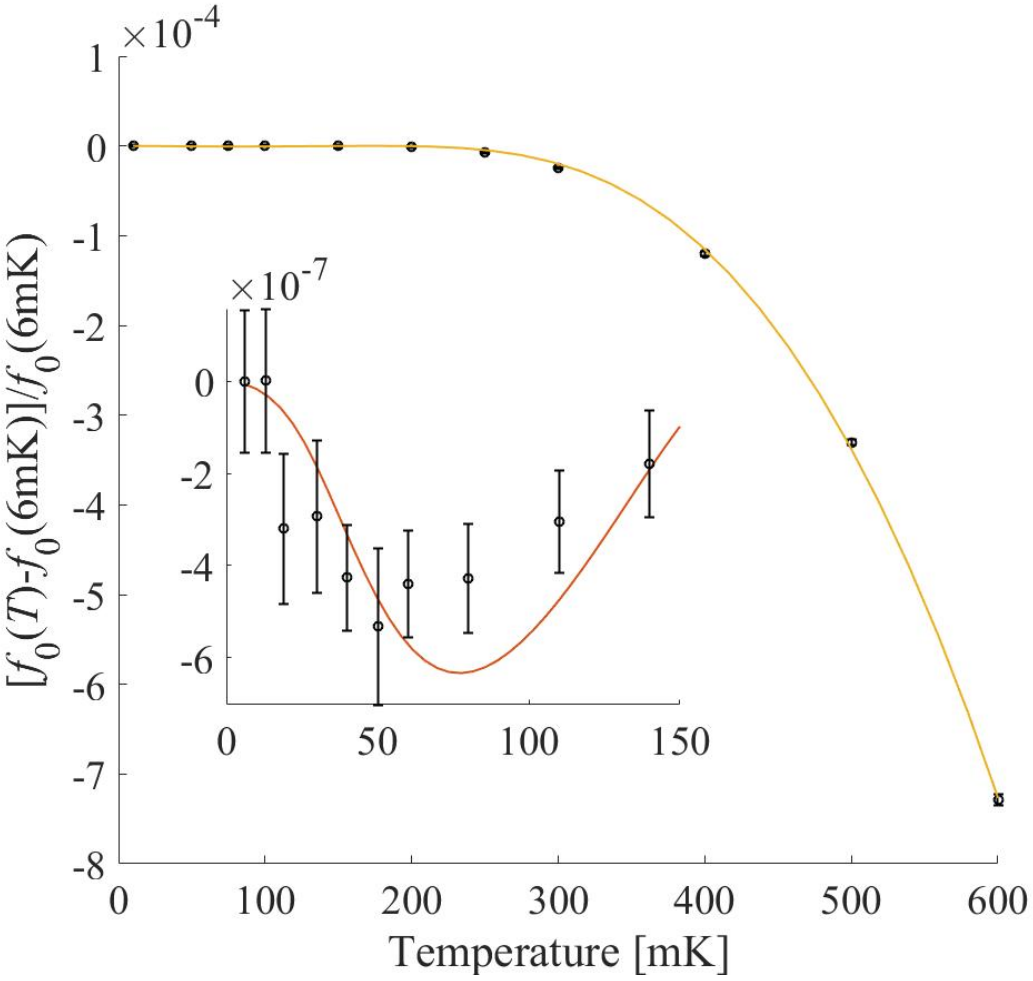

Figure 2.6: Temperature dependent fundamental ($\lambda/2$) mode resonant frequency $f_0(T)$ of the Al CPW resonator on sapphire substrates at an external microwave excitation creating around one circulating photon. The inset highlights the low temperature regime where the frequency shift is dominated by the TLS mechanism. The dots are experimental data and solid line is the model fit to Eq. (2.2).

The fit to the frequency shift data is shown in Fig.2.6, and the extracted fitting parameters indicate that the aluminum superconducting gap at zero temperature is $\Delta_{S0} \sim$170 μeV, a value close to the BCS gap approximation which is $1.76 k_B T_c$ with

transition temperature $T_c = 1.12\,K$. The values of the other fitting parameters are $\alpha \approx 0.014$, and $\delta_0 = 9.6 \times 10^{-6}$. The values of α and δ_0 are consistent with other results on a variety of similar superconducting resonators[85, 89, 121, 95].

2.4 Model for the internal loss in the coplanar waveguide resonator

Since the temperature dependent internal loss is dominated by the well-known thermal quasiparticles above 150 mK, this analysis focuses only on the low temperature data, which is well described by the two level systems model. We start with a brief review of the conventional standard tunneling model (STM) of TLSs [77, 79, 82] that was first developed to understand the specif heat and thermal conductivity measurements in glassy materials [122].

2.4.1 Conventional model for two-level systems

The conventional STM is based on a simple model of quantum mechanical double well potential which is described by the Hamiltonian, $H_{TLS} = \frac{1}{2}\begin{pmatrix} -\Delta & \Delta_0 \\ \Delta_0 & \Delta \end{pmatrix}$ where Δ is the asymmetry of the double well potential and Δ_0 is the tunneling barrier energy between the potential wells [82]. The splitting between the two eigenenergies of the TLS is thus $\varepsilon = \sqrt{\Delta^2 + \Delta_0^2}$. A typical resonator hosts an ensemble of TLS with different values of Δ and Δ_0 with their (assumed continuous) distribution function given as $P(\Delta, \Delta_0) = P_0/\Delta_0$, where $P_0 \approx 10^{44} J^{-1} m^{-3}$ is the density of states for TLSs. The distribution function is uniform in Δ in the conventional TLS model, but could take on a very weak dependence $\propto \Delta^{\mu}$ with $\mu \sim 0.3$ for a system

of very strongly interacting TLSs, [123, 124, 125]. For simplicity and generality, the following model uses the conventional distribution function, which is constant in Δ. The fit with non-zero μ can be found in the Sec. 2.4.4.3.

The dynamics of a single TLS can be described by the linearized Bloch equations of the pseudospin $\vec{S}(t) = \vec{S}^0(t) + \vec{S}^1(t)$, where $\vec{S}^0$ is the solution to the homogeneous system without the external field, and $\vec{S}^1$ is the linear solution with frequency ω of the driving field. Under the rotating wave approximation, the Bloch equations become: [82, 116, 126]

$$i\frac{d\langle S^+\rangle}{dt} = \Omega\langle S_z^0\rangle - (\omega - \varepsilon/\hbar + i\Gamma_2)\langle S^+\rangle \tag{2.3}$$

$$\frac{d\langle S_z^0\rangle}{dt} = \Omega\,\mathrm{Im}\langle S^+\rangle - \Gamma_1\left(\langle S_z^0\rangle - m\right)\Big) \tag{2.4}$$

where $S^+ = S_x^1 + iS_y^1$, Γ_1 and Γ_2 are the two phenomenological rates that describe the longitudinal (S_z) and transverse ($S_{x,y}$) relaxations, and $m = \tanh(\varepsilon/(2k_BT))/2$ is the equilibrium value of the $\langle S_z^0\rangle$. The Rabi frequency Ω characterizing the absorbed power, $\Omega \propto \sqrt{P_{ab}}$, is defined as

$$\Omega = \frac{2d_0\Delta_0}{\hbar\varepsilon}|\vec{E}| \tag{2.5}$$

where d_0 is the maximum transition electric dipole moment of the TLS with energy splitting ε, $\vec{E}$ is the applied microwave electric field on the TLS dipole.

In STM, the dielectric response of a single TLS can be obtained from the stationary solution to $\langle S^+\rangle$ [77, 79, 126]:

$$\chi_{\mathrm{res}} = \frac{\langle S^+\rangle}{\Omega} = \frac{m(\omega - \varepsilon/\hbar - i\Gamma_2)}{(\omega - \varepsilon/\hbar)^2 + \Gamma_2^2(1 + \Omega^2\Gamma_1^{-1}\Gamma_2^{-1})} \tag{2.6}$$

The single TLS loss corresponds to the imaginary part of the response function in Eq.(2.6) which is in the form of a Lorentzian in $\varepsilon/\hbar$ centered at ω with a width:

$$w = \Gamma_2\sqrt{1+\kappa} \tag{2.7}$$

where $\kappa = \Omega^2\Gamma_1^{-1}\Gamma_2^{-1}$. The total dielectric loss is simply the integral of the single TLS contribution Eq.(2.6) over the distribution of TLSs Eq.(2.33) [79, 82, 116].

$$\delta_{TLS} = \frac{1}{\epsilon_r\epsilon_0}\iiint P(\varepsilon,\Delta_0)\left(\frac{\Delta_0 d_0}{\varepsilon}\right)^2\frac{\cos^2\theta}{\hbar}\frac{m\Gamma_2}{\Gamma_2^2(1+\kappa)+(\varepsilon/\hbar-\omega)^2}d\varepsilon d\Delta_0 d\theta \tag{2.8}$$

where $\epsilon_r\epsilon_0$ is the permittivity of the host dielectric material, $P(\varepsilon,\Delta_0)$ is obtained from Eq.(2.33) with a change of variable from Δ to ε and θ is the angle between the applied electric field and the TLS dipole moment.

For a typical TLS with $\varepsilon/h \approx 5$ GHz and at reasonably low temperatures and powers, the width of its response $w \approx \Gamma_2 \sim 1$ MHz $\ll \omega$. Due to this sharp Lorentzian response function, the total loss is dominated by the resonant TLS whose energies $\varepsilon \sim \hbar\omega$. Before analytically evaluating the integral in Eq.(2.8), the expressions for $\Gamma_{1,2}$ need to be introduced.

The longitudinal relaxation rate (Γ_1) of a single TLS is dominated by the phonon process: [103, 104, 80, 116]

$$\Gamma_1 = \left(\frac{\Delta_0}{\varepsilon}\right)^2\left[\frac{\gamma_L^2}{v_L^5}+\frac{2\gamma_T^2}{v_T^5}\right]\frac{\varepsilon^3}{2\pi\rho\hbar^4}\coth(\frac{\varepsilon}{2k_BT}) = \left(\frac{\Delta_0}{\varepsilon}\right)^2\Gamma_1^{\max} \tag{2.9}$$

where γ_L and γ_T are the longitudinal and transverse deformation potentials, respectively, v_L and v_T are the longitudinal and transverse sound velocities, ρ is the mass density, and $\Gamma_1^{\max}$ is the maximum Γ_1 for the TLS with energy splitting ε, when $\Delta_0 = \varepsilon$.

The transverse relaxation rate (Γ_2) is defined as

$$\Gamma_2 = \Gamma_2^{\rm ph} + \Gamma_{\rm ds}$$

$$\text{where} \quad \Gamma_2^{\rm ph} = \Gamma_1/2 \quad \text{and} \quad \Gamma_{\rm ds} \sim 10^{-3}(k_B T/\varepsilon_{\rm max})^{\mu} k_B T/\hbar \quad [127, 124] \qquad (2.10)$$

$\Gamma_{\rm ds}$ is the dephasing rate of the resonant TLS energy level ε, caused by its interactions with thermally activated TLSs whose $\varepsilon \lesssim k_B T$, valid for low temperature measurement ($T < 1$ K) [127], and is typically larger than the longitudinal relaxation rate Γ_1. μ again comes from the Δ^{μ} energy dependence in the distribution function $P(\Delta, \Delta_0)$. $\mu = 0$ for conventional model and $\mu \sim 0.3$ for an ensemble of very strongly interacting TLSs.

After substituting the expressions for Γ_1, Γ_2 and Ω from Eqs. (2.9, 2.10, 2.5) into the integral for the loss Eq.(2.8) and using $\mu = 0$, the famous STM prediction of the TLS loss is obtained, [104]

$$\delta_{TLS} = \frac{\pi P_0 d_0^2}{3\epsilon_r \epsilon_0} \frac{\tanh\left[\hbar\omega/(2k_B T)\right]}{\sqrt{1 + (\Omega/\Omega^c)^2}} \qquad (2.11)$$

where $\Omega^c \propto \sqrt{\Gamma_1^{\rm max} \Gamma_2}$ is the critical Rabi frequency that characterizes the saturation of the TLS. The loss is expected to have an inverse square root dependence on power after the TLS saturation, $\delta_{TLS} \sim \Omega \propto P_{ab}^{-0.5}$ for $\Omega \gg \Omega^c$.

To compare the STM with the experimental data, the power dependence of the measured loss $Q_i^{-1}(T)$ is shown below in Fig.2.7 at different temperatures below the onset of thermal quasiparticle effects.

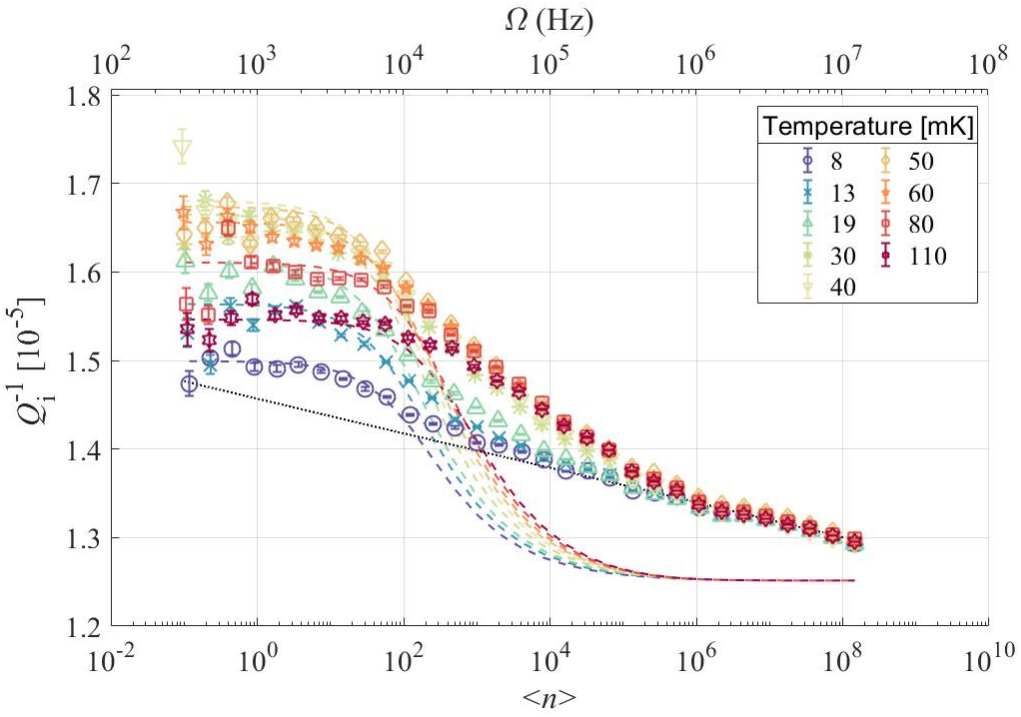

Clearly, the loss shows a gradual power dependence above the low-power sat-

uration, similar to previous experimental observations[128, 89, 129, 98], and is not consistent with STM from Eq.(2.11) shown as the dashed curves. The Rabi frequency Ω on the upper axis, as given in Eq.(2.5), depends on the electric field experienced by the TLS dipole, which is estimated from the electric field calculation in the CST simulation as shown in Fig.2.8.

According to the simulation, on the resonance at 3.647 GHz, the electric field can attain a maximum of 6×10^8 V/m on the substrate-vacuum interface at the corner of the center strip that is part of the coupling capacitor on the input side. This calculation was done under a 0.5 watt excitation level. An average electric field of the adjacent area is estimated to be 1.16×10^8 V/m. By scaling this power down to that required to achieve one circulating photon in the resonator, we estimate the average electric field of the region nearby the coupling capacitor of the resonator to be 0.2 V/m. The Rabi frequency Ω on the x-axis in Fig. 2.7 and 2.10 is then estimated from this electric field and a dipole moment $d_0 \sim 8 \times 10^{-30}$C m or 2.4 Debye based on [130, 131].

To account for the slower power dependence, many improvements on the STM have been proposed, such as introducing more than one species of TLSs in the dielectrics, [132, 133, 134, 135, 136] and accounting for the nonuniform field distribution in the resonator [86]. In addition, there is another approach that generalizes the STM to include a random telegraph noise on the TLS energy level due to strong interactions between a few TLSs [137, 126, 124], resulting in the generalized tunneling model (GTM) that can produce the logarithmic power dependence shown as the black dotted line in Fig. 2.7.

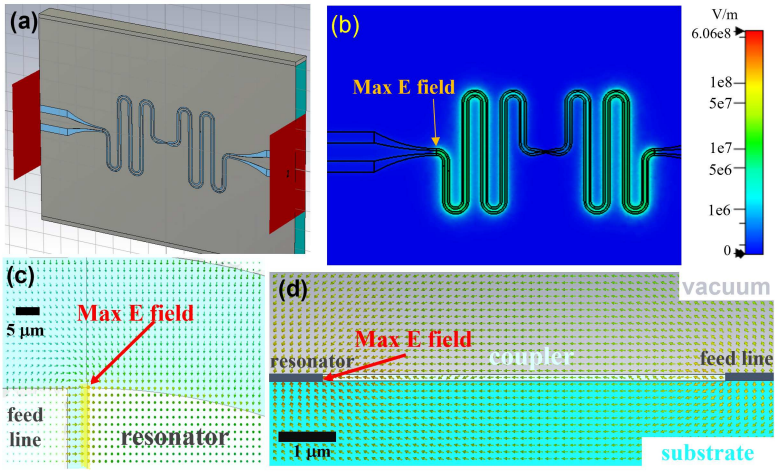

Figure 2.8: CPW resonator model in CST microwave studio. a) The geometry of the CPW resonator model in CST. The coupling capacitors and the entire resonator structure reproduce those in the experiment. b) The top view of the E-field strength on the substrate-vacuum interface at the fundamental resonance of 3.647 GHz, which has a node in the center of the resonator, a typical standing wave pattern in a half wavelength resonator. The E-field vector is mostly in-plane and perpendicular to the center line. (c) The close-up top view of the E-field vector plot on the substrate-vacuum interface near the coupling capacitor. The maximum E-field is found around the corner of the center strip that is part of the coupling capacitor. The E-field that contributes to the TLS model is estimated from the average of the field along the resonator side of the coupler about $1.16 \times 10^8\ Vm^{-1}$, highlighted in the yellow-orange line. (d) The side view of the E-field vector plot on the cross section through the coupler at the center strip corner. The maximum is at the corner of the center strip on the substrate-vacuum interface.

However, none of the existing models predicts a strong temperature dependence of loss below the TLS saturation. To interpret this unusual loss reduction in our aluminum resonators at low power and low temperature, we go beyond the assumption of a uniform distribution of TLSs and invoke the discrete TLS contribution to the loss at low temperatures. A simple modification that sums over the discrete and detuned responses of TLSs near the resonance as in Eq. (2.30) is proposed. When combined with GTM, this model reproduces the full power and temperature dependence of the loss data: the gradual power dependence at high power as well as the observed anomalous temperature dependence of loss for $\langle n \rangle < 10^2$ and $T < 50$ mK. It should be emphasized that the discrete TLS assumption is independent of GTM. Attempts to apply the discrete and detuned TLS formalism to the modified versions of STM are summarized in Sec.2.4.4. To lay the foundations of the proposed model, the following sections introduce key concepts of GTM and derive several expressions used in the final model.

2.4.2 Effect of fluctuators on the TLS loss

The dephasing rate $\Gamma_{\rm ds}$ introduced in Eq.(2.10) describes the spectral diffusion resulting from an average of weak interactions among TLS [82, 124], which cannot incorporate stochastic and discrete strong interactions following a Poisson process, such as those from fluctuators [138, 139, 126, 137, 124, 140]. Fluctuators can be modeled as incoherent TLS whose $\Gamma_2^{\rm ph} \geq \varepsilon$, as opposed to the coherent TLSs introduced above in STM[124].

The fluctuators can be modeled as following a thermally activated tunneling process with rate $\gamma = \gamma_0 \exp(\frac{-E_a}{k_B T})$, where E_a is the activation energy. For a uniform distribution of $E_a \in [E_{a,min},\ E_{a,max}]$, the distribution of the fluctuator rates is thus $P(\gamma) = P_{\text{f0}}/\gamma$ in an exponentially wide range $[\gamma_{\min}, \gamma_{\max}]$, with $\gamma_{\min} = \gamma|_{E_a = E_{a,max}} \sim$ constant in T and $\gamma_{\max} = \gamma|_{E_a = E_{a,min}} \propto \exp(\frac{-E_{a,min}}{k_B T})$ [126, 124]. The random telegraphic noise with a slow jump rate γ happens infrequently during the measurement time, and thus cannot be averaged over to contribute to the spectral diffusion as in Eq. (2.10).

If strongly coupled with the coherent resonant TLSs, the fluctuators can move the latter in and out of resonance with a jump rate γ and effectively create a random telegraphic noise on the energy level $\varepsilon \to \varepsilon + \xi(t)$, which modifies the Bloch equations as follows [82, 116, 126]:

$$
\begin{aligned}
i\frac{\mathrm{d}\langle S^+\rangle}{\mathrm{d}t} &= \Omega\langle S_z^0\rangle - (\omega - (\varepsilon + \xi(t))/\hbar + i\Gamma_2)\langle S^+\rangle \\
\frac{\mathrm{d}\langle S_z^0\rangle}{\mathrm{d}t} &= \Omega\,\mathrm{Im}\langle S^+\rangle - \Gamma_1\left(\langle S_z^0\rangle - m\right)
\end{aligned}
\tag{2.12}
$$

The exact solution to the Bloch equation will depend on the relationship between $\gamma, \Omega, \Gamma_1^{\max}$, and Γ_2. $\Gamma_1^{\max}$ is abbreviated to Γ_1 for clarity in the following discussion, which mainly focuses on the interaction between fluctuators and one resonant TLS. Thus, the distribution of values of Γ_1 for an ensemble of TLSs is not invoked until the last step of integration to calculate the loss, and is not relevant to the fluctuators-induced effect. To systematically present the predictions from the different solutions to the mater equations under different limits, this section is

structured according to the three regimes of the rate γ, namely high $\gamma > \Omega, \Gamma_2$, intermediate $\gamma \approx \Omega$ or Γ_2, and low $\gamma < \Gamma_1$.

2.4.2.1 Low γ fluctuators

For low γ fluctuators ($\gamma_{\min} < \gamma < \Gamma_1$), the single TLS response is given by the stationary solution to Eq.(2.3,2.4), since the TLS dynamics is much faster than the jump rates γ. We can further separate the analysis for two different types: the common weakly-coupled fluctuators which shift the energy level of TLSs by a small energy ξ and result in a widening of the spectral width of the TLS, and the rare strongly-coupled fluctuators whose ξ is large enough and produce large stochastic jumps on the TLS energy level ε.

The weakly-coupled fluctuators induce detunings that follow a Lorentzian distribution with width $\Gamma_{\rm f} \propto (k_{\rm B}T/\hbar)(k_{\rm B}T/\varepsilon_{\max})^{\mu} \lesssim \Gamma_2$ similar to the spectral diffusion[124]:

$$P(\xi(t)) = \frac{1}{\pi}\frac{\Gamma_{\rm f}}{\Gamma_{\rm f}^2 + \xi(t)^2} \tag{2.13}$$

The single TLS response under a single weak fluctuator can be obtained from Eq.(2.6) by replacing ε with $\varepsilon + \xi(t)$ [124]:

$$\chi_{\rm res} = \frac{\langle S^+ \rangle}{\Omega} = m\frac{\omega - (\varepsilon + \xi(t))/\hbar - i\Gamma_2}{(\omega - (\varepsilon + \xi(t))/\hbar)^2 + \Gamma_2^2(1+\kappa)} \tag{2.14}$$

where $\kappa = \Omega^2/(\Gamma_1\Gamma_2)$. Integrating the imaginary part of Eq.(2.14) over the distribution of detuning $P(\xi(t))$ and the distribution of the fluctuator rate $P(\gamma)$ in the

range $\gamma \in [\gamma_{\min}, \Gamma_1]$, one can obtain the single TLS loss:

$$\delta(\varepsilon) = P_{\mathrm{f0}} \ln\left(\frac{\Gamma_1}{\gamma_{\min}}\right) \frac{m}{\sqrt{1+\kappa}} \frac{\Gamma_2\sqrt{1+\kappa} + \Gamma_{\mathrm{f}}}{(\Gamma_2\sqrt{1+\kappa} + \Gamma_{\mathrm{f}})^2 + (\omega - \varepsilon/\hbar)^2} \tag{2.15}$$

The second fraction is in the form of a Lorentzian with width $\Gamma_2\sqrt{1+\kappa} + \Gamma_{\mathrm{f}}$, and the first term is the same as the STM formula. The STM loss is recovered if one sets $\Gamma_{\mathrm{f}} = 0$. For a continuous distribution of TLSs such as $P(\varepsilon, \Delta_0)$, the total internal loss is calculated by integrating Eq.(2.15) over the distribution function $P(\varepsilon, \Delta_0)$:

$$\delta_{TLS} = \frac{P_{\mathrm{f0}}}{\epsilon_r \epsilon_0} \iiint P(\varepsilon, \Delta_0) \left(\frac{\Delta_0 d_0}{\varepsilon}\right)^2 \frac{\cos^2\theta}{\hbar} \ln\left(\frac{\Gamma_1}{\gamma_{\min}}\right) \frac{m}{\sqrt{1+\kappa}} \frac{(\Gamma_2\sqrt{1+\kappa} + \Gamma_{\mathrm{f}})}{(\Gamma_2\sqrt{1+\kappa} + \Gamma_{\mathrm{f}})^2 + (\varepsilon/\hbar - \omega)^2} d\varepsilon d\Delta_0 d\theta \tag{2.16}$$

Clearly, the last fraction in the integral is a Lorentzian which evaluates to a constant after integration over ε, resulting in the same prediction for internal loss as the STM [124].

The distribution $P(\xi(t))$ may not apply to the strongly-coupled fluctuators which completely shift the TLS in and out of resonance, since there are typically only a few strong fluctuators in surface dielectrics [124]. They contribute to the imaginary part of a single TLS response as a random telegraph noise (i.e. $\xi(t)$ in Eq.(2.14)). The internal loss is still in the form of the STM loss Eq.(2.6), but could be reduced by the strong fluctuators occasionally moving the coherent TLS in and out resonance.

Three methods were used to estimate the average effect of the low γ fluctuators on the internal loss. Intuitively, we could estimate the total loss by summing up the

contribution from all the TLSs near the resonance. The key assumption is the low density of the resonant TLSs which justifies the discrete treatment. An estimation based on [141] yields ~ 1 TLS in the bandwidth of the resonance for a volume of TLS-inhabiting dielectrics around 30 μm^3, which supports our assumption. The first method is thus a summation of all the single TLS loss in the form of Eq.(2.15) near the resonance with $\varepsilon = ...\hbar(\omega+\nu) - 2\Delta\varepsilon, \hbar(\omega+\nu) - \Delta\varepsilon, \hbar(\omega+\nu), \hbar(\omega+\nu) + \Delta\varepsilon, \hbar(\omega+\nu) + 2\Delta\varepsilon, ...$, and is given in Eq.(2.30). A finite detuning less than the average energy spacing in the TLS spectrum, $\hbar\nu < \Delta\varepsilon$, is included such that the TLS closest to resonance will not give a diverging response as $T \to 0$, and instead contributes to the loss as $m\Gamma_2\Delta\varepsilon/(\hbar\nu^2) \propto T$ at low temperature. This detuning is a consequence of a sparse TLS distribution where $\Delta\varepsilon/\hbar \gtrsim \Gamma_2$. Thus, any given TLS is rarely on resonance due to the low density of states. We should emphasize that this treatment is independent from the master equation formalism for the fluctuators, and can be applied to STM with low TLS density where the use of distribution function $P(\varepsilon, \Delta_0)$ is inappropriate.

The second method assumes that the detuning ν is not much larger than Γ_2 so that the distribution $P(\xi(t))$ for the weakly-coupled fluctuators can still be applied to the case $\xi/\hbar \sim \nu \lesssim \Gamma_2$. The probability of a TLS with a detuning ν to be on resonance under the influence of the low γ fluctuators can be calculated by integrating $P(\xi(t))$:

$$P_{\text{on resonance}} = \frac{1}{\pi}\arctan(\frac{\xi}{\hbar\Gamma_{\text{f}}})\Big|_{\hbar(\nu-\Gamma_2)}^{\hbar(\nu+\Gamma_2)} \tag{2.17}$$

which also leads to a monotonic increasing temperature dependence below 50 mK

as in the data.

The third method estimates the number of strongly-coupled fluctuators capable of moving the coherent TLS in and out of resonance. Since the energy drift caused by fluctuators is directly related to the interaction energy, which is dipole-dipole like, $U(r) \sim r^{-3}$, we could find a volume around the near-resonant TLS which hosts fluctuators that interact strongly enough. For $\Gamma_2 < \nu$, the TLS is detuned, and the criterion for being a strong fluctuator is that the induced energy shift can bring the TLS in resonance such that $\hbar(\nu - \Gamma_2) < U(r) < \hbar(\nu + \Gamma_2)$. This volume is a spherical shell with inner and outer radius defined by the bounds on the interaction energy $U(r)$. For $\Gamma_2 > \nu$, the TLS is already in resonant, and the strong fluctuators are those that move the TLS out of resonance, with $U(r) > \hbar(\Gamma_2 - \nu)$. This volume is a sphere with radius defined by $U(r) = \hbar(\Gamma_2 - \nu)$. The total number of strong fluctuators can then be estimated as:

$$N_{\text{strong fluctuators}} = P_0 V_{\text{strong fluctuators}} k_{\text{B}} T \propto \begin{cases} \frac{2\Gamma_2^2}{\nu^2 - \Gamma_2^2} & (\Gamma_2 < \nu) \\ \frac{\Gamma_2}{\Gamma_2 - \nu} & (\Gamma_2 > \nu) \end{cases} \tag{2.18}$$

where the density of states for TLSs from Eq.(2.33) is used, and the energy range is set to the thermal energy $k_{\text{B}}T$. The two expressions Eq.(2.17,2.18) are plotted below as a function of Γ_2.

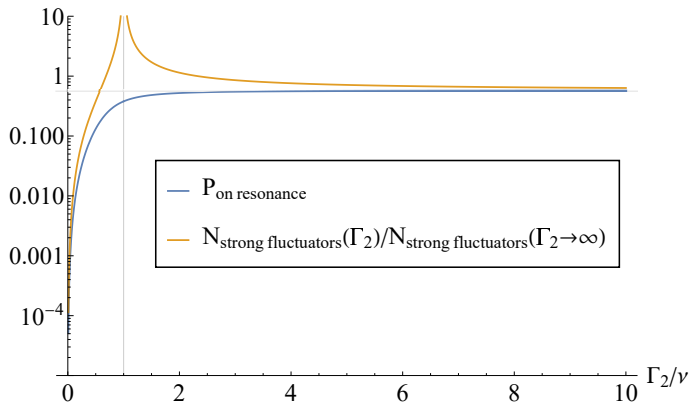

Figure 2.9: The blue curve is the probability for a TLS detuned with ν to be resonant under the influence of weakly-coupled fluctuators. The yellow curve is the normalized estimated number of strongly-coupled fluctuators. They are plotted as a function of Γ_2, which also represents their temperature dependence. It can be concluded that for both the strong and weak fluctuators, as temperature decreases ($\Gamma_2/\nu \to 0$) the TLS are increasingly detuned.

The x axis of Fig. 2.9, Γ_2 is normalized by the detuning ν. When Γ_2 increases to ν, the probability for TLSs to be resonant under the weak fluctuators (Blue curve in Fig. 2.9) approaches a constant $2/\pi \arctan(\Gamma_2/\Gamma_f)$, which is denoted by the horizontal line where $\Gamma_f = 0.8\Gamma_2$. The interpretation of the number of strong fluctuators (Yellow curve in Fig. 2.9) is more nuanced. When $\Gamma_2 < \nu$, the coherent TLS itself is detuned, the strong fluctuators shift the TLS in resonance, and therefore their number is positively correlated with the TLS response. However, for $\Gamma_2 > \nu$, the strong fluctuators shift the already resonant TLS out of resonance, and thus their number is negatively correlated with the TLS response. Consequently, as Γ_2 or temperature increases, the resonant response becomes stronger. The divergence near

$\Gamma_2 \sim \nu$ represents the failure of this estimation in the range where any arbitrarily small shift can move the TLS in and out of resonance, and the strong fluctuator volume goes to infinity. In reality, this volume is bounded by the host material for TLSs. For $\Gamma_2 \gg \nu$, the case of the TLS exactly on resonance is recovered, and the number of strong fluctuators is clearly independent of temperature. A numerical estimate of $N_{\text{strong flucutators}}(\Gamma_2/\nu \to \infty)$ gives $\lesssim 1$ for typical weakly interacting TLSs [124]. In both estimates, the detuned TLS becomes resonant more often as Γ_2 or temperature increases, which qualitatively explains the increase in loss in temperature at low temperatures in the measurement.

It should be noted that if applied to the TLS exactly on resonance ($\Gamma_2/\nu \to \infty$), the above arguments will lead to the conclusion that low γ fluctuators present no temperature dependence for both the strong and weak low γ fluctuators, which forms the basis of the claim that no anomalous temperature dependence on the loss is expected in the original GTM work [124].

2.4.2.2 High γ fluctuators

For fluctuators that induce fast jump rates on the resonant TLS, $\gamma \gtrsim \Omega, \Gamma_{1,2}$, their effects on the dynamics are described by the master equation [126]:

$$\frac{\partial \rho}{\partial t} + \frac{\mathrm{d}}{\mathrm{d}\vec{S}}\left(\frac{\mathrm{d}\vec{S}}{\mathrm{d}t}\rho\right) = \gamma[\delta(\langle S_z^0\rangle - m)\delta(\langle S_x^1\rangle)\delta(\langle S_y^1\rangle) - \rho] \tag{2.19}$$

where $\vec{S} = (\langle S_x^1\rangle, \langle S_y^1\rangle, \langle S_z^0\rangle)$ and ρ is the probability for a TLS to be in the state $\vec{S}$. The case for high γ fluctuators is particularly simple, where the fast random telegraph noise is averaged out. Thus, $\mathrm{d}\vec{S}/\mathrm{d}t$ is solved from Eq.(2.3,2.4) with $\xi(t) =$

0. The average y-component response of the single TLS with energy splitting ε can then be solved from the master equation Eq.(2.19) as:

$$\overline{\langle S_y^1 \rangle} = \int \rho \langle S_y^1 \rangle \mathrm{d}\vec{S} = \frac{m\Omega}{\sqrt{1+\frac{\Omega^2}{(\gamma+\Gamma_1)(\gamma+\Gamma_2)}}} \frac{\sqrt{(\gamma+\Gamma_2)^2+\Omega^2\frac{\gamma+\Gamma_2}{\gamma+\Gamma_1}}}{(\gamma+\Gamma_2)^2+\Omega^2\frac{\gamma+\Gamma_2}{\gamma+\Gamma_1}+(\omega-\varepsilon/\hbar)^2} \tag{2.20}$$

where again the second fraction is in the form of a Lorentzian with width w given as

$$w = \sqrt{(\gamma+\Gamma_2)^2+\Omega^2\frac{\gamma+\Gamma_2}{\gamma+\Gamma_1}} \tag{2.21}$$

This width is guaranteed to be larger than ν for large γ. Therefore, we could still proceed with integrating the Lorentzian (the second fraction) in Eq.(2.20) over ε, which leads to a constant independent of temperature and power. After another integration over the distribution $P(\gamma)$, we can express the total internal loss as

$$\delta = m\delta_0 \mathrm{arcsinh}\left(\frac{\gamma}{\Omega}\right)\Big|_{\max(\Omega,\sqrt{\Gamma_2^2+\nu^2})}^{\gamma_{\max}} \xrightarrow{\gamma_{\max}\gg\Omega\gg\Gamma_1,\Gamma_2} m\delta_0 \ln(\frac{\gamma_{\max}}{\Omega}) \tag{2.22}$$

This expression explains the high power limit of the data in Fig. 2.7 where the losses from different temperatures converge to a linear trend in the linear-log plot. This high γ fluctuator loss will saturate to a constant value $\sim m\ln\left(\gamma_{\max}/\sqrt{\Gamma_2^2+\nu^2}\right)$ once $\Omega \lesssim \Gamma_2$. Thus, it will not affect the low power behavior of the TLS loss. The rate $\sqrt{\Gamma_2^2+\nu^2}$ is calculated from the characteristic rate of the TLS dynamics with $\xi(t)=0$ and characterizes the boundary between fast and intermediate jump rates γ.

2.4.2.3 Intermediate γ fluctuators

When γ is comparable to Ω and/or $\Gamma_{1,2}$, several jumps could be expected before the TLS relaxes to its ground state. Therefore, the interaction among the fluctuators need to be accounted for, which complicates the modelling compared to the low and high γ fluctuators. The dynamical effect is still described by a similar master equation Eq.(2.19) for high γ fluctuators with ρ replaced by ρ_k for each different state k of the fluctuators. Moreover, the fast random telegraph noise is not averaged out, and we need to do the substitution $\varepsilon \to \varepsilon_k = \varepsilon + \xi_k$. The dynamics of the transverse component can be treated as stationary in a rotating wave approximation ($d\langle S^+\rangle/dt = 0$). The resulting master equation to be solved is then [126]

$$\frac{\partial \rho_k}{\partial t} + \frac{\mathrm{d}}{\mathrm{d}z}[(\Gamma_1(m-z) - \Xi_k z)\rho_k] = \gamma_{kn}\rho_n \tag{2.23}$$

$$y_k = \frac{-\Omega\Gamma_2}{\Gamma_2^2 + (\varepsilon_k/\hbar - \omega)^2} z_k \tag{2.24}$$

where $\langle S_z^0\rangle$, $\langle S_y^1\rangle$ are abbreviated as z and y, $\Xi_k = \Omega^2\Gamma_2/[(\varepsilon_k/\hbar - \omega)^2 + \Gamma_2^2]$, and γ_{kn} is the transition rate between the fluctuator state k and n. Γ_1 and m are not subscripted with k since their ε_k dependence contains a slowly varying function in the form $\tanh[\varepsilon_k/(2k_\mathrm{B}T)]$ that should not vary much near the resonance. z_k can be solved from Eq.(2.23) and substituted in Eq.(2.24) to obtain y_k

$$y_k = \frac{-\Omega\Gamma_2}{\Gamma_2^2 + (\varepsilon_k - \omega)^2} \frac{p_k}{1 + \frac{1+p_k\gamma/\Gamma_1}{\gamma+\Gamma_1}\Xi_k} \tag{2.25}$$

where p_k is the probability for a TLS to have energy ε_k, and $\gamma = \sum_n(\gamma_{kn} + \gamma_{\mathrm{nk}})$ is the total effective jump rate for fluctuator state k. The single TLS y-component

response with the energy level ε_k can then be calculated from integrating Eq.(2.25) over the probability distribution $P(\gamma) \propto 1/\gamma$

$$\overline{y_k} \propto \frac{-m\Omega\Gamma_2}{\Gamma_2^2 + (\varepsilon_k - \omega)^2} \left(\frac{1}{1+\kappa_k} \ln \frac{\gamma_\mathrm{h}}{\gamma_\mathrm{l}} + \frac{\kappa_k(1-p_k)}{(1+\kappa_k)(1+p_k\kappa_k)} \ln \frac{1+\kappa_k+\gamma_\mathrm{h}/\Gamma_1(1+p_k\kappa_k)}{1+\kappa_k+\gamma_\mathrm{l}/\Gamma_1(1+p_k\kappa_k)} \right) \tag{2.26}$$

where $\kappa_k = \Xi_k/\Gamma_1$ is reduced to $\kappa = \Omega^2/(\Gamma_1\Gamma_2)$ when the TLS is on resonance ($\varepsilon_k = \hbar\omega$). The upper and lower bounds for the intermediate fluctuators are obtained from the TLS dynamics as $\gamma_\mathrm{h} \gtrsim \Xi_k + \Gamma_1$, $\sqrt{\Gamma_2^2 + (\varepsilon_k/\hbar - \omega)^2} \gtrsim \gamma_\mathrm{l}$.

The total loss can then be obtained from summing up the contribution from all the different energy levels of TLSs just as in Eq.(2.30).

$$\begin{aligned} \delta =& \frac{\delta_0}{\pi} \sum_k \frac{m\Gamma_2}{\Gamma_2^2 + (\varepsilon_k - \omega)^2} \\ & \left(\frac{1}{1+\kappa_k} \ln \frac{\gamma_\mathrm{h}}{\gamma_\mathrm{l}} + \frac{\kappa_k(1-p_k)}{(1+\kappa_k)(1+p_k\kappa_k)} \ln \frac{1+\kappa_k+\gamma_\mathrm{h}/\Gamma_1(1+p_k\kappa_k)}{1+\kappa_k+\gamma_\mathrm{l}/\Gamma_1(1+p_k\kappa_k)} \right) \end{aligned} \tag{2.27}$$

If one assumes that the energy drift ξ_k induced by the individual fluctuator follows the same Lorentzian distribution $P(\xi)$ as the weak fluctuators in Sec.2.4.2.1, the total drift will follow a Lorentzian distribution with a wider width $P(\xi) \propto N\Gamma_\mathrm{f}/((N\Gamma_\mathrm{f})^2 + \xi^2)$ for N fluctuators affecting the TLSs in the case of intermediate fluctuators. For a large enough ensemble of fluctuator, this width $N\Gamma_\mathrm{f}$ is comparable to the detuning ν , then the broadening of the TLS energy levels will ensure the existence of the resonant TLS. Therefore, the continuous distribution of TLSs $P(\varepsilon, \Delta_0)$ can be applied. The final result of the internal loss is then converted into an integral

$$\delta = \delta_0 \int \frac{m\Gamma_2}{\Gamma_2^2 + (\varepsilon - \omega)^2} \left(\frac{1}{1+\kappa(\varepsilon)} \ln \frac{\gamma_h}{\gamma_l} + \frac{\kappa(\varepsilon)(1-p)}{(1+\kappa(\varepsilon))(1+p\kappa(\varepsilon))} \right. \tag{2.28}$$
$$\left. \ln \frac{1+\kappa(\varepsilon)+\gamma_h/\Gamma_1(1+p\kappa(\varepsilon))}{1+\kappa(\varepsilon)+\gamma_l/\Gamma_1(1+p\kappa(\varepsilon))} \right) \mathrm{d}\varepsilon$$

$$\delta \propto m \left(\frac{1}{1+\kappa} \ln \frac{\gamma_\mathrm{h}}{\gamma_\mathrm{l}} + \frac{\kappa(1-p)}{(1+\kappa)(1+p\kappa)} \ln \frac{1+\kappa+\gamma_\mathrm{h}/\Gamma_1(1+p\kappa)}{1+\kappa+\gamma_\mathrm{l}/\Gamma_1(1+p\kappa)} \right) \tag{2.29}$$

where we replace κ_k with a continuous variable $\kappa(\varepsilon)$. It is also assumed that all the states near the resonance shared the same probability: $p_k = p \ \forall k$, and is typically small for a system of many ($\sim$ 10) fluctuators (see supplementary material for [126]), and thus ignored in the final model. $\gamma_{h,l}$ are the upper and lower bounds of the jump rates and are defined previously. These limits translate to a range in power Ω where the intermediate fluctuate model dominates the power dependence of the loss: $\Gamma_2 \gtrsim \Omega \gtrsim \sqrt{\Gamma_1\Gamma_2}$. Within this range, the loss from intermediate γ fluctuators is approximately $\delta_0 \ln[(\Omega^2+\Gamma_2^2)/(2\Omega^2)]$, a faster logarithmic power dependence than Eq. (2.22). At higher powers, the loss becomes constant $\sim m\ln(2)$. At lower power, the loss saturates to another constant $m\ln(\Gamma_2/\Gamma_1)$.

In summary, the three different fluctuation rates correspond to three different power ranges for the power dependence of the loss. In the high power limit $\Omega \gtrsim \Gamma_2$, the effect of fluctuators that induce large γ dominates and leads to a logarithmic power dependence; in the intermediate power regime $\Gamma_2 \gtrsim \Omega \gtrsim \sqrt{\Gamma_1\Gamma_2}$, the fluctuators with intermediate γ give rise to a faster logarithmic power dependence, but meanwhile the saturation of TLSs just as in STM has a comparable or even stronger power dependence and overlap in the same power regime; and finally in the low power limit $\Omega < \sqrt{\Gamma_1\Gamma_2}$, the typical TLS saturation in STM is recovered as the contributions

from all three different types of fluctuators become constant in power. The above description qualitatively matches our experimental observation in Fig. 2.7.

2.4.3 Fit to the internal loss measurements

Although the power dependence of our data as in Fig. 2.7 agrees with the effect of fluctuators in the GTM, the original model does not reproduce the observed temperature dependence. The GTM predicts the same temperature dependence of the TLS loss in the low power limit as in STM [124] shown as the orange dashed curve in Fig. 2.10 (b), which clearly deviates from the extracted low power loss of TLSs. To reconcile this difference, we propose a simple modification to the TLS model to account for the discrete coherent TLS near the resonance. Consider the discrete form of the integral in the TLS loss for low γ fluctuators, Eq. (2.16),

$$\delta_{TLS} = \frac{P_0 d_0^2 \Delta\varepsilon}{3\hbar\epsilon_r\epsilon_0} \ln\left(\frac{\Gamma_1}{\gamma_{\min}}\right) \sum_n \tanh\left(\frac{\varepsilon_n}{2k_B T}\right) \frac{\Gamma_2 + \Gamma_f/\sqrt{1+\kappa}}{(\Gamma_2\sqrt{1+\kappa} + \Gamma_f)^2 + (\varepsilon_n/\hbar - \omega)^2} \quad (2.30)$$

where the index n denotes the coherent TLS near the resonance and $\Delta\varepsilon$ is the average energy spacing in the TLS spectrum. We believe that Eq.(2.30) is justified since the number of coherent TLSs inside the resonator bandwidth is ~ 1 for a TLS-inhabiting volume around $100\mu m^3$ [141], and many previous works have observed the individual TLS in microwave resonators [142, 143, 130, 131]. For the TLS exactly on resonance, $\varepsilon = \hbar\omega$, its loss $\delta_{TLS} \sim \Gamma_2^{-1} \propto T^{-1}$ at low power, and is the classic result for the single TLS model in STM[144]. However, this stands in clear contrast to the observed reduction in loss at low temperature in Fig. 2.5 (b) and Fig. 2.10.

It is thus required that the TLS is not always on resonance ($\nu = \varepsilon_0/\hbar - \omega \neq 0$ where ε_0 stands for the energy level of the coherent TLS closest to resonance), a reasonable assumption given the sparse TLS distribution in the frequency spectrum for a small volume of TLS-inhabiting dielectrics. Mathematically, the width of the Lorentzian in the summation $w = \Gamma_2\sqrt{1+\kappa} + \Gamma_\mathrm{f}$ dictates the transition from the low temperature reduced loss to the high temperature equilibrium result. For small w, a discrete sum will deviate from the integral since the Lorentzian is under-sampled. While for a Lorentzian with large w, a discrete sum with the same sampling rate will approximate the integral better. Specifically, at low powers ($\kappa \ll 1$), $w = \Gamma_2 + \Gamma_\mathrm{f}$ increases with the temperature and $w = \Gamma_2 + \Gamma_\mathrm{f} \sim \nu$ marks the transition temperature between the two regimes. For low temperatures ($w \ll \nu$), the Lorentzian term becomes roughly proportional to $w = \Gamma_2 + \Gamma_\mathrm{f}$ which gives the almost linear temperature dependence of loss. For higher power, w increases with κ, which pushes the transition temperature lower and suppresses the low temperature reduction in loss. And eventually at high powers ($\kappa \gg 1$) such that $w > \nu$ for all temperatures, the equilibrium temperature dependence $m = (1/2)\tanh(\hbar\omega/(2k_BT))$ in STM is recovered in the entire temperature range. The same discrete summation can be applied to Eq. (2.29) for intermediate γ fluctuators. On the other hand, Eq. (2.22) for high γ fluctuators is only modified with the substitution $\Gamma_2 \to \sqrt{\Gamma_2^2 + \nu^2}$ due to the sparse TLSs assumption (See Sec.2.4.2.2). The final model that combines all three contributions is able to reproduce the full temperature ($T = 8 - 110$ mK) and power ($\langle n \rangle = 10^{-1} - 10^{8}$) dependence of the loss shown as the solid curves in Fig. 2.10 (a).

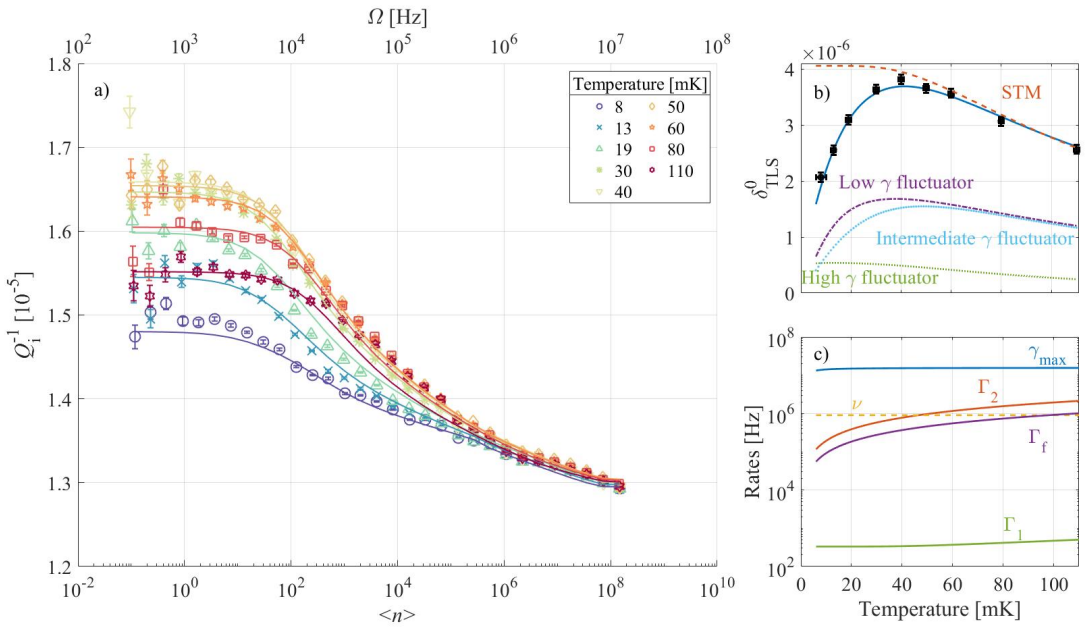

Figure 2.10: a) The least squares fit of the discrete GTM, together with a constant background loss, to the full power and temperature dependence of the measured internal loss below 150 mK. b) Plot of $\delta^0_{TLS}(T)$ extracted from the average of the low power loss below the TLS saturation in Fig. 2.7. The orange dashed curve is the temperature dependence of STM loss below saturation power $\propto \tanh(\varepsilon/(2k_BT))$. The purple dash-dotted (light blue densely dotted) curve is from the discrete summation of the individual TLS contributions for low (intermediate)-γ fluctuators at zero applied power. The green dotted curve is the temperature dependent low power limit of the TLS loss induced by high γ fluctuators. The blue solid curve is the sum of contributions from the low, intermediate, and high γ fluctuators. c) Comparison of the temperature dependent rates determined from the least squares fit.

The fit shows reasonable agreement with the data, with root mean squared error RMSE = 0.0124. There are in total 10 fitting parameters, fewer degrees of

freedom compared to fitting the data from different temperatures individually. The different contributions to the loss below the TLS saturation power are plotted in Fig. 2.10 (b) illustrating that the discrete TLSs coupled to low and intermediate γ fluctuators are responsible for the loss reduction. The different rates in the model determined from the fit are summarized in Fig. 2.10 (c). The numerical values for $\Gamma_{1,2}$ and $\gamma_{max,min}$ are typical for TLSs in amorphous materials [124]. The rates also satisfy the following assumptions in the model: $\Gamma_2 \gtrsim \Gamma_\mathrm{f}$, and $\gamma_\mathrm{max} \gg \Gamma_2$. In addition, the low temperature loss reduction occurs around 40 mK as expected, when $\Gamma_2 + \Gamma_\mathrm{f} < \nu$, the width of the response is smaller than the detuning between the TLS and the resonance. The other quantities extracted from the fit are listed below: the volume of TLS-inhabiting dielectrics, 10 μm^3, the intrinsic TLS loss, $\delta_0^{TLS} = 3.85 \times 10^{-6}$, the other loss, $\delta_{other} = 1.29 \times 10^{-5}$, and the minimum fluctuator rate $\gamma_\mathrm{min} = 4.5 \times 10^{-2}$ Hz.

2.4.4 Alternative models for fitting the temperature and power dependent loss

None of the existing models of TLSs shows a strong temperature dependence of loss below the TLS saturation. Hence alternative models need to be combined with the discrete TLS formalism to account for the loss reduction at low temperatures. Here we examine two models commonly adopted to explain the slow power dependence above the TLS saturation power, as well as an alternative version of the discrete GTM fit used in Sec.2.4.3 in which an energy dependent density of states

($\mu \neq 0$) is assumed.

2.4.4.1 Two TLS model

The two TLSs or, by extension, multiple TLSs model is a popular alternative in explaining the slower power dependence than STM. The multiple species of TLSs could be attributed to nonuniform field distribution in the resonator [129], different dipole moments of the TLS [136], and different microscopic origins of the TLS [134]. The exact model for the TLS loss is simply a sum of two different STM loss contributions:

$$\delta_{TLS} = \sum_n \delta_0^{TLS,1} \frac{m_n \Gamma_2}{\Gamma_2^2(1+\kappa) + (\varepsilon_n/\hbar - \omega)^2} + \delta_0^{TLS,2} \frac{m_n \Gamma_2}{\Gamma_2^2(1+\eta\kappa) + (\varepsilon_n/\hbar - \omega)^2} \quad (2.31)$$

where $m_n = \tanh(\varepsilon_n/(2k_BT))$ and its subscript explicitly denotes its dependence on ε_n. The difference between the two species of the TLSs is encoded in their intrinsic losses $\delta_0^{TLS,1}, \delta_0^{TLS,2}$ which accounts for different participation ratios, and the factor η which could be due to different field strength experienced by the TLS dipoles, different dipole moments, or different relaxation rates of the two species of TLSs. The resulting fit in Fig. 2.11 shows a systematic deviation between the data and the fit, with RMSE = 0.021.

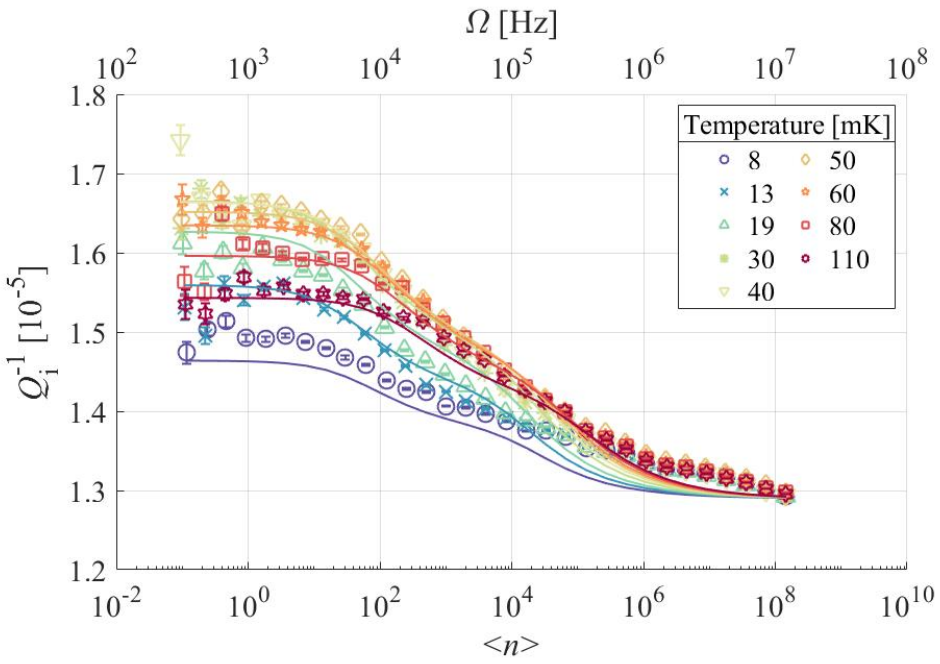

Figure 2.11: The discrete two species of TLSs model fit to the loss data.

There are 9 fitting parameters in this model. The resulting relaxation rates from the fit are $\Gamma_2 = 4.7 \times 10^5$ to $2 \times 10^7 Hz$ and $\Gamma_1 = 6.8 \times 10^3$ to $10^4 Hz$. The losses from the different contributions are determined as $\delta_{other} = 1.29 \times 10^{-5}$, $\delta_0^{TLS,1} = 6.9 \times 10^{-6}$, and $\delta_0^{TLS,2} = 6.8 \times 10^{-6}$. The other fitting parameters are volume of the TLS-inhabiting dielectrics $2\mu m^3$, the asymmetry ratio $\eta = 18$, and the exponent of the power dependent density of states of TLSs $\mu = 0.2$. We should note that this fit might be improved by including more species of TLSs. However, this multiple-TLS model lacks a physical motivation and is not considered in this work.

2.4.4.2 Power law fit

Another well-known phenomenological fitting method introduces a free power law dependence to the saturation power term $1+\kappa$ [89]. The model when combined with the discrete formalism becomes

$$\delta_{TLS} = \delta_0 \sum_n \frac{m_n \Gamma_2}{\Gamma_2^2 (1+\kappa)^\beta + (\varepsilon_n/\hbar - \omega)^2} \tag{2.32}$$

where β is the exponent for the free power law dependence, and $\beta = 1$ corresponds to the STM prediction.

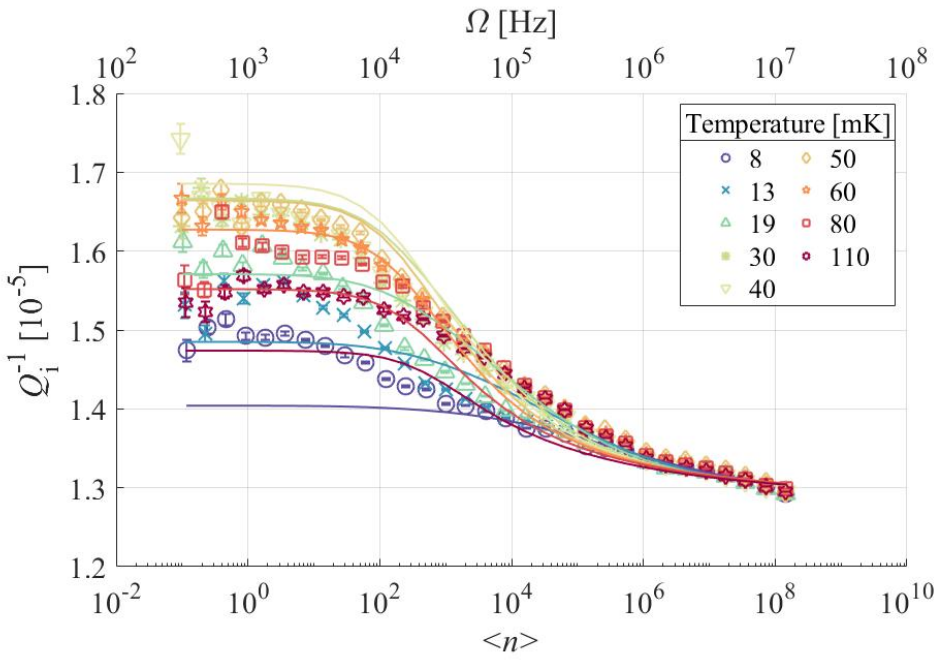

Figure 2.12: The discrete power law fit to the loss data.

The discrete free power law fit has a large deviation from the data as shown in Fig. 2.12, with RMSE = 0.036. The 8 fitting parameters are the power law exponent $\beta = 0.38$, the exponent in the energy dependent density of states of TLSs $\mu = 0.2$, the volume of TLS-inhabiting dielectrics $2.6\mu m^3$, the loss from other mechanisms

$\delta_{other} = 1.29 \times 10^{-5}$, the intrinsic TLS loss $\delta_0 = 8 \times 10^{-6}$, and the two relaxation rates are $\Gamma_1 = 700$ to $10^3 Hz$ and $\Gamma_2 = 3.3 \times 10^4$ to $1.4 \times 10^6 Hz$.

Moreover, neither of the above alternative models provides a clear interpretation of the physics in the TLS loss, since the phenomenological fitting parameters could have different microscopic origins, i.e. nonuniform field distribution, or different dipole moments or relaxation rates among several distinct ensembles of TLS. Not only does the discrete form of GTM in this work generate better fits to the measured loss, but it also provides a clear physical explanation for the observed loss: the low spectral density of coherent TLSs and their interactions with the fluctuators are responsible for the observed temperature and power dependence.

2.4.4.3 Fit with energy dependent density of states

In Faoro and Ioffe's original work on GTM, an energy dependent density of states (DOS) for the TLSs is assumed [124],

$$P(\Delta, \Delta_0) = (1+\mu)\left(\frac{\Delta}{\Delta_{\max}}\right)^{\mu} \frac{P_0}{\Delta_0} \tag{2.33}$$

where $\mu \sim 0.3$ and $\Delta_{\max} \sim \varepsilon_{\max} \sim k_B(100K)$. The small exponent μ approximately characterizes the logarithmic reduction of the density of states of TLSs at low energy in a system of interacting dipoles [123]. The energy dependent DOS will lead to a small correction in the linear temperature dependence of the dephasing rate, $\Gamma_{\rm ds} \sim 10^{-3}(k_B T/\varepsilon_{\max})^{\mu} k_B T/\hbar$. The model with an energy dependent density of states where μ is a free fitting parameter is used to fit to our data and is shown in Fig. 2.13.

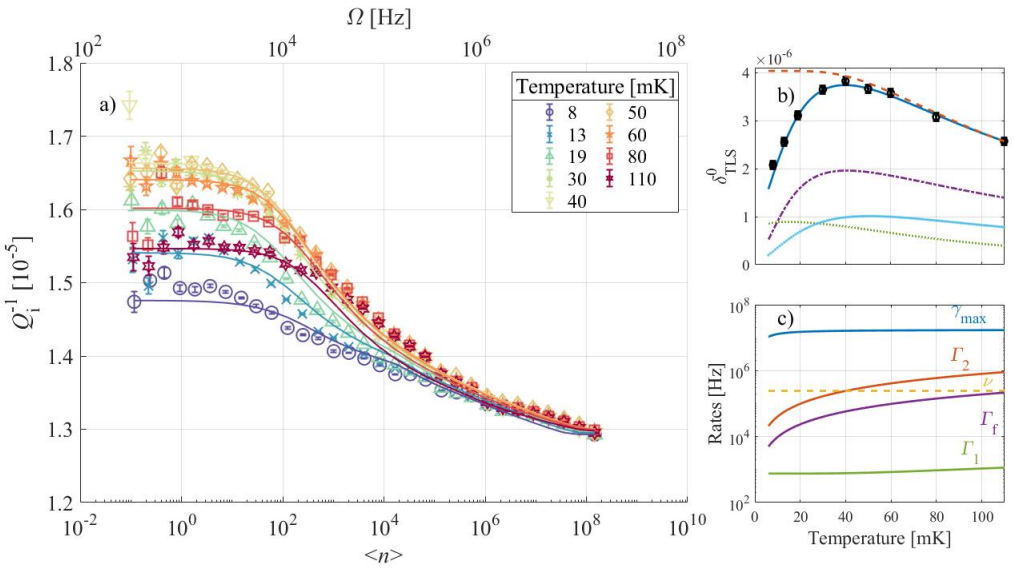

Figure 2.13: a) The least squares fit of the discrete GTM, together with an energy dependent density of state and a constant background loss, to the full power and temperature dependence of the measured internal loss below 150 mK. b) Plot of $\delta^0_{TLS}(T)$ extracted from the average of the low power loss below the TLS saturation in Fig. 2.7. The orange dashed curve is the temperature dependence of STM loss below saturation power $\propto \tanh(\varepsilon/(2k_BT))$. The purple dash-dotted (light blue densely dotted) curve is from the discrete summation of the individual TLS contributions for low (intermediate)-γ fluctuators at zero applied power. The green dashed curve is the temperature dependent low power limit of the TLS loss induced by high γ fluctuators. The blue solid curve is the sum of contributions from the low, intermediate, and high γ fluctuators. c) Comparison of the temperature dependent rates determined from the least squares fit.

The fit shows reasonable agreement with the data, with RMSE = 0.014,

slightly larger than that of the $\mu = 0$ fit in Sec.2.4.3. suggesting that the assumption of energy dependent DOS is not necessary. There are in total 11 fitting parameters. The different contributions to the loss below the TLS saturation power are plotted in Fig. 2.13 (b). Similar to the fit in Sec.2.4.3, the discrete TLSs coupled to low and intermediate γ fluctuators are responsible for the loss reduction. Different rates in the fit are summarized in Fig. 2.13 (c), with typical numerical values for TLS in amorphous materials [124]. The rates also satisfy $\Gamma_2 \gtrsim \Gamma_{\rm f}$, $\gamma_{\rm max} \gg \Gamma_2$. In addition, the low temperature loss reduction occurs around 40 mK as expected, when $\Gamma_2 + \Gamma_{\rm f} < \nu$, the width of the response is smaller than the detuning between the TLS and the resonance. The other quantities extracted from the fit are listed below: the volume of TLS-inhabiting dielectrics, 18.5 μm^3, the intrinsic TLS loss, $\delta_0^{TLS} = 5.5 \times 10^{-6}$, the other loss, $\delta_{other} = 1.29 \times 10^{-5}$, and the minimum fluctuator rate $\gamma_{\rm min} = 2.9 \times 10^{-4}$ Hz, and the exponent for the energy dependent density of states $\mu = 0.2$.

2.5 Discussion

The discrete and detuned TLSs formalism will not affect the high γ-fluctuator contribution to internal loss, since the width of Lorentzian in the calculation of loss of high γ fluctuators w is widened by γ such that $w \sim \gamma > \Delta\varepsilon/\hbar$ (See Sec.2.4.2.2), which is indicated by the almost flat region in the green dotted curve at low temperature in Fig. 2.10 (b). However, the loss from intermediate γ fluctuators could be subject to the low coherent TLS density but to a lesser degree than that from

the low γ fluctuators, since although the bandwidth of their response $\sim \Gamma_2$ is the same (See Sec. 2.4.2.3), there are many intermediate-γ-fluctuator-induced sublevels for one TLS in one Rabi cycle which effectively increases the density of the available TLS energy levels. In order to avoid over fitting, this effect was not included in the model where the same density of states for TLSs are assumed for those coupled to intermediate γ fluctuators and the low γ fluctuators. Thus, the same $\Delta\varepsilon$ value is shared for the two different contributions. This simplification could lead to an underestimation of the loss in the intermediate power region, as illustrated by the deviation between the fit and data from $\langle n \rangle = 10^2$ to 10^6.

The discrete TLSs formalism only approximates the effect of a sparse spectral density of TLSs where despite the spectral diffusion with a width Γ_2, and the random telegraph noise characterized by the rate γ, the coherent TLS spends most of its time detuned from the resonance. The assumptions of even energy spacing between TLSs, $\Delta\varepsilon$, and constant energy levels, are convenient for numerical evaluation of the model, but are not necessary to reproduce the loss reduction at low temperature. Two other estimations of the probability of the TLS being on resonance, as well as the number of strongly coupled fluctuators that can bring a detuned TLS into resonance, are given in Sec.2.4.2.1. Both calculations show that for any TLS with a spectral width Γ_2 and a detuning to the resonance ν, the TLS becomes less likely to be on resonance once $\Gamma_2(T) < \nu$ with decreasing temperature, qualitatively agreeing with the experimentally observed loss reduction at low temperature.

The treatment above is largely classical where the TLSs are treated as dipoles under classical field. A quantum mechanical approach that studies the Jaynes-

Cummings model of a single TLS strongly coupled to a photon predicts a linear temperature dependence of the loss similar to our observation [144]. However, it should be noted that the photon frequency in our measurement (3.64 GHz) corresponds to weak photon-TLS coupling, since the Rabi frequency from the effective field of a single photon is much weaker than the relaxation rates $\Gamma_{1,2}$. Additionally, the loss from strongly coupled TLSs is predicted to show saturation in power at $\langle n \rangle \sim 1$, clearly lower than the observed saturation in the data at $\langle n \rangle \sim 10$ which corresponds to the weak coupling regime and reproduces the classical result [144].

Although the fluctuators significantly affect the internal loss of TLSs, they should have limited effect on the frequency shifts [124]. The proposed discrete and detuned TLSs formalism would not modify the STM frequency shift prediction either, because unlike the Lorentzian response function that governs the internal loss, the response function for frequency shift does not have a resonant shape and is not sensitive to the reduced sampling from the discrete TLSs.

Ever since the importance of the TLS interactions in amorphous solids was recognized by Yu and Leggett [145], there have been numerous experimental works demonstrating evidence of the TLS interactions,[138, 137, 146] and theoretical works treating the interacting TLSs beyond STM [147, 148, 149], with a recent example by Burin and Maksymov where they used a similar Master equation formalism [90]. However, the fluctuations in the energy levels are averaged over to form the spectral diffusion, unlike the fluctuators introduced by Faoro and Ioffe [126, 124], and the loss is predicted to have a power dependence faster than STM by a logarithmic factor, contrary to our observation.

2.5.1 Non-Equilibrium Quasiparticle Treatment and $n_{\rm qp}$ and $Q_{\rm qp}$ Estimates

At higher temperatures (above 150 mK), the quasiparticle effects become important, which corresponds to the upturn in loss in Fig. 2.5. The quasiparticles loss is related to its density n_{qp} as,

$$\frac{1}{Q_{\rm qp}} = \frac{2\alpha}{\pi}\frac{\sinh(\zeta)K_0(\zeta)n_{\rm qp}}{N_0\sqrt{2\pi k_B T\Delta_{S0}}}$$

$$\text{where} \quad n_{\rm qp} = n_{\rm th} + n_{\rm noneq} = 2N_0\sqrt{2\pi k_B T\Delta_{S0}}\exp\left(-\frac{\Delta_{S0}}{k_B T}\right) + n_{\rm noneq} \qquad (2.34)$$

where $n_{\rm noneq}$ is the non-equilibrium quasiparticle density. Similar to the fit for frequency shift, the model with only $n_{\rm th}$ matches our data with the same set of fitting parameters $\Delta_0 = 170\ \mu eV$ and $\alpha = 0.014$.

A calculation of the increased quasiparticle density including both thermal and non-equilibrium quasiparticles at high photon numbers in the half wavelength resonator based on Mattis-Bardeen equations [150, 151] is performed.

This model (scattering model) was established by considering the coupled quasiparticle and phonon systems[68]. The details of this model are described in [69, 70, 71] which employ numerical methods to discretize the distribution of quasiparticles $f(E)$ at energy E and the phonon distribution $n(\Omega)$ at energy Ω by solving the kinetic equations in steady state for a given flux of microwave and higher-frequency photons.

The calculation is performed by assuming the fridge base temperature $T_{\rm b} = 10\,mK$, the resonator drive frequency 3.6442 GHz ($\hbar\omega = 23\,\mu eV$), superconducting

Name	Symbol	Value
Superconducting gap	Δ_{S0}	188μeV
RF photon energy	$\hbar\omega$	23μeV
Intrinsic quality factor	Q_i	10^5
Intrinsic quality factor	Q_c	1.5×10^6
Quasiparticle-phonon time		438 ns[70]
Characteristic phonon time		0.26 ns[70]
Phonon escape time		0.17 ns[70]
Resonator volume		8.6×10^{-14}m^3
Base temperature	T_b	10 mK
Phonon effective temperature	T_{eff}	189 mK

Table 2.1: Parameters used for our non equilibrium quasi-particle calculation.

energy gap $\Delta_{\text{S0}} = 188\ \mu eV$, $Q_{\text{i}} = 10^5$, $Q_{\text{c}} = 1.5 \times 10^6$ which we obtain from fitting the resonance, resonator center conductor volume $8.6 \times 10^{-14}\ m^3$ and effective temperature $T_{\text{eff}} = 189\ mK$ due to stray light illumination and radiation which creates enhanced phonon generation, as described by the Parker model [152]. Table 2.1 lists all of the parameter values used in this model.

Fig. 2.14 (a) and Fig. 2.14 (b) show the calculated quasiparticle distribution and phonon distribution, respectively, for three selected circulated numbers of photons in the half wavelength resonator.

The black dashed line in Fig. 2.14(a) indicates the thermal distribution of

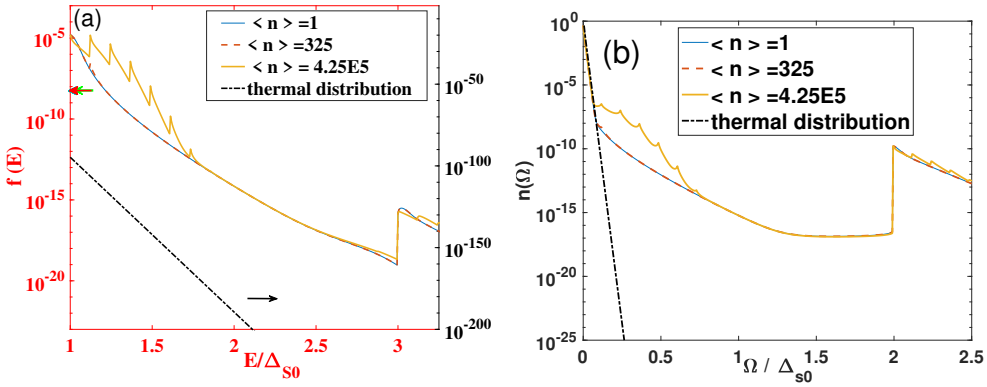

Figure 2.14: The calculated quasiparticle distribution $f(E)$ (a) and phonon distribution $n(\Omega)$ (b) as a function of normalized energy for different circulating numbers of photons in the half wavelength resonator. Note that in the plot of $f(E)$, a double y axis is used due to the different scales of thermal and non-equilibrium distributions.

quasiparticles without any microwave excitation at $T_\mathrm{b} = 10\ mK$. At low circulating photon numbers ($\langle n \rangle = 1$ or 325), the quasiparticle distribution is enhanced significantly above the T_b thermal distribution, and the phonon distribution is also enhanced. At high circulating photon numbers, jumps appear in the electron and phonon distributions every $\hbar\omega$ because microwave drive at high power significantly affects the distributions. Big step jumps at $E = 3\Delta_{\mathrm{S0}}$ and $\Omega = 2\Delta_{\mathrm{S0}}$ are due to pair breaking and recombination processes.

From the quasiparticle distribution $f(E)$, one can calculate the quasiparticle density, n_{qp}, by numerical integration over all energy, with its density of states $\rho(E)$

$$n_{\mathrm{qp}} = 4N_0 \int_{\Delta_{\mathrm{S0}}}^{\infty} f(E)\rho(E)dE \quad \text{with} \quad \rho(E) = \frac{E}{\sqrt{E^2 - \Delta_{\mathrm{S0}}^2}} \tag{2.35}$$

The calculated n_{qp} at different circulated photon numbers $\langle n \rangle$ are shown in

Fig. 2.15(a). Because this calculation is performed at the 10 mK fridge base temperature, we can set $n_{\rm qp} = n_{\rm noneq}$, since the number of thermal quasiparticles is extremely small. The calculated $n_{\rm qp}$ is around 50 μm^{-3} when $\langle n \rangle < 10^6$. In addition, the calculated result of $n_{\rm qp}$ as a function of fridge/bath temperature ($T_{\rm b}$) at $\langle n \rangle = 1$ is shown in Fig.2.15(b) as circle dots. When the bath temperature is below 150 mK, $n_{\rm qp}$ remains constant. This is consistent to the assumptions made in the frequency shift fit at low temperature where quasiparticle density is a constant. The continuous line of Fig.2.15(b) is from Eq. (2.34).

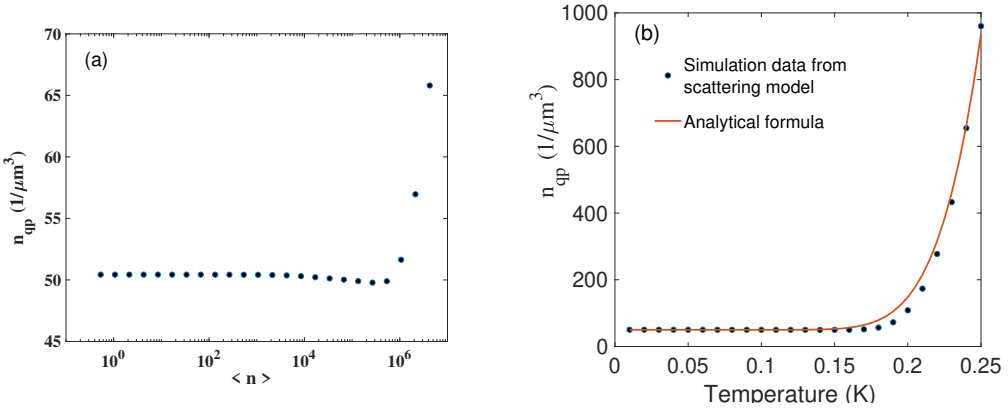

Figure 2.15: a) The calculated quasiparticle density as a function of circulating photon numbers in the half wavelength resonator. Here $T_{\rm b} = 10\,mK$ and $T_{\rm eff} = 189\,mK$. b) The calculated quasiparticle density as a function of fridge temperature at $\langle n \rangle = 1$. Note that the dots are calculated from the non-equilibrium model, and the solid line is from Eq. (2.34) .

For the quality factor due to the quasiparticles, $Q_{\rm qp}$ is defined as

$$\frac{1}{Q_{\rm qp}} = \alpha \frac{\sigma_1}{\sigma_2} \tag{2.36}$$

where the kinetic inductance ratio $\alpha = 0.0185$ was obtained from the frequency shift fit in Sec.2.3. The real and imaginary parts of the complex conductivity $\sigma = \sigma_1 - i\sigma_2$ can be expressed respectively by the Mattis-Bardeen formula [150] given by

$$\frac{\sigma_1}{\sigma_{\mathrm{N}}}(\omega) = \frac{2}{\hbar\omega}\int_{\Delta_{\mathrm{S0}}}^{\infty} [f(E) - f(E+\hbar\omega)]\, g_1(E) dE \tag{2.37}$$

$$\frac{\sigma_2}{\sigma_{\mathrm{N}}}(\omega) = \frac{2}{\hbar\omega}\int_{\Delta_{\mathrm{S0}}-\hbar\omega}^{\infty} [f(E) - 2f(E+\hbar\omega)]\, g_2(E) dE \tag{2.38}$$

where σ_N is the normal-state conductivity, $g_1(E) = h_1(E, E+\hbar\omega)\rho(E)$ and $g_2(E) = h_1(E, E+\hbar\omega)\frac{E}{\sqrt{\Delta_{\mathrm{S0}}^2 - E^2}}$ with $h_1(E, E') = (1 + \frac{\Delta_{\mathrm{S0}}^2}{E*E'})\rho(E')$. Here we use the non-equilibrium distribution function $f(E)$ discussed above.

The calculated result of Q_{qp} as a function of average circulated photon numbers is shown in Fig. 2.16. In the regime of low circulating photon numbers, Q_{qp} remains a constant and then gradually increases as the circulating photon numbers in the half wavelength resonator increase. Overall, the Q_{qp} is on the order of 10^7, and this result verifies our assumption that $Q_{\mathrm{qp}} > Q_{\mathrm{TLS0}}$ in the $Q_{\mathrm{i}}(T)$ fitting. In other words, the loss in the half wave length resonator at low temperatures and low circulating photon numbers is dominated by the TLS losses.

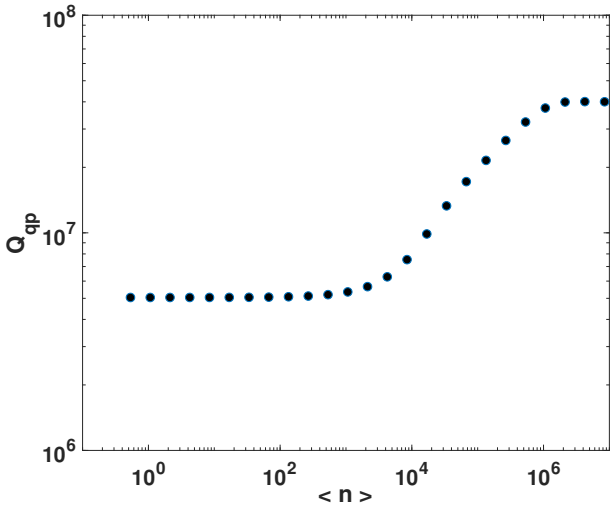

Figure 2.16: The calculated quality factor of quasi-particle as a function of circulating photon numbers $\langle n \rangle$ in the half wavelength resonator. Here $T_{\rm b} = 10\,mK$ and $T_{\rm eff} = 189\,mK$, and other parameters are listed in Table 2.1.

However, the results lack any strong temperature or power dependence below 100 mK. Note that this calculation includes the dynamics of the finite lifetime of non-equilibrium quasiparticles due to recombination and trapping [153, 152, 154, 155].

Chapter 3

Hysteretic rf SQUID Metamaterials

The original proposal for a superconducting magnetometer was to use a hysteretic rf SQUID with the parameter $\beta_{\rm rf} = L_{\rm geo}/L_{\rm JJ} > 1$ [156, 21, 157], due to their simple architecture. The hysteretic rf SQUID is subject to an external dc flux to be determined while also inductively coupled to a tank LC circuit. This circuit is driven by an rf current at its resonant frequency, where the inductor provides the rf drive to the rf SQUID and the the capacitor reads the output voltage. There are hysteretic jumps (which will be introduced later in this chapter) in the total flux of the SQUID as a response to a sweep of the applied flux. These jumps are the dominant contributions to the dissipation in the operation, which degrade the quality factor of the tank circuit and change the read out voltage. and this forms the basis of the operation of the hysteretic rf SQUID magnetometer. However, as the fabrication process of Josephson junctions matured, reproducible dc SQUIDs where the sizes of the two junctions can be well controlled, became the mainstream of modern designs of high-resolution magnetometers due to their higher sensitivity.

Although hysteretic rf SQUIDs have since lost their popularity in magnetometer applications, the multistability arising from the hysteresis could lead to interesting nonlinear dynamics [158, 159, 160, 161, 162, 163, 164, 165, 166]. In addition, the coupling among meta-atoms gives rise to remarkable collective behaviors of the

metasurface, such as chimera states [167, 168, 169, 170, 171, 172, 173], disorder-dominated states [26, 174, 175], and coherent modes of oscillation [176]. Such states have been directly imaged by laser scanning microscopy in the superconducting state under microwave magnetic flux [177, 178].

The single rf SQUID resonance frequency is tunable under applied dc magnetic flux, with a period of one flux quantum and the upper-frequency limit scaling as $\sqrt{1+\beta_{\rm rf}}$. Thus, hysteretic rf SQUIDs are expected to have enhanced ranges of tunable self-resonant frequency. The previous experimental works in this area [23, 41, 44, 28, 30, 24, 179] restricted the parameter $\beta_{\rm rf}$ to remain below unity to avoid hysteresis, thus simplifying the behavior and analysis of those meta-atoms. In addition, prior work generally constrained the SQUID arrays to having small mutual-inductive coupling among them, which resulted in behavior very similar to that of single-SQUIDs. The small $\beta_{\rm rf}$ value also limited the frequency tuning range, and the rather sparse packing of the meta-atoms resulted in weak overall response from the metamaterial. These issues are addressed with new generations of rf SQUID metamaterials discussed in this chapter and the next.

3.1 Resistively and capacitively shunted junction model for a single rf SQUID

First we shall review the consequences of flux quantization in a single rf SQUID loop to establish our notation and approach to setting up and solving the equations of motion for the gauge-invariant phase. The circuit diagram of an rf SQUID is illus-

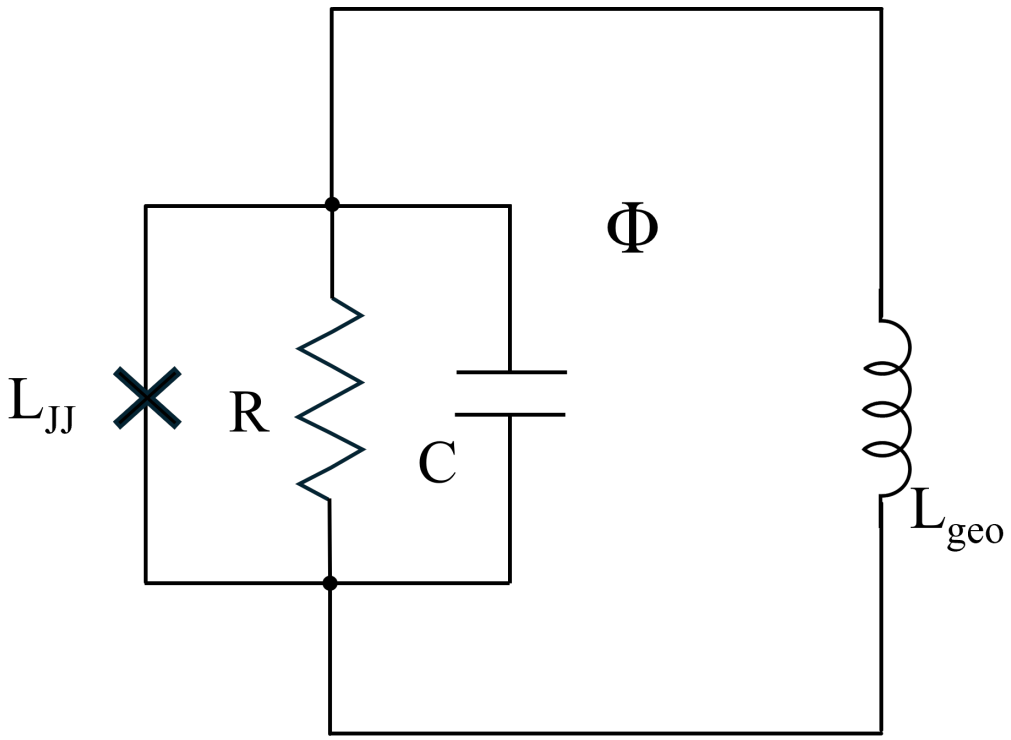

Figure 3.1: The circuit model of an rf SQUID with a magnetic flux Φ threading the loop.

trated in Fig. 3.1 , where the resistively and capacitively shunted junction (RCSJ) and the geometric inductance of the SQUID loop are both incorporated on the circuit model.

The total flux Φ in the rf SQUID loop and gauge-invariant phase difference δ across the junction are related through the statement of flux quantization in a superconducting loop, which requires the order parameter to be single-valued upon going on a continuous and closed loop c through the superconducting material. Mathematically, this self-consistency condition results in [180, 181],

$$2\pi n = \delta + \frac{2e}{\hbar}\Phi, \tag{3.1}$$

where $n = 0, \pm 1, \pm 2, ...$ and Φ is the magnetic flux through any surface that ter-

minates on the continuous circuit c. This can be re-written as, $\Phi = n\Phi_0 - \frac{\Phi_0}{2\pi}\delta$, where $\Phi_0 = \frac{h}{2e}$ is the flux quantum. Without loss of generality, taking $n = 0$ in the SQUID loop, the expression is simplified to $\Phi = -\frac{\Phi_0}{2\pi}\delta$. We shall assume that the SQUID loop maintains quasi-static flux quantization from dc through the microwave frequency range so that Eq. (3.1) holds for both the rf and dc flux in a single galvanically-connected rf SQUID loop. One would expect that Eq. (3.1) remains valid for all situations in which the superconducting order parameter has a well-defined phase throughout the material, which should extend to time scales as short as the order parameter relaxation time, expected to be in the ps range, except close to T_c [21, 182].

The total flux in the loop can be expressed as [180, 181, 183, 184],

$$\Phi = -\Phi_{\text{app}} + \Phi_{\text{ind}} \tag{3.2}$$

where Φ_{app} stands for the applied flux and the induced flux is $\Phi_{\text{ind}} = L_{\text{geo}}I$ for a single isolated SQUID with a loop inductance L_{geo} carrying current I. The sign convention for Φ_{app} is chosen to account for the diamagnetic response of the superconducting loop, resulting in opposite signs for applied and induced fluxes.

The current I in the junction is expressed using the RCSJ model where the junction is treated as a parallel combination of three branches: an ideal Josephson junction, a capacitor C and a shunt resistor R [185]. The total current from the three branches is thus:

$$I = I_{\text{JJ}} + I_{\text{R}} + I_{\text{C}} = I_{\text{c}} \sin\delta + \frac{V}{R} + C\frac{dV}{dt}$$

Using the second Josephson equation, one can relate the voltage drop on the junction

V to the time derivative of the gauge-invariant phase as $V = \frac{\Phi_0}{2\pi}\dot{\delta}$, where the over-dot denotes time derivative. In this case, the response current can be written as,

$$I = I_c \sin\delta + \frac{\Phi_0}{2\pi}\frac{\dot{\delta}}{R} + C\frac{\Phi_0}{2\pi}\ddot{\delta} \tag{3.3}$$

The flux quantization condition, Eq. (3.2) can now be expressed as, [176]

$$\Phi_{dc} + \Phi_{rf}\sin(\omega t) = \frac{\Phi_0}{2\pi}\delta + L_{geo}(I_c \sin\delta + \frac{\Phi_0}{2\pi}\frac{\dot{\delta}}{R} + C\frac{\Phi_0}{2\pi}\ddot{\delta}), \tag{3.4}$$

whose normalized form reads

$$\phi_{dc} + \phi_{rf}\sin(\Omega\tau) = \delta + \beta_{rf}\sin\delta + \gamma\frac{d\delta}{d\tau} + \frac{d^2\delta}{d\tau^2}, \tag{3.5}$$

where Φ_{dc} and Φ_{rf} are the dc and rf magnetic flux applied to the rf SQUID and we assume time-harmonic rf flux at a single frequency ω. The over-dot $\dot{\square}$ represents derivative with respect to time. The equation can be reduced into the dimensionless form with the following substitutions: $\phi_{dc,rf} = 2\pi\Phi_{dc,rf}/\Phi_0$, $\beta_{rf} = 2\pi L_{geo}I_c/\Phi_0$ (also referred to as β_L in the literature), $\gamma = \sqrt{L_{geo}/C}/R$, $\tau = \omega_{geo}t = t/\sqrt{L_{geo}C}$, and $\Omega = \omega/\omega_{geo} = \omega\sqrt{L_{geo}C}$. Note that we also introduce the geometric resonance $\omega_{geo} = 1/\sqrt{L_{geo}C}$, which is the self-resonant frequency of the rf SQUID meta-atom in the absence of the Josephson effect.

Equation (3.5) is a driven second-order nonlinear differential equation for the gauge-invariant phase as a function of time, $\delta(\tau)$, which dictates the response of the metamaterial to external electromagnetic fields. Solving for $\delta(\tau)$ allows one to calculate all observable properties of the system, including dissipation in the resistor R.

3.1.1 Linear-limit solution to the RCSJ model for a single rf SQUID

Before exploring the full numerical solution, an analytical solution can be obtained under the weak applied rf flux approximation, where we only expect the linear response for the rf SQUID. With a low driving amplitude, the rf response is vanishingly small, $|\delta_{\rm rf}| \ll 1$, so that any nonlinear rf response is negligible. Therefore, the solution takes the following form $\delta = \delta_{\rm dc} + \delta_{\rm rf}\exp(i\Omega\tau)$ [24]. After substituting the solution ansatz into the equation of motion, Eq.(3.5), the resulting equations can be separated into dc and rf components:

$$\phi_{\rm dc} = \delta_{\rm dc} + \beta_{\rm rf}\sin\delta_{\rm dc} \tag{3.6}$$

$$\phi_{\rm rf}\sin(\Omega\tau) = (1+\beta_{\rm rf}\cos\delta_{\rm dc})\delta_{\rm rf} + \gamma\frac{d\delta_{\rm rf}}{d\tau} + \frac{d^2\delta_{\rm rf}}{d\tau^2} \tag{3.7}$$

The dc component is an algebraic equation in $\delta_{\rm dc}$ which can be solved numerically. The solutions to the dc equation are illustrated in Fig. 3.2 for different values of $\beta_{\rm rf}$. For $\beta_{\rm rf} > 1$, the solution for $\delta_{dc}(\Phi_{dc}/\Phi_0)$ becomes multi-valued leading to hysteresis during a dc flux sweep, which gives rise to the definition of the hysteretic SQUID: those with $\beta_{\rm rf}$ greater than unity. Applying a Fourier transform to the right hand side of Eq. (3.7), we can obtain the resonance condition when a nontrivial solution exists for zero applied rf flux:

$$1 + \beta_{\rm rf}\cos\delta_{\rm dc} + i\gamma\Omega - \Omega^2 = 0.$$

The resulting dimensionless resonant frequency is solved as

$$\Omega_R = \frac{i\gamma}{2} + \frac{1}{2}\sqrt{4(1+\beta_{\rm rf}\cos\delta_{\rm dc}) - \gamma^2}. \tag{3.8}$$

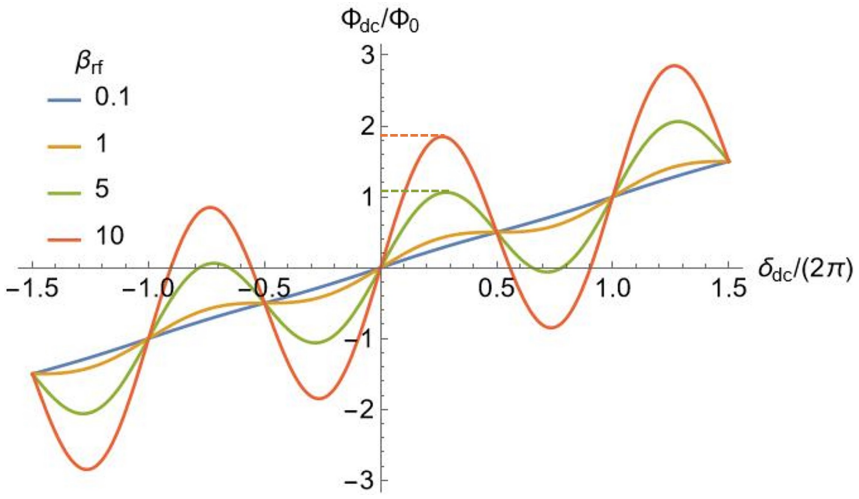

Figure 3.2: Illustration of solutions to the single SQUID dc equation: $\phi_{\rm dc} = \delta_{\rm dc} + \beta_{\rm rf} \sin \delta_{\rm dc}$ for different $\beta_{\rm rf}$. The solution $\delta_{\rm dc}(\Phi_{\rm dc}/\Phi_0)$ becomes multi-valued for $\beta_{\rm rf} > 1$.

where we only keep the solutions with positive real parts. For loss $\gamma \ll 1$,

$$\Omega_R = \sqrt{1 + \beta_{\rm rf} \cos \delta_{\rm dc}}. \tag{3.9}$$

The resonance frequency can then be solved after substituting the dc component solution $\delta_{\rm dc}$ from Eq.(3.6). This resonance agrees with the result from the circuit model in Eq.(1.9), which can be easily verified: $\omega_{\rm geo}\Omega_R = \omega_0$. The solved resonance frequencies as a function of dc flux for three different values of $\beta_{\rm rf}$ are plotted in Fig. 3.3.

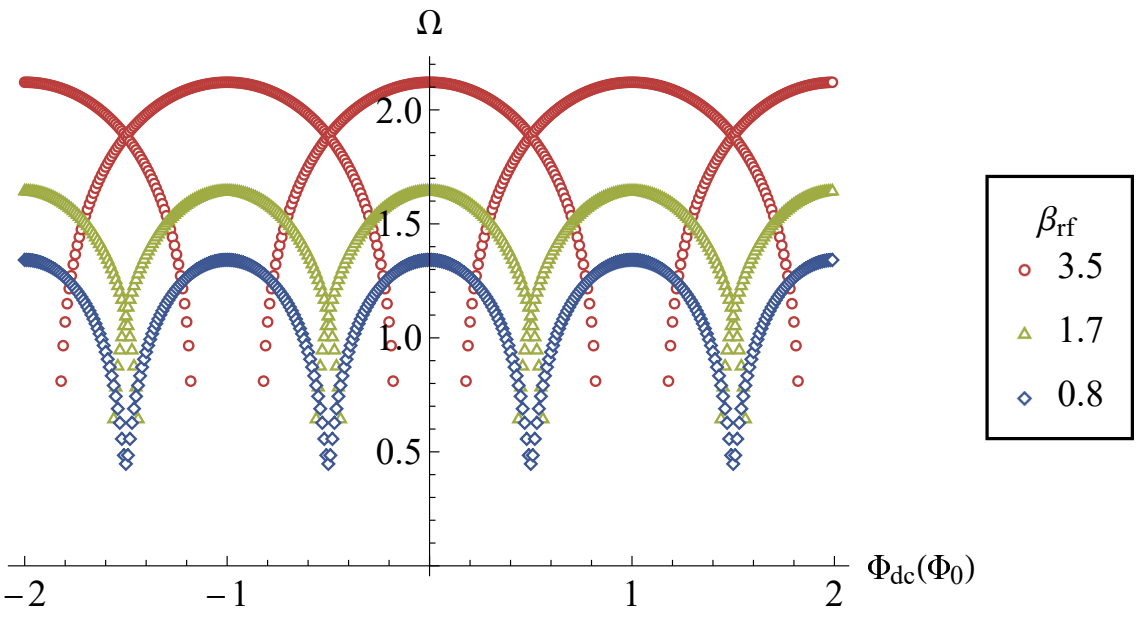

Figure 3.3: Single SQUID resonance frequency $\Omega = \omega/\omega_{geo}$ as a function of applied dc flux from linear solution for $\beta_{\rm rf} = 3.5,\ 1.7,\ 0.8$. The resonant frequencies are tuned by applied dc flux in periods of Φ_0, and peak around integer values of Φ_0, and decreases as the dc flux approaches half integers of Φ_0 as expected for rf SQUIDs. For $\beta_{\rm rf} > 1$, the resonance curve for the SQUID crosses the curve from the adjacent periods at half integers of Φ_0. The region of overlap between the curves corresponds to the multi-valued range in Fig. 3.2.

For $\beta_{\rm rf} < 1$, the resonance is tuned with applied dc flux between the frequencies $\Omega_{\rm min} = \sqrt{1-\beta_{\rm rf}}$ and $\Omega_{\rm max} = \sqrt{1+\beta_{\rm rf}}$. There is no overlap between any curves corresponding to the one-to-one mapping for $\beta_{\rm rf} < 1$ in their dc solution shown in Fig. 3.2. As one increases $\beta_{\rm rf}$, the resonance frequency in Eq. 3.9 grows. In addition to the increase in resonance frequency, the tuning curve also expands the range in applied dc flux where the resonance can be continuously tuned without any jumps

above half integers of Φ_0, which corresponds to the higher peaks in the oscillation in the dc solution curve in Fig. 3.2. If one initializes the phase δ at 0, the dc solution curve can be traced out for a range of values for $\Phi_{\rm dc}$ before reaching a peak $\Phi_{\rm dc0}$ (as highlighted by the dashed lines in Fig. 3.2), where upon further increasing $\Phi_{\rm dc}$, $\delta_{\rm dc}$ needs to make a discontinuous jump to another value. The location of this peak can be determined by setting $d\Phi_{\rm dc}/d\delta_{\rm dc} = 0$:

$$\begin{aligned} \frac{d}{d\delta_{\rm dc}}(\delta_{\rm dc} + \beta_{\rm rf}\sin\delta_{\rm dc})|_{\delta_{\rm dc}=\delta_{\rm dc0}} &= 0, \\ 1 + \beta_{\rm rf}\cos\delta_{\rm dc0} &= 0, \\ \delta_{\rm dc0} &= \arccos\left(-\frac{1}{\beta_{\rm rf}}\right). \end{aligned}$$

Therefore, we can substitute the solution $\delta_{\rm dc0}$ to determine $\phi_{\rm dc0} = 2\pi\Phi_{\rm dc0}/\Phi_0$,

$$\phi_{\rm dc0} = \delta_{\rm dc0} + \beta_{\rm rf}\sin\delta_{\rm dc0} = \arccos\left(-\frac{1}{\beta_{\rm rf}}\right) + \sqrt{{\beta_{\rm rf}}^2 - 1} \tag{3.10}$$

The parameter $\Phi_{\rm dc0}$ is plotted as a function of $\beta_{\rm rf}$ in Fig. 3.4, which illustrates the expansion of the tuning curve in width.

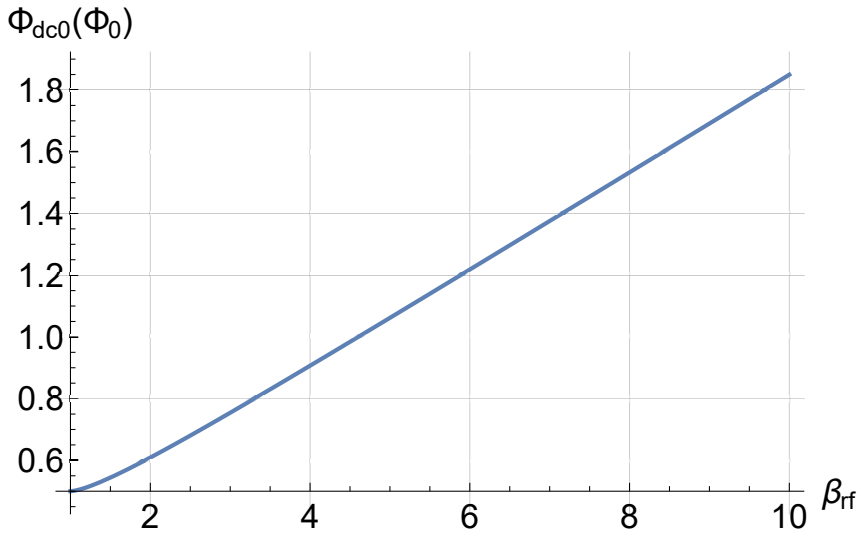

Figure 3.4: The smallest positive dc flux value $\Phi_{\rm dc0}$ for a peak in the dc solution, as shown in Fig. 3.2, as a function of $\beta_{\rm rf}$ for $\beta_{\rm rf} > 1$. $\Phi_{\rm dc0}$, which also corresponds to the half width of the dc flux tuning curve in Fig. 3.3, increases monotonically with $\beta_{\rm rf}$.

When $\Phi_{\rm dc0}$ reaches Φ_0, $\beta_{\rm rf} = \beta_{\rm rf,c1} \sim 4.60$, the width of the tuning curve can span $2\Phi_0$ in the applied dc flux, which could lead to potential period doubling in the dc flux tuning, as illustrated in Sec. 3.4.4. In this case, upon changing the dc flux, the dc solution can skip over the next period and land on the branch $2\Phi_0$ away. The next critical $\beta_{\rm rf}$ value is $\beta_{\rm rf,c2} \sim 7.79$, where the SQUID can jump to the solution branch $3\Phi_0$ away and present potential period tripling in their dc flux tuning.

3.1.1.1 Multistability in hysteretic rf SQUIDs

To better understand the dynamics of the SQUID, we can extract the effective potential energy $U_{eff}(\delta)$ from the dynamical equation, Eq.(3.5). The terms $\phi_{\rm dc} +$

$\phi_{\rm rf}\sin(\Omega\tau) - \delta - \beta_{\rm rf}\sin\delta$ can be regarded as an external force acting on a 'phase point' particle in the effective (time-dependent) potential $U_{\rm eff} = \delta^2/2 - \beta_{\rm rf}\cos\delta - (\phi_{\rm dc} + \phi_{\rm rf}\sin(\Omega\tau))\delta$, plotted below.

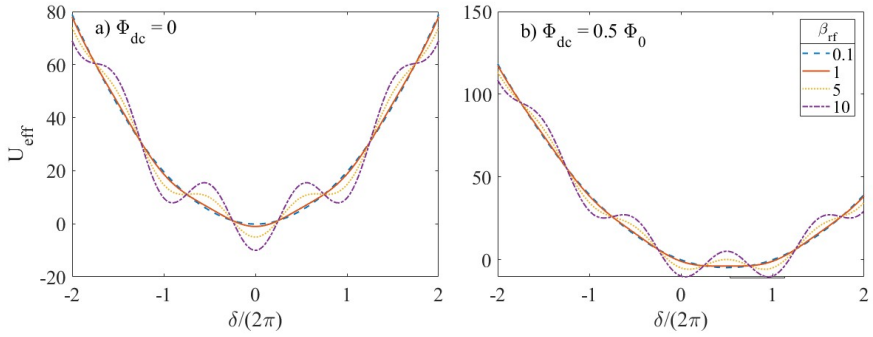

Figure 3.5: Effective potential $U_{\rm eff}$ for a single SQUID as a function of δ at a) 0 applied dc flux and b) $0.5\Phi_0$ applied dc flux. The SQUID becomes multi-stable for large $\beta_{\rm rf}$, as indicated by the multiple minima in the potential. The multistability begins for $\beta_{\rm rf} \gtrsim 4.60$ at 0 applied dc flux, and $\beta_{\rm rf} > 1$ at $0.5\Phi_0$ applied dc flux. The rf flux provides an oscillation in the offset of the parabola which changes the locations of the local minima periodically. At large rf drive amplitudes, the barriers between the potential minima can even disappear and enable the solutions to move between them.

There exists more than one local minimum in the potential for large $\beta_{\rm rf}$. In particular, at $\Phi_{\rm dc} = 0.5\Phi_0$, as one increases $\beta_{\rm rf} > 1$, a double well potential is developed which has been employed in realizing flux qubits [186]. The two minima around $\delta/(2\pi) = 0.5$ correspond to the two stable solutions for the dc equation shown in Fig. 3.2. There are in total three intersections between a horizontal line at $\Phi_{\rm dc} = 0.5\Phi_0$ and the solution curve for $\beta_{\rm rf}$ slightly larger than one, where the

center one at $(\Phi_{\rm dc}/\Phi_0, \delta_{\rm dc}/(2\pi)) = (0.5, 0.5)$ is the unstable equilibrium represented by the local maximum at the center of the double well potential. Upon further increasing $\beta_{\rm rf}$ above $\beta_{\rm rf,c2} \sim 7.79$ whose $\Phi_{\rm dc0} = 1.5\Phi_0$, two additional local minima appeared in the potential landscape as illustrated in Fig. 3.5 (b). At $\Phi_{\rm dc} = 0$, the potential evolves from having one local minimum to three when $\beta_{\rm rf}$ is increased across $\beta_{\rm rf,c1} \sim 4.6$, again corresponding to the three stable solutions found in the $\Phi_{\rm dc} = 0$ intersection with the solution curve in Fig. 3.2. The other two unstable solutions correspond to the two local maxima in the potential.

3.1.1.2 Analytical expression for the SQUID resonance

The expression for the SQUID resonance obtained so far, Eq.(3.9), still requires a numerical solution to $\delta_{\rm dc}$. The equation of motion can be separated into dc and rf components and solved separately (see Eqs.(3.6) and (3.7)). However, the dc component equation contains a transcendental function. To obtain a closed-form solution, we can further assume the applied dc flux is weak and expand the trigonometric terms up to the third order in $\delta_{\rm dc}$, i.e. $\sin\delta_{\rm dc} \sim \delta_{\rm dc} - \delta_{\rm dc}^3/6$, $\cos\delta_{\rm dc} \sim 1 - \delta_{\rm dc}^2/2$. The numerical accuracy of this expansion is illustrated in Fig. 3.6 for $\beta_{\rm rf} = 5.83$. Again, consider the solution in the form $\delta(t) = \delta_{\rm dc} + \delta_{\rm rf}\exp(i\Omega\tau)$ valid in the low applied rf flux limit, and substitute it into the equation of motion, Eq. 3.5,

$$\phi_{\rm dc} = \delta_{\rm dc} + \beta_{\rm rf}(\delta_{\rm dc} - \frac{\delta_{\rm dc}^3}{6}) \tag{3.11}$$

$$\phi_{\rm rf} = (1 + \beta_{\rm rf}(1 - \frac{\delta_{\rm dc}^2}{2}) + i\gamma\Omega - \Omega^2)\delta_{\rm rf}, \tag{3.12}$$

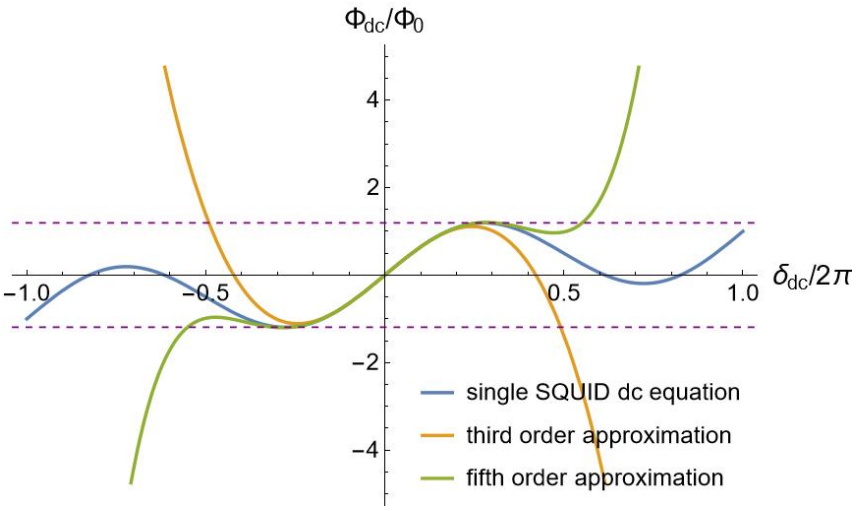

Figure 3.6: Illustration of the single SQUID dc equation: $\phi_{dc} = \delta_{\rm dc} + \beta_{\rm rf} \sin \delta_{\rm dc}$ and its power series approximation. The third order approximation has acceptable accuracy in the range $[-\Phi_{\rm dc0},\ \Phi_{\rm dc0}]$, outlined by the purple horizontal dashed lines.

where the dc component is a depressed cubic equation (without a second order term) in $\delta_{\rm dc}$ in the form $x^3 + px + q = 0$, where $p = -6(1 + {\beta_{\rm rf}}^{-1})$, $q = 6\phi_{\rm dc}/\beta_{\rm rf}$. For $\Phi_{\rm dc} \in (-\Phi_{\rm dc0}, \Phi_{\rm dc0})$, there are three distinct real roots given by by F. Viète [187] ,

$$x_k = 2\sqrt{-\frac{p}{3}} \cos\left[\frac{1}{3}\arccos\left(\frac{3q}{2p}\sqrt{-\frac{3}{p}}\right) - \frac{2k\pi}{3}\right] \text{ for } k = 0, 1, 2. \tag{3.13}$$

The middle root where $k = 1$ corresponds to the solution branch from the zero initial condition as shown in Fig. 3.6. Substituting the dc flux solution into the rf component resonance condition, we obtained the resonance frequency:

$$\Omega_R = \frac{i\gamma}{2} + \frac{1}{2}\sqrt{4(1 + \beta_{\rm rf}(1 - \delta_{\rm dc0}^2/2)) - \gamma^2}.$$

For loss $\gamma \ll 1$,

$$\begin{aligned} \Omega_R &= \sqrt{1 + \beta_{\rm rf}(1 - \delta_{\rm dc0}^2/2)} \\ &= \sqrt{1 + \beta_{\rm rf}}\sqrt{1 - 4\cos^2\left[\frac{1}{3}\arccos\left(\frac{-3\phi_{\rm dc}\sqrt{\beta_{\rm rf}}}{(2 + 2\beta_{\rm rf})^{1.5}}\right) - \frac{2\pi}{3}\right]}, \end{aligned} \tag{3.14}$$

which is a closed-form formula for $\Omega_R(\phi_{\rm dc})$. The resonance curves obtained from the above expression, Eq.(3.14), from the first dc-flux tuning period for different $\beta_{\rm rf}$ are shown in Fig. 3.7, which closely follow the numerical solutions in Fig. 3.3.

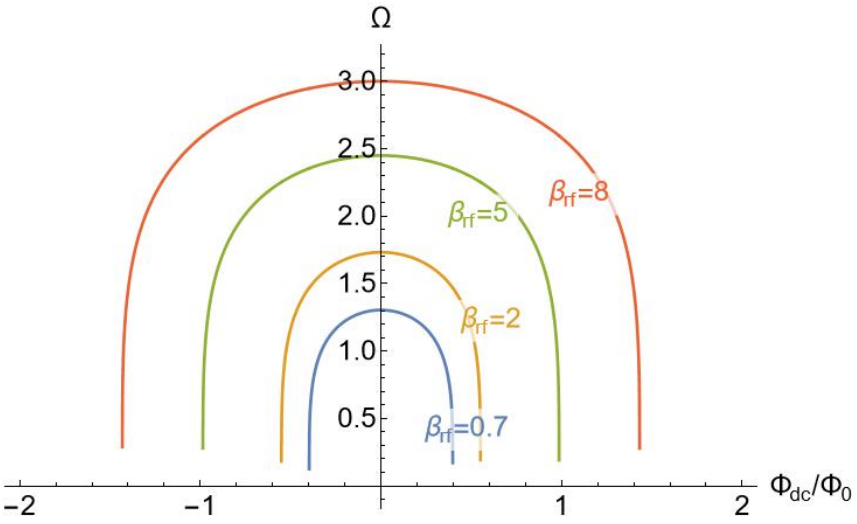

Figure 3.7: The resonance frequency inside the first dc-flux tuning period solved from the weak dc and rf field approximation (Eq.(3.14)). The resonance frequency shifts up for higher $\beta_{\rm rf}$, and the width of the $\Phi_{\rm dc}$ tuning curve increases at the same time.

3.1.2 Numerical solution to the RCSJ model for a single rf SQUID

To go beyond the weak rf field assumption imposed by the linear-limit solution, we used the differential equation solver LSODA from Python that is based on ODEPACK in FORTRAN. The solver is designed to solve initial value problems.

Therefore, the equation of motion, Eq.(3.5) is first converted into the following form:

$$\begin{aligned}\frac{d\delta}{d\tau} =& \dot{\delta} \\ \frac{d\dot{\delta}}{d\tau} =& \frac{d^2\delta}{d\tau^2} = \phi_{\rm dc} + \phi_{\rm rf}\sin(\Omega\tau) - (\delta + \beta_{\rm rf}\sin\delta + \gamma\dot{\delta})\end{aligned} \tag{3.15}$$

The equations now describe an initial value problem with two coupled variables δ and $\dot{\delta}$. The numerical solution is obtained after solving the above system Eq.(3.15) for hundreds of rf cycles to ensure that the rf SQUIDs have reached steady state response. The typical experimental measurement for an rf SQUID varies several parameters such as frequency of the rf drive, the value of the applied dc or rf flux, to see their tuning pattern. In our numerical simulation, the parameter sweep is achieved by solving the gauge-invariant phase evolution $\delta(\tau)$ under one particular set of parameters and then feeding the solutions to the next set of parameters as the initial values.

3.1.2.1 Simulation of the microwave transmission through a waveguide loaded with the rf SQUIDs

To compare with experimental results, one needs to convert the solutions for $\delta(\tau)$ into measurable quantities. Here, we assume that the only lossy element is the resistive channel of the junction, and this dissipation leads to the change in transmission magnitude through the metamaterial [30],

$$P_{\rm dissipation}(f) = \sum_i \frac{V_i(f)^2}{R} = \sum_i \left(\frac{\Phi_0\hat{\dot{\delta}}_i(f)}{2\pi}\right)^2 /R \tag{3.16}$$

$$S_{21}(f) = 10\log_{10}(1 - P_{\rm dissipation}(f)/P_{\rm incident}(f)), \tag{3.17}$$

where the summation is over all the SQUIDs in the sample, $\hat{\dot{\delta}}(f)$ is the Fourier transform of the time derivative of the gauge-invariant phase difference, V is the voltage drop across the junction, the sub-gap resistance R is assumed to be 500 Ω for all the SQUIDs studied here, P_{incident} is the total rf power incident on the waveguide hosting the metamaterial (which provides the rf flux bias to the SQUIDs), and S_{21} is the transmission coefficient through the metamaterial. Since our measurement is carried out in the frequency domain, all the quantities above are evaluated at a given frequency f as explicitly stated in Eq.(3.17). The quantity P_{incident} is related to the applied rf flux Φ_{rf} as follows. For the experimental setup in Fig. 3.8, the sample lies in the center of a rectangular waveguide and is perpendicular to the rf magnetic field of the propagating TE_{10} mode.

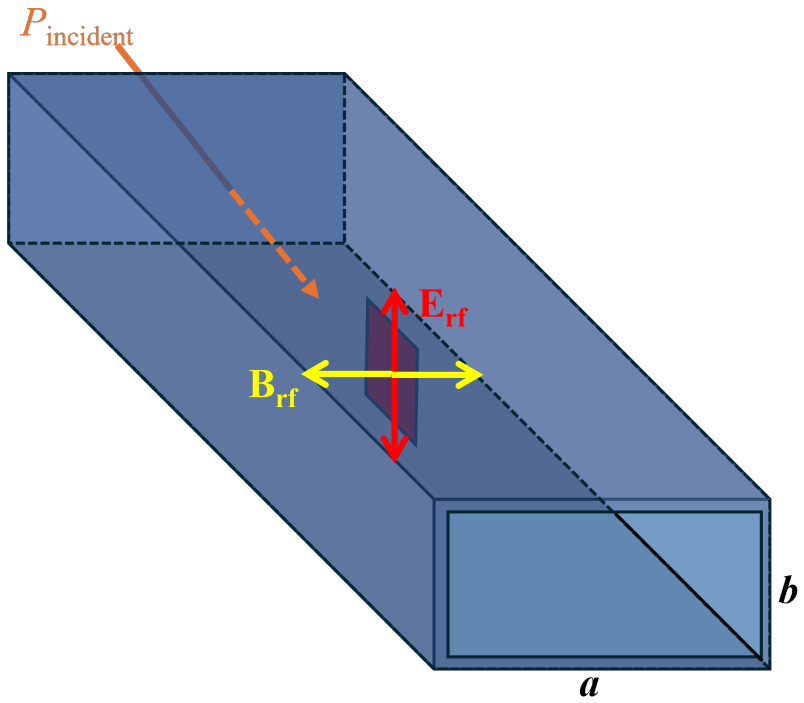

Figure 3.8: Illustration of the geometry of the waveguide transmission measurement. The directions of the B_{rf} field for the TE_{10} mode at the center of the waveguide is always perpendicular to the sample in the given configuration. The waveguide interior dimensions are a and b.

The rf magnetic field, and thus the rf flux Φ_{rf} at the location of the SQUIDs, can be calculated from the incident power P_{incident}, the waveguide dimensions, and the frequency [44],

$$B_{\mathrm{rf}} = \sqrt{4\mu_0 \beta P_{\mathrm{incident}}/(2\pi f ab)} \tag{3.18}$$

where the propagation constant $\beta = \sqrt{(2\pi f/c)^2 - (\pi/a)^2}$, c is the speed of light, and a, b are the interior dimensions of the rectangular waveguide (see Fig. 3.8). One can estimate the wavelength of the propagating microwave through the waveguide

as $2\pi/\beta \sim 21$ mm at $f = 20$ GHz, 5 to 10 times larger than the typical sample size. Thus the SQUID arrays are sub-wavelength structures in the metamaterial limit. The applied rf flux can then be determined as $\Phi_{\rm rf} = B_{\rm rf} \times A_{\rm eff}$, where $A_{\rm eff}$ is the effective flux trapping area and is not the same as the geometrical loop area, because of the flux focusing produced by the superconducting wiring.

3.1.2.2 Flux focusing

Due to the Meissner effect, the magnetic field is expelled out of a superconductor and concentrates near the edges and surfaces. In a two dimensional superconducting circuit subjected to a perpendicular magnetic field, the locally enhanced field can lead to flux focusing where the flux trapped in a closed superconducting loop is larger than the simple estimate given as the product of the applied perpendicular field B_0 and the open loop geometrical area $A_{\rm SQUID\ loop}$ [188, 189]. The factor of the increase for a single SQUID is given by [189] as $\Phi/(B_0 A_{\rm SQUID\ loop}) \approx a_{\rm SQUID}/(a_{\rm SQUID} - 2w)$ where $a_{\rm SQUID}$ is the side length of the SQUID and w is the width of the wiring as illustrated in Fig. 3.24. The effect of flux focusing can be verified by the static magnetic field simulation in CST as shown in Fig. 3.9. The superconductor is approximated as a perfect diamagnet whose magnetic permeability $\mu \approx 0$. The flux in the loop is obtained by integration of the normal component of B field which is 1.25 times larger than the simple estimate from $B_0 A_{\rm SQUID\ loop}$, close to the single SQUID focusing factor $a_{\rm SQUID}/(a_{\rm SQUID} - 2w) \sim 1.285$ provided in Ref. [189].

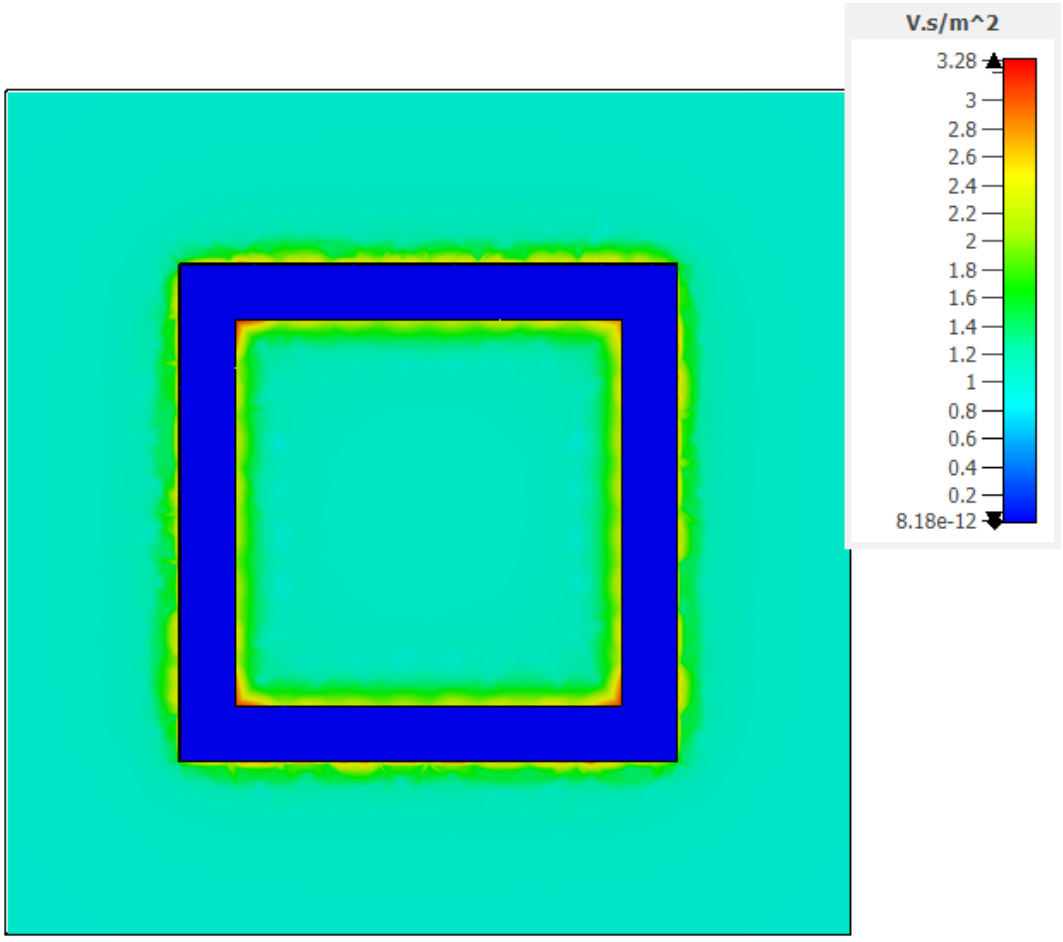

Figure 3.9: Simulation of the static magnetic field in the presence of a perfect diamagnetic loop under an applied perpendicular field of $B_0 = 1\ T$. The quantity plotted is the normal component of the magnetic field in the units of Tesla.

3.1.2.3 Sample numerical solutions for the single rf SQUID

After Fourier transforming the numerical solution $\dot{\delta}(t)$ to the frequency domain $\dot{\delta}(f)$, and substituting it into Eq.(3.17) , we obtain the simulated transmission through the metamaterial-loaded waveguide as a function of driving frequency and applied dc flux, illustrated below in Fig. 3.10.

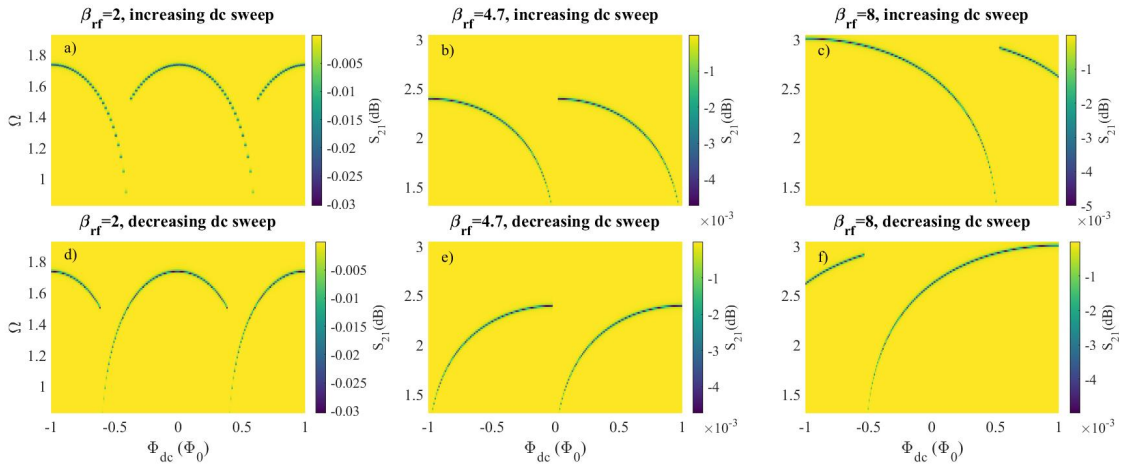

Figure 3.10: The magnitude of simulated transmission S_{21} (dB) for single SQUIDs with $\beta_{\rm rf} = 2,\ 4.7,\ 8$ at applied rf flux $\Phi_{\rm rf} = 2 \times 10^{-3}\Phi_0$ while under increasing and decreasing dc flux sweep. There exists hysteresis in dc flux sweep for these SQUIDs with $\beta_{\rm rf} > 1$ as shown by the change of the direction of the 'tails' in the tuning curve. As discussed in Sec. 3.1.1, when $\beta_{\rm rf} > \beta_{\rm rf,c1} \sim 4.6$, the tuning curve spans a range larger than $2\Phi_0$, and only less than half of the full tuning curve is visible in these sweeps.

Single SQUIDs with $\beta_{\rm rf} = 2,\ 4.7,\ 8$ and under increasing and decreasing dc flux sweep are solved numerically, as shown in Fig. 3.10. We initialize the SQUIDs in a stationary state at the applied dc flux, i.e. $\delta = \pm 2\pi$ for $\Phi_{\rm dc}$ starting at $\pm\Phi_0$.

The hysteresis in dc flux sweep has been illustrated by the difference between the calculations with different flux sweeping directions. When the dc flux increases monotonically, the solution evolves from the previous state with lower dc flux, which leads to a tuning curve continuing the trend from the left and extending to the right until the next flux jump Φ_{dc0}, and vice versa for the decreasing dc flux sweep. In addition, for SQUIDs with β_{rf} higher than $\beta_{\mathrm{rf,c1}}$, their tuning curve in dc flux can span a range larger than $2\Phi_0$. Thus, the flux jumps occur at higher Φ_{dc0}, well into the next period of the tuning curve, leading to a short segment of the curve present in the simulation, as demonstrated in Fig. 3.10 for $\beta_{\mathrm{rf}} = 4.7,\ 8$. The multistability associated with high β_{rf} can also lead to a sensitive dependence of the solution on the step size in the dc flux sweep, as demonstrated in Fig. 3.11.

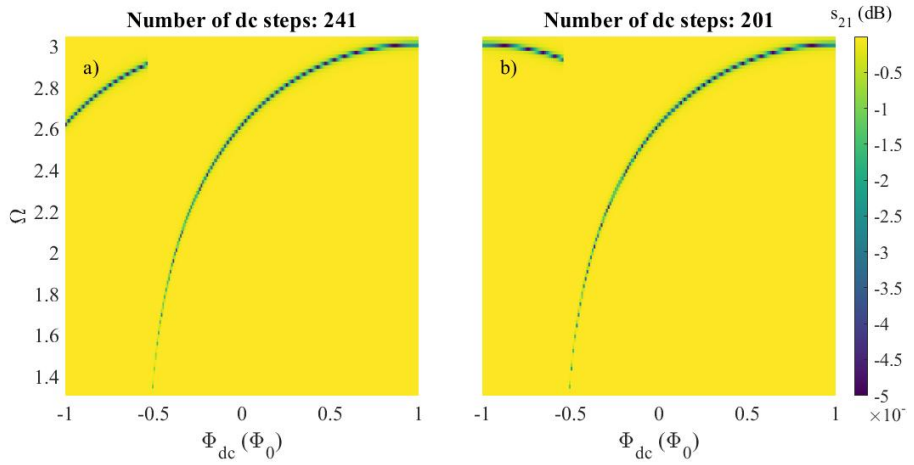

Figure 3.11: The magnitude of simulated transmission S_{21} (dB) for single SQUID with $\beta_{\rm rf} = 8$ at applied rf flux $\Phi_{\rm rf} = 2 \times 10^{-3}\Phi_0$ and under decreasing dc flux sweep from $+1$ Φ_0 of 241 steps in a) and 201 steps in b). When the solution evolves with a small step in dc flux sweep, the resonance jumps from the tuning curve centered at $\Phi_{\rm dc} = \Phi_0$ to the curve centered at $\Phi_{\rm dc} = 0$, as in a). In contrast, the resonance jumps to the tuning curve centered at $\Phi_{\rm dc} = -\Phi_0$ under a larger step in dc flux sweep shown in b).

The SQUIDs are initialized at $\delta = 2\pi$ in both Fig. 3.11 a) and b). The resonance follows through the tuning curve from $+1$ Φ_0 to -0.5 Φ_0 in both cases in Fig. 3.11. However, under a finer dc flux step with 241 steps in the dc flux sweep, the resonance jumps to the neighboring tuning curve in a). In contrast, with 201 steps in the same dc flux sweep and thus larger dc flux step, the resonance jumps to the next nearest neighbor which shows up as $2\Phi_0$ periodicity in the dc flux sweep.

The numerical solution allows us to study the SQUID response at rf drives beyond the linear limit, where $\delta_{\rm rf} \lesssim 1$. The results are summarized in Fig. 3.12

for a single SQUID with $\beta_{\rm rf} = 4.7$ at eight different rf powers. The applied rf flux amplitudes at a frequency of 20 GHz, according to Eq.(3.18), are (0.0019, 0.0613, 0.109, 0.194, 0.345 ,0.613, 1.938, 6.13) Φ_0 for a) - h) in Fig. 3.12. The hysteresis in dc flux sweep is prominent at low applied rf flux amplitudes a) - d) where the tuning curves are asymmetric in one period of dc flux sweep.

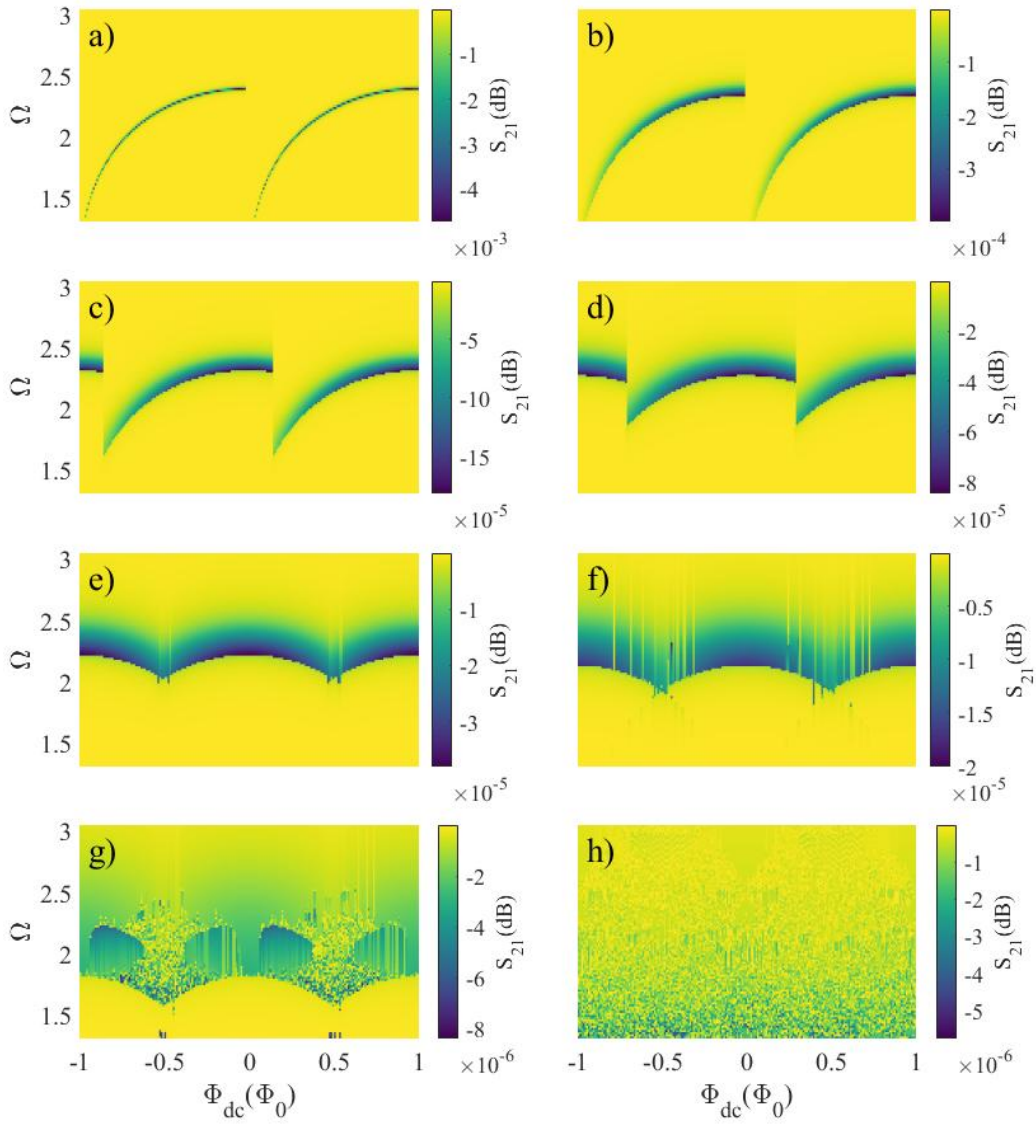

Figure 3.12: The magnitude of simulated transmission for single SQUID with $\beta_{\mathrm{rf}} = 4.7$ under decreasing dc flux sweep at different rf powers P_{incident}: (-80, -50, -45, -40, -35, -30, -20, -10) dBm for a) - h).

At higher applied rf flux amplitudes e) - g), the hysteresis is suppressed, which can be understood through the effective potential of the rf SQUID in Fig. 3.5). The

rf drive effectively moves the potential left and right periodically in δ space. Under large drives, the SQUID solutions can more easily overcome the potential barrier of the local minima and reach the global minimum, which removes the multistability and lifts the hysteresis in the dc flux sweep. The degree of tunability of SQUID resonance frequency in dc flux also decreases with increasing rf flux amplitude, and the resonance approaches the geometric resonance frequency, as expected for rf SQUIDs [44]. In the limit of very high rf drive, $\delta_{\rm rf} > 1$, however $\sin\delta$ is always bounded in $[-1, 1]$, and thus dominated over by δ. Therefore, the RCSJ equation of motion Eq. 3.5 is approximated as

$$\phi_{\rm dc} + \phi_{\rm rf} \sin\Omega\tau = \delta + \gamma\frac{d\delta}{d\tau} + \frac{d\delta^2}{d\tau^2} \tag{3.19}$$

which becomes a model for a driven damped harmonic oscillator described by linear dynamics with a constant resonance at $\Omega = 1$ (the geometric resonance). Hence the equation of motion of the rf SQUID linearizes in both the weak and strong limit of rf driving amplitude.

3.2 Model for a system of inductively coupled rf SQUIDs

So far we have only dealt with one single rf SQUID in isolation. For the inductively coupled rf SQUID metamaterial, the currents in the rf SQUID loops interact with each other via the magnetic fields that they generate. The single-SQUID rf flux relation, Eq.(3.2), can be generalized to a system of many interacting SQUIDs as $\vec{\Phi}_{\rm ind} = \overleftrightarrow{L}\,\vec{I}$, where the inductance matrix $\overleftrightarrow{L}$ contains self-inductances on its diagonal and mutual inductances between SQUIDs in the off-diagonal elements

[176]. The vector $\vec{I}$ are the currents in all the SQUID loops in the system. The flux quantization condition, Eq. (3.4) can now be written for a system of inductively-coupled identical rf SQUIDs as, [176]

$$\vec{\Phi}_{\rm dc} + \vec{\Phi}_{\rm rf}\sin(\omega t) = \frac{\Phi_0}{2\pi}\vec{\delta} + \overleftrightarrow{L}(I_{\rm c}\sin\vec{\delta} + \frac{\Phi_0}{2\pi}\frac{\dot{\vec{\delta}}}{R} + C\frac{\Phi_0}{2\pi}\ddot{\vec{\delta}}),$$

whose normalized form reads

$$\vec{\phi}_{\rm dc} + \vec{\phi}_{\rm rf}\sin(\Omega\tau) = \vec{\delta} + \overleftrightarrow{\kappa}(\beta_{\rm rf}\sin\vec{\delta} + \gamma\frac{d\vec{\delta}}{d\tau} + \frac{d^2\vec{\delta}}{d\tau^2}), \tag{3.20}$$

where $\vec{\Phi}_{\rm dc}$ and $\vec{\Phi}_{\rm rf}$ are the vectors of dc and rf magnetic flux applied to each SQUID in the array, respectively, and we assume time-harmonic rf flux at a single frequency ω. Here $\vec{\delta}$ is the array of gauge-invariant phase differences on the junctions in all of the rf SQUIDs in the array, $\overleftrightarrow{\kappa} = \overleftrightarrow{L}/L_{\rm geo}$ is the dimensionless inductive coupling matrix. Note that Eq. (3.20) assumes that every SQUID in the array has identical values for critical current I_c, RCSJ parameters R and C, and $L_{\rm geo}$, hence also identical values for $\beta_{\rm rf}$. The multistability resulting from the high $\beta_{\rm rf}$, combined with the coupling among different rf SQUIDs, can lead to interesting nonlinear dynamics in the system. We should first start with a simple case of just two inductively coupled hysteretic rf SQUIDs.

3.2.1 Two inductively coupled hysteretic rf SQUIDs

For two identical inductively-coupled rf SQUIDs (called 1 and 2), their equations of motion can be expressed explicitly as

$$\begin{aligned}
\phi_{\rm dc} + \phi_{\rm rf}\sin(\Omega\tau) &= \delta_1 + \left(\beta_{\rm rf}\sin\delta_1 + \gamma\frac{d\delta_1}{d\tau} + \frac{d^2\delta_1}{d\tau^2}\right) + \kappa\left(\beta_{\rm rf}\sin\delta_2 + \gamma\frac{d\delta_2}{d\tau} + \frac{d^2\delta_2}{d\tau^2}\right), \\
\phi_{\rm dc} + \phi_{\rm rf}\sin(\Omega\tau) &= \delta_2 + \left(\beta_{\rm rf}\sin\delta_2 + \gamma\frac{d\delta_2}{d\tau} + \frac{d^2\delta_2}{d\tau^2}\right) + \kappa\left(\beta_{\rm rf}\sin\delta_1 + \gamma\frac{d\delta_1}{d\tau} + \frac{d^2\delta_1}{d\tau^2}\right)
\end{aligned} \tag{3.21}$$

where the dimensionless coupling constant $\kappa = M/L_{\rm geo}$ accounts for the mutual inductance between the two rf SQUIDs and its magnitude is typically $\lesssim 10^{-1}$. The coupling is negative for SQUIDs in a co-planar geometry studied in this chapter, but could become positive when the two SQUID loops start to overlap, which is one of the topics addressed in Chapter 4. The two inductively-coupled rf SQUIDs can be studied with the same linear-limit analytical treatment, and the nonlinear numerical solution, as used for the single SQUID, as discussed previously in Sec. 3.1.

Under weak rf drive ($|\delta_{\rm rf}| \ll 1$), the dc component for the equations of motion are

$$\begin{aligned}
\phi_{\rm dc} &= f(\delta_{1,\rm dc}, \delta_{2,\rm dc}) = \delta_{1,\rm dc} + \beta_{\rm rf}\sin\delta_{1,\rm dc} + \kappa\beta_{\rm rf}\sin\delta_{2,\rm dc} \\
\phi_{\rm dc} &= f(\delta_{2,\rm dc}, \delta_{1,\rm dc}) = \delta_{2,\rm dc} + \beta_{\rm rf}\sin\delta_{2,\rm dc} + \kappa\beta_{\rm rf}\sin\delta_{1,\rm dc}
\end{aligned} \tag{3.22}$$

To simplify our notations, (δ_1, δ_2) will be used in the place of $(\delta_{1,\rm dc}, \delta_{2,\rm dc})$ for the rest of this section. Their solutions are illustrated in Fig. 3.13 below as the intersections of the three curves, $f(\delta_1, \delta_2) = f(\delta_2, \delta_1)$, $f(\delta_1, \delta_2) = \phi_{\rm dc}$, and $f(\delta_2, \delta_1) = \phi_{\rm dc}$.

To better understand the dc equation solutions, let's examine the condition

that is independent of applied flux, $f(\delta_1, \delta_2) = f(\delta_2, \delta_1)$:

$$\delta_1 + \beta_{\rm rf} \sin \delta_1 + \kappa\beta_{\rm rf} \sin \delta_2 = \delta_2 + \beta_{\rm rf} \sin \delta_2 + \kappa\beta_{\rm rf} \sin \delta_1.$$

For asymmetric solution where $\delta_1 \neq \delta_2$, we have

$$\frac{\sin \delta_1 - \sin \delta_2}{\delta_1 - \delta_2} = \frac{1}{(\kappa - 1)\beta_{\rm rf}}. \tag{3.23}$$

This equation describes the portions of the blue curves outside the lines $\delta_1 = \delta_2$ in Fig. 3.13. The blue line represents the trivial solution where the two SQUIDs are synchronized. We can interpret the condition for existence of asymmetric solutions Eq.(3.23) geometrically. The left hand side is the slope of the secant of the function $\sin x$. For $\beta_{\rm rf} \ll 1$, the slope is almost vertical and Eq.(3.23) has no solution since $|\kappa - 1|\beta_{\rm rf} < 1$ which requires that $|(\sin \delta_1 - \sin \delta_2)/(\delta_1 - \delta_2)| > 1$. According to the mean value theorem, it can be expressed as $(\sin \delta_1 - \sin \delta_2)/(\delta_1 - \delta_2) = d(\sin \delta)/d\delta|_{\delta=\delta_3} = \cos \delta_3$, where δ_3 is in between δ_1 and δ_2. The trigonometric function $\cos x \leq 1$ for all real x, and thus there are no asymmetric solutions in $\delta_{1,2}$ for $|\kappa - 1|\beta_{\rm rf} < 1$ as shown in Fig. 3.13(a-c).

However, with large coupling strength, we can achieve $|\kappa - 1|\beta_{\rm rf} > 1$ where asymmetric solutions are possible, even for $\beta_{\rm rf} < 1$, as illustrated in Fig. 3.14. These additional solutions can lead to multistability and distinguish the two coupled SQUIDs from the single SQUID where multistability is only expected for hysteretic SQUIDs with $\beta_{\rm rf} > 1$.

For a fixed coupling κ, as $|\kappa - 1|\beta_{\rm rf}$ increases above one, the magnitude of the slope of the secant line decreases and the secant line intersects with the sine curve at two points, δ_1 close to δ_2. These solutions are represented by the blue 'ellipses'

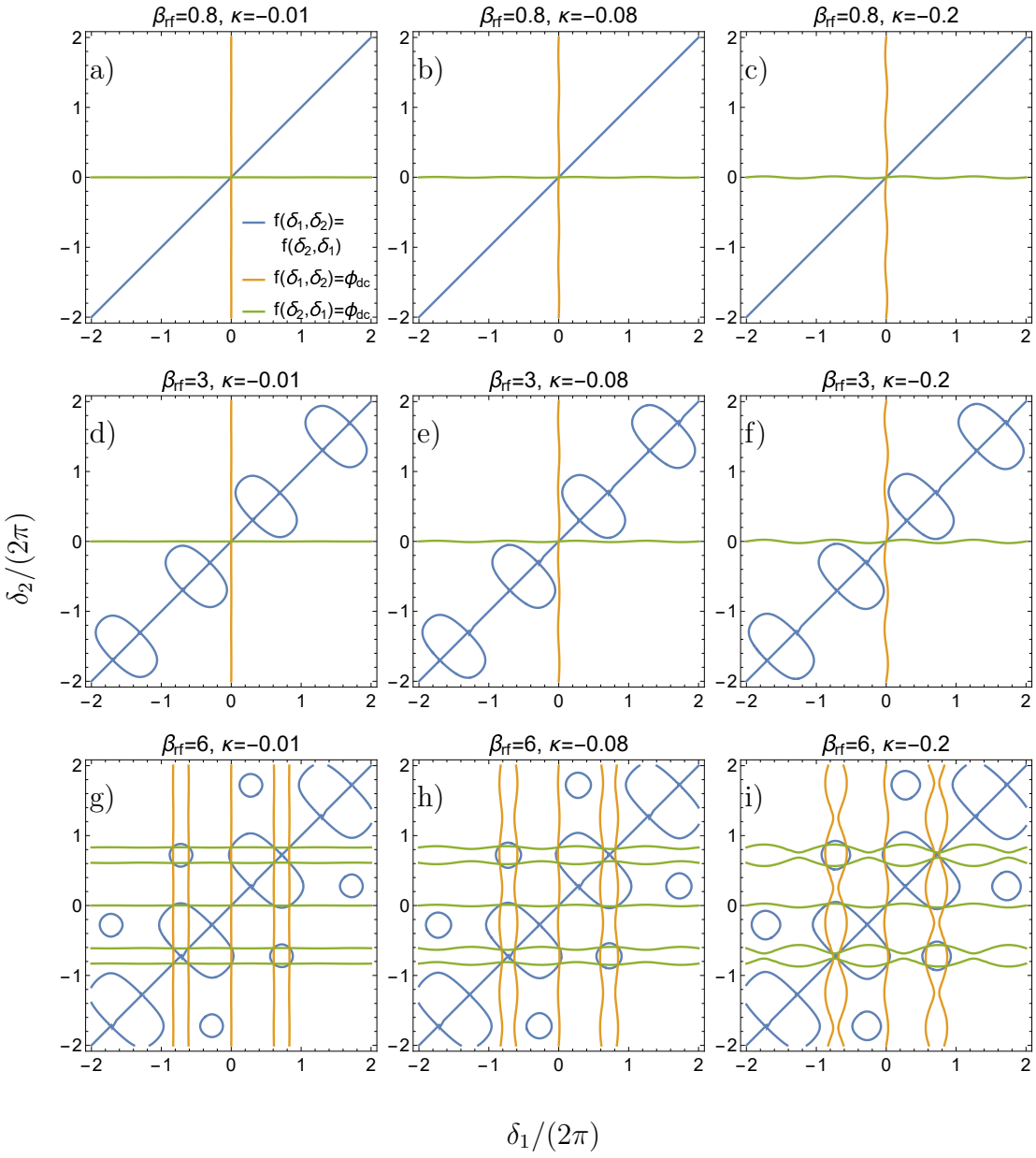

Figure 3.13: The dc solution curves for the two SQUIDs with $\beta_{\rm rf} = 0.8, 3, 6$ and $\kappa = -0.01, -0.08, -0.2$, at zero dc flux in the (δ_1, δ_2) space. The solutions to the dc equation are marked by the intersections of the three different-colored curves (blue, green and orange). One can clearly observe that just as for the single SQUID, the dc solution becomes multi-stable at high $\beta_{\rm rf}$.

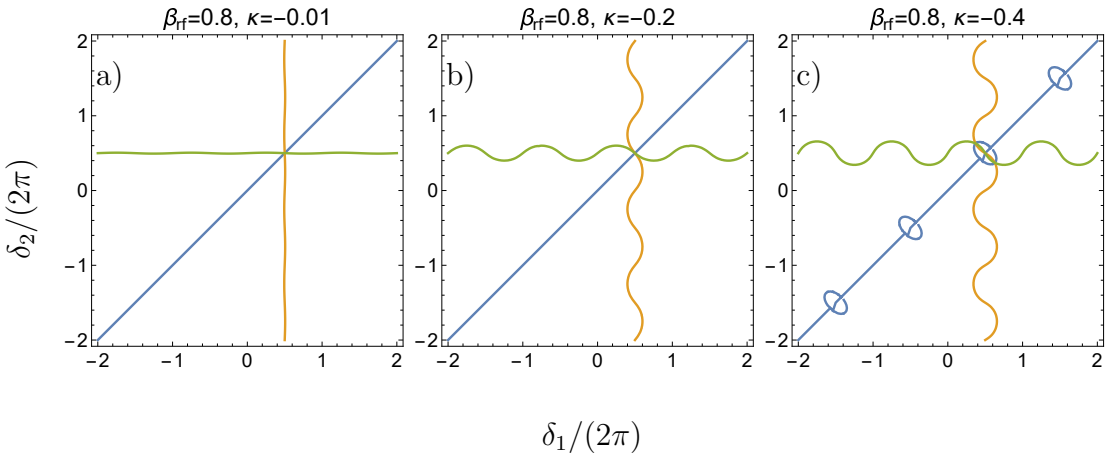

Figure 3.14: The dc solution curves for the two SQUIDs with $\beta_{\rm rf} = 0.8$ and $\kappa = -0.01, -0.2, -0.4$, at dc flux $\Phi_{\rm dc} = 0.5\Phi_0$ in the (δ_1, δ_2) space. When $|\kappa - 1|\beta_{\rm rf} > 1$, one should expect multi-stability at half flux quantum of applied dc flux, in contrast to the multi-stability condition for a single SQUID, which requires $\beta_{\rm rf} > 1$.

near the diagonal line centered around the half flux quantum points as shown in Fig. 3.13(d-i). The onset of the additional blue 'circles' off the diagonal in Fig. 3.13 at large $\beta_{\rm rf}$ are closely related to the critical values, $\beta_{\rm rf,c1}$ and $\beta_{\rm rf,c2}$ introduced in Sec. 3.1.1. When $|\kappa - 1|\beta_{\rm rf}$ is further increased to $\beta_{\rm rf,c1}$, the magnitude of the slope becomes shallower so that the secant line can intersect with the sine curve on points one dc-flux period away from each other as shown by the orange line in Fig. 3.15. These solutions correspond to the blue 'circles' next to the diagonal line where $|\delta_1 - \delta_2| > 2\pi$. The next critical value $\beta_{\rm rf,c2}$ signifies the appearance of another set of 'circles' where δ_1 and δ_2 can be more than 4π away, corresponding to the green line in Fig. 3.15.

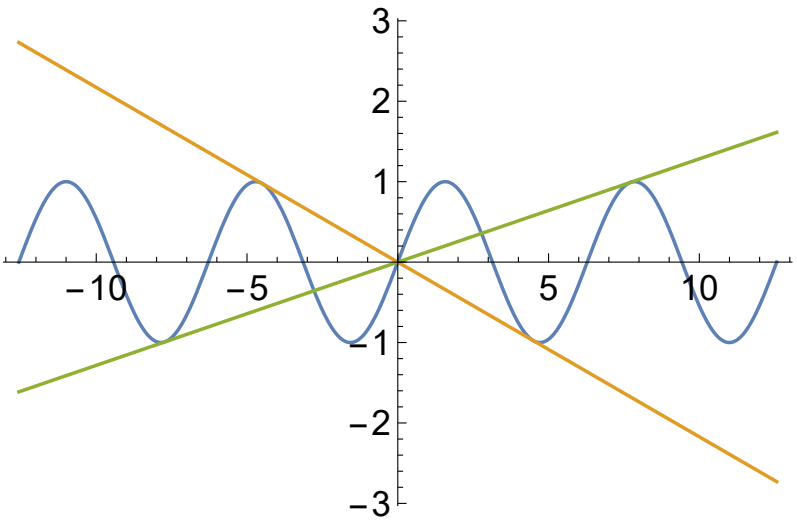

Figure 3.15: Illustration of the solution to Eq. 3.23, where the left hand side corresponds to a secant line on the sine curve shown in blue here. At the critical $\beta_{\rm rf}$ values, the secant line can intersect with the sine curve at points more than one period away which are responsible for the blue 'circles' off the diagonal in Fig. 3.13.

We can gain more insight to the dc flux dependence of the two coupled hysteretic SQUIDs with $\beta_{\rm rf} = 6.26$ and $\kappa = -0.08$ by following through the evolution of the dc solutions as a function of changing applied dc flux.

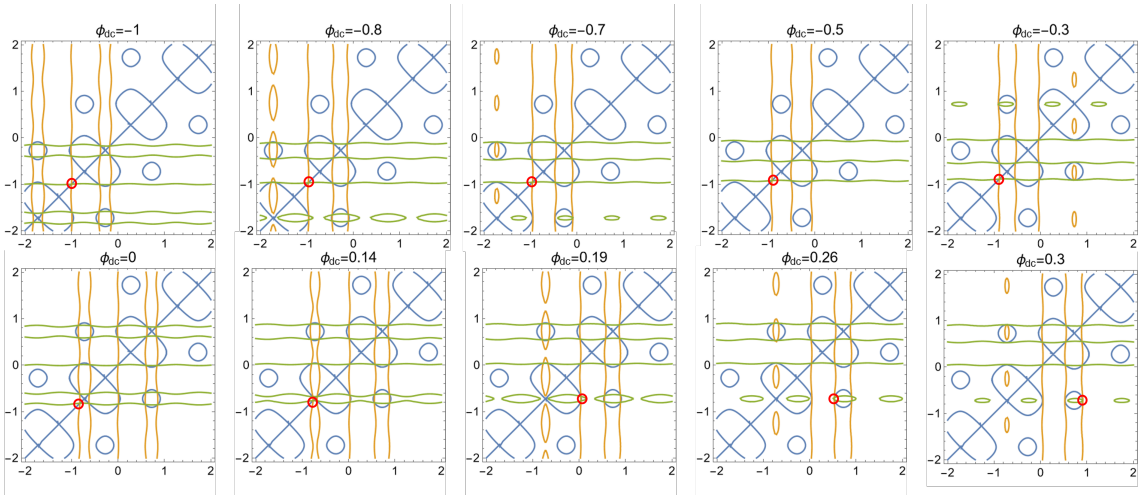

Figure 3.16: Evolution of the dc solution curves in dc flux for two coupled hysteretic SQUIDs with $\beta_{\rm rf} = 6.26$ and $\kappa = -0.08$. The red dots track one potential path for the solutions as dc flux increases from $-1\Phi_0$ to $0.3\Phi_0$, where the solution jumps from the symmetric states represented by the diagonal line to the asymmetric states on the 'circles'.

We can initialize the SQUIDs in the state $\delta_1 = \delta_2 = -2\pi$ at $\Phi_{\rm dc} = -\Phi_0$, and the dc solutions are tracked by the red circles in Fig. 3.16 as applied dc flux increases. The two SQUIDs are in the coherent state where $\delta_1 = \delta_2$ until $\Phi_{\rm dc} = 0.19$. When the solution on the symmetric branch disappeared between $\Phi_{\rm dc} = 0.14$ and $\Phi_{\rm dc} = 0.19$, it has to jump to the next available solution, for which there are four candidates. The closest solutions in the (δ_1, δ_2) phase space are the four intersections between the ellipse and the green and yellow curves. The ones below the main diagonal corresponding to an almost 2π change in δ_1 and small change in δ_2 are picked in the illustration in Fig. 3.16. We can compare the dc flux dependence for different couplings κ by plotting the critical dc flux $f_{c,1(2)}$ when the solution enters (leaves)

the blue 'circles' as in Fig. 3.17.

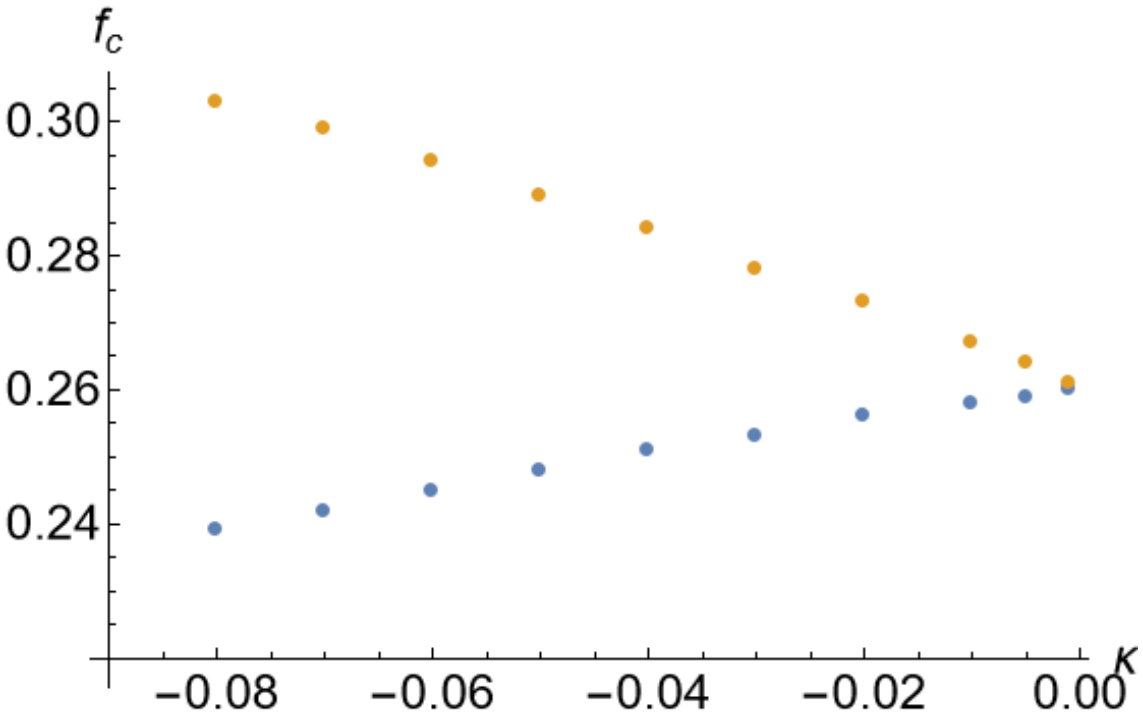

Figure 3.17: The critical dc flux $f_{c,1}$ (blue) and $f_{c,2}$ (yellow) as functions of coupling strength κ. When the coupling becomes stronger, the region where the solution stays on the asymmetric states, represented by the 'circles' in Fig. 3.13, grows larger.

Clearly, the dc flux solutions from the SQUIDs with stronger coupling remain asymmetric for a larger range of applied dc flux, as indicated by the large difference between $f_{c,1}$ and $f_{c,2}$ in Fig. 3.17 for larger $|\kappa|$. The asymmetric solutions lead to coexistence of two different SQUID states even though they are initialized under the same conditions. For a larger system, the solutions with different δs give rise to multiple resonances observed under one applied dc flux as illustrated later numerically in Fig. 3.23 and experimentally in Fig. 3.32.

3.2.2 Larger systems of inductively coupled hysteretic rf SQUIDs

The methods outlined in Sec. 3.1.1 and 3.1.2 can be easily extended to larger systems of coupled SQUIDs to obtain the linear-limit analytical and full numerical solutions. The equations of motion under the weak rf flux approximation for a system of inductively coupled SQUIDs are:

$$\vec{\phi}_{\rm dc} = \vec{\delta}_{\rm dc} + \beta_{\rm rf} \overleftrightarrow{\kappa} \sin \vec{\delta}_{\rm dc} \tag{3.24}$$

$$\vec{\phi}_{\rm rf} \sin(\Omega\tau) = \vec{\delta}_{\rm rf} + \overleftrightarrow{\kappa} \left((\beta_{\rm rf} {\rm diag}(\cos \vec{\delta}_{\rm dc})) \vec{\delta}_{\rm rf} + \gamma \frac{d\vec{\delta}_{\rm rf}}{d\tau} + \frac{d^2 \vec{\delta}_{\rm rf}}{d\tau^2} \right) \tag{3.25}$$

Again, the dc solutions are first obtained from the algebraic dc component in Eq.(3.24). Applying a Fourier transform to the rf component in Eq. (3.25) turns it into a linear system:

$$\vec{\phi}_{\rm rf} \sin(\Omega\tau) = \left(\overleftrightarrow{1} + \overleftrightarrow{\kappa} (\beta_{\rm rf} {\rm diag}(\cos \vec{\delta}_{\rm dc}) + i\gamma\Omega - \Omega^2) \right) \vec{\delta}_{\rm rf} \tag{3.26}$$

The SQUIDs become resonant when the response matrix in the large parenthesis become singular with zero determinant, corresponding to the existence of nontrivial solutions under zero drive amplitude. The resonance condition is expressed as

$$\det \left(\overleftrightarrow{1} + \overleftrightarrow{\kappa} (\beta_{\rm rf} {\rm diag}(\cos \vec{\delta}_{\rm dc}) + i\gamma\Omega - \Omega^2) \right) = 0 \tag{3.27}$$

The resonance frequencies are determined as the solutions to the above characteristic equation in dimensionless frequency Ω and plotted below in Fig. 3.18 for weakly and strongly coupled 5×5 arrays of SQUIDs with the same parameter $\beta_{\rm rf} = 5.56$ and $\gamma = 0.027$. The coupling matrix $\overleftrightarrow{\kappa}$ are determined from the mutual inductances obtained from a FastHenry calculation for the entire array, where the SQUID loops are discretized into rectangular filaments.

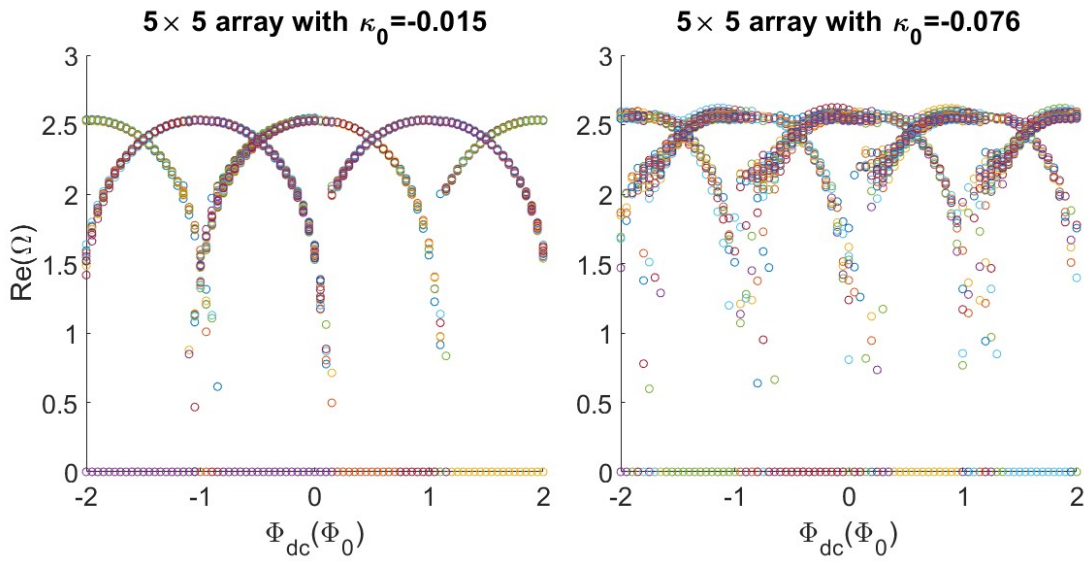

Figure 3.18: Real parts of the dimensionless eigenfrequencies Ω solved from the characteristic equation Eq.(3.27) for two 5×5 arrays of SQUIDs with the same parameters $\beta_{\rm rf} = 5.56$ and $\gamma = 0.027$ and under increasing dc flux sweep. The left panel has weak inductive coupling in the system where the coupling between the nearest neighbor is $\kappa_0 = -0.015$, and the right panel has strong inductive coupling where $\kappa_0 = -0.076$.

The eigenfrequencies from the weakly coupled system where the nearest neighbor coupling $\kappa_0 = -0.015$ in the left panel resemble the single SQUID resonance in Fig. 3.3. However, the stronger coupling ($\kappa_0 = -0.076$) lifts the degeneracy of the eigenfrequencies, demonstrated in the right panel of Fig. 3.18. The multistability from the strong coupling, as illustrated in Fig. 3.13 and 3.14 for a pair of SQUIDs, is responsible for the spread of eigenfrequencies near the jumps between different tuning curves in the right panel.

The value of the eigenfrequencies can be verified by the resonance frequency

calculated from the circuit model for a single SQUID in Eq.(1.9). To extended this model from a single SQUID to a large coupled system of N SQUIDs, we need to generalize the concept of the geometric inductance. In a SQUID loop carrying current I, $L_{\rm geo} = \Phi_{\rm ind}/I$, is the ratio between the induced flux and the loop current. For a system of SQUIDs, the induced flux is now due to all the SQUIDs in the coupled system. Consider a coherent system where all the SQUIDs share the same current I, the induced flux on SQUID i is $\Phi_{i,\rm ind} = \sum_{j=1}^{N} L_{i,j} I$. Its effective inductance is then $L_{i,\rm eff} = \Phi_{\rm ind}/I = \sum_{j=1}^{N} L_{i,j}$. We can then express the resonance frequency for SQUID i in the coherent mode in terms of the effective inductance:

$$\omega_{i,0} = \sqrt{(L_{i,\rm eff}^{-1} + L_{\rm JJ}^{-1})C^{-1}}$$

$$\Omega_{i,0} = \frac{\omega_{i,0}}{\omega_{\rm geo}} = \sqrt{\frac{L_{\rm geo}}{L_{i,\rm eff}} + \beta_{\rm rf}\cos\delta_{\rm dc}} = \sqrt{\frac{1}{\sum_{j=1}^{N}\kappa_{i,j}} + \beta_{\rm rf}\cos\delta_{\rm dc}} \tag{3.28}$$

Since all the SQUID loops are assumed to be in a co-planar geometry, the mutual inductances are all negative which constitute an antiferromagnetically coupled system. The term $\sum_{j=1}^{N}\kappa_{i,j}$ is therefore less than 1, making the resonance of the SQUIDs in this coupled system higher than an isolated single SQUID. Under zero applied dc flux when all the SQUIDs are in the state $\delta = 0$, we can determine the resonance of the center SQUID in the 5×5 system as $\Omega_0 = 2.58$ for the left panel of Fig. 3.18, and $\Omega_0 = 2.67$ for the right, agreeing with the eigenfrequencies solved from Eq.(3.27). In fact, if we consider the coherent eigenmode, $\vec{v}_{\rm coh} = (1, 1, ..., 1)^T$, the resonance condition is then

$$\left(\overleftrightarrow{1} + (\beta_{\rm rf}\cos\delta_{\rm dc} + i\gamma\Omega - \Omega^2)\overleftrightarrow{\kappa}\right)\vec{v}_{\rm coh} = 0 \tag{3.29}$$

The solution for Ω in the ith row for $\gamma \ll 1$ reproduces $\Omega_{i,0}$ given in the circuit

model, Eq.(3.28).

Note that the data points on the x-axes ($\mathrm{Re}[\Omega] = 0$) of Fig. 3.18 are the pure imaginary solutions, which is a consequence of having $\beta_{\mathrm{rf}} > 1$. As a consequence, in Eq.(3.29), the term $\beta_{\mathrm{rf}} \cos\delta_{\mathrm{dc}}$ can be less than -1, and this imposes pure imaginary Ω solutions.

We should now examine the direct numerical solution for large arrays. Similar to solving the single SQUID in Sec. 3.1.2, the model is formulated as a system of initial value problems:

$$\begin{aligned} \frac{d\vec{\delta}}{d\tau} =& \dot{\vec{\delta}} \\ \frac{d\dot{\vec{\delta}}}{d\tau} =& \frac{d^2\vec{\delta}}{d\tau^2} = \overleftrightarrow{\kappa}^{-1}(\vec{\phi}_{\mathrm{dc}} + \vec{\phi}_{\mathrm{rf}}\sin(\Omega\tau) - \vec{\delta}) - \beta_{\mathrm{rf}}\sin\vec{\delta} - \gamma\dot{\vec{\delta}}. \end{aligned} \tag{3.30}$$

The solutions to the $2n$ variables for n SQUIDs are obtained under varying applied dc/rf flux and rf drive frequency, as described in Sec. 3.1.2. The simulated transmission spectra of two systems of different size with the same parameter $\beta_{\mathrm{rf}} = 5.56$ are compared below in Fig. 3.19. The strongly coupled system contains more meta-atoms contributing to the stronger response in the simulated transmission (note the scales for S_{21} for the two plots). The resonance also occurs at higher frequency in the strongly coupled system as predicted by Eq.(3.28), which gives $\Omega_0 \sim 2.70$ for a SQUID near the center of the strongly coupled system, and $\Omega_0 \sim 2.58$ for the corresponding SQUID in the weakly coupled array. The coherence among the SQUIDs can be quantified by the modified Kuramoto order parameter [190, 26]:

$$R_K = \left| \frac{\sum_i \hat{\delta}_i}{\sum_i |\delta_i|} \right| \tag{3.31}$$

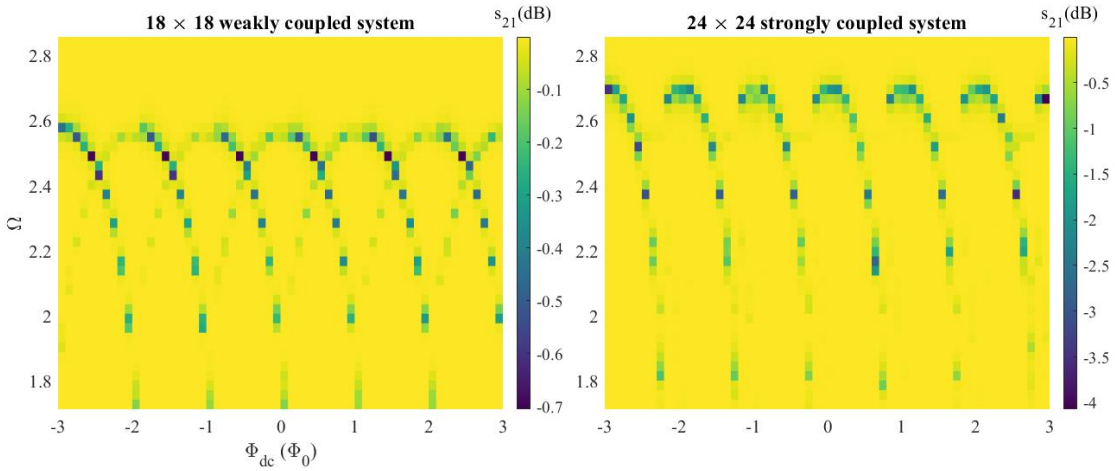

Figure 3.19: The magnitude of simulated transmission for two systems of SQUIDs with $\beta_{\mathrm{rf}} = 5.56$ under increasing dc flux sweep from -3 to $3\Phi_0$, left: 18×18 system with weak coupling ($\kappa_0 = -0.015$) and right: 24×24 system with strong coupling ($\kappa_0 = -0.076$). The hysteretic jumps during the dc flux sweep are expected from the multistability. The resonances in the strongly coupled system are higher than the weakly coupled system as expected from Eq.(3.28) where strong antiferromagnetic coupling leads to smaller effective inductances.

where we use $\hat{\square}$ to denote the complex value of the gauge-invariant phase differences after the Fourier transform. Their phases are relative to the rf drive, which acts as a global clock. When the system is completely asynchronized, the phase will distribute uniformly between 0 and 2π and $\sum_i \hat{\delta}_i \approx 0$ leading to $R_K = 0$. On the other hand, when all the SQUIDs oscillate at the same frequency and phase, the system is coherent, and $R_K = 1$. The modified Kuramoto order parameters for the two systems studied above are plotted in Fig. 3.20.

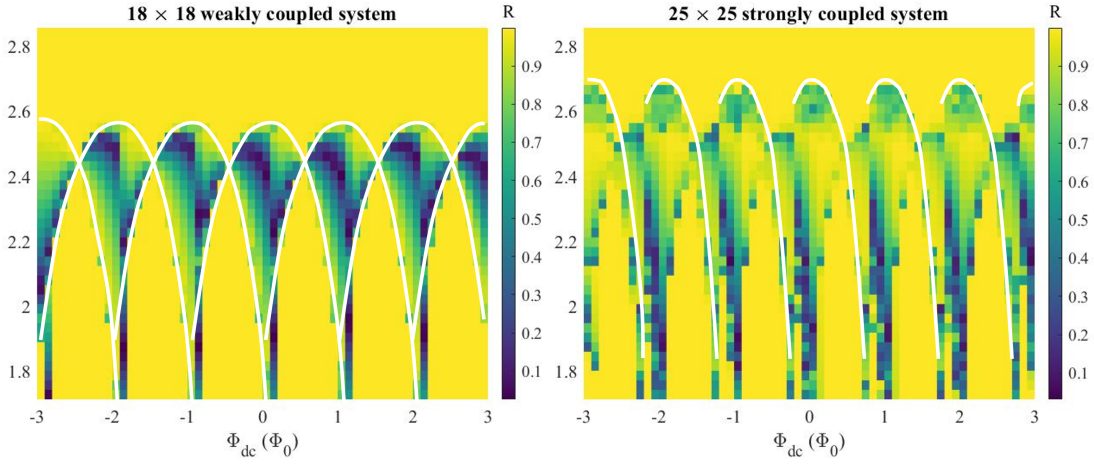

Figure 3.20: The modified Kuramoto order parameters R_K for the weakly and strongly coupled systems as studied in Fig. 3.19. The strongly coupled system is more coherent near the intersections between the two neighboring tuning curves as highlighted in white, obtained from an interpolation of the transmission dip in Fig. 3.19.

The strongly coupled system is more coherent overall as represented by the smaller dark blue region in Fig. 3.20, especially near the intersections between the two neighboring tuning curves, which are colored white. We can gain more in-

sight by investigating the solutions to individual SQUIDs. Several solutions to the gauge invariant phase differences with tuning patterns deviating from the average are selected and plotted in Fig. 3.21.

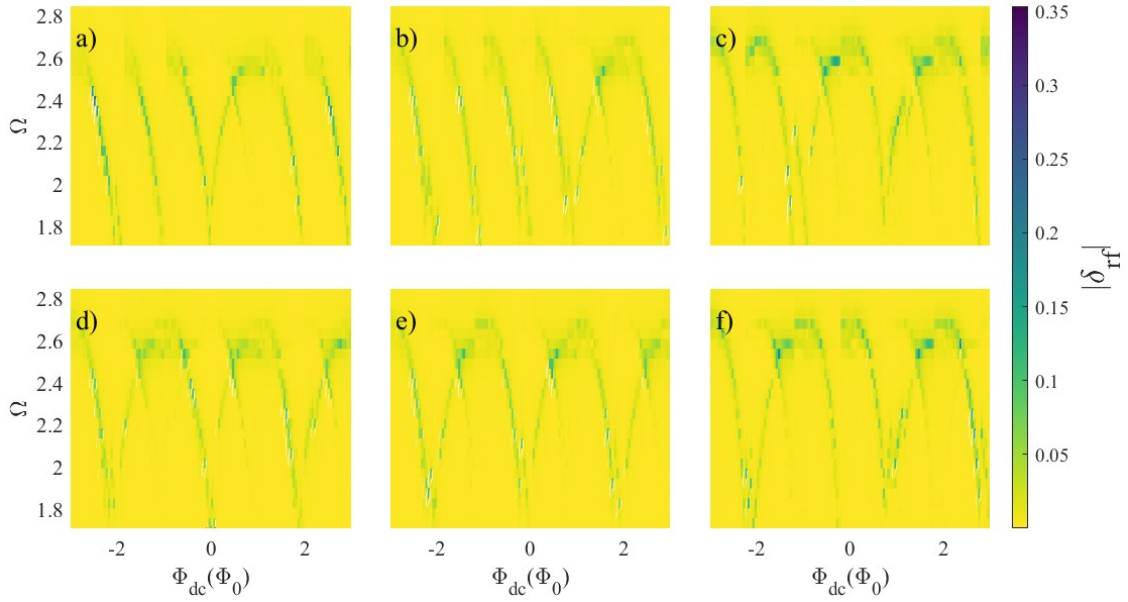

Figure 3.21: The amplitude of δ_{rf} for the selected individual SQUIDs in the strongly coupled 24×24 array. These resonances differ from the average response where the tuning is perfectly periodic with applied dc flux under periodicity of $1\Phi_0$. The tuning curves could skip the nearest neighbor curve, which leads to $2\Phi_0$ periodicity in dc flux tuning as in panels d), e). Panels a)-c), and f) show some combination of both $2\Phi_0$ and $1\Phi_0$ tuning periodicities.

Panels d) and e) show $2\Phi_0$ periodicity in flux tuning in Fig. 3.21, which has not been observed in the conventional non-hysteretic rf SQUID metamaterials before. The change in flux tuning periodicity is a consequence of the increased multistability in the hysteretic rf SQUID. A similar dc flux dependence can be realized in a single

hysteretic SQUID as illustrated in Fig. 3.11 b). However, these SQUIDs are in the minority in the array where the average response is dominated by the Φ_0 periodicity. The SQUIDs with abnormal tuning behaviors as in Fig. 3.21 have been recorded and labeled in Fig. 3.22 below.

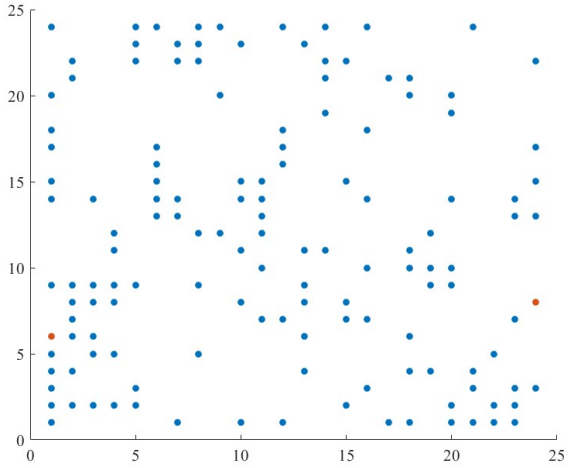

Figure 3.22: The map of the 'outlier' SQUIDs in the 24×24 strongly coupled system whose dc flux dependence deviates from the Φ_0 periodicity . The row and column indices of these SQUIDs are recorded and plotted as circles. The orange circles stand for the two SQUIDs with complete $2\Phi_0$ dc flux tuning periodicity as in Fig. 3.21 d) and e).

Figure Fig. 3.22 shows that the SQUIDs with abnormal dc flux dependence are more likely to reside on the boundary of the array, where the effective coupling is weaker due to the lack of neighbors. The two SQUIDs with purely $2\Phi_0$ periodicity (orange circles) are on the opposite edges of the array. Other than this general trend, the 'outlier' SQUIDs seem to distribute randomly throughout the array, which is expected for a multistable system such as the hysteretic rf SQUID array.

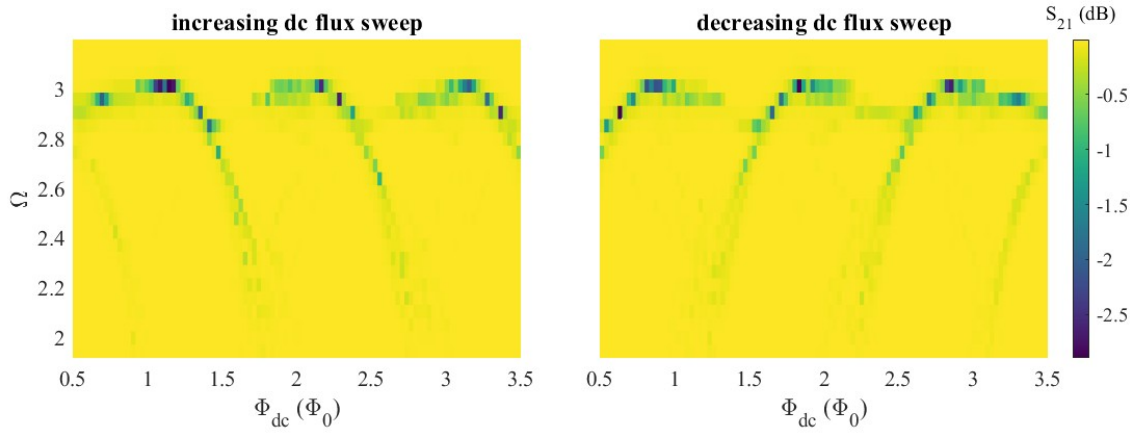

Figure 3.23: The magnitude of simulated transmission for a strongly coupled system of 24×24 SQUIDs with $\kappa_0 = -0.076$ and $\beta_{\rm rf} = 6.26$ under increasing and decreasing dc flux sweeps. The hysteresis is clearly demonstrated in the contrast of the resonances from different dc sweep directions.

Last but not least, the same hysteresis in dc flux sweep for the single SQUID with $\beta_{\rm rf} > 1$ is expected in a large system of hysteretic SQUIDs and is illustrated in the numerical solutions plotted below for a system of 24×24 strongly coupled ($\kappa_0 = -0.076$) and hysteretic ($\beta_{\rm rf} = 6.26$) SQUIDs in Fig. 3.23.

We can observe a similar hysteresis in the dc sweep to the single SQUID studied in Sec. 3.1.2.3. In addition, the multistability of the large coupled system leads to the coexistence of multiple resonances under one applied dc flux around (0.75, 1.75, 2.75) Φ_0 for the increasing dc flux and around (1.25, 2.25 3.25) Φ_0 for the decreasing sweep, as depicted in Fig. 3.23. The coherent branch is continuing the main tuning curve towards lower frequencies and shows as a long 'tail' in the direction of the dc flux sweep. The incoherent branches are the solutions whose δ jumps to the next period or even two periods away and shows as an extension of

the tuning curves from the next or the second next periods. These tuning curves also show an asymmetric shape around the integer flux quanta as a consequence of the different branches visited before and after the integer flux quanta in the dc flux sweep. However, the numerical solutions to the larger system are not sensitive to the step size in the dc flux sweep, different from that of the single SQUID shown in Fig. 3.11. The calculations have been carried out at both finer and coarser dc flux steps and result in the same $1\Phi_0$ periodicity behavior as illustrated in Fig. 3.23.

3.3 Experiment

A series of new-generation rf SQUID metamaterials with hysteretic meta-atoms whose $\beta_{\mathrm{rf}} > 1$ was designed and fabricated. Their electromagnetic responses at microwave frequency were also characterized in this work. The details of the experiment is discussed in this section.

3.3.1 SQUID samples

The samples presented in this thesis are fabricated by the STAR Cryoelectronics Selective Niobium Anodization Process (SNAP) and Selective Niobium Etching Process (SNEP). The Nb films have a critical temperature of $T_c = 9.2\ K$. A representative rf SQUID meta-atom is shown in Fig. 3.24.

The SQUID arrays are lithographically defined on a Si substrate, and no ground plane is present in our sample.

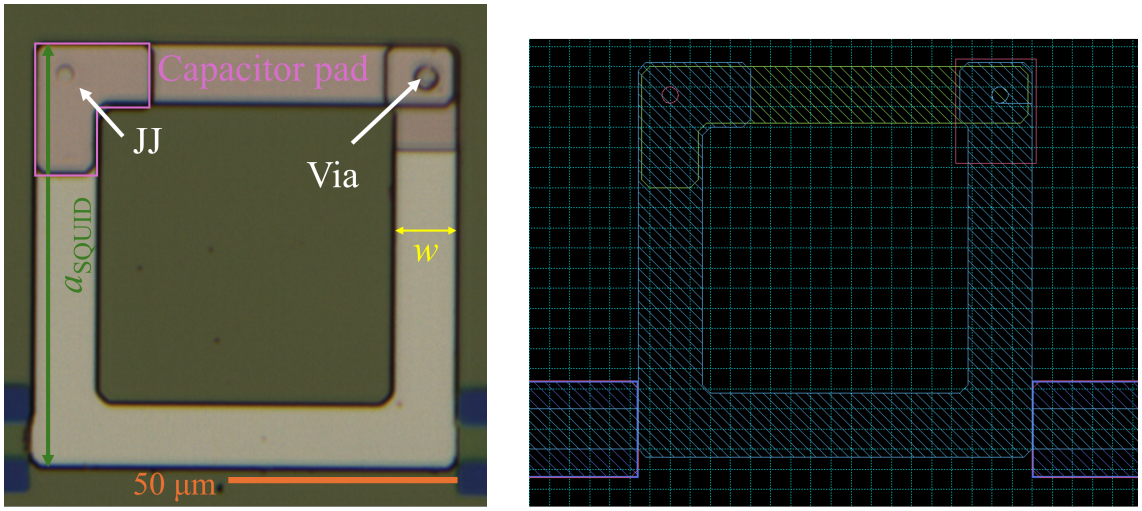

Figure 3.24: Design of a single rf SQUID meta-atom in the metamaterial. Left: micrograph of a single rf SQUID. The junction is formed in the direction perpendicular to the plane, between the two different Nb wiring layers in beige and pink colors respectively. A via is necessary to complete the circuit of the rf SQUID. Right: the design file of the same rf SQUID

3.3.1.1 SQUID design

There are several constraints in our hysteretic SQUID design due to the limitations in the fabrication and measurement capability. First, the SQUID resonance $\sqrt{1+\beta_{\rm rf}\cos\delta_{\rm dc}}f_{\rm geo}$ should be in the measurable frequency band dictated by the microwave apparatus: the WR-42 waveguide has a frequency pass band from14 to 28 GHz. For hysteretic SQUIDs with $\beta_{\rm rf} > 1$, one needs large loop inductance $L_{\rm geo}$, or large SQUID capacitance C, to maintain a low resonance frequency. Second, the parameter $\beta_{\rm rf} = L_{\rm geo}/L_{\rm JJ}$ should be kept reasonably small ($\lesssim 10$) to avoid extreme hysteresis. Third, one also needs to reduce the SQUID wiring width to achieve strong inductive coupling between the meta-atoms. In our design the line width is 16 μm, and this also limits the size of the capacitor. Lastly, the Josephson junction cannot be smaller than the critical dimension of the fabrication process, which specifies the minimum junction geometry as a circle with 3μm diameter. Considering all of the constraints in the design, we need large $L_{\rm geo}$ since C is limited by the relatively narrow wiring width, and thus a large $L_{\rm JJ}$ to maintain a small $\beta_{\rm rf} \lesssim 10$, which translates to a low critical current density in the junction, an uncommon requirement for Josephson junction foundries, since most superconducting electronics applications prefer high Josephson energy ($E_J = \Phi_0 I_c/(2\pi)$), and thus high critical current of the junction. Consequently, the STAR Cryoelectronics Niobium process with Josephson junction critical current density $J_c = 1\ \mu{\rm A}/\mu{\rm m}^2$ [191] is chosen to fabricate the samples. The spread in critical currents of junctions across a 4 inch wafer is roughly 10 to 20%, but could be within a few percent for a small area

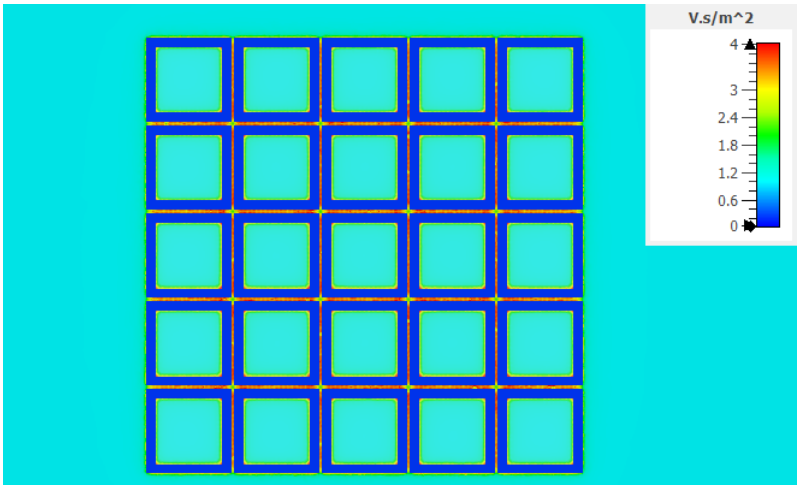

Figure 3.25: Simulation of flux focusing in a 5×5 SQUID array. A uniform field of $B_0 = 1$ T is applied to the array. And the wiring is assumed to be perfectly diamagnetic.

of a 4 mm × 4 mm chip, according to the manufacturer, Robin Cantor of Star Cryoelectronics.

As discussed in Sec. 3.1.2.2, the applied flux is focused into a single SQUID loop in the presence of the superconducting circuits. A similar flux focusing is expected in an array of SQUIDs, which we have simulated in the static magnetic field solver in CST (see Fig. 3.25). The flux focusing factors are different depending on the location of the SQUID in the array, giving rise to an intrinsic inhomogeneity in the applied dc and rf flux. Intuitively, the SQUIDs in the center should experience higher flux than the SQUIDs on the edges, since the flux screened by the Meissner effect of the superconducting wires can leave the sample from the edges but the screened flux have to go through the neighboring SQUID loops for a center SQUID. The SQUID at the center of the 5 × 5 array experience a flux focusing of 1.36

times the background, while the focusing factor for the corner SQUID is 1.24 times. Therefore, a distribution of applied flux which peaks at the center and drop to 90% at the corners is expected.

3.3.1.2 SNAP fabrication

SNAP fabrication starts by first depositing the Nb/Al-AlO_x/Nb trilayer with $J_c = 1\ \mu A/\mu m^2$ on a Si wafer with room temperature resistivity of $1 \sim 100\ \Omega$ cm. The penetration depth of the Nb film is specified to be $\lambda = 90$ nm by the manufacturer. This trilayer is then patterned with a wet etch that defines the base layer of the SQUID loop, the vias between the top and the base wiring layers of the SQUID, as well as the anodization rails connecting all of the SQUIDs to the edge of the wafer. The anodization rails are required to supply a voltage bias to the Nb layers for the anodization process in the next step. The junctions, anodization rails, and the area surrounding the vias[1] are protected by photoresist, while the remaining exposed Nb is anodized to form the 100 nm-thick insulating dielectric layer of Nb_2O_5. Previous measurements of the dielectric constant of Nb_2O_5 made

[1] A via is required to electrically connect the top and base wiring layers of the SQUID to establish a galvanically-connected loop. Therefore, in SNAP fabrication, one needs to etch through the trilayer to expose the edge of the base Nb layer and to protect the etched area with photoresist during the following anodization process. To ensure a good electrical contact and avoid introducing unintended small junctions with low critical current and high junction inductance, a large area (≈ 60 times the area of the junction) surrounding the via should be protected with photoresist to form a very large-area junction. This large junction will act as a via, and will not otherwise affect the operation of the rf SQUID, at least at low rf power.

by this process yield $\epsilon_r = 29$ [192, 193]. Next, the second Nb layer is deposited and patterned to form the top wiring layer of the SQUID. After the SQUIDs are defined, the anodization rails connecting the SQUIDs are finally removed with a wet etch. Both the top and bottom Nb layers have thickness greater than, but comparable to, 2λ. Therefore, we can assume an approximately uniform current distribution in the cross-section of the Nb wiring.

3.3.1.3 SNEP fabrication

The first generation of the SQUID samples was made with a slightly more complicated process, the Selective Niobium Etch Process (SNEP) from STAR Cryoelectronics. This process begins with the same Nb/Al-AlO_x/Nb trilayer deposition. However, instead of anodization, the junctions are defined by a reactive ion etch (RIE) on the top Nb layer of the trilayer. The entire trilayer is then patterned and etched to form the base wiring layer. A layer of SiO_2 with a thickness of 300 nm is then deposited with plasma enhanced chemical vapor deposition (PECVD), and this serves as the insulating dielectric between the top and base layers. The dielectric deposition is then followed by another etch to open contact vias through the SiO_2 layer. Next, the top Nb wiring layer is deposited and patterned. The process concludes with a final passivation of the wafer by depositing a layer of SiO_2. In addition to its complexity, the unit area capacitance from the dielectric SiO_2 in SNEP is very low, ≈ 0.15 fF/μm^2, compared to that for the Nb_2O_5 dielectric in SNAP, which is ≈ 2.5 fF/μm^2. Therefore, to maintain a low self-resonance frequency for the rf

SQUID, a larger capacitor pad is needed for samples made by the SNEP process, which further constrains the design.

3.3.2 Experimental Setup

The rf SQUID metamaterial is embedded in the center of a brass WR-42 waveguide, which has a cut-off frequency of approximately 14.1 GHz, and provides good transmission above 15 GHz. The sample is oriented along the direction of the wave propagation and its planar surface is perpendicular to the rf magnetic field in the first propagating TE mode of the waveguide, which both bias the the rf SQUID metamaterial and is used to measure the response of the sample. The dc magnetic flux is provided by a superconducting Helmholtz coil mounted on the outside of the waveguide and oriented to apply a nominally uniform field perpendicular to the SQUID array surface. The microwave transmission S_{21} through the sample-loaded waveguide is measured by a microwave vector network analyzer (VNA), as shown in Fig. 3.26. The amplitude of the incident signal is reduced by input attenuators to carefully control the rf flux $\phi_{\rm rf}$ witnessed by the sample. The transmitted signal is amplified by a cryogenic amplifier and by a room temperature amplifier, before being measured by the VNA. Note that no wires are connected to the rf SQUIDs, and there are no galvanic contacts between different SQUIDs, hence all changes to the properties of the metamaterial occur by strictly 'wireless' means.

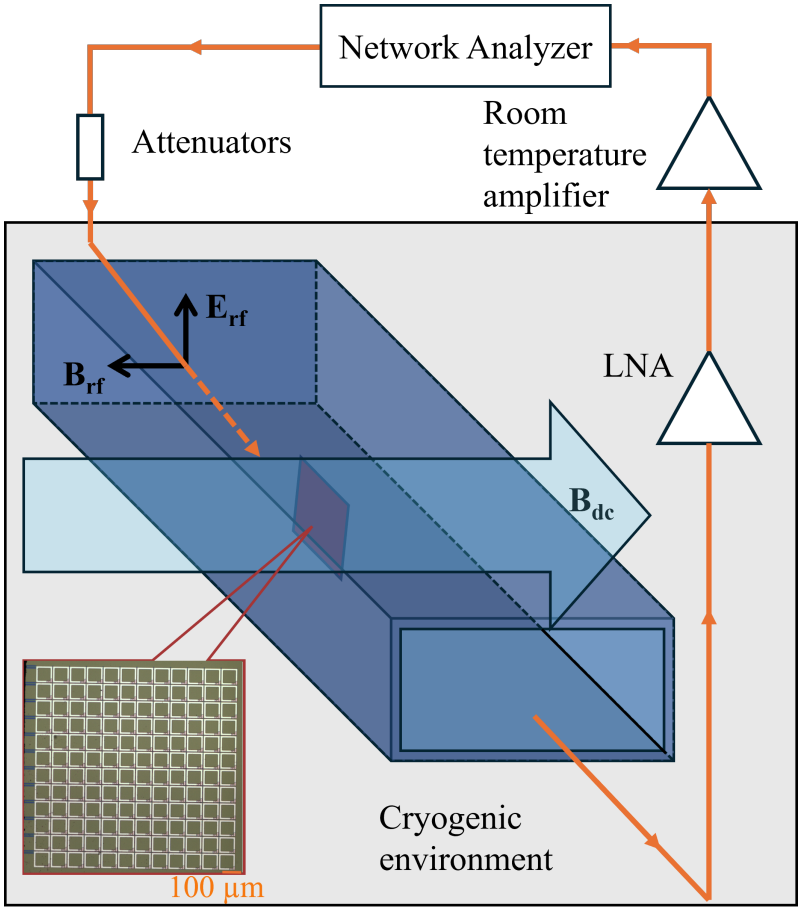

Figure 3.26: Schematic of the rf SQUID metamaterial transmission measurement, showing the waveguide which hosts the metamaterial, the rf and dc field components, the microwave network analyzer, as well as attenuators and amplifiers. Inset: optical image of the SQUID array sample made with the SNAP process. The blue shaded links between SQUIDs are the remnants of the anodization rails after wet etch. Variables that can be controlled in the experiment include Φ_{rf}, Φ_{dc}, rf driving frequency f, and sample temperature T.

Pictures of the physical setup are shown below in Fig. 3.27. In a) and b), the setup is mounted in a cryostat for cooling down below the T_c of the Nb film to a

base temperature around 4.6 K measured on the exterior of the waveguide adapter. The entire system is enclosed in a mu-metal shield to reduce the background dc magnetic field. The temperature and dc flux control are realized by a heater shown in c), and a Helmholtz coil pair shown in d). The sample needs to be oriented to be perpendicular to the rf magnetic field. A Rohacell block with a slit open in the center to hold the SQUID array sample is inserted into the waveguide as shown in e) and f). Rohacell is a structural foam whose dielectric properties are very close to those of air and thus does not affect the transmission through the waveguide. The sample is not thermally grounded to the waveguide wall, and the measurement was performed several hours after the system cooled down to base temperature to ensure that the SQUIDs reach thermal equilibrium.

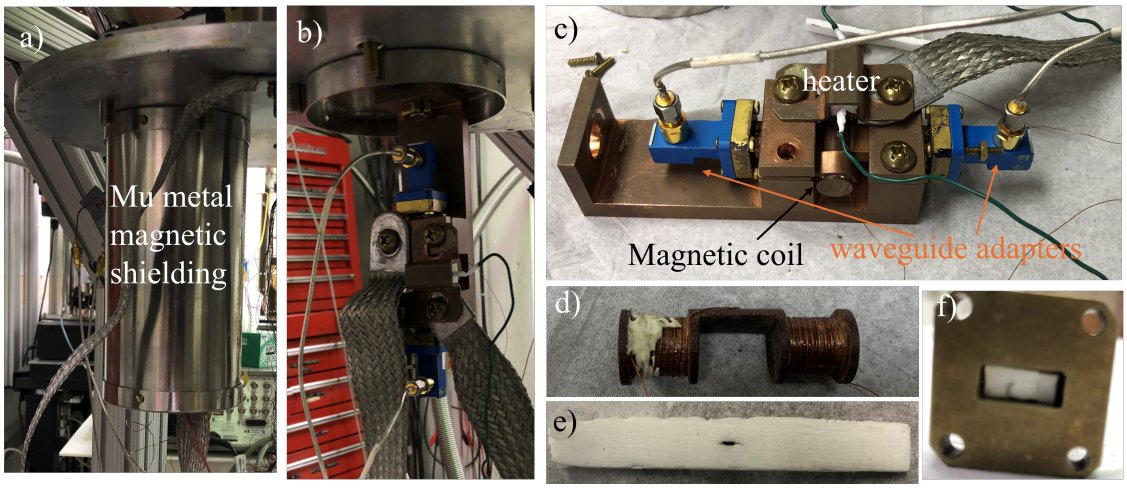

Figure 3.27: Pictures of the measurement setup for SQUID metamaterials. a) The entire setup is enclosed in a magnetic shielding can to reduce background dc magnetic field. b) The waveguide housing the SQUID metamaterial is attached to the C-shaped holder which is mounted on the cryostat. c) The magnetic coil supplying the dc bias field and the heater for changing the temperature are both attached to the C-shaped holder. d) The close-up picture of the magnetic coil with a wire connecting the two coils forming a Helmholtz coil configuration. e) The SQUID sample mounted in a Rohacell holder. f) The SQUID and the holder inserted into the waveguide to maintain the desired configuration where the SQUID sample is perpendicular to the rf magnetic field, as shown in Fig. 3.26.

The coil in this measurement setup is not an ideal Helmholtz coil, since the separation between the two coils is much larger than the radius of the coil and the wiring density of the coil is low, as illustrated in Fig. 3.27 d). In addition, the radius of the coil, 4.9 mm, is very close to the size of the sample arrays: 2 mm $\times$ 2 mm to 4 mm $\times$ 4 mm. Therefore, the applied magnetic field should be expected to be

nonuniform on the sample plane. The field distribution of the coil under a constant applied current is simulated in the static magnetic solver in CST and plotted in Fig. 3.28.

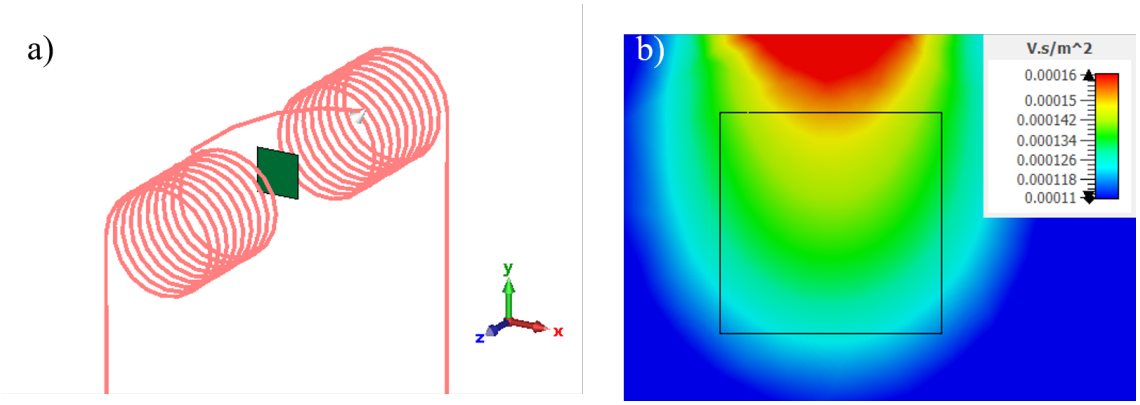

Figure 3.28: Static magnetic field simulation of the dc magnetic flux coil in our setup. There is a constant current of 1 A along the wire shown as red in a). Panel b) plots the resulting z component of the magnetic field on the cross-section at the sample plane shaded in green in a). The x-component of the current in the wire connecting the two parts of the Helmholtz coil is responsible for the significant z-component magnetic field gradient shown in b).

The geometry of the coil is reproduced in the simulation in Fig. 3.28 a). The resulting field distribution in the sample plane shows a gradient of flux which peaks around the wire connecting the two parts of the coil. The black frame in Fig. 3.28 b) outlines the boundary of a 4 mm $\times$ 4 mm chip. Evidently, the field throughout this sample shows a gradient where the bottom edge is experiencing only 80% of the field on the top edge of the sample. The design of the coil can be improved to reduce the gradient. For instance, the wire connecting the two parts can be arranged to

be parallel to z direction and also moved further away from the sample in the y-direction. On the other hand, it has been shown theoretically that a larger gradient in applied dc flux throughout the sample from 0 to more than 0.2 Φ_0 can lead to formation of a chimera states in a SQUID metamaterial [173].

3.4 Measurement results on inductively coupled hysteretic SQUID metamaterials

3.4.1 Data processing to recover the metamaterial resonances in the transmission measurement

As expected from the small volume fraction of the SQUID array in the waveguide, the microwave response of the metamaterial is very weak. A direct transmission measurement S_{21} through the waveguide cannot resolve the SQUID resonance modes, as shown in Fig. 3.29.

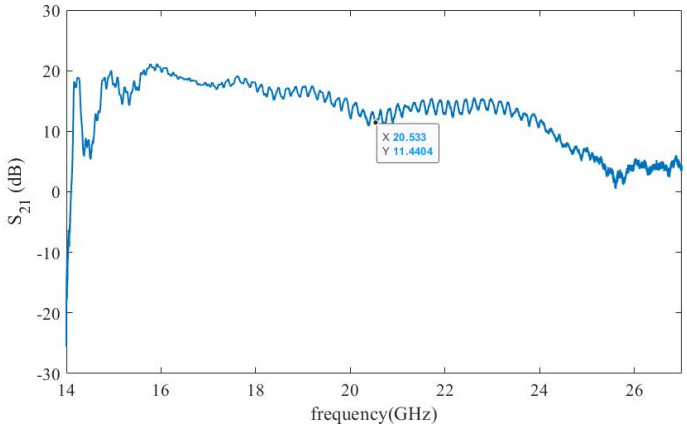

Figure 3.29: A typical measured transmission on the rf SQUID array. The expected resonance is marked in the spectrum, which cannot be distinguished from the parasitic modes from the standing wave in the apparatus due to imperfect cable connections in the microwave transmission line.

The highlighted data point is the resonance predicted at this condition. However, there is not any feature near this frequency standing out from the background. To extract the SQUID response, the background transmission that is independent of the applied dc flux is removed by first averaging over the transmission spectra $\overline{S}_{21}$ at different dc fluxes, and then subtracting it from the individual frequency spectrum as described. The difference in transmission ΔS_{21} is further processed with a moving average filter over 50 data points to smooth out the frequency dependence. At last, a linear background in the frequency dependent transmission $\Delta S_{21,\text{background}}(f) = Af + b$ is removed to level the response so that the background is at zero in a broad frequency band. The signal in Fig. 3.29 after this processing is plotted in Fig. 3.30, where the rf SQUID metamaterial response is manifested.

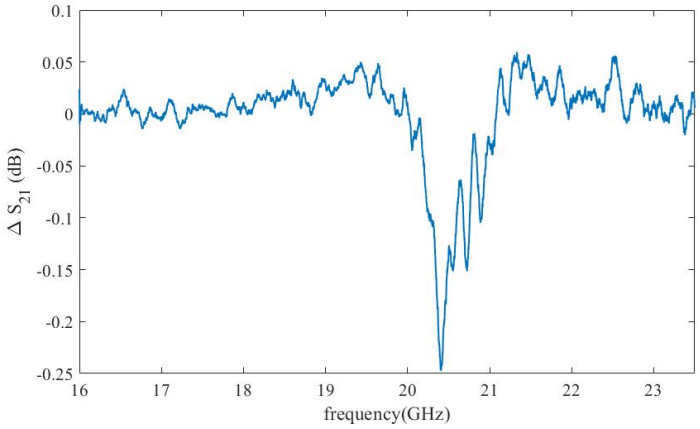

Figure 3.30: The transmission after the signal processing described in the text. The SQUID resonance is now clearly visible in the spectrum.

3.4.2 Hysteretic SQUID array (SNAP 161D)

We discuss first the sample SNAP 161D (shown in Fig. 3.31) with conventional response periodic in $1\Phi_0$ in applied dc flux sweep. The SQUID meta-atom making up this array has the following parameters listed in Table 3.1.

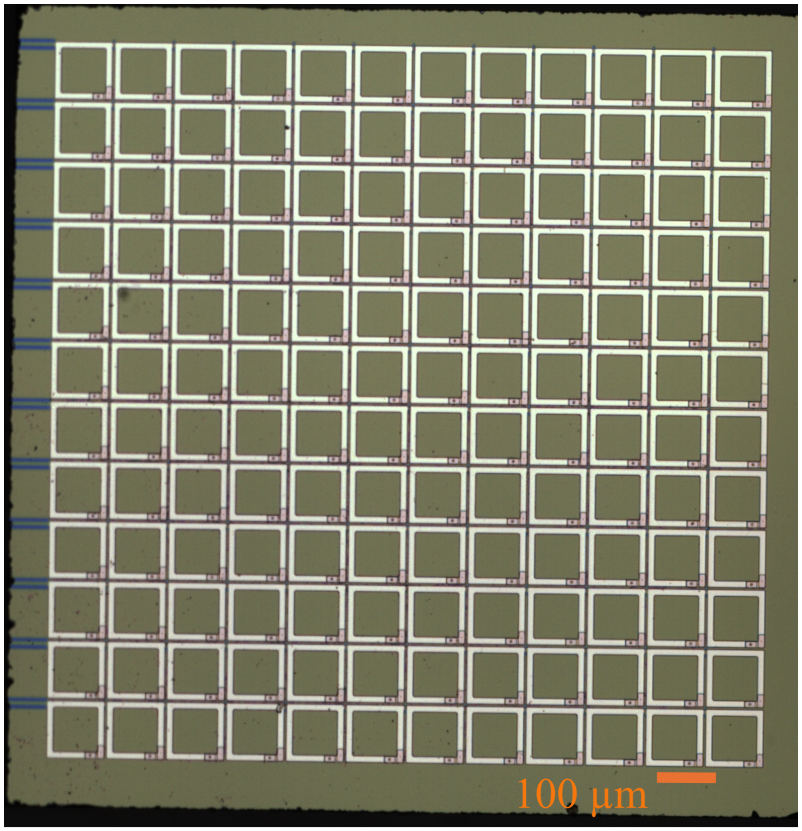

Figure 3.31: Micrograph of the sample SNAP 161D, a 12 × 12 rf SQUID array with $\beta_{\rm rf} = 5.48$ and nearest neighbor coupling $\kappa_0 = -0.069$. The sample is $\sim$ 2 mm × 2 mm in size.

The transmission response is measured and processed as described previously in Secs. 3.3.2 and 3.4.1. The resulting ΔS_{21} in a range of frequency of the rf drive and applied dc flux is plotted below in Fig. 3.32.

Parameter	Symbol	Value
SQUID hysteresis parameter	β_{rf}	5.483
Geometric inductance	L_{geo}	255.3pH
SQUID Capacitance	C	1.42pF
Geometric resonance	f_{geo}	8.36GHz
Nearest neighbor coupling M_0/L_{geo}	κ_0	-0.069
Side length of the SQUID meta-atom	a_{SQUID}	132μm
Wiring width of the SQUID loop	w	16μm
Gap between the nearest neighboring SQUID wirings	d	4μm
Effective area of the SQUID due to flux focusing	A_{eff}	$13600\mu\mathrm{m}^2$

Table 3.1: Parameters for the individual meta-atoms making up sample SNAP 161D, as well as their coupling.

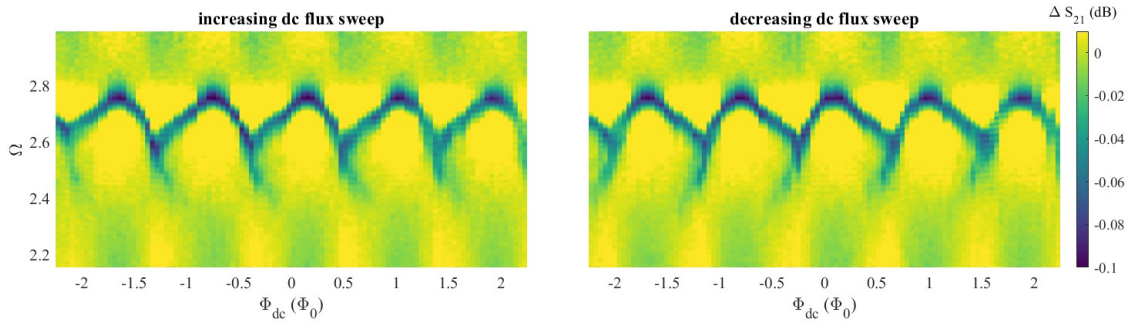

Figure 3.32: The magnitude of measured transmission for the 12×12 strongly coupled SQUID array (SNAP 161D) as a function of normalized frequency ($\Omega = f/f_{\text{geo}}$) and applied dc flux swept in increasing (left) and decreasing (right) sweep direction at 1.8×10^{-4} Φ_0 applied rf flux, and 4.65 K. Note that flux focusing has been included in the determination of Φ_{dc} presented here.

The SQUID resonances are tunable under dc flux with $0.9\Phi_0$ periodicity, slightly less than one, which could be caused by an overestimation of the applied dc flux if the sample is not aligned perfectly to the axis of the dc magnetic coil. The flux experienced by a sample whose normal direction at angle θ from the axis of the dc magnetic coil is decreased by $\cos\theta$. A 90% reduction corresponds to an angle $\theta = 25°$, an acceptable offset in our setup.

More importantly, the hysteresis in dc flux sweep is observed from the comparison between the increasing and decreasing dc flux sweep in Fig. 3.32. As expected for hysteretic SQUIDs $\beta_{\text{rf}} > 1$, only segments of one tuning curve is realized and the jumps from one curve to the next lead to a hysteretic response in dc flux sweep (see the discussion in Sec. 3.1.2.3). The asymmetric shapes of the tuning curved and the coexistence of multiple resonances under one applied dc flux can be attributed

to the multistability of the system, as predicted for a strongly coupled system of hysteretic SQUIDs in Fig. 3.23.

3.4.3 Large weakly coupled hysteretic SQUID array (SNAP 174)

In contrast to the clean dc flux dependence of the resonances in SNAP 161D, the larger SQUID arrays with higher $\beta_{\rm rf} = 6.26$ have shown more complex response. The sample SNAP 174, an 18×18 SQUID array, is shown below in Fig. 3.33 with the design parameters given in Table 3.2.

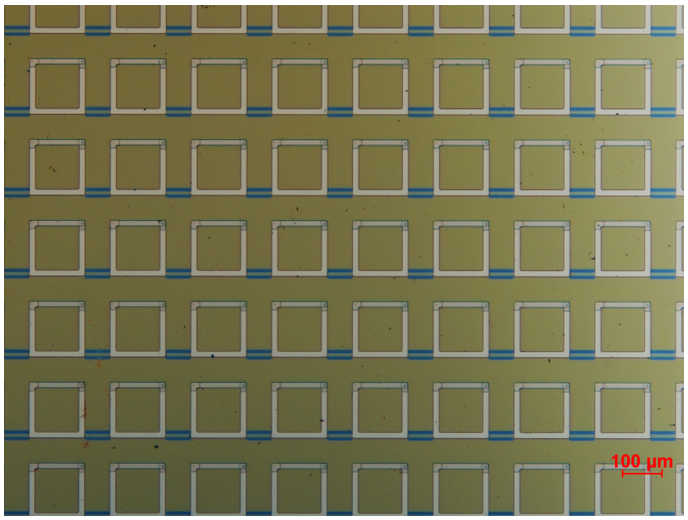

Figure 3.33: Micrograph of the sample SNAP 174, a 18×18 rf SQUID array with $\beta_{\rm rf} = 6.26$ and nearest neighbor coupling $\kappa_0 = -0.015$. The sample is ~ 4 mm $\times$ 4 mm in size.

The spacing between the neighboring SQUIDs is set at 64μm, half of the size of the SQUID, $a_{\rm SQUID} - w$. The distance between the SQUIDs gives rise to a low mutual inductance coupling constant, with the nearest neighbor coupling $\kappa_0 = -0.015$. The frequency and dc flux dependent microwave transmissions through this array are

Parameter	Symbol	Value
SQUID hysteresis parameter	β_{rf}	6.26
Geometric inductance	L_{geo}	291.4pH
SQUID Capacitance	C	1.42pF
Geometric resonance	f_{geo}	7.80GHz
Nearest neighbor coupling M_0/L_{geo}	κ_0	-0.015
Side length of the SQUID meta-atom	a_{SQUID}	144μm
Wiring width of the SQUID loop	w	16μm
Gap between the nearest neighboring SQUID wirings	d	64μm
Effective area of the SQUID due to flux focusing	A_{eff}	$13600\mu\mathrm{m}^2$

Table 3.2: Parameters for the individual meta-atoms making up sample SNAP 174, as well as their coupling.

plotted in Fig. 3.34.

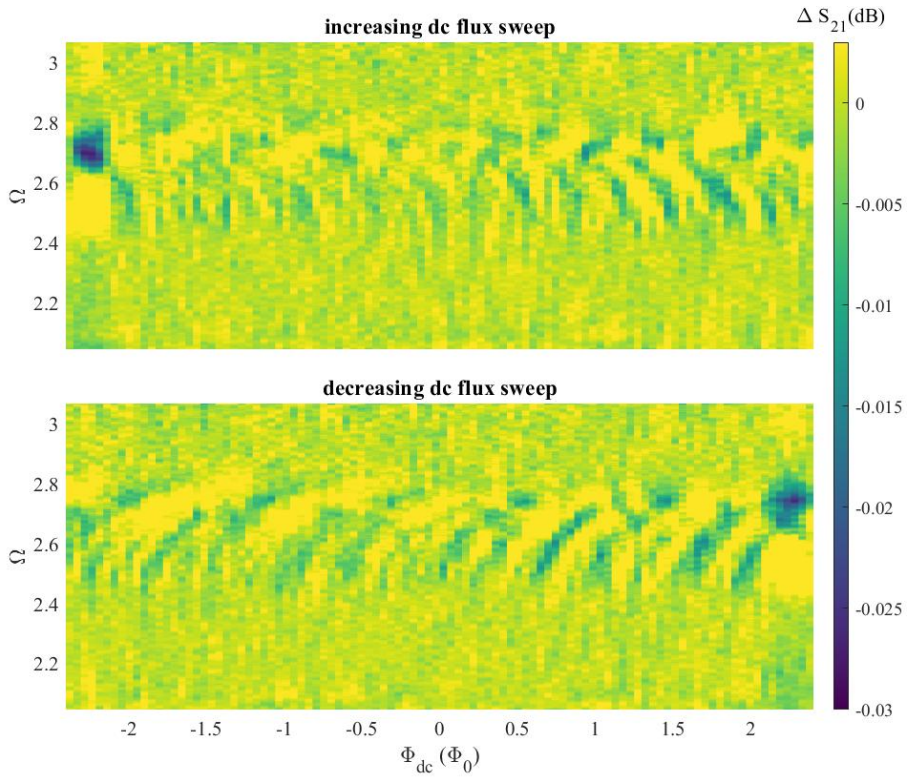

Figure 3.34: The magnitude of measured transmission for the 18×18 weakly coupled SQUID array (SNAP174) as a function of frequency and applied dc flux swept in increasing (top) and decreasing (bottom) directions at 3×10^{-4} Φ_0 applied rf flux, and 4.85 K.

The measurements are performed with increasing applied dc flux sweep in the top panel and decreasing in the bottom. A strong hysteresis in the dc flux sweep is demonstrated after comparing the transmission from the two measurements. When the dc flux increases (decreases), the right (left) halves of the tuning curves are visible. The hysteresis is a consequence of large β_{rf}, as discussed previously. The dc flux tuning pattern is periodic in $1\Phi_0$, but a spread of tuning curves centered around

different applied dc flux are observed, which is similar to the response in a one-dimensional array of non-hysteretic SQUIDs observed in [194]. Jung attributed the range of dc flux biases to trapped Abrikosov vortices. With an imperfect magnetic shielding, an inhomogeneous background dc bias field is present. Magnetic vortices can form in the superconducting film when cooled down below T_c under an applied dc magnetic field, which leads to locally enhanced field in the sample and exacerbates the inhomogeneity in the dc flux bias on the array.

The large spread of tuning curves is only observed in SNAP174 and could be caused by the dc flux inhomogeneity due to its larger size compared to SNAP 161D. Nevertheless, as discussed in the next section, Sec. 3.4.4, a sample of the same size but stronger coupling thus denser packing has shown a very coherent response under dc flux tuning with no spread in dc flux of the tuning curves. Therefore, the weak coupling together with the multistability from the high β_{rf} SQUIDs is likely responsible for the spread in the tuning curves.

To better resolve the tuning curves from SNAP174, we sweep the dc flux around a set point first decreasing and then increasing the applied dc flux. The full tuning is reconstructed by combing two different sweeps, one starting at the set point and decreasing, the other starting at the set point but increasing.

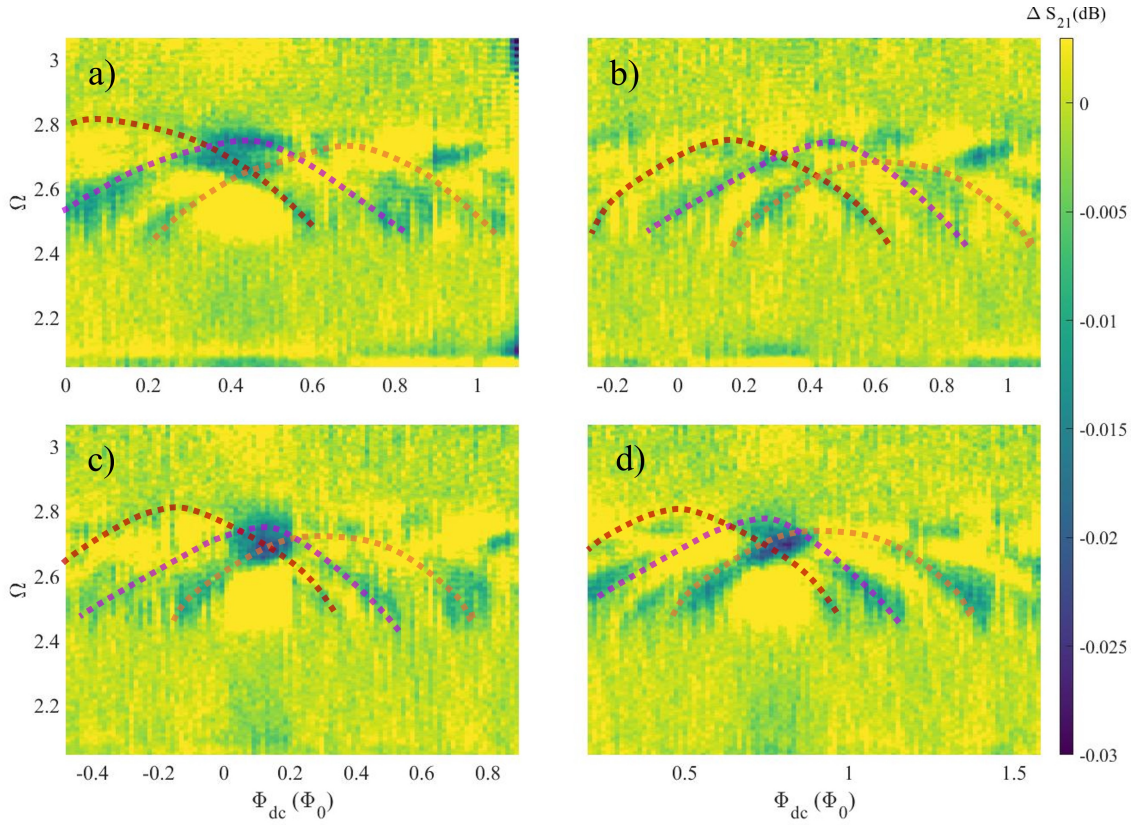

Figure 3.35: The magnitude of measured transmission for the 18×18 weakly coupled SQUID array (SNAP174) as a function of frequency and applied dc flux swept around four different set points: $[0.5,\ 0.4,\ 0.2,\ 0.9]\Phi_0$ for a) - d). The applied flux first decreases from the set points and then is swept back up above the set points. The transmission plots combine the regions of decreasing flux sweep and the region of increasing flux sweep above the set points to resolve the full tuning curves of the hysteretic SQUIDs. The measurements were performed at 3×10^{-4} Φ_0 applied rf flux, and 4.85 K.

There are three distinct branches visible inside each dc flux tuning period as outlined by the dashed curves as in Fig. 3.35. The response is enhanced at the intersections between the different branches. The three branches are about $0.2\Phi_0$

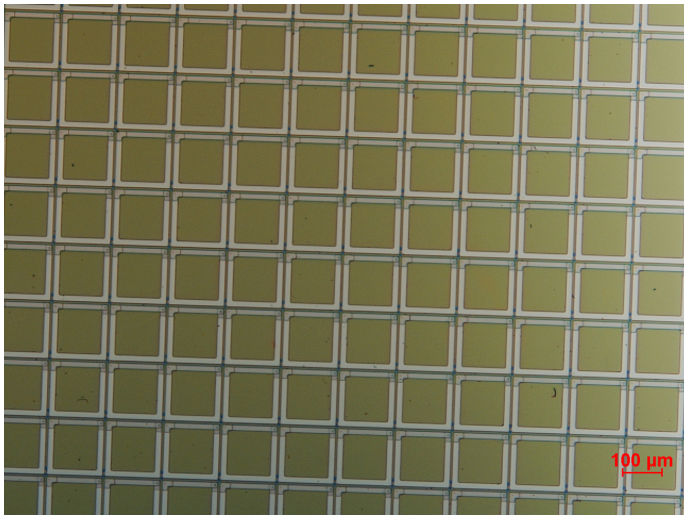

Figure 3.36: Micrograph of the sample SNAP 175, a 24 × 24 rf SQUID array with $\beta_{\rm rf} = 6.26$ and nearest neighbor coupling $\kappa_0 = -0.078$. The sample is ~ 4 mm $\times$ 4 mm in size.

apart, such a large spread of constant offsets in applied dc flux cannot be simply explained by the gradient of the applied flux due to the coil geometry (see Sec. 3.3.2) or the flux focusing (see Sec. 3.3.1.1).

3.4.4 Large strongly coupled hysteretic SQUID array (SNAP 175)

The sample SNAP 175 is an array of similar SQUIDs with the same $\beta_{\rm rf} = 6.26$, but stronger inductive couplings ($\kappa_0 = -0.076$) thus denser packing of the SQUIDs ($d = 5$ μm, $A_{\rm eff} = 17060\mu{\rm m}^2$), as shown in Fig. 3.36. The capacitance of the SQUID is also increased in the design to $C = 1.64$ pF to reduce the geometric resonance to $f_{\rm geo} = 7.28$ GHz, which compensates the increased SQUID resonance frequency due to the strong coupling, according to Eq.(3.28).

The transmission of the SQUID array is measured under various dc flux and

frequencies of the rf drive, and two sample responses are plotted in Fig. 3.37.

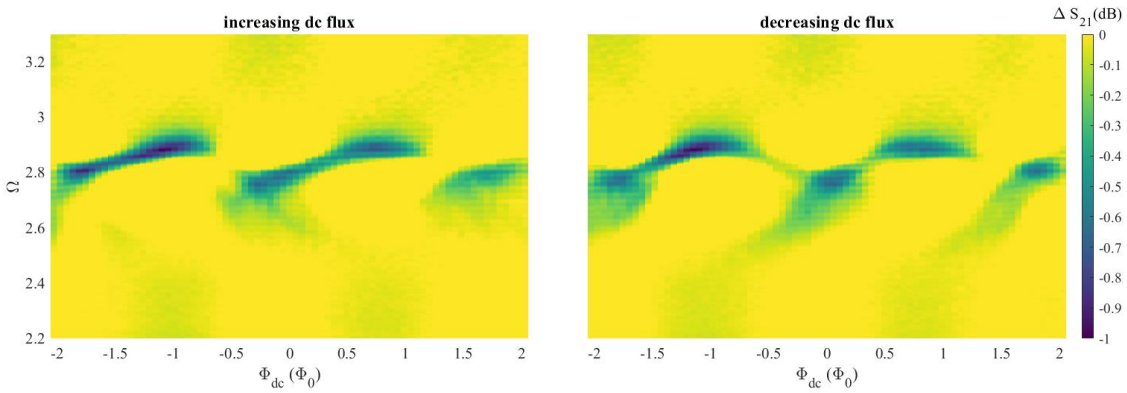

Figure 3.37: The magnitude of measured transmission of the 24×24 strongly coupled SQUID array (SNAP175) as a function of frequency and applied dc flux at 3×10^{-5} Φ_0 applied rf flux, and 4.82 K. The resonance tuning curve is periodic in $2\Phi_0$ as opposed to Φ_0 for single SQUIDs and previously investigated non-hysteretic SQUID arrays

Again, a clean dc flux tuning pattern with hysteresis in different dc flux sweep directions has been observed, similar to the sample SNAP161D in Sec. 3.4.2. However, the tuning pattern is now periodic in $2\Phi_0$ as opposed to our previous experimental and theoretical results, which show $1\Phi_0$ periodicity. Although period doubling in dc flux tuning is observed in the numerical solution for a single SQUID (see Fig. 3.11), and some SQUIDs in a large coupled system (see Fig. 3.21), the large majority of the responses still follow the canonical $1\Phi_0$ periodicity in their dc flux tuned resonances, as seen in Fig. 3.19 and 3.22. We should also note that the flux gradient present in the system due to the coil geometry cannot explain the abnormal response, just as in Sec. 3.4.3 for the weakly coupled system.

Fig. 3.38 shows a numerical calculation on the SNAP 175 sample with a dc

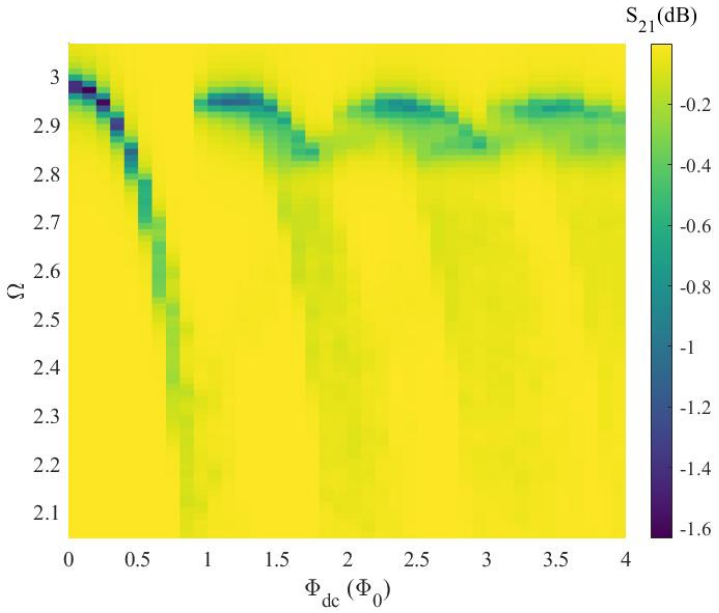

Figure 3.38: The magnitude of simulated transmission of SNAP 175 with a gradient of applied dc flux where one edge only experiences 80% of the field at the other edge. The tuning pattern is still $1\Phi_0$ periodic in the applied dc flux.

flux gradient of 80% from one edge of the array to the other. The responses in Fig. 3.38 are still periodic in $1\Phi_0$, while the tuning curves present larger spreads for higher dc flux bias, agreeing with the observation in a previous work [176]. The strongly coupled multistable system together with a spread of dc flux bias might be able to reproduce the experimentally observed period doubling, as discussed later in Sec. 3.5. In addition to the dc flux dependence, the rf power dependence of the transmission is also characterized and summarized in Fig. 3.39 below.

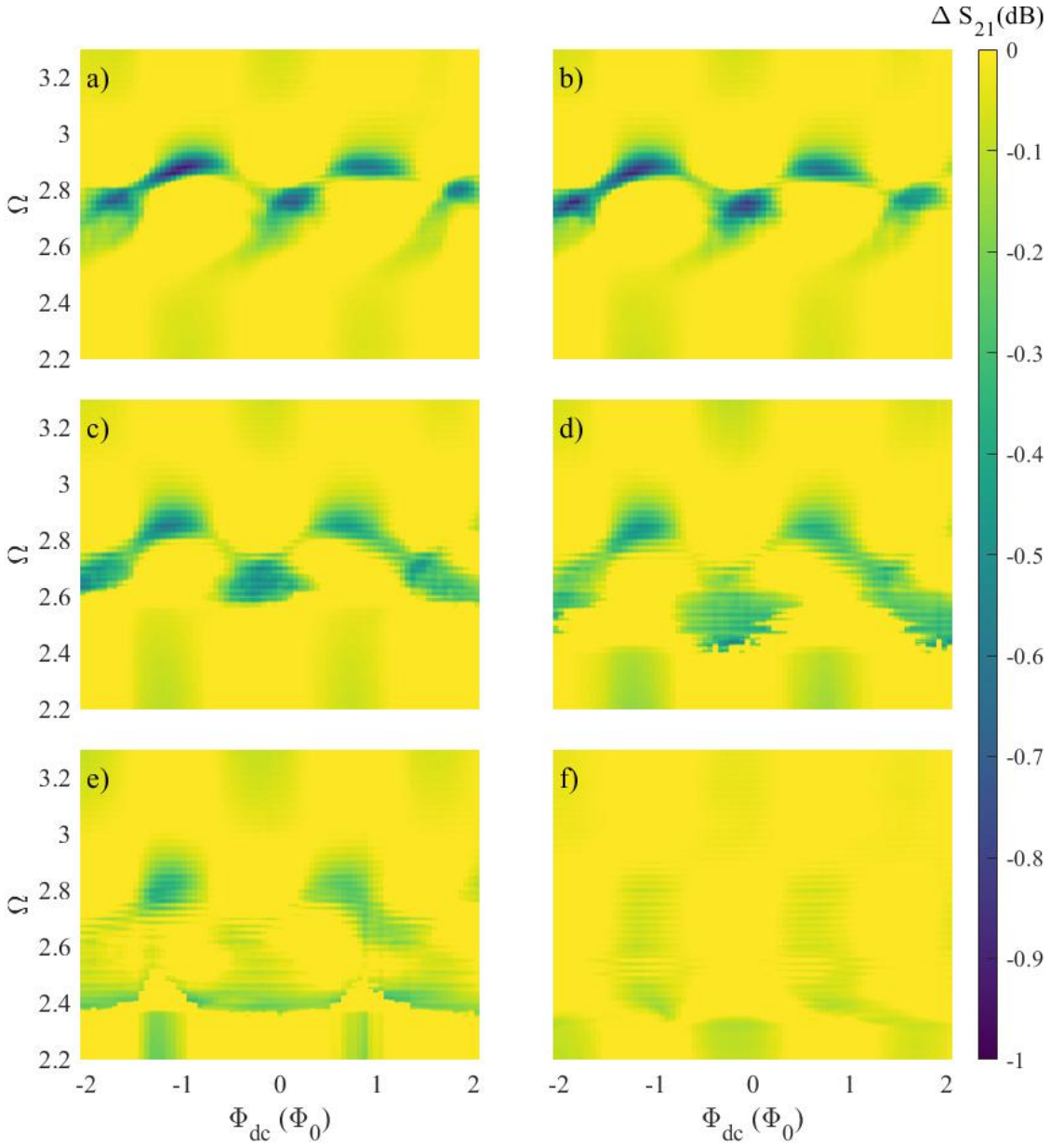

Figure 3.39: The magnitude of measured transmission of the the 24 × 24 strongly coupled SQUID array (SNAP175) as a function of frequency and decreasing applied dc flux at 4.82 K and six different incident powers P_{incident} (-62, -57, -51, -49, -47, -42) dBm for a) - f).

The transmission for SNAP 175 is measured at six different applied rf flux

amplitudes: (0.022, 0.04, 0.08, 0.1, 0.13, 0.23) Φ_0, where the rf flux is calculated at 20 GHz. As the rf flux increases, the $2\Phi_0$ periodicity in dc flux tuning is preserved. Moreover, the tuning curves become more symmetric around integer flux quanta as predicted for a single hysteretic SQUID in Fig. 3.12, where the strong rf flux can drive the solutions out of the local minima in the potential landscape and thus effectively reduce the multistability of the system.

3.5 Discussion

We have so far observed the expected hysteresis in dc flux sweeps in all three samples with high β_{rf}. The asymmetric shapes of the tuning curves in Fig. 3.32 for a small strongly coupled system (SNAP161D) can also be explained by the multistability in the numerical solution, Fig. 3.23. However, as one increases the size of the system, more exotic behaviors present in the measurement have not yet been reproduced by our model of coupled hysteretic SQUIDs. It should be mentioned that the 4 mm $\times$ 4 mm chip is almost touching the side wall of the WR-42 waveguide whose smallest dimension is 4.32 mm. This relatively large sample size also creates significant dc and rf flux gradients in the sample.

Despite the lack of a thorough understanding, an empirical model combining the dc flux bias spread observed in SNAP 174 and an artificial tuning patterns with $2\Phi_0$ periodicity in applied dc flux is proposed and bears some resemblance to the measurements in Fig. 3.37. We start with the single SQUID tuning pattern in the linear limit obtained from Eq.(3.14). A spread of dc bias from -0.3 to +0.3 Φ_0 is

then imposed to the copies of the single SQUID responses leading to the spread of the tuning curve centred around $\Phi_{dc} = 0$. We then enforce the dc flux tuning period of $2\Phi_0$ by skipping the next period in the tuning pattern to the one after, according to the dc flux sweep direction. The results are shown in Fig. 3.40

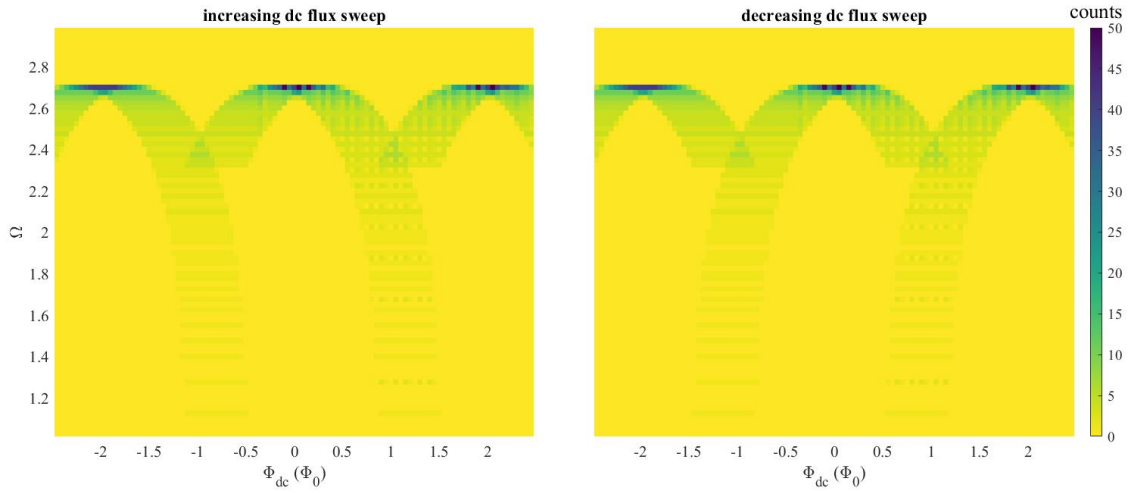

Figure 3.40: Density plot of the SQUID resonances from a system with a spread of dc flux bias from -0.3 to +0.3 Φ_0. The coupling in the system is ignored and the individual SQUID responses are treated as copies of the single SQUID resonance. The tuning curve with $2\Phi_0$ periodicity is achieved by skipping the next period of the tuning curve in the direction of the dc flux sweep.

The tuning curve near the even integer flux quanta in Fig. 3.40 are symmetric in shape and shows no hysteresis in dc flux sweep, as a result of overlapping responses from many SQUIDs under the spread of dc biases centered around $\Phi_{dc} = 0$. On the other hand, near the jumps between the different flux tuning periods, the tails in Fig. 3.37 are reproduced. The enhanced response at the intersections between the spreads of tuning curves from different periods also mimics the measurement.

Therefore, a strongly coupled system that strictly follows $2\Phi_0$ periodicity under dc flux tuning and subject to a spread of dc flux bias should be able to produce the measured transmission in Sec. 3.4.4. However, further theoretical works are required to justify the period doubling and the large spread of the constant offsets to the applied dc flux.

Chapter 4

Overlapping rf SQUID Metamaterials

There have been proposals for three-dimensional (3D) versions of metamaterials consisting of superconducting qubits [195] and rf SQUIDs [33], as well as an experimental realization of a 3D superconducting metamaterial based on spiral resonators [12]. In this work, we built three dimensional arrays of rf SQUIDs and employed them as metamaterials for the first time. By stacking the SQUIDs vertically, we introduce *positive* mutual inductive coupling for nearest neighbors, very different from the co-planar geometry and, more importantly, add the qualitatively new aspect of strong *capacitive* coupling that permits high frequency currents to flow between SQUID loops. To the best of our knowledge, such coupling has not been considered in the past in any aspect of SQUID physics or technology, and can lead to dramatic new properties of coupled SQUIDs. Our three-dimensional (3D) SQUID metamaterials have flux-quantized loops mixed with non-flux-quantized loops. These latter loops are enabled by the capacitors that host displacement currents between SQUIDs. Faraday's law is applied to all of the non-SQUID loops, in addition to the flux quantization condition in the appropriate loops.

Parasitic capacitive coupling can also occur in superconducting digital electronics (SCDE) that are based on the propagation of ps-duration single-flux quantum voltage pulses between logic circuit elements [196]. The pulses are processed by

means of inductive loops, typically based on superconducting wires including Josephson junctions, essentially acting as non-resonant SQUIDs. It is well-established that state-of-the-art SCDE suffers from an inefficient use of space on chip in many practical computing and signal processing applications. This is due to the fact that SCDE is based on magnetic flux, as opposed to the monopole electric charge utilized in CMOS electronics, and the resulting need to create and control dipole sources, such as current loops, transformers, inductors, etc. [197]. One way to mitigate this problem is to create three-dimensional circuit layouts in which logic and wiring layers are distributed in the third dimension, separated by ground planes [198]. However, this three-dimensional geometry can introduce new and unexpected coupling effects between circuits. Our inductively and capacitively coupled rf SQUID metamaterials can act as a surrogate test-bed to study coupling effects in future highly-integrated SCDE circuits.

Quantum computers utilize large arrays of qubits with controlled interactions (typically either inductive or capacitive) between many pairs of qubits [199, 200, 201, 202]. For charge and phase qubits, the nearest-neighbour interactions are enabled by capacitors, rather than inductors [203, 204, 205, 206, 201]. Of recent interest is the design of a tunable coupler transmon that is capacitively coupled to a pair of qubits to achieve high-fidelity two-qubit gates [207, 208, 209, 210]. Our rf SQUID metamaterials differ in that multiple coupling capacitors are included, creating a highly integrated network of both capacitive and inductive coupling between all of the SQUIDs. We note that the effects of both capacitive and inductive coupling between rf SQUIDs has been considered as a step in deriving the quan-

tum Hamiltonian of arrays of interacting qubits [211, 212]. For the flux qubits, the nearest-neighbor inductive coupling can be adjusted by introducing an intermediary SQUID between the qubits to be coupled, whose properties are tuned by a local magnetic flux [213, 214, 215, 216]. Another approach is to have two qubits share a common wiring loop bond. This bond may have a variable kinetic inductance, or Josephson inductance, that depends on the sum of the currents flowing in the two qubit loops through that bond [217, 218, 219]. Our coupling design is uniquely different in that it introduces interactions through a combination of inductive and high-frequency capacitive coupling. The possibility exists to tune the capacitive coupling through external manipulation of the dielectric material in the capacitor.

4.1 Overlapping SQUID array design

Since the fabrication processes only allow for a single trilayer for the junction definition, one cannot simply stack two independently-defined layers of 2D rf SQUID arrays in the third dimension. One of the layers must be shifted in-plane so that its junction pad avoids that of the other layer of SQUIDs, and this constraint creates the peculiar overlapping geometry studied here shown in Fig.4.1. To achieve the most symmetric configuration, the overlapping area between the SQUIDs from the two layers is designed to be roughly a quarter of the single-SQUID loop area. The shifted stack between the two 2D rf SQUID arrays results in the many overlapping capacitors C_{ov} between SQUID loops from different layers. The overlapping SQUID geometry is better illustrated in the three dimensional reconstruction below

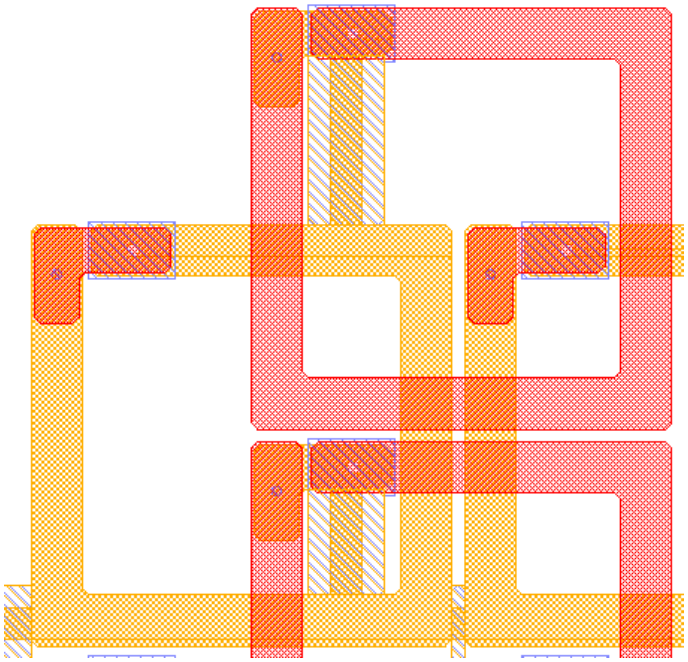

Figure 4.1: Design file of the overlapping SQUID sample SNAP161A

where the separation between the top and bottom wiring layers is exaggerated. The junctions and vias connecting the two layers are also shown in the schematics The design parameters for the overlapping SQUID metamaterial sample SNAP 161A is summarized in Table.4.1

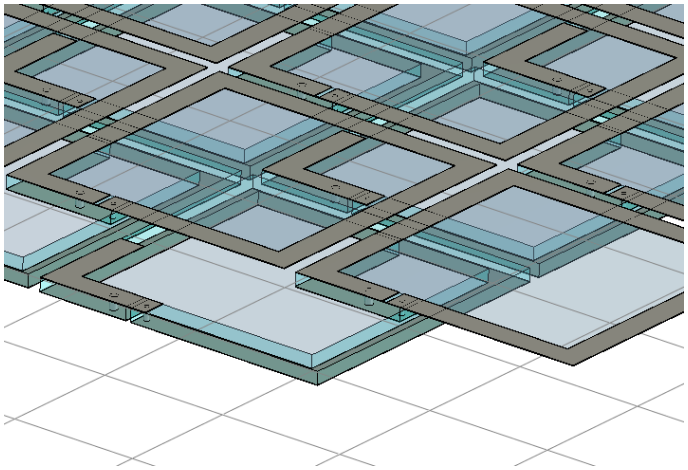

Figure 4.2: Three dimensional reconstruction of the overlapping SQUID sample with a large separation between the top and bottom layers for easy visualization.

Parameters	Symbols	Values
Gap between nearest SQUID wiring	d	4 μm
Wiring width	w	16 μm
SQUID loop side length	a_{SQUID}	132 μm
SQUID self capacitance (RCSJ)	C	1.42 pF
Overlapping capacitance	C_{ov}	0.657 pF
Junction critical current $(4.2K)$	I_c	7 μA
Geometric Inductance	L_{geo}	255.2 pH
SQUID parameter $L_{\mathrm{geo}}/L_{\mathrm{JJ}}$	β_{rf}	5.483
Mutual inductance between the overlapping neighbors	M_1	8.56 pH
Mutual inductance between the in-plane nearest neighbors	M_2	-17.4 pH

Table 4.1: Design parameters for the overlapping SQUID metamaterial sample SNAP 161A. See Fig. 4.3(b) for definitions of d, w, and a_{SQUID}.

The mutual inductances in the last two rows of the Table 4.1 represent the inductive coupling in the absence of the overlapping capacitors. However, under the strong capacitive coupling studied in this work, the rf currents can leave the SQUID loop through the capacitor nodes, breaking the uniformity of the current within one SQUID loop. The mutual inductance alone is thus no longer sufficient to correctly treat the coupling between SQUIDs.

4.2 Model for overlapping SQUIDs

4.2.1 Two corner-coupled SQUIDs

The simplest model for overlapping SQUIDs is a pair of rf SQUID loops having wiring layers overlapping each other at the corner, and the overlapping portions are separated by a thin dielectric layer, which forms two capacitors whose capacitance $C_{\rm ov}$ is comparable to that of the junction, C (see Fig. 4.3 (b)). It should be noted that these overlapping capacitors *do not* include Josephson coupling between the superconducting wires, but do create a route for high-frequency displacement currents to flow between the wiring loops of neighboring SQUIDs. The capacitors shunt the SQUID loop, breaking the uniformity of high-frequency currents in the loops, which leads to different currents in the non-junction branches $I_{a1(b1)}$ from the currents in the junction branches $I_{a0(b0)}$ as illustrated in Fig. 4.3 (a). Note that the overlapping capacitors have no direct influence on the dc currents, which are constrained to flow *only* through individual SQUID loops.

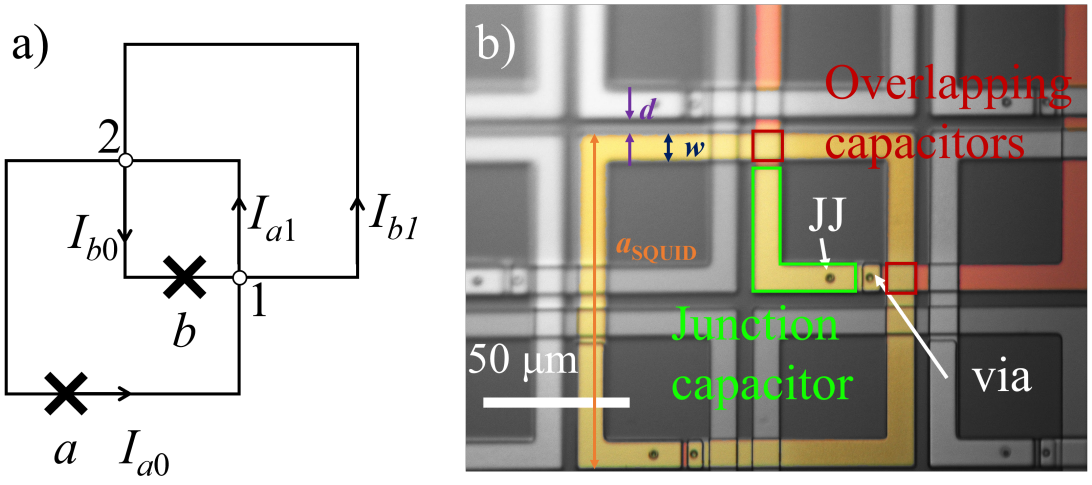

Figure 4.3: a) Schematic diagram of a pair of corner-coupled rf SQUIDs with overlapping wiring layers, creating capacitors labeled 1 and 2, along with the two nominally identical Josephson junctions a and b represented with an "×". Junction currents I_{a0} and I_{b0} differ from the corresponding non-junction currents I_{a1} and I_{b1}, in general. b) Micrograph of a small section of a $7 \times 7 \times 2$ metamaterial made up of corner-coupled SQUIDs (fabricated by the SNEP process), where one representative pair of the capacitively-coupled SQUIDs is highlighted. The different colors of the wiring correspond to different lithographic layers of the device.

4.2.1.1 Loops in the two corner-coupled SQUIDs

Following the same flux-to-current approach in Sec. 3.1, one can write down the flux quantization conditions for the two corner-coupled SQUIDs (called a and b) as follows:

$$\begin{pmatrix} \Phi_a^{\text{app}} \\ \Phi_b^{\text{app}} \end{pmatrix} = \frac{\Phi_0}{2\pi} \begin{pmatrix} \delta_a \\ \delta_b \end{pmatrix} + \begin{pmatrix} \Phi_a^{\text{ind}} \\ \Phi_b^{\text{ind}} \end{pmatrix}$$

$$\text{with} \begin{pmatrix} \Phi_a^{\text{ind}} \\ \Phi_b^{\text{ind}} \end{pmatrix} = \begin{pmatrix} L_{a,a0} & M_{a,b0} & L_{a,a1} & M_{a,b1} \\ M_{b,a0} & L_{b,b0} & M_{b,a1} & L_{b,b1} \end{pmatrix} \begin{pmatrix} I_{a0} \\ I_{b0} \\ I_{a1} \\ I_{b1} \end{pmatrix} \tag{4.1}$$

where the induced flux is expressed as contributions from different *segments* of the two SQUID loops on the second line. The elements of the first (second) row in the inductance matrix are determined as the *partial inductance* between the individual segments denoted by the subscript, and the galvanically connected SQUID loop a (b) [220, 221]. Partial inductance is a concept that generalizes the inductance of a closed loop to that of segments in the loop. Consider a segment 1 in a closed loop c that is experiencing a time-varying magnetic field due to the current in segment 2 in a closed loop d. The total flux in the closed loop is simply $\Phi = \iint \vec{B} \cdot d\vec{S} = \oint_c \vec{A} \cdot d\vec{l}$ where the magnetic field and the vector potential are due to the current in segment 2. We can assign the flux contribution from individual segments as follows: $\Phi = \oint_c \vec{A} \cdot d\vec{l} = \sum_i \int_{s_i \in c} \vec{A} \cdot d\vec{l}$. The partial inductance between segments 1 and 2 is then defined as the ratio, $M_{1,2} = \int_1 \vec{A} \cdot d\vec{l}/I_2$. Consequently, it follows

that for a closed loop c, $M_{c,2} = \sum_{s_i \in c} M_{s_i,2}$, and between two closed loops c and d, $M_{c,d} = \sum_{s_j \in d} M_{c,s_j}$.

Although Eq. (4.1) relates the flux to the currents, the non-junction currents $I_{a1,b1}$ are not yet expressed as functions of the gauge-invariant phase differences $\delta_{a,b}$ and their time derivatives. To obtain the equations of motion in $\vec{\delta}$, one needs to invoke Faraday's law on the center overlapping loop from capacitor 1 to 2 to junction b and back to capacitor 1 in Fig. 4.3 (a), as well as current conservation on the capacitor nodes. This will allow us to solve for $I_{a1,b1}$ in terms of the gauge-invariant phases.

4.2.1.2 Faraday's law applied to the center overlapping loop

There is no need to consider Faraday's law in the formulation of the equations for the non-overlapping SQUIDs, since it is implicitly incorporated in the flux quantization condition Eq. (3.20). In fact, applying Faraday's law to a single SQUID loop will result in the time derivative of Eq. (3.20). On the other hand, its application is necessary for a superconducting loop interrupted by capacitors, such as the small center loop carrying currents I_{b0} and I_{a1} formed by the two overlapping corner-coupled SQUIDs in Fig. 4.3 (a). By applying Faraday's law to this center loop (denoted cen), one finds:

$$V_b - V_1 + V_2 = \dot{\Phi}^{\text{app}}_{\text{cen}} - \dot{\Phi}^{\text{ind}}_{\text{cen}} \tag{4.2}$$

$$\Phi^{\text{ind}}_{\text{cen}} = M_{\text{cen},a0} I_{a0} + L_{\text{cen},b0} I_{b0} + L_{\text{cen},a1} I_{a1} + M_{\text{cen},b1} I_{b1}$$

where V_1, V_2 are the voltages across the capacitors at nodes 1 and 2, V_b is the voltage across the junction of SQUID loop b, and the currents $I_{a0,b0,a1,b1}$ are labeled in Fig. 4.3 (a). Again, the partial inductances $M_{\mathrm{cen},a0}, L_{\mathrm{cen},b0}, L_{\mathrm{cen},a1}, M_{\mathrm{cen},b1}$ from each segment to the center overlapping loop (cen) are involved in the second line of the expression.

4.2.1.3 Conservation of current through the overlapping capacitors

The effect of capacitive coupling on the corner-coupled SQUIDs are understood through the conservation of currents applied to the overlapping capacitors:

$$I_{a0} = I_{a1} + C_{\mathrm{ov}}\dot{V}_1 \tag{4.3a}$$

$$I_{b0} = I_{b1} - C_{\mathrm{ov}}\dot{V}_1 \tag{4.3b}$$

$$I_{a0} = I_{a1} - C_{\mathrm{ov}}\dot{V}_2 \tag{4.3c}$$

$$I_{b0} = I_{b1} + C_{\mathrm{ov}}\dot{V}_2, \tag{4.3d}$$

where nodes 1 and 2 have identical capacitance C_{ov} based on our design. The current conservation statements, Eqs. (4.3), reduce to the following relations:

$$I_{a0} + I_{b0} = I_{a1} + I_{b1} \tag{4.4}$$

$$\dot{V}_1 = -\dot{V}_2 \tag{4.5}$$

The flux equation Eq. (4.1) allows us to express the non-junction currents I_{a1} and I_{b1} in terms of the junction currents and the gauge-invariant phases, in other words

$I_{a1}(I_{a0}, I_{b0}, \delta_a, \delta_b)$, $I_{b1}(I_{a0}, I_{b0}, \delta_a, \delta_b)$ as;

$$I_{a1} = \mathrm{CD}^{-1}\left[\begin{pmatrix} L_{b,b1} & M_{a,b1} \end{pmatrix}\begin{pmatrix} \Phi_a^{\mathrm{app}} - \frac{\Phi_0}{2\pi}\delta_a \\ -\Phi_b^{\mathrm{app}} + \frac{\Phi_0}{2\pi}\delta_b \end{pmatrix} - \det\begin{pmatrix} L_{a,a0} & M_{a,b1} \\ M_{b,a0} & L_{b,b1} \end{pmatrix} I_{a0} - \det\begin{pmatrix} M_{a,b0} & M_{a,b1} \\ L_{b,b0} & L_{b,b1} \end{pmatrix} I_{b0}\right] \tag{4.6}$$

$$I_{b1} = \mathrm{CD}^{-1}\left[\begin{pmatrix} M_{b,a1} & L_{a,a1} \end{pmatrix}\begin{pmatrix} -\Phi_a^{\mathrm{app}} + \frac{\Phi_0}{2\pi}\delta_a \\ \Phi_b^{\mathrm{app}} - \frac{\Phi_0}{2\pi}\delta_b \end{pmatrix} - \det\begin{pmatrix} L_{a,a1} & L_{a,a0} \\ M_{b,a1} & M_{b,a0} \end{pmatrix} I_{a0} - \det\begin{pmatrix} L_{a,a1} & M_{a,b0} \\ M_{b,a1} & L_{b,b0} \end{pmatrix} I_{b0}\right] \tag{4.7}$$

The definition of CD is given in Appendix A. The current conservation statement Eq.(4.4) now becomes a constraint on $\delta_a, \delta_b, I_{a0}, I_{b0}$ after substituting $I_{a1,b1}$ from Eqs. (4.6, 4.7):

$$\begin{pmatrix} \kappa_a & \kappa_b \end{pmatrix}\begin{pmatrix} I_{a0} \\ I_{b0} \end{pmatrix} = \begin{pmatrix} L_{\delta a}^{-1} & L_{\delta b}^{-1} \end{pmatrix}\begin{pmatrix} \Phi_a^{\mathrm{app}} - \frac{\Phi_0}{2\pi}\delta_a \\ \Phi_b^{\mathrm{app}} - \frac{\Phi_0}{2\pi}\delta_b \end{pmatrix}, \tag{4.8}$$

where $\kappa_{a,b}$ and $L_{\delta a,\delta b}$ are defined in Appendix A. The time derivatives of junction voltages in Eq. (4.5), $\dot{V}_1 = -\dot{V}_2$, are solved from Faraday's law, Eq. (4.2) with $I_{a1,b1}$ given by Eqs. (4.6, 4.7):

$$\dot{V}_1 = [(1+\kappa_{\mathrm{v}b})\dot{V}_b + \kappa_{\mathrm{v}a}\dot{V}_a + L_{\mathrm{I}b}\ddot{I}_{b0} + L_{\mathrm{I}a}\ddot{I}_{a0} - \ddot{\Phi}_{\mathrm{cen}}^{\mathrm{app}} - \kappa_{\mathrm{v}a}\ddot{\Phi}_a^{\mathrm{app}} - \kappa_{\mathrm{v}b}\ddot{\Phi}_b^{\mathrm{app}}]/2 \tag{4.9}$$

The parameters $\kappa_{\mathrm{v}a}, \kappa_{\mathrm{v}b}, L_{\mathrm{I}a}, L_{\mathrm{I}b}$ are defined in Appendix A. One can see that Eq. (4.9) is a 4th-order differential equation in $\delta_{a,b}$, by noting that $I_{a0,b0}$ given in

the RCSJ model Eq. (3.3) brings two more time derivatives into the equation. The expression for $\dot{V}_1$ Eq. (4.9) can then be substituted into the current laws Eq. (4.3) to obtain solutions for the non-junction currents $I_{a1,b1}(I_{a0,b0}, \ddot{I}_{a0,b0}, \ddot{\delta}_{a,b})$:

$$I_{a1} = I_{a0} - C_{\rm ov}\dot{V}_1 \tag{4.10}$$

$$I_{b1} = I_{b0} + C_{\rm ov}\dot{V}_1 \tag{4.11}$$

4.2.1.4 Equation of motion for gauge invariant phase differences

The flux equations for the two SQUID loops can now be set up after obtaining the non-junction currents in Eqs. (4.10, 4.11). Assuming that the applied dc and rf flux amplitudes are the same in both SQUID loops, and that the rf flux is sinusoidal at a single frequency ω with amplitude $\Phi_{\rm rf}$, the flux equation, Eq. (4.1), becomes:

$$\begin{pmatrix} \Phi_{\rm dc} + \Phi_{\rm rf}\sin(\omega t) \\ \\ \Phi_{\rm dc} + \Phi_{\rm rf}\sin(\omega t) \end{pmatrix} = \frac{\Phi_0}{2\pi}\begin{pmatrix} \delta_a \\ \\ \delta_b \end{pmatrix} + \begin{pmatrix} L_{\rm geo} & M \\ \\ M & L_{\rm geo} \end{pmatrix}\begin{pmatrix} I_{a0} \\ \\ I_{b0} \end{pmatrix} + C_{\rm ov}\begin{pmatrix} -L_{\delta a}\dot{V}_1 \\ \\ L_{\delta b}\dot{V}_1 \end{pmatrix}, \tag{4.12}$$

where the induced flux (last two terms on the right hand side of Eq. (4.12)) is separated into two contributions: the first is that for conventional inductively-coupled SQUIDs with mutual inductance M, and the second is a correction due to the overlapping capacitors. The term with the inductance matrix can be regarded as the limit without capacitive coupling, when $C_{\rm ov} = 0$. Consequently, the current becomes uniform inside the SQUID loops such that $I_{a0} = I_{a1}$, $I_{b0} = I_{b1}$. The 2×4 inductance matrix in Eq. (4.1) is then reduced to the 2×2 matrix above with self inductance of

the SQUID loop determined as $L_{\rm geo} = L_{a,a0} + L_{a,a1} = L_{b,b0} + L_{b,b1}$, and the mutual inductance between the two SQUID loops $M = M_{b,a0} + M_{b,a1} = M_{a,b0} + M_{a,b1}$, which can be positive, zero, or negative depending on the overlapping area between the two SQUID loops. The last term in Eq. (4.12) involving $C_{\rm ov}$ brings in qualitatively new phenomena in the high frequency response of coupled rf SQUIDs.

4.2.1.5 Linear-limit solutions

To analytically understand the two corner-coupled SQUID system, one can start by simplifying the equations in the low-driving-amplitude linear limit when $|\phi_{\rm rf}| \ll 1$, similar to Sec.3.1.1. The full solution to $\delta(t)$ of any individual SQUID can be separated into its dc and rf components: $\delta = \delta_{\rm rf} \exp(i\omega t) + \delta_{\rm dc}$ [24]. The junction current from the RCSJ model under the weak rf flux approximation is $I = I_{\rm dc} + I_{\rm rf}(t) = I_c \sin(\delta_{\rm dc}) + I_c \cos(\delta_{\rm dc})\delta_{\rm rf}(t) + i\omega\Phi_0/(2\pi R)\delta_{\rm rf}(t) - \omega^2\Phi_0 C/(2\pi)\delta_{\rm rf}(t)$, where the terms with second or higher order in $\delta_{\rm rf}$ are dropped. After substituting the expressions for I_{a0} and I_{b0} in the equation of motion Eq. (4.12), and converting

to the non-dimensional vector format, one obtains a system of algebraic equations:

$$\vec{\phi}_{\rm dc} = \vec{\delta}_{\rm dc} + \beta_{\rm rf} \overleftrightarrow{\kappa} \sin \vec{\delta}_{\rm dc}$$

$$\vec{\phi}_{\rm rf} = \overleftrightarrow{\chi} \vec{\delta}_{\rm rf}, \tag{4.13}$$

$$\text{with } \overleftrightarrow{\chi} = (\overleftrightarrow{1} - \alpha\Omega^2 \lambda_{\rm cov} \overleftrightarrow{\kappa}_{\rm loop})^{-1}$$

$$[(\overleftrightarrow{1} + \overleftrightarrow{\kappa} \beta_{\rm rf} {\rm diag}(\cos \vec{\delta}_{\rm dc}) + i\gamma \overleftrightarrow{\kappa} \Omega -$$

$$\left(\overleftrightarrow{\kappa} + \lambda_{\rm cov} \overleftrightarrow{\kappa}_{\rm loop} (\overleftrightarrow{\kappa}_{\delta} + \overleftrightarrow{\kappa}_{\rm I} \beta_{\rm rf} {\rm diag}(\cos \vec{\delta}_{\rm dc})) \right) \Omega^2$$

$$+ \lambda_{\rm cov} \overleftrightarrow{\kappa}_{\rm loop} \overleftrightarrow{\kappa}_{\rm I} (-i\gamma\Omega^3 + \Omega^4)] \tag{4.14}$$

where $\overleftrightarrow{\kappa}$, $\overleftrightarrow{\kappa}_{\rm loop}$, $\overleftrightarrow{\kappa}_{\delta}$, and $\overleftrightarrow{\kappa}_{\rm I}$ are defined in Appendix A. Here $\overleftrightarrow{\kappa}$ is the 2×2 conventional inductive coupling matrix for the two SQUIDs without capacitive coupling, as in the middle term on the right hand side of Eq. (4.12). The resonance occurs when the determinant of the response tensor is zero, $\det(\overleftrightarrow{\chi}) = 0$. The real part of the solutions to this characteristic equation in $\Omega = \omega/\omega_{\rm geo}$ are the resonance frequencies, plotted in Fig. 4.4 as a function of dc flux applied to the SQUIDs, for the particular rf SQUID design used in our experiments (parameters are given in Appendix A and Table.4.1).

The characteristic equation is only sixth order in Ω, since the matrix $\overleftrightarrow{\kappa}_{\rm I}$ in front of the $(-i\gamma\Omega^3 + \Omega^4)$ term in Eq. (4.14) is singular. There are thus six roots, and only the three positive ones are shown in Fig. 4.4. The tuning curves of eigenfrequencies are periodic in applied dc flux with a periodicity of Φ_0, with each curve centered at an integer multiple of Φ_0. However, each resonant solution curve extends beyond the domain of $\pm 1\Phi_0$ and overlaps the adjacent curves due to the hysteresis from the SQUID loop, since $\beta_{\rm rf} > 1$.

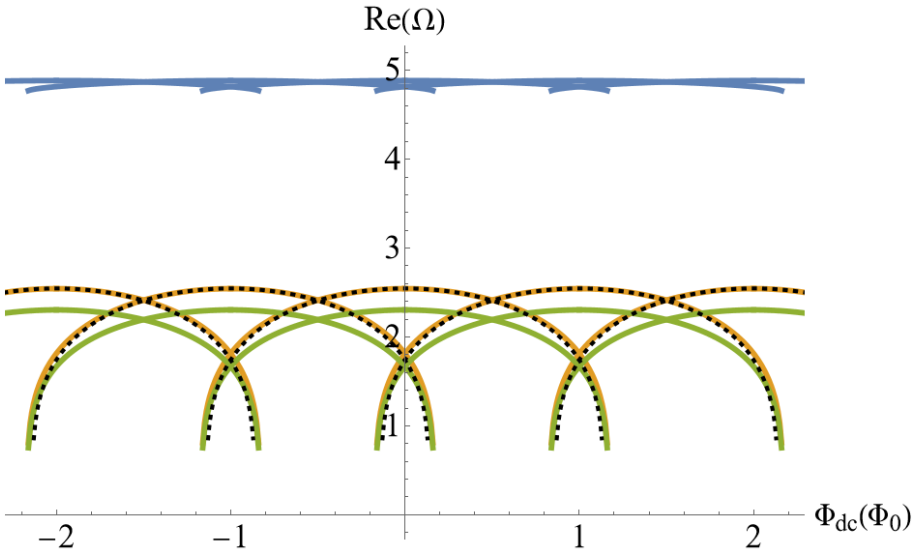

Figure 4.4: Real part of eigenfrequency solutions $Re(\Omega)$ from the characteristic equation $\det(\overleftrightarrow{\chi}) = 0$ in the linear limit for the two corner-coupled SQUIDs, as a function of dc magnetic flux $\Phi_{\rm dc}$ in units of Φ_0. The solid curves with three different colors correspond to the three positive solutions to the characteristic equation, while the black dotted curve is the eigenfrequency for a single SQUID with the same parameters. Due to the hysteretic response of the SQUIDs ($\beta_{\rm rf} > 1$), multiple dc flux tuning curves overlap each other in the same range of applied dc flux.

The three resonances cover a much broader frequency range compared to that of a single SQUID, which is shown as a black dotted curve on top of the yellow curve in Fig. 4.4. The second mode (yellow curve) out of the three resonances closely follows the dc-flux tunability of a single SQUID loop resonance.

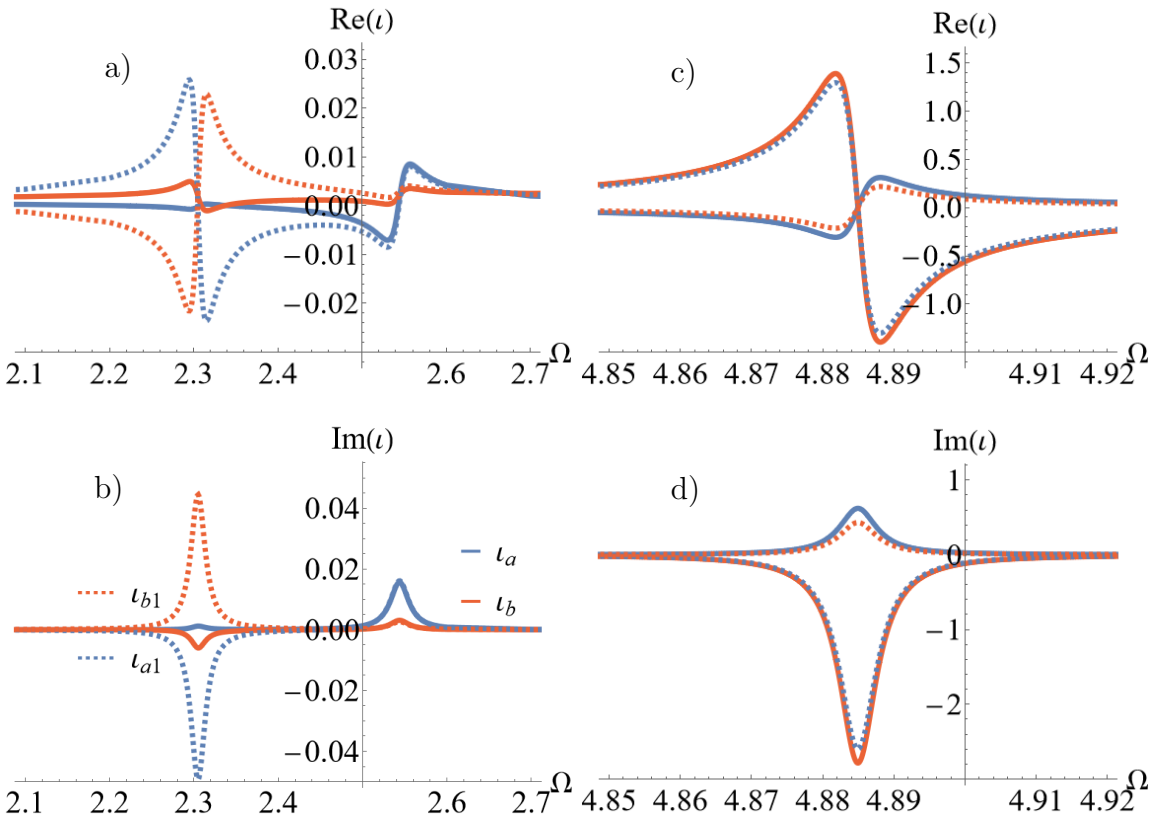

Figure 4.5: a), b) Real and imaginary parts of the solved dimensionless currents $\iota = 2\pi L_{\text{geo}} I/\Phi_0$ between $\Omega = 2.1$ and 2.7, for the linearized case of two corner-coupled SQUIDs at zero dc flux. c), d) Real and imaginary parts of the solved currents between $\Omega = 4.8$ and 5. The solid curves are the solutions to the junction currents $\iota_{a0,b0}$, while the dashed curves are the non-junction currents, $\iota_{a1,b1}$. Blue curves are for the currents in loop a, and red for loop b.

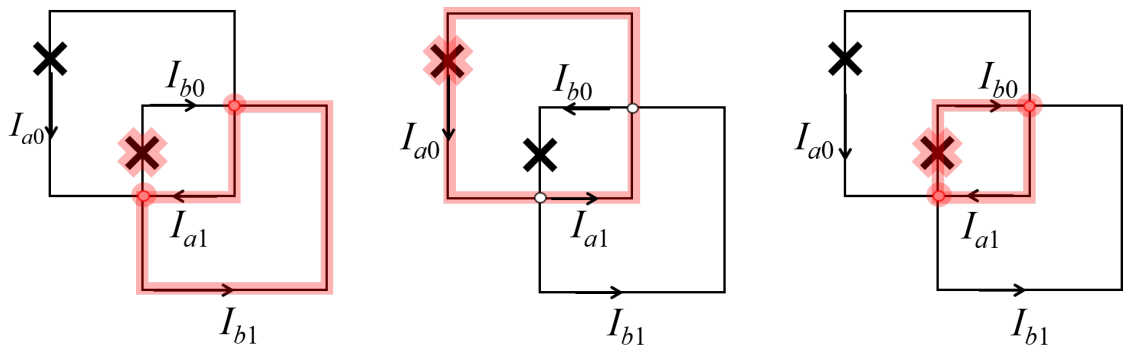

Figure 4.6: The dominant rf (not dc) current distribution for the three linearized eigenmodes from low to high frequencies at zero dc flux. The dominating junction and the "loop" in the mode are shaded in red. The capacitor nodes are shaded red when the rf current passes through the capacitors in the corresponding mode.

To better understand the nature of the other two modes, one can examine the solutions $\vec{\delta}_{\rm rf}$ to the linearized equations, Eqs. (4.13, 4.14) at the corresponding eigenfrequencies. In particular, the current values ($I_{a0,b0,a1,b1}$) in the SQUID loops as a function of frequency at zero dc flux are shown in Fig. 4.5, expressed as the dimensionless currents $\iota = 2\pi L_{\rm geo} I/\Phi_0$. The currents indeed undergo resonances near the three eigenfrequencies $\Omega \sim 2.3,\ 2.55,\ 4.88$ in Fig. 4.4 for zero dc flux. After comparing the current values from the three different eigenmodes, the dominant current distribution for each mode can be summarized in the schematics in Fig. 4.6, where the branches with strong currents are highlighted in red. The second mode at $\Omega \sim 2.55$ clearly stands out as the only mode where the current remains uniform inside one SQUID loop, just as in side-by-side pairs of inductively-coupled SQUIDs, which explains the match between the single SQUID eigenfrequency and the second mode in Fig. 4.4.

The frequencies for the modes can also be estimated quantitatively from the current distribution in the circuit. For a single SQUID loop, the resonance can be predicted from the lumped element model, $\Omega_{\rm res} = \omega_{\rm res}/\omega_{\rm geo} = (LC)^{-0.5}/\omega_{\rm geo} = \sqrt{(L_{\rm geo}^{-1} + L_{\rm JJ}^{-1})C^{-1}}/\omega_{\rm geo} = \sqrt{1+\beta_{\rm rf}\cos\delta}$. This circuit model can be generalized to one SQUID loop a in a large coupled system discussed in Sec.3.2.2:

$$\begin{aligned}\Omega_{\rm res} &= \sqrt{(L_{a,\rm eff}^{-1} + L_{\rm JJ}^{-1})C^{-1}}/\omega_{\rm geo} \\ &= \sqrt{\frac{L_{\rm geo}}{L_{a,\rm eff}} + \beta_{\rm rf}\cos\delta}\end{aligned} \tag{4.15}$$

where the loop inductance has changed from the geometric inductance $L_{\rm geo}$ to the effective inductance $L_{a,\rm eff}(\omega) = \Phi_a^{\rm ind}(\omega)/I_{a0}(\omega)$, accounting for the coupling from other SQUID loops in the large system. For instance, in the low power linear limit, a planar inductively coupled system has antiferromagnetic couplings among the SQUIDs. Thus, $L_{\rm eff}$ is always lower than $L_{\rm geo}$, resulting in a slightly higher $\Omega_{\rm res}$ than expected for the single SQUID design parameter. This property no longer holds true in an overlapping system. In particular, for the two corner-coupled SQUIDs model, $\Phi_a^{\rm ind}$ is given in Eq. (4.1). The resulting $L_{\rm eff}$ and $\Omega_{\rm res}$ calculated for the loop a and b at the three resonance modes are listed in Table 4.2. As a consequence of the nonuniform current distribution in one SQUID loop, the real part of the effective inductance can take on much wider range of values from higher than $L_{\rm geo}$ to large negative values. The corresponding resonant frequencies agree with the eigenfrequencies $\Omega_{\rm eig}$ solved from the linearized characteristic equation shown in Fig. 4.4.

The inductance of a circuit generally scales with its size. Therefore, the longer

Mode	1	2	3
$L_{a,\mathrm{eff}}/L_{\mathrm{geo}}$	$-5.35 + 1.09i$	$1.01 + 0.006i$	$0.054 - 0.001i$
$L_{b,\mathrm{eff}}/L_{\mathrm{geo}}$	$-5.15 + 2.04i$	$1.15 - 0.16i$	$0.054 + 0.001i$
$\mathrm{Re}(\Omega_{a,\mathrm{res}}(\delta = 0))$	2.30	2.54	4.91
$\mathrm{Re}(\Omega_{b,\mathrm{res}}(\delta = 0))$	2.31	2.52	4.90
$\mathrm{Re}(\Omega_{\mathrm{eig}}(\delta = 0))$	2.31	2.54	4.89

Table 4.2: Effective inductance values of SQUID loops a and b, $L_{\mathrm{a(b),eff}}$, in the three resonant modes of the corner-coupled rf SQUIDs. Comparison between the real parts of the resonant frequencies $\mathrm{Re}(\Omega_{a(b),\mathrm{res}})$ calculated from the effective inductance for the SQUID loop $a(b)$ in the three eigenmodes (1-3), and the real part of their corresponding eigenfrequencies $\mathrm{Re}(\Omega_{\mathrm{eig}})$ deduced from solutions to Eqs. (4.13) at zero applied dc flux.

dominant current branches in the left two modes in Fig. 4.6 contribute to a larger effective inductance magnitude compared to the third mode, where the short segments dominate the current distribution. A larger effective inductance in magnitude corresponds to a smaller correction to the resonance frequency as in Eq. (4.15) for $\beta_{rf} > 1$. In contrast, the smaller effective inductance in the third mode in Fig. 4.6 leads to a much higher resonance than predicted for a single SQUID. The apparent difference in dc flux tunability between the highest frequency mode and the other modes can also be explained by the magnitude of effective inductance. The small effective inductance leads to a large $L_{\rm geo}/L_{\rm eff}$ that renders the dc tuning term represented by $\beta_{\rm rf}\cos\delta$ less effective in Eq. (4.15).

4.2.1.6 Full nonlinear numerical solutions

Although analytical solution to the system of equations at rf flux driving levels beyond the linear limit is difficult, we can obtain the full nonlinear solution numerically. For the convenience of the numerical solver, the equations are first converted into dimensionless form as in Eq. (3.20) with the additional introduction of dimensionless currents: $\iota = 2\pi L_{\rm geo} I/\Phi_0$. In the general practice of numerically solving a system of differential equations, the equations are first reformulated as a system of first order initial value problems. The equations of motion Eq. (4.12) consist of two flux equations, each a 4th-order differential equation for δ. However, due to the constraint in Eq. (4.8) relating $\delta_{a,b}$ and $I_{a0,b0}$, there are only six degrees of freedom, two less than otherwise expected. This can be illustrated by manipulating the above

matrix expression (Eq. (4.12)) as follows: $L_{\delta a}^{-1}$Row 1 + $L_{\delta b}^{-1}$Row 2, which is equivalent to the constraint in Eq. (4.8). Therefore, instead of solving the overdetermined system in Eq. (4.12) directly with eight variables, one should reduce the system to one equation of motion for one of the SQUIDs, along with the constraint Eq. (4.8), and establish the initial value problems with six variables: $\delta_{a,b}$, $\dot{\delta}_{a,b}$, ι_{a0}, $\dot{\iota}_{a0}$, as follows.

$$\frac{d\delta_a}{d\tau} = \dot{\delta}_a \tag{4.16a}$$

$$\frac{d\delta_b}{d\tau} = \dot{\delta}_b \tag{4.16b}$$

$$\frac{d\dot{\delta}_a}{d\tau} = \ddot{\delta}_a = \iota_{a0} - \beta_{\mathrm{rf}} \sin\delta_a - \gamma\dot{\delta}_a \tag{4.16c}$$

$$\frac{d\dot{\delta}_b}{d\tau} = \ddot{\delta}_b = \iota_{b0} - \beta_{\mathrm{rf}} \sin\delta_b - \gamma\dot{\delta}_b =$$

$$\kappa_b^{-1} \begin{pmatrix} \kappa_{\delta a}^{-1} \\ \\ \kappa_{\delta b}^{-1} \end{pmatrix} \cdot (\vec{\phi}^{\mathrm{app}} - \vec{\delta}) - \frac{\kappa_a}{\kappa_b}\iota_{a0} - \beta_{\mathrm{rf}} \sin\delta_b - \gamma\dot{\delta}_b \tag{4.16d}$$

$$\frac{d\iota_{a0}}{d\tau} = \dot{\iota}_{a0} \tag{4.16e}$$

$$\frac{d\dot{\iota}_{a0}}{d\tau} = \ddot{\iota}_{a0} = \frac{1}{\lambda_{\mathrm{cov}}\kappa_{\delta a}(\kappa_a\kappa_{\mathrm{I}b} - \kappa_b\kappa_{\mathrm{I}a})}$$

$$\Bigg[\begin{pmatrix} \kappa_b - \kappa_1/\kappa_{\delta a} \\ \\ -\kappa_1/\kappa_{\delta b} \end{pmatrix} \cdot (\vec{\phi}^{\mathrm{app}} - \vec{\delta})$$

$$- (\kappa_b - \kappa_a\kappa_1)\iota_{a0}$$

$$+\lambda_{\mathrm{cov}}\kappa_{\delta a}(\begin{pmatrix} \kappa_{\mathrm{v}a}\kappa_b - \kappa_{\mathrm{I}b}/\kappa_{\delta a} \\ \\ \kappa_b + \kappa_{\mathrm{v}b}\kappa_b - \kappa_{\mathrm{I}b}/\kappa_{\delta b} \end{pmatrix} \cdot \dddot{\vec{\delta}} - \alpha\ddot{\phi}^{\mathrm{app}}) \Bigg] \tag{4.16f}$$

where $\phi^{\rm app} = \phi_{\rm dc} + \phi_{\rm rf}\sin(\Omega\tau)$ is the dimensionless applied flux. The second time derivatives in δ in Eqs. (4.16 c, d) are related to the currents using the RCSJ model, Eq. (3.3). The constraint Eq. (4.8) is invoked to express ι_{b0} in Eq. (4.16 d). The second time derivative of current ($\ddot{\iota}_{a0}$) in Eq. (4.16 f) is obtained from the equation of motion Eq. (4.12). All other parameters are defined in Appendix A. The resulting system of initial value problems was solved with the LSODA function from SciPy based on the FORTRAN library ODEPACK. The transmission through the system is then calculated from the solutions to δs as described in Sec.3.1.2.1.

The resulting transmission at low applied rf flux amplitude ($\Phi_{\rm rf} \sim 10^{-3}\Phi_0$), near the linear limit, as a function of dimensionless driving frequency Ω and dc flux is plotted in Fig. 4.7. The dark bands represent the resonances in the rf SQUID system, where the amplitudes of the rf currents in the SQUID loops, and thus the dissipated powers in the junctions, are maximized. Unlike the case for a pair of side-by-side rf SQUIDs, which have two resonant modes, there are now three distinct modes tuned by the applied dc magnetic flux. The red lines in Fig. 4.7 show the dispersion of the linearized solutions from Eq. (4.13), and show good agreement with the solutions to the full nonlinear equations, Eqs. (4.16), in the weak-driving limit.

4.2.1.7 Nonlinear Properties of the Corner-Coupled SQUIDs

Here we examine the evolution of the three corner-coupled modes as the amplitude of the rf driving flux is increased. Figure 4.8 shows the evolution of the

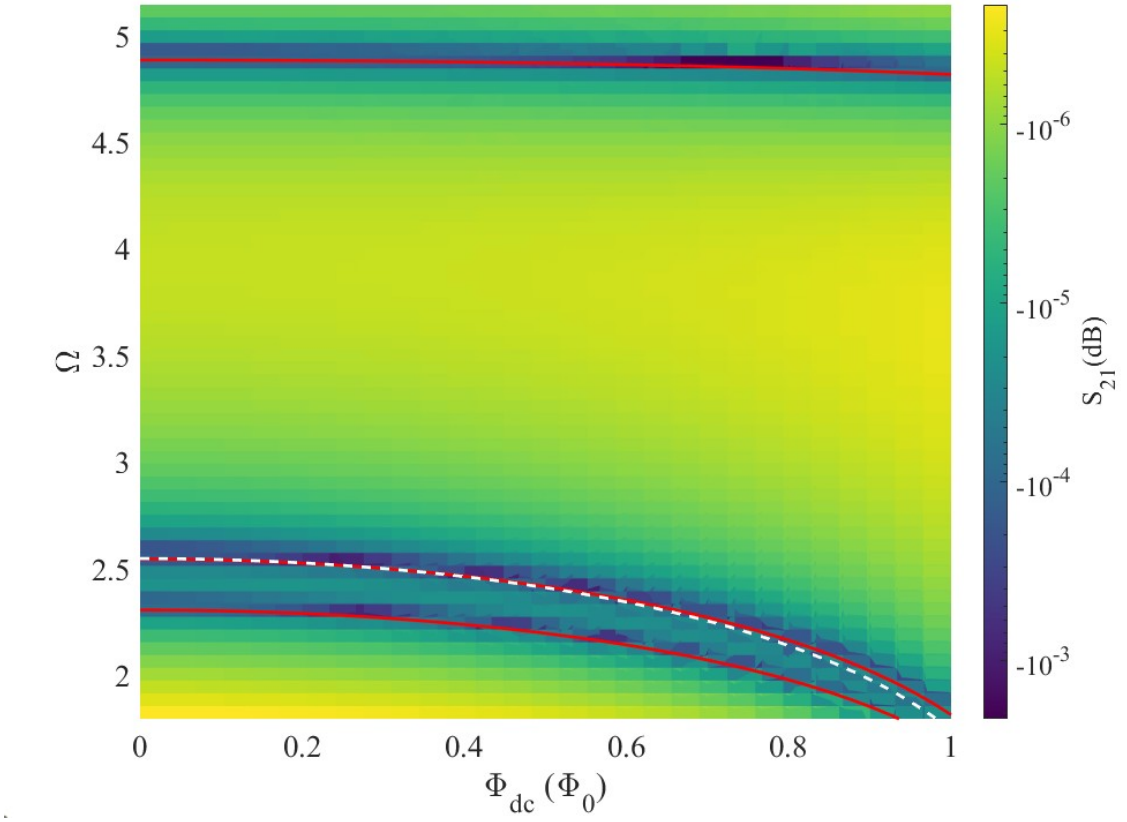

Figure 4.7: Nonlinear solutions to the two corner-coupled SQUIDs at $\Phi_{\mathrm{rf}} \sim 10^{-3}\Phi_0$. The quantity plotted is the magnitude of transmission $S_{21}(dB)$ on a logarithmic color scale, as a function of dimensionless frequency $\Omega = \omega/\omega_{\mathrm{geo}}$ and applied dc magnetic flux in units of the flux quantum Φ_0. The white dashed curve corresponds to the eigenfrequency for a single SQUID with the same parameters, and the red curves are the eigenfrequencies from the linear limit solutions for the two corner-coupled SQUIDs as in Sec.4.2.1.5.

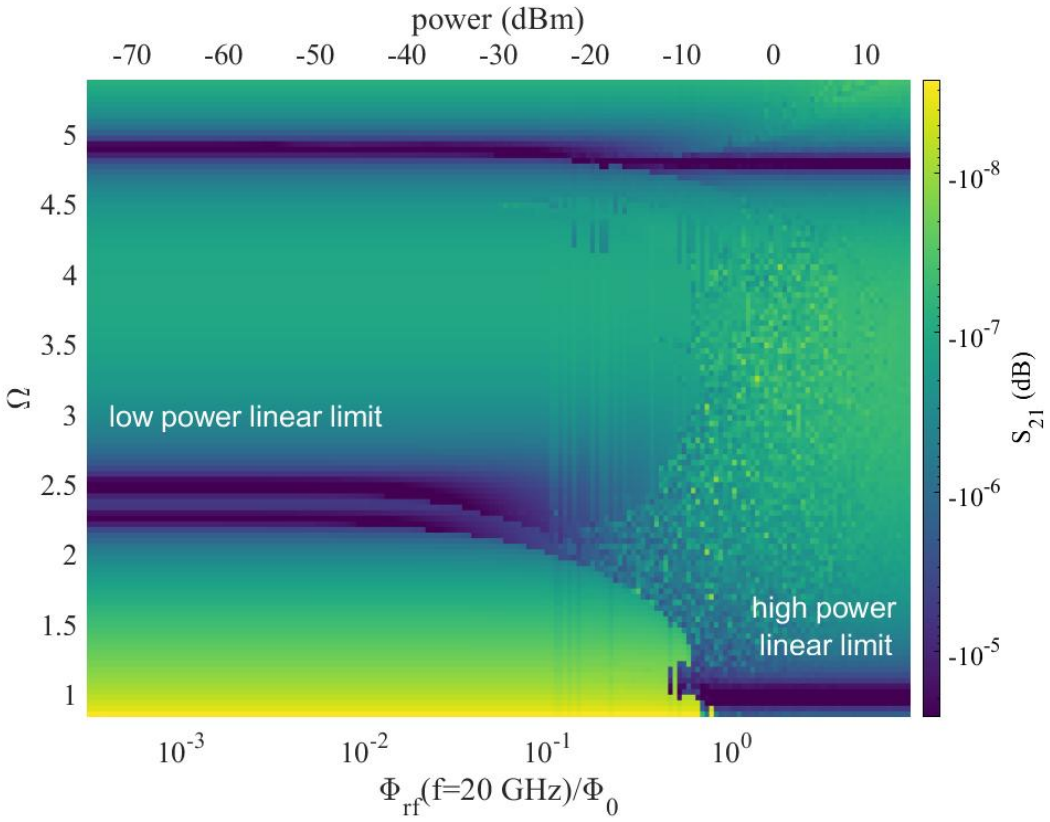

Figure 4.8: Nonlinear solutions to the two corner-coupled SQUIDs for $\Phi_{\rm dc} = 0$. The quantity plotted is the magnitude of transmission $S_{21}(dB)$ on a logarithmic color scale, as a function of applied rf magnetic flux amplitude in units of the flux quantum Φ_0 and dimensionless frequency $\Omega = \omega/\omega_{\rm geo}$. The linear limit discussed in Sec. 4.2.1.5 is reproduced at low applied power on the left of the plot. Upon increasing $\Phi_{\rm rf}$ above Φ_0, the high-power linear limit is achieved where the SQUID loop resonance is suppressed to the geometric frequency ($\Omega = 1$).

resonant modes from the linear limit $\Phi_{\rm rf}/\Phi_0 \sim 10^{-3}$ at zero dc flux to higher rf flux amplitudes. All three modes show a suppression of their resonant frequencies in a manner similar to that observed for single rf SQUIDs [44]. Note that the two lower frequency modes show substantial tuning with rf flux amplitude, but the high-frequency mode is only weakly affected since they are dominated by currents in non-junction branches which is less sensitive to the applied magnetic flux. Also note that all three modes achieve linear response again at high driving amplitudes, in the sense that the resonant frequencies are independent of rf flux amplitude when $\Phi_{\rm rf} \gtrsim \Phi_0$. This behavior was observed before [44] and can be attributed to the $\vec{\delta}$ term in Eq. 3.20. At large rf driving amplitudes the $\sin\vec{\delta}$ term averages to zero, leaving just a leading-order $\vec{\delta}$ term that reduces the equation of motion to the form of a harmonic oscillator. Further examination of the nonlinear properties of these hysteretic SQUID metamaterials will the subject of future work.

4.2.2 Two edge-coupled SQUIDs

Edge-coupled SQUIDs refer to those with entire left or right side of the rectangular SQUID overlapping with another SQUID. Two edge-coupled SQUIDs form the minimal model for the 1D overlapping chain of SQUIDs as shown in the Fig. 4.9. The designed properties for a single SQUID in this overlapping chain is listed in the table below.

The same analysis, namely using Faraday's law on the overlapping loop and Kirchhoff's current law on the overlapping capacitors, can be applied. However,

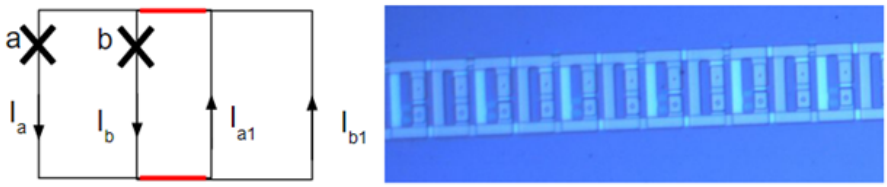

Figure 4.9: Left: Schematics of two edge-coupled SQUIDs model. The red lines highlight the overlapping capacitors formed between the two SQUID loops. Right: picture of an overlapping SQUID chain sample.

there is one key difference worth to note here that the overlapping capacitors have lengths about half of the SQUID size and is no longer suitable to be treated as a node as in the previous corner-coupled case. In fact, these two parallel planes form an approximately loss-less transmission line where the voltage and current along the line $I(x,t)$, $V(x,t)$ follow telegrapher equations with the wavelength given as

$$\lambda = \frac{2\pi}{k} = \frac{2\pi}{\omega\sqrt{lc}} = \frac{2\pi d_{\text{ov}}}{\omega\sqrt{L_{\text{ov}}C_{\text{ov}}}} \tag{4.17}$$

where l and c are the inductance and capacitance per unit length. For typical microwave frequencies, $\omega \in [2\omega_0, 4\omega_0]$, the wavelength $\lambda \in [14d_{\text{ov}}, 27d_{\text{ov}}]$ calculated based on the design parameter of our 1D overlapping chain sample where $C_{\text{ov}} = 1.88$ pF, $L_{\text{ov}} = 1.52$ pH. Therefore, $I(x,t)$, $V(x,t)$ are only changing slowly along the overlapping capacitor. Instead of dealing with the spatially dependent currents and voltages, we can simplify the problem by discretizing the transmission line, i.e. using the distributed element model where each overlapping part is separated into segments of inductances and overlapping capacitors as in Fig.4.10.

The current $I(x,t)$ in the telegrapher equation is the difference between the

Parameter	Symbol	Numerical value
Junction inductance	L_{JJ}	46.54 pH
Geometric inductance	L_{geo}	142.3 pH
SQUID self capacitance (RCSJ)	C	1.54 pF
Junction resistance	R	500 Ω
Geometric resonance	f_{geo}	10.75 GHz
SQUID hysteresis parameter	β_{rf}	3.06
Damping parameter	γ	0.0192

Table 4.3: Designed properties for a single SQUID in the overlapping 1D chain sample

currents from the top and bottom conductor in the transmission line. The sum of these currents is in fact constant in space. Thus, $I_{\mathrm{comm}} = I_a + I_b = I_{a1} + I_{b1} = I_{a2} + I_{b2} = I_{a3} + I_{b3} = I_{a4} + I_{b4}$. Since the gap between the top and bottom layer is very small compared to the planar structure in our SQUID design, the top and bottom conductors in the transmission line share the same mutual inductance to other planar loops. Consequently, the current difference $I(x,t)$ does not contribute to flux to the planar loops.

Our objective is the same as previously, to express I_{ai}, I_{bi} in terms of δs and their time derivatives. It should be first noted that due to symmetry of the geometry, the currents through the upper and lower overalpping capacitors are the same, while the voltages across them are of opposite signs. We can attack this

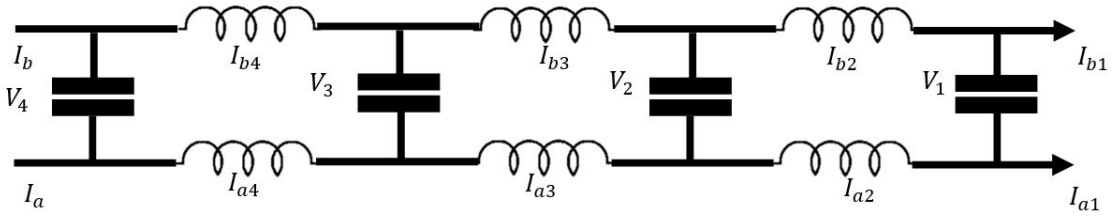

Figure 4.10: Schematics of the distributed element model of the overlapping part, where the capacitor is discretized in to three segments and four nodes.

problem systematically by applying Faraday's laws to the known current loops to find the voltages, and then solve for the currents next to the voltage node in the transmission line. Specifically, we start by applying Faraday's law to the loop formed by the two junctions where we can solve for V_4, and then express $I_{a4},\ I_{b4}$. We then apply Faraday's law to the side loop formed by $I_{a4},\ I_{b4},\ V_4,\ V_3$ and solve for V_3. Repeating the same procedure on the subsequent side loops, the expressions for all the currents and voltages are then obtained. This method implicitly assumes that the net flux on any planar loop due to the transmission line in differential mode (e.g. $I_{ai} = I/2,\ I_{bi} = -I/2$) is approximately zero. Similar to the two corner-coupled SQUIDs, there is an additional constraint after solving for I_{a1} and I_{b1} from the flux quantization conditions of the two SQUID loops, since we need to impose the current conservation $I_a + I_b = I_{a1} + I_{b1}$.

4.2.2.1 One branch for the overlapping capacitors in the two edge-coupled SQUIDs model

Let's study the simplest case with only one branch for the transmission line. Thus, the transmission line is formed by two inductors carrying currents $I_{a2},\ I_{b2}$ and two capacitors with voltages $V_1,\ V_2$. There are in total four loops to apply Faraday's laws and flux quantization conditions. We can express the induced fluxes for these loops in the following reduced inductance matrix.

$$\begin{pmatrix} \Phi_a \\ \Phi_b \\ \Phi_{ab} \\ \Phi_{a1b1} \end{pmatrix} = \begin{pmatrix} L_a & M_b & L_{a1} & M_{b1} & L_{\text{comm}} \\ M_a & L_b & M_{a1} & L_{b1} & L'_{\text{comm}} \\ L'_a & L'_b & M'_{a1} & M'_{b1} & M_{\text{comm}} \\ M''_a & M''_b & L''_{a1} & L''_{b1} & M'_{\text{comm}} \end{pmatrix} \begin{pmatrix} I_a \\ I_b \\ I_{a1} \\ I_{b1} \\ I_{\text{comm}} \end{pmatrix}, \tag{4.18}$$

where the numerical values of the inductance matrix for our SQUID design are given as

$$\begin{pmatrix} L_a & M_b & L_{a1} & M_{b1} & L_{\text{comm}} \\ M_a & L_b & M_{a1} & L_{b1} & L'_{\text{comm}} \\ L'_a & L'_b & M'_{a1} & M'_{b1} & M_{\text{comm}} \\ M''_a & M''_b & L''_{a1} & L''_{b1} & M'_{\text{comm}} \end{pmatrix} = \begin{pmatrix} 80.4 & -5.78 & 36.37 & 14.28 & 25.53 \\ 14.35 & 33.18 & -5.84 & 83.59 & 25.53 \\ 70.97 & -29.69 & 9.26 & 4.92 & 5.94 \\ 4.92 & 9.26 & -32.95 & 74.23 & 5.94 \end{pmatrix} \text{pH}.$$

Since the small difference in the wiring thickness from different layers has a negligible effect on the inductances, we would use $L_{\text{comm}} = L'_{\text{comm}}$ and $M_{\text{comm}} = M'_{\text{comm}}$ in all the following discussion. It should also be noted that $L_{\text{geo}} = L_a + L_{a1} + L_{\text{comm}} = L_b + L_{b1} + L_{\text{comm}}$, $M = M_b + M_{b1} + L_{\text{comm}} = M_a + M_{a1} + L_{\text{comm}}$. The top two rows in

Eq.(4.18) are the fluxes on the SQUID loops and are used in the flux quantization conditions. The bottom two rows are used in Faraday's law. The Faraday's loops' subscripts are chosen based on the currents in the respective loop. For example, Φ_{ab} is the induced flux on the loop formed by the segments with currents I_a and I_b (see Fig.4.9). The two flux quantization conditions and the two Faraday's laws are listed below:

$$\Phi_a^{\text{app}} = \frac{\Phi_0}{2\pi}\delta_a + \Phi_a \tag{4.19}$$

$$\Phi_b^{\text{app}} = \frac{\Phi_0}{2\pi}\delta_b + \Phi_b \tag{4.20}$$

$$V_a - 2V_2 - V_b = \dot{\Phi}_{ab}^{\text{app}} - \dot{\Phi}_{ab} \tag{4.21}$$

$$-2V_1 = \dot{\Phi}_{a1b1}^{\text{app}} - \dot{\Phi}_{a1b1} \tag{4.22}$$

We can use the flux quantization conditions to express $I_{a1},\ I_{b1}$,

$$I_{a1} = \begin{vmatrix} L_{a1} & M_{a1} \\ M_{b1} & L_{b1} \end{vmatrix}^{-1} \left(L_{b1}\Phi_a^{a1,b1} - M_{b1}\Phi_b^{a1,b1} \right) \tag{4.23a}$$

$$I_{b1} = \begin{vmatrix} L_{a1} & M_{a1} \\ M_{b1} & L_{b1} \end{vmatrix}^{-1} \left(L_{a1}\Phi_b^{a1,b1} - M_{a1}\Phi_a^{a1,b1} \right), \tag{4.23b}$$

and substitute them into the two Faraday's laws to solve for $V_1,\ V_2$:

$$V_1 = \frac{1}{2}\left(-\dot{\Phi}_{a1b1}^{\text{app}} + M_a''\dot{I}_a + M_b''\dot{I}_b + M_{\text{comm}}(\dot{I}_a + \dot{I}_b) + \dot{\Phi}_{a1b1}^{a1,b1} \right) \tag{4.24a}$$

$$V_2 = \frac{1}{2}\left(-\dot{\Phi}_{ab}^{\text{app}} + L_a'\dot{I}_a + L_b'\dot{I}_b + M_{\text{comm}}(\dot{I}_a + \dot{I}_b) + V_a - V_b + \dot{\Phi}_{ab}^{a1,b1} \right), \tag{4.24b}$$

where

$$\Phi_a^{a1,b1} = \Phi_a^{\rm app} - (L_a + L_{\rm comm})I_a - (M_b + L_{\rm comm})I_b - \frac{\Phi_0}{2\pi}\delta_a$$

$$\Phi_b^{a1,b1} = \Phi_b^{\rm app} - (L_b + L_{\rm comm})I_b - (M_a + L_{\rm comm})I_a - \frac{\Phi_0}{2\pi}\delta_b$$

$$\Phi_{a1b1}^{a1,b1} = L''_{b1}I_{b1} + L''_{a1}I_{a1}$$

$$= \begin{vmatrix} L_{a1} & M_{a1} \\ M_{b1} & L_{b1} \end{vmatrix}^{-1} \left(L''_{b1}(L_{a1}\Phi_b^{a1,b1} - M_{a1}\Phi_a^{a1,b1}) + L''_{a1}(L_{b1}\Phi_a^{a1,b1} - M_{b1}\Phi_b^{a1,b1}) \right)$$

$$\Phi_{ab}^{a1,b1} = M'_{b1}I_{b1} + M'_{a1}I_{a1}$$

$$= \begin{vmatrix} L_{a1} & M_{a1} \\ M_{b1} & L_{b1} \end{vmatrix}^{-1} \left(M'_{b1}(L_{a1}\Phi_b^{a1,b1} - M_{a1}\Phi_a^{a1,b1}) + M'_{a1}(L_{b1}\Phi_a^{a1,b1} - M_{b1}\Phi_b^{a1,b1}) \right).$$

The constraint $I_a + I_b = I_{a1} + I_{b1}$ is then expressed as

$$I_a + I_b = \begin{vmatrix} L_{a1} & M_{a1} \\ M_{b1} & L_{b1} \end{vmatrix}^{-1} \left((L_{b1} - M_{a1})\Phi_a^{a1,b1} + (L_{a1} - M_{b1})\Phi_b^{a1,b1} \right),$$

with its dimensionless form given as

$$\iota_a + \iota_b = \begin{vmatrix} L_{a1} & M_{a1} \\ M_{\neg b1} & L_{b1} \end{vmatrix}^{-1} \left((L_{b1} - M_{a1}) \left(L_{\rm geo}\phi_a^{\rm app} - (L_a + L_{\rm comm})\iota_a - (M_b + L_{\rm comm})\iota_b - L_{\rm geo}\delta_a \right) \right.$$

$$\left. +(L_{a1} - M_{b1}) \left(L_{\rm geo}\phi_b^{\rm app} - (L_b + L_{\rm comm})\iota_b - (M_a + L_{\rm comm})\iota_a - L_{\rm geo}\delta_b \right) \right)$$

$$\kappa_{\iota a}\iota_a + \kappa_{\iota b}\iota_b = \kappa_{\delta a}(\phi^{\rm app} - \delta_a) + \kappa_{\delta b}(\phi^{\rm app} - \delta_b), \tag{4.25}$$

where $\phi^{\rm app} = \phi_{\rm dc} + \phi_{\rm rf}\sin(\Omega\tau) = \phi_a^{\rm app} = \phi_b^{\rm app}$, $\kappa_{\iota a} = 4.31$, $\kappa_{\iota b} = 1.98$, $\kappa_{\delta a} = 4.07$,$\kappa_{\delta b} = 1.01$.

We then use the current conservation to express $I_{a1},\ I_{b1}$ with the solutions for

$V_1,\ V_2$ given in Eq.(4.24a,4.24b):

$$\begin{aligned} I_{a1} &= I_a + \frac{C_{\rm ov}}{2}\dot{V}_1 + \frac{C_{\rm ov}}{2}\dot{V}_2 \\ &= I_a + \frac{C_{ov}}{4}\Big(-\ddot{\Phi}^{\rm app}_{a1b1} - \ddot{\Phi}^{\rm app}_{ab} + (L'_a + M''_a + 2M_{\rm comm})\ddot{I}_a \\ &+(L'_b + M''_b + 2M_{\rm comm})\ddot{I}_b + \dot{V}_a - \dot{V}_b + \ddot{\Phi}^{a1,b1}_{a1b1} + \ddot{\Phi}^{a1,b1}_{ab}\Big) \qquad (4.26a) \\ I_{b1} &= I_b - \frac{C_{\rm ov}}{2}\dot{V}_1 - \frac{C_{\rm ov}}{2}\dot{V}_2 \\ &= I_b - \frac{C_{\rm ov}}{4}\Big(-\ddot{\Phi}^{\rm app}_{a1b1} - \ddot{\Phi}^{\rm app}_{ab} + (L'_a + M''_a + 2M_{\rm comm})\ddot{I}_a \\ &+(L'_b + M''_b + 2M_{\rm comm})\ddot{I}_b + \dot{V}_a - \dot{V}_b + \ddot{\Phi}^{a1,b1}_{a1b1} + \ddot{\Phi}^{a1,b1}_{ab}\Big). \qquad (4.26b) \end{aligned}$$

The final equations of motions can then be obtained by substituting Eq.(4.26) into the flux quantization conditions Eq.(4.19,4.20):

$$\begin{aligned} \Phi_{\rm dc} + \Phi_{\rm rf}\sin(\omega t) &= \frac{\Phi_0}{2\pi}\delta_a + L_a I_a + M_b I_b + L_{a1} I_{a1} + M_{b1} I_{b1} + L_{\rm comm}(I_a + I_b) \\ &= \frac{\Phi_0}{2\pi}\delta_a + (L_a + L_{a1} + L_{\rm comm})I_a + (M_b + M_{b1} + L_{\rm comm})I_b \\ &\quad + \frac{(L_{a1} - M_{b1})C_{\rm ov}}{4}\ddot{\Phi}_{\rm ov} \qquad (4.27) \\ \Phi_{\rm dc} + \Phi_{\rm rf}\sin(\omega t) &= \frac{\Phi_0}{2\pi}\delta_b + M_a I_a + L_b I_b + M_{a1} I_{a1} + L_{b1} I_{b1} + L_{\rm comm}(I_a + I_b) \\ &= \frac{\Phi_0}{2\pi}\delta_b + (M_a + M_{a1} + L_{\rm comm})I_a + (L_b + L_{b1} + L_{\rm comm})I_b \\ &\quad + \frac{(M_{a1} - L_{b1})C_{\rm ov}}{4}\ddot{\Phi}_{\rm ov}, \qquad (4.28) \end{aligned}$$

where

$$\ddot{\Phi}_{\rm ov} = -\ddot{\Phi}^{\rm app}_{a1b1} - \ddot{\Phi}^{\rm app}_{ab} + (L'_a + M''_a + 2M_{\rm comm})\ddot{I}_a + (L'_b + M''_b + 2M_{\rm comm})\ddot{I}_b$$
$$+ \frac{\Phi_0}{2\pi}(\ddot{\delta}_a - \ddot{\delta}_b) + \begin{vmatrix} L_{a1} & M_{a1} \\ M_{b1} & L_{b1} \end{vmatrix}^{-1} \Big[(L''_{b1}L_{a1} - L''_{a1}M_{b1} + M'_{b1}L_{a1} - M'_{a1}M_{b1})$$
$$(\ddot{\Phi}^{\rm app}_b - (L_b + L_{\rm comm})\ddot{I}_b - (M_a + L_{\rm comm})\ddot{I}_a - \frac{\Phi_0}{2\pi}\ddot{\delta}_b)$$
$$+ (L''_{a1}L_{b1} - L''_{b1}M_{a1} + M'_{a1}L_{b1} - M'_{b1}M_{a1})(\ddot{\Phi}^{\rm app}_a - (L_a + L_{\rm comm})\ddot{I}_a$$
$$- (M_b + L_{\rm comm})\ddot{I}_b - \frac{\Phi_0}{2\pi}\ddot{\delta}_a)\Big]$$

The dimensionless forms of Eq.(4.27,4.28) are

$$\vec{\phi}_{\rm dc} + \vec{\phi}_{\rm rf}\sin(\Omega\tau) = \vec{\delta} + \overleftrightarrow{\kappa}\vec{\iota} + \begin{pmatrix} \kappa_{\rm cla} \\ \kappa_{\rm clb} \end{pmatrix} \Big[-\kappa_\phi \ddot{\phi}^{\rm app} + \kappa_{\rm ia}\ddot{\iota}_a + \kappa_{\rm ib}\ddot{\iota}_b + \ddot{\delta}_a - \ddot{\delta}_b$$
$$+\kappa_b\left(\ddot{\phi}^{\rm app} - \kappa^b_b\ddot{\iota}_b - \kappa^a_b\ddot{\iota}_a - \ddot{\delta}_b\right) + \kappa_a\left(\ddot{\phi}^{\rm app} - \kappa^b_a\ddot{\iota}_b - \kappa^a_a\ddot{\iota}_a - \ddot{\delta}_a\right)\Big] \quad (4.29)$$

where

$$\overleftrightarrow{\kappa} = \begin{pmatrix} 1 & \kappa_1 \\ \kappa_1 & 1 \end{pmatrix}$$

$$\kappa_1 = M/L_{\text{geo}} = 0.239$$

$$\kappa_{\text{cla}} = (L_{a1} - M_{b1})C_{\text{ov}}/(4L_{\text{geo}}C) = 0.047$$

$$\kappa_{\text{clb}} = (M_{a1} - L_{b1})C_{\text{ov}}/(4L_{\text{geo}}C) = -0.19$$

$$\kappa_\phi = (A_{a1b1} + A_{ab})/A_{\text{SQUID}} = 1.27 \text{ (ratio of the areas in the corresponding loops)}$$

$$\kappa_{\text{ia}} = (L'_a + M''_a + 2M_{\text{comm}})/L_{\text{geo}} = 0.617$$

$$\kappa_{\text{ib}} = (L'_b + M''_b + 2M_{\text{comm}})/L_{\text{geo}} = -0.06$$

$$\kappa_b = \begin{vmatrix} L_{a1} & M_{a1} \\ M_{b1} & L_{b1} \end{vmatrix}^{-1} (L''_{b1}L_{a1} - L''_{a1}M_{b1} + M'_{b1}L_{a1} - M'_{a1}M_{b1}) = 1.03$$

$$\kappa_b^b = (L_b + L_{\text{comm}})/L_{\text{geo}} = 0.413$$

$$\kappa_b^a = (M_a + L_{\text{comm}})/L_{\text{geo}} = 0.28$$

$$\kappa_a = \begin{vmatrix} L_{a1} & M_{a1} \\ M_{b1} & L_{b1} \end{vmatrix}^{-1} (L''_{a1}L_{b1} - L''_{b1}M_{a1} + M'_{a1}L_{b1} - M'_{b1}M_{a1}) = -0.49$$

$$\kappa_a^b = (M_b + L_{\text{comm}})/L_{\text{geo}} = 0.139$$

$$\kappa_a^a = (L_a + L_{\text{comm}})/L_{\text{geo}} = 0.744.$$

We should note that the first three terms of the right hand side of the equation is the same as the equation for two side-by-side SQUIDs. In a similar manner to Sec.4.2.1.6 for the two corner-coupled SQUIDs, the solutions can be obtained from Eq.(4.29) for one SQUID and the constraint, Eq.(4.25), relating ι_a, ι_b and reducing

the degrees of freedom to 6.

Linear-limit solutions

Following the same treatment as in Sec.4.2.1.5, we can apply the weak rf field approximation and arrive at the linear system below

$$\vec{\varphi}^{\text{app}} = (\overleftrightarrow{1} + \Omega^2 \overleftrightarrow{\kappa}_{\text{cl}\delta})\vec{\delta} + (\overleftrightarrow{\kappa} + \Omega^2 \overleftrightarrow{\kappa}_{\text{cl}\iota})\vec{\iota}, \tag{4.30}$$

where

$$\overleftrightarrow{\kappa}_{\text{cl}\delta} = \begin{pmatrix} \kappa_{\text{cla}}(\kappa_a - 1) & \kappa_{\text{cla}}(\kappa_b - 1) \\ \kappa_{\text{clb}}(\kappa_a - 1) & \kappa_{\text{clb}}(\kappa_b - 1) \end{pmatrix}$$

$$\overleftrightarrow{\kappa}_{\text{cl}\iota} = \begin{pmatrix} \kappa_{\text{cla}}(\kappa_b\kappa_b^b + \kappa_a\kappa_a^b - \kappa_{\text{ia}}) & \kappa_{\text{cla}}(\kappa_a\kappa_a^a + \kappa_b\kappa_b^a - \kappa_{\text{ib}}) \\ \kappa_{\text{clb}}(\kappa_b\kappa_b^b + \kappa_a\kappa_a^b - \kappa_{\text{ia}}) & \kappa_{\text{clb}}(\kappa_a\kappa_a^a + \kappa_b\kappa_b^a - \kappa_{\text{ib}}) \end{pmatrix}$$

$$\vec{\varphi}^{\text{app}} = \begin{pmatrix} 1 + \kappa_\phi\kappa_{\text{cla}}\omega^2 \\ 1 + \kappa_\phi\kappa_{\text{clb}}\omega^2 \end{pmatrix} \phi^{\text{app}}$$

The linear limit solution is obtained from the rf component with $\vec{\iota}_{\text{rf}} = (\beta_{\text{rf}}\,\text{diag}(\cos\vec{\delta}_{\text{dc}}) + i\Omega\gamma - \Omega^2)\vec{\delta}_{\text{rf}}$,

$$\vec{\varphi}_{\text{rf}}^{\text{app}} = \overleftrightarrow{\chi}\vec{\delta}_{\text{rf}}, \tag{4.31}$$

$$\text{where}\overleftrightarrow{\chi} = \overleftrightarrow{1} + \Omega^2\overleftrightarrow{\kappa}_{\text{cl}\delta} + (\overleftrightarrow{\kappa} + \Omega^2\overleftrightarrow{\kappa}_{\text{cl}\iota})(\beta_{\text{rf}}\,\text{diag}(\cos\vec{\delta}_{\text{dc}}) + i\Omega\gamma - \Omega^2) \tag{4.32}$$

Similar to Sec.4.2.1.5, the resonance condition corresponds to $\det(\overleftrightarrow{\chi}) = 0$, and the resulting eigenfrequencis are plotted in Fig.4.11. As expected from the six degrees of freedom, there are three positive eigenfrequency solutions just as in Sec.4.2.1.5.

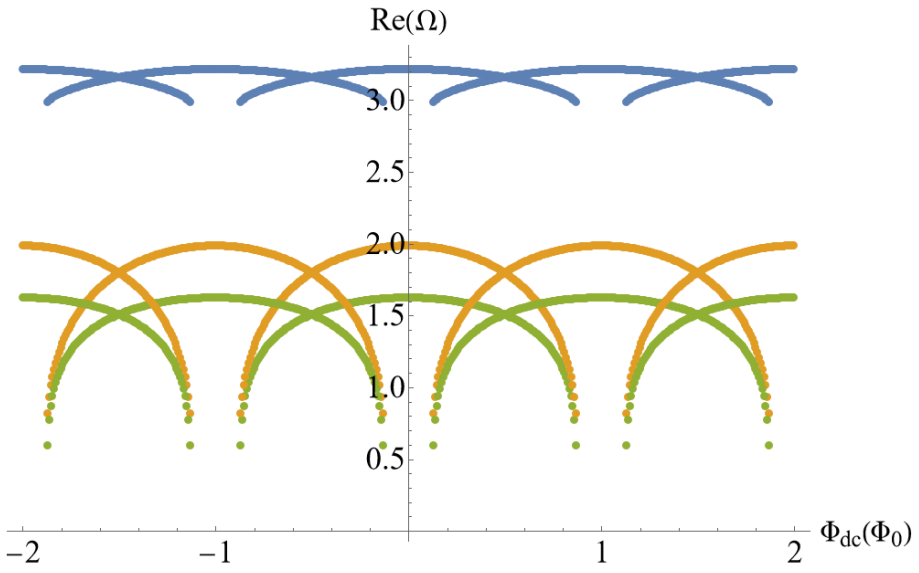

Figure 4.11: Real part of eigenfrequency solutions $Re(\Omega)$ from the characteristic equation $\det(\overleftrightarrow{\chi}) = 0$ in the linear limit for the one-branch model of the two edge-coupled SQUIDs, as a function of dc magnetic flux $\Phi_{\rm dc}$ in units of Φ_0.

However, due to the large overlapping loop in the center contributing to a larger inductance than the corner-coupled case, the highest frequency mode occurs at a lower frequency $\Omega \sim 3$ in the edge-coupled geometry.

Full nonlinear numerical solutions

The solution to the nonlinear system can be obtained numerically as in Sec.4.2.1.6, where the six variables for the equation of motions are $\delta_a,\ \delta_b,\ \dot{\delta}_a,\ \dot{\delta}_b,\ \iota_a,\ \dot{\iota}_a$. The

system of first-order initial value problems for the numerical solver is listed below:

$$\frac{d\delta_a}{d\tau} = \dot{\delta}_a \tag{4.33a}$$

$$\frac{d\delta_b}{d\tau} = \dot{\delta}_b \tag{4.33b}$$

$$\frac{d\dot{\delta}_a}{d\tau} = \ddot{\delta}_a = \iota_a - \beta_{\mathrm{rf}} \sin\delta_a - \gamma\dot{\delta}_a \tag{4.33c}$$

$$\frac{d\dot{\delta}_b}{d\tau} = \ddot{\delta}_b = (\kappa_{\delta a}(\phi^{\mathrm{app}} - \delta_a) + \kappa_{\delta b}(\phi^{\mathrm{app}} - \delta_b) - \kappa_{\iota a}\iota_a)/\kappa_{\iota b} - \beta_{\mathrm{rf}} \sin\delta_b - \gamma\dot{\delta}_b \tag{4.33d}$$

$$\frac{d\iota_a}{d\tau} = \dot{\iota}_a \tag{4.33e}$$

$$\frac{d\dot{\iota}_a}{d\tau} = \ddot{\iota}_a(\delta_a, \delta_b, \dot{\delta}_a, \dot{\delta}_b, \iota_a, \ddot{\phi}^{\mathrm{app}}, \phi^{\mathrm{app}}), \tag{4.33f}$$

where the last line is the solution of $\ddot{\iota}_a$ from the constraint Eq.(4.25) and the flux quantization for loop a, Eq.(4.27) whose numerical form is given as

$$\ddot{\iota}_a(\delta_a, \delta_b, \dot{\delta}_a, \dot{\delta}_b, \iota_a, \ddot{\phi}^{\mathrm{app}}, \phi^{\mathrm{app}}) =$$

$$-9.09\delta_a + 1.04\delta_b + 4.49\sin\delta_a - 3.47\sin\delta_b + 0.028\dot{\delta}_a - 0.022\dot{\delta}_b - 10.3\iota_a + 1.12\ddot{\phi}^{\mathrm{app}} + 8.05\phi^{\mathrm{app}}.$$

The transmission at low rf power from the numerical solution with the applied dc flux swept from $1\Phi_0$ to 0 is plotted in Fig. 4.12 which follows the predicted frequency tuning from the linear-limit calculation.

4.2.2.2 Two branches for the overlapping capacitors in the two edge-coupled SQUIDs model

A more complex model where the transmission line consists of three capacitor nodes, and two inductance segments for each side of the transmission line is considered in this section. There are now five independent loops to apply Faradays' law

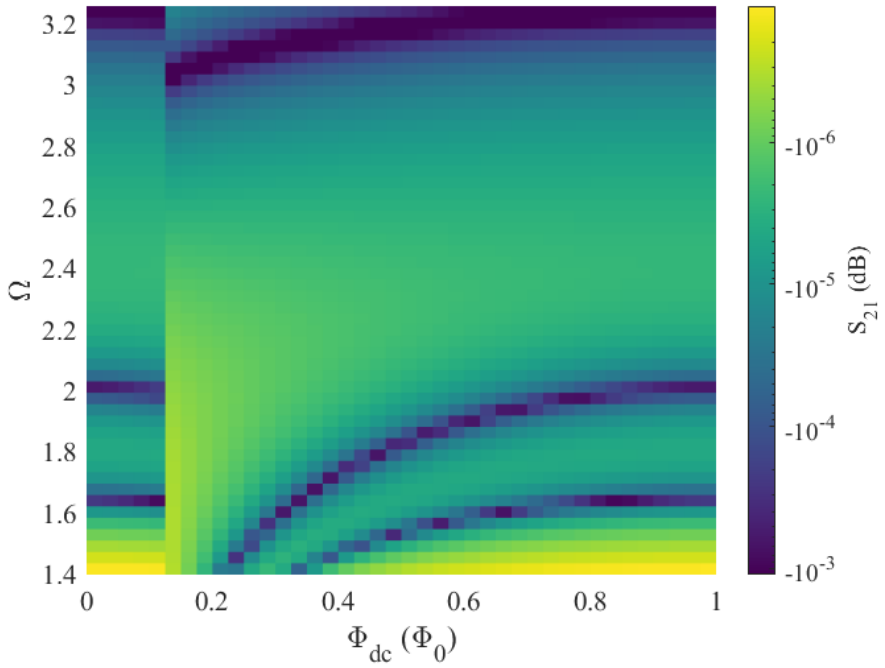

Figure 4.12: The magnitude of transmission calculated from the nonlinear solution to the one-branch model for the two edge-coupled SQUIDs at $\Phi_{\rm rf} \sim 10^{-3}\Phi_0$, as a function of applied dc flux $\Phi_{\rm dc}$ from $1\Phi_0$ to 0.

and the flux quantization. The resulting induced flux linkage for each segment is summarized blow.

$$\begin{pmatrix} \Phi_a \\ \Phi_b \\ \Phi_{ab} \\ \Phi_{a1b1} \\ \Phi_{a2b2} \end{pmatrix} = \begin{pmatrix} L_a & M_b & L_{a1} & M_{b1} & L_{\rm comm} & 0 \\ M_a & L_b & M_{a1} & L_{b1} & L_{\rm comm} & 0 \\ L'_a & L'_b & M'_{a1} & M'_{b1} & M_{\rm comm} & 0 \\ M''_a & M''_b & L''_{a1} & L''_{b1} & M_{\rm comm} & 0 \\ 0 & 0 & 0 & 0 & 0 & L_{a2b2} \end{pmatrix} \begin{pmatrix} I_a \\ I_b \\ I_{a1} \\ I_{b1} \\ I_{\rm comm} \\ I_{\rm diff2} \end{pmatrix} \tag{4.34}$$

where the current $I_{\rm diff2}$ is the difference between the currents on loop a and loop b for segment $a2$, $b2$. For the same SQUID loops geometry as in Sec. 4.2.2.1, the

inductances associated with the new side loop $a2-b2$ are calculated as $L_{a2b2} = 0.176$ pH. And as discussed previously, the mutual inductance between the side loops and

Similar to the one-branch overlapping capacitors model in Sec. 4.2.2.1, the non-junction branch currents and voltages are obtained from the flux relations. There are two flux equations for the two SQUID loops, Eq. 4.35a and 4.35b, and another two equations from Faraday's law of the non-continuous loops $a-b$, Eq.4.35c and $a1-b1$, Eq.4.35d. In addition, since there are three nodes and two segments for the transmission line, two side loops $a2-b2$ and $a3-b3$ are formed. Therefore, one additional equation from the Faraday's law on one of the side loop (loop $a2-b2$ is chosen here without loss of generality) is needed, Eq.4.35e.

$$\Phi_a^{\text{app}} = \frac{\Phi_0}{2\pi}\delta_a + \Phi_a \tag{4.35a}$$

$$\Phi_b^{\text{app}} = \frac{\Phi_0}{2\pi}\delta_b + \Phi_b \tag{4.35b}$$

$$V_a - 2V_3 - V_b = \dot{\Phi}_{ab}^{\text{app}} - \dot{\Phi}_{ab} \tag{4.35c}$$

$$-2V_1 = \dot{\Phi}_{a1b1}^{\text{app}} - \dot{\Phi}_{a1b1} \tag{4.35d}$$

$$V_1 - V_2 = -\dot{\Phi}_{a2b2} \tag{4.35e}$$

Additionally from the current conservation laws applied to the three nodes, the currents can be expressed as

$$I_{\text{diff2}} = I_{b2} - I_{a2} = I_{b1} + c\dot{V}_1 - (I_{a1} - c\dot{V}_1) = I_{b1} - I_{a1} + 2c\dot{V}_1 \tag{4.36a}$$

$$I_{a1} = I_a + c(\dot{V}_1 + \dot{V}_2 + \dot{V}_3) \tag{4.36b}$$

$$I_{b1} = I_b - c(\dot{V}_1 + \dot{V}_2 + \dot{V}_3) \tag{4.36c}$$

where $c = C_{ov}/3$ is the capacitance on each node.

The same expressions for $I_{a1}(I_a, I_b, \delta_a, \delta_b)$, $I_{b1}(I_a, I_b, \delta_a, \delta_b)$, $V_1(\dot{I}_a, \dot{I}_b, \dot{\delta}_a, \dot{\delta}_b)$, $V_3(\dot{I}_a, \dot{I}_b, \dot{\delta}_a, \dot{\delta}_b)$ as in Eq.(4.23,4.24) are obtained, where V_3 corresponds to V_2 in Sec.4.2.2.1. Consequently, I_{diff2} can be expressed in terms of $\delta_{a,b}$, $I_{a,b}$ and their time derivatives. With all the other quantities known, V_2 can be solved as

$$V_2 = V_1 + L_{a2b2}\dot{I}_{\text{diff2}}(\dot{I}_a, \dot{I}_b, \dot{\delta}_a, \dot{\delta}_b, \dddot{I}_a, \dddot{I}_b, \dddot{\delta}_a, \dddot{\delta}_b) \tag{4.37}$$

This expression can then be substituted in Eq. 4.36c to solve for I_{a1}, which contains a term of $\ddddot{I}$, or $d^6\delta/d\tau^6$. Therefore, the equation of motions for the SQUIDs are 6th-order differential equations in time.

Full nonlinear numerical solutions

As in the previous cases, the constraint on I_a, I_b, δ_a, δ_b gives the expression $I_b(I_a, \delta_a, \delta_b)$. With $I_b, \dot{I}_b, \ddot{I}_b, \dddot{I}_b$ known, the degree of freedom is reduced from 12 (sixth-order equation of motions for two SQUIDs) to 8 (sixth order equation of motion for SQUID a and only two independent degrees of freedom: δ_b, $\dot{\delta}_b$ in loop b). In addition, we should reduce the equations to dimensionless forms for the convenience of the numerical solver by introducing the dimensionless voltage $u_2 = 2\pi V_2/(\Phi_0\omega_{\text{geo}})$. The final equation of motions for the numerical solver can then be

expressed by eight variables : $\delta_a,\ \dot{\delta}_a,\ \delta_b,\ \dot{\delta}_b,\ \iota_a,\ \dot{\iota}_a,\ \ddot{\iota}_a,\ u_2$ as follows

$$\frac{d\delta_a}{d\tau} = \dot{\delta}_a \tag{4.38a}$$

$$\frac{d\delta_b}{d\tau} = \dot{\delta}_b \tag{4.38b}$$

$$\frac{d\dot{\delta}_a}{d\tau} = \ddot{\delta}_a = \iota_a - \beta_{\mathrm{rf}} \sin\delta_a - \gamma\dot{\delta}_a \tag{4.38c}$$

$$\frac{d\dot{\delta}_b}{d\tau} = \ddot{\delta}_b = (\kappa_{\delta a}(\phi^{\mathrm{app}} - \delta_a) + \kappa_{\delta b}(\phi^{\mathrm{app}} - \delta_b) - \kappa_{\iota a}\iota_a)/\kappa_{\iota b} - \beta_{\mathrm{rf}} \sin\delta_b - \gamma\dot{\delta}_b \tag{4.38d}$$

$$\frac{d\iota_a}{d\tau} = \dot{\iota}_a \tag{4.38e}$$

$$\frac{d\dot{\iota}_a}{d\tau} = \ddot{\iota}_a \tag{4.38f}$$

$$\frac{d\ddot{\iota}_a}{d\tau} = \dddot{\iota}_a = (u_2 - \kappa_{3\mathrm{d}\delta a}\dddot{\delta}_a - \kappa_{3\mathrm{d}\delta b}\dddot{\delta}_b - \kappa_{\mathrm{d}\delta a}\dot{\delta}_a - \kappa_{\mathrm{d}\delta b}\dot{\delta}_b -$$

$$\kappa_{\mathrm{d}\iota a}\dot{\iota}_a - \kappa_{3\mathrm{d}\phi\mathrm{app}}\dddot{\phi}^{\mathrm{app}} - \kappa_{\mathrm{d}\phi\mathrm{app}}\dot{\phi}^{\mathrm{app}})/\kappa_{3\mathrm{d}\iota a} \tag{4.38g}$$

$$\frac{du_2}{d\tau} = \kappa_{\mathrm{cov}}^{-1}(\iota_{a1} - \iota_a - \kappa_{\mathrm{cov}}(\dot{u}_1 + \dot{u}_3)) \tag{4.38h}$$

where $\dddot{\delta}_{a,b}$ can be obtained from taking another time derivative on Eq. 4.38c, 4.38d. The numerical values for the factors are as follows $\kappa_{3\mathrm{d}\delta a} = 5.9\times10^{-4},\ \kappa_{3\mathrm{d}\delta b} = -4.5\times 10^{-4}$, $\kappa_{\mathrm{d}\delta a} = 0.592$, $\kappa_{\mathrm{d}\delta b} = -0.457,\ \kappa_{\mathrm{d}\iota a} = 0.403,\ \kappa_{3\mathrm{d}\phi\mathrm{app}} = -4.5\times10^{-4},\ \kappa_{\mathrm{d}\phi\mathrm{app}} = -0.453,\ \kappa_{3\mathrm{d}\iota a} = 4.0\times10^{-4},\ \kappa_{\mathrm{cov}} = 0.407$. The resulting transmission from the numerical solution done with applied dc flux swept from $1\Phi_0$ to 0 is plotted in Fig.4.13. The resonance in the calculated transmission coincide with those in Fig.4.12 for the one-branch model, which is expected since the transmission lines formed by the overlapping capacitors are very short compared to the wavelength.

We should note that instead of using $\ddot{\iota}_a$, the equations of motion are expressed in u_2 using Eq.(4.37) to simplify the calculation. This substitution motivates us to consider nodal voltages as the variables for the equations of motion. In fact, it is

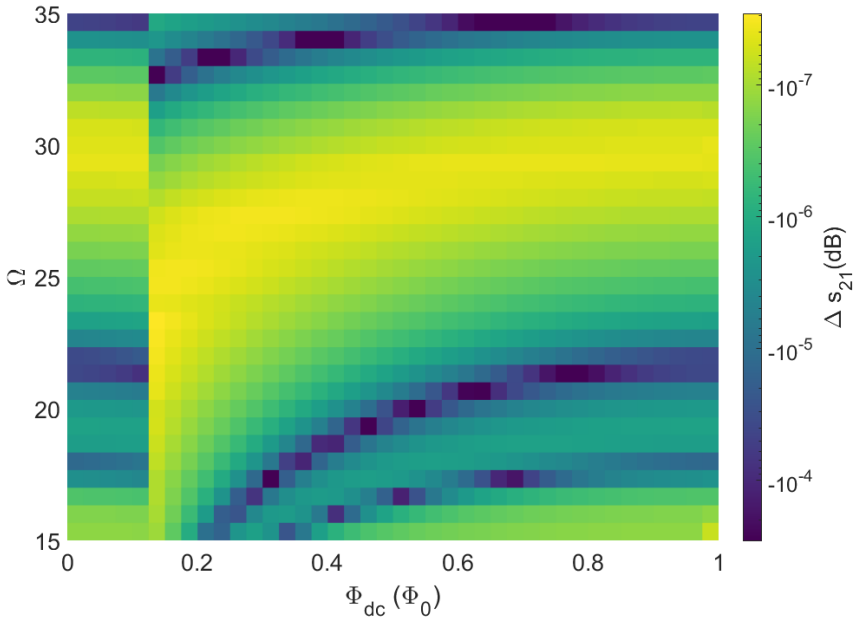

Figure 4.13: The magnitude of transmission calculated from the nonlinear solution to the two-branch model for the two edge-coupled SQUIDs at $\Phi_{\mathrm{rf}} \sim 10^{-3}\Phi_0$, as a function of applied dc flux Φ_{dc} from $1\Phi_0$ to 0.

discussed in the later section (Sec.4.2.3) that formulating the problem with only gauge-invariant phase differences and the voltages is a more general approach to solve any sized overlapping SQUID system compared to the formalism with the junction currents outlined so far.

Linear-limit solutions

Inspired by the previous discussion, we will now attempt to find the linear-limit solution for the two-branch model of two edge-coupled SQUIDs using voltages as the variables. The voltages needed for expressing the non-junction branch currents are $V = V_1 + V_2 + V_3$ and $v = V_2 + V_3$, since $I_{a1} = I_a + c(\dot{V}_1 + \dot{V}_2 + \dot{V}_3)$, $I_{b1} = I_b - c(\dot{V}_1 + \dot{V}_2 + \dot{V}_3)$, and $I_{\text{diff2}} = I_b - I_a - 2c(\dot{V}_2 + \dot{V}_3)$. We can rearrange the three Faraday's laws in Eq.(4.35e) as follows:

$$V_a - V_b - 2v = \dot{\Phi}^{\text{app}}_{ab} + \dot{\Phi}^{\text{app}}_{a1b1} - \dot{\Phi}_{ab} - \dot{\Phi}_{a1b1} - \dot{\Phi}_{a2b2}$$

$$V_a - V_b - 2V = 2\dot{\Phi}^{\text{app}}_{a1b1} + \dot{\Phi}^{\text{app}}_{ab} - 2\dot{\Phi}_{a1b1} - \dot{\Phi}_{ab} - 2\dot{\Phi}_{a2b2}$$

Combined with the flux quantization equations in Eq.(4.35e), we have obtained a 4×4 system in the dimensionless form:

$$\begin{pmatrix} \phi^{\text{app}} \\ \phi^{\text{app}} \\ \dot{\phi}^{\text{app}}_{ab} + \dot{\phi}^{\text{app}}_{a1b1} \\ 2\dot{\phi}^{\text{app}}_{a1b1} + \dot{\phi}^{\text{app}}_{ab} \end{pmatrix} = \begin{pmatrix} \delta_a + \phi_a(\delta_a, \delta_b, U) \\ \delta_b + \phi_b(\delta_a, \delta_b, U) \\ \dot{\phi}_{ab}(\delta_a, \delta_b, U) + \dot{\phi}_{a1b1}(\delta_a, t\delta_b, U) + \dot{\phi}_{a2b2}(\delta_a, \delta_b, u) + \dot{\delta}_a - \dot{\delta}_b - 2u \\ \dot{\phi}_{ab}(\delta_a, \delta_b, U) + 2\dot{\phi}_{a1b1}(\delta_a, \delta_b, U) + 2\dot{\phi}_{a2b2}(\delta_a, \delta_b, u) + \dot{\delta}_a - \dot{\delta}_b - 2U \end{pmatrix}, \tag{4.39}$$

where $u = 2\pi v/(\Phi_0\omega_{\text{geo}})$ and $U = 2\pi v/(\Phi_0\omega_{\text{geo}})$ are the dimensionless voltages. After applying the weak rf field approximation and Fourier transform, the linear

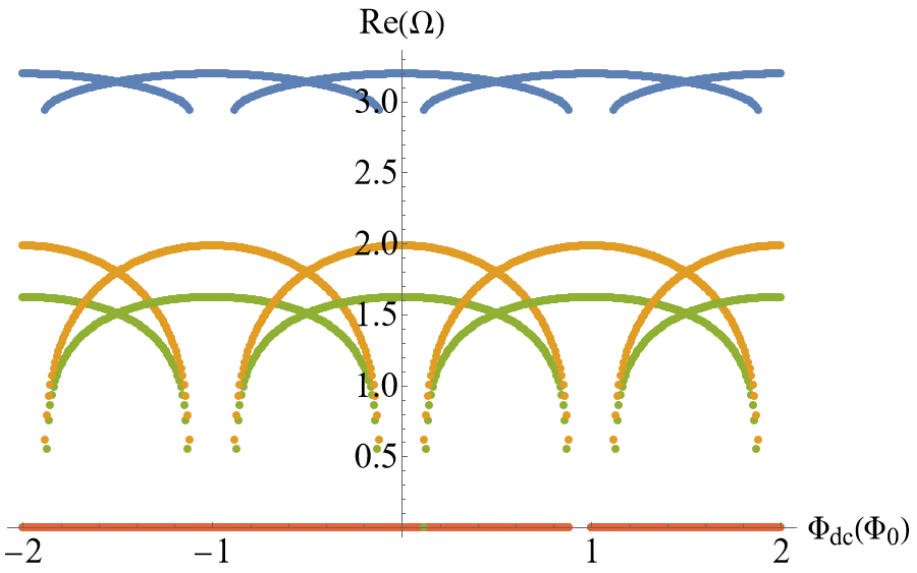

Figure 4.14: Real part of eigenfrequency solutions $Re(\Omega)$ from the characteristic equation in the linear limit for the two-branch model of the two edge-coupled SQUIDs, as a function of dc magnetic flux $\Phi_{\rm dc}$ in units of Φ_0.

form of the system becomes

$$\begin{pmatrix} \phi^{\rm app} \\ \phi^{\rm app} \\ \dot{\phi}^{\rm app}_{ab} + \dot{\phi}^{\rm app}_{a1b1} \\ 2\dot{\phi}^{\rm app}_{a1b1} + \dot{\phi}^{\rm app}_{ab} \end{pmatrix} = \begin{pmatrix} 1+\hat{\imath}_{a,\rm rf} & \kappa_1\hat{\imath}_{b,\rm rf} & i\kappa_{aU}\Omega & 0 \\ \kappa_1\hat{\imath}_{a,\rm rf} & 1+\hat{\imath}_{b,\rm rf} & i\kappa_{bU}\Omega & 0 \\ i\Omega + i\kappa_{ua}\Omega\hat{\imath}_{a,\rm rf} & -i\Omega + i\kappa_{ub}\Omega\hat{\imath}_{b,\rm rf} & \kappa_{uU}\Omega^2 & -2+\kappa_{uu}\Omega^2 \\ i\Omega + i\kappa_{Ua}\hat{\imath}_{a,\rm rf} & -i\Omega + i\kappa_{Ub}\hat{\imath}_{b,\rm rf} & -2+\kappa_{UU}\Omega^2 & \kappa_{Uu}\Omega^2 \end{pmatrix} \begin{pmatrix} \delta_a \\ \delta_b \\ U \\ u \end{pmatrix}, \tag{4.40}$$

where $\hat{\imath}_{a,\rm rf} = i\gamma\Omega - \Omega^2 + \beta_{\rm rf}\cos\delta_{a,\rm dc}$, $\hat{\imath}_{b,\rm rf} = i\gamma\Omega - \Omega^2 + \beta_{\rm rf}\cos\delta_{b,\rm dc}$, $\kappa_{aU} = 0.0631$, $\kappa_{bU} = -0.256$, $\kappa_{ua} = 0.449$, $\kappa_{ub} = 0.49$, $\kappa_{uU} = 0.294$, $\kappa_{uu} = 0.001$, $\kappa_{Ua} = 0.293$, $\kappa_{Ub} = 1.11$, $\kappa_{UU} = 0.6$, $\kappa_{Uu} = 0.002$. Again imposing the resonant condition that requires a singular response matrix, we can solve the characteristic equation for the eigenfrequencies Ω whose real parts are shown in Fig.4.14. As a consequence of

the short transmission lines formed by the overlapping capacitors, the two-branch model gives the same eigenfrequency values as the one-branch model except for the purely imaginary eigenfrequency shown in red in the eigenfrequency plot, Fig.4.14 . Therefore, the one branch-model would be sufficient to model the edge-coupled SQUIDs.

4.2.3 A more general formalism for larger systems of overlapping SQUIDs

Building upon the formalism developed for the two corner-coupled SQUIDs in sections 4.2.1-4.2.1.7, we now consider the larger systems of overlapping SQUIDs as exemplified in Fig. 4.15. One major difference in the larger systems compared to two corner-coupled SQUIDs is the introduction of a new kind of circuit loop enclosing an area outside any galvanically connected SQUID loop. To better distinguish the different loop circuits in the large systems, and to streamline the discussion, some common vocabulary should be established. Highlighted in blue in Fig. 4.15 (a) is a new loop, named the "extra-SQUID" loop, while the loop formed at the corners of two overlapping SQUIDs, as studied in the two-SQUID case, is referred to as a "partial loop", colored red in Fig. 4.15 (a). Together with the conventional galvanically-connected SQUID loops, these three types of loop circuits dictate the dynamics of the gauge-invariant phases through either Faraday's law (e.g. Eq. (4.2)), or the flux quantization condition in the SQUID loop (e.g. Eq. (3.20)).

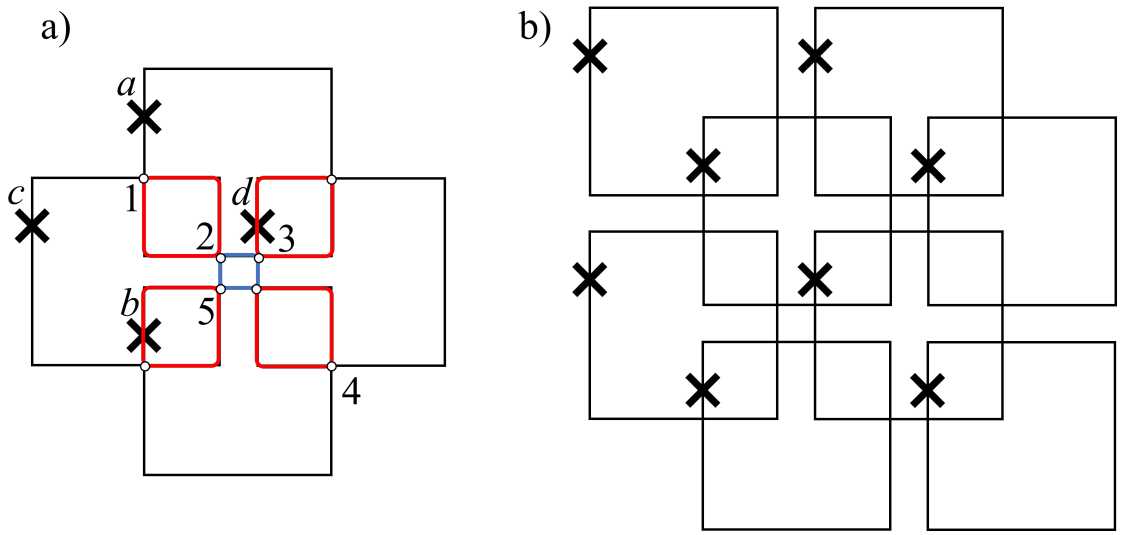

Figure 4.15: Schematics for larger overlapping SQUID systems. For any corner-coupled overlapping system, there are three different types of loops involved in the dynamics of the gauge-invariant phases: the galvanically-connected SQUID loops (black lines), the partial loops (highlighted in red), and the extra-SQUID loops (highlighted in blue). a) The minimal system that contains all three different types of circuits is the four corner-coupled SQUIDs. b) represents a typical square array of $N \times N \times 2$ SQUIDs (here with $N = 2$)). An array with $N = 12$ has been characterized experimentally in this work.

Another challenge in modelling the larger system is the fact that each SQUID loop is broken into many segments by the additional capacitive nodes formed by the overlap with wiring of several neighboring SQUIDs. For instance, each SQUID in Fig. 4.15 (a) has 4 capacitor nodes and thus 4 segments. There are in total 16 segments, each with a different current. Attempting to follow a similar treatment to that used for the two corner-coupled SQUIDs in Sec.4.2.1, one would need to ex-

press the 12 non-junction currents in terms of 4 junction currents, 4 gauge-invariant phase differences and their time derivatives. The number of unknown currents can be further reduced by invoking current conservation laws on the SQUID loops requiring zero net current into any SQUID. The constraints need to be applied to all SQUID loops but one, since the net current into the last SQUID is equal to the net current leaving the rest of the SQUID loops which is already zero due to the current conservation laws. The number of independent non-junction currents is thus $12 - (4 - 1) = 9$, which still could not be completely determined from 4 flux quantization conditions (Eq. (3.20)) from the 4 SQUID loops. We should note that applying Faraday's laws to the 5 non-SQUID loops only relates the time derivatives of the currents, not the currents themselves.

To circumvent this problem, the model should be reformulated in terms of the voltages across the capacitor nodes as the variables instead of the junction currents as done in Sec.4.2.1. This choice of variables is natural considering the Lagrangian of a circuit where flux and voltage substitute for position and velocity in the formalism. The junction currents are expressed using the RCSJ model in Eq. (3.3) in terms of the set of $\vec{\delta}$, and their time derivatives. The non-junction currents are obtained from current conservation laws on the capacitor nodes (e.g. Eq. 4.3). For the four corner-coupled SQUIDs in Fig. 4.15 (a), there are in total 8 capacitor nodes. Due to the current conservation laws mentioned above, the number of independent voltages is reduced to 5, corresponding to the number of non-SQUID loops. This system can then be set up and solved analytically as demonstrated in Sec. 4.2.6. This voltage formalism turns out to be a more general approach for

modeling overlapping SQUIDs compared to the current formalism followed in Sec. 4.2.1 for the two corner-coupled SQUIDs. The following section 4.2.4 illustrates the application of the voltage formalism to the two corner-coupled SQUIDs, and arrives at the same eigenfrequency solutions as found in Sec. 4.2.1.

4.2.4 Voltage formalism for two corner-coupled SQUIDs

Due to its simple geometry, the model for two corner-coupled SQUIDs can be completely expressed through the currents in each wiring segment, as discussed in Sec. 4.2.1. Here we present the alternative method to set up and solve the equations of motion using the more general voltage formalism. This approach is convenient for modelling larger arrays of capacitively coupled rf SQUIDs.

The junction currents $I_{a0,b0}$ can be expressed in terms of $\delta_{a,b}$ and $\dot{V}_1$ from the equation of motion, Eq. (4.12):

$$\begin{aligned}
\begin{pmatrix} I_{a0} \\ I_{b0} \end{pmatrix} &= \overleftrightarrow{L}^{-1} \\
\begin{pmatrix} C_{\mathrm{ov}} L_{\delta a} \dot{V}_1 - \Phi_0 \delta_a/(2\pi) + \Phi_{\mathrm{app}} \\ -C_{\mathrm{ov}} L_{\delta b} \dot{V}_1 - \Phi_0 \delta_b/(2\pi) + \Phi_{\mathrm{app}} \end{pmatrix} & \\
\begin{pmatrix} \iota_{a0} \\ \iota_{b0} \end{pmatrix} &= \overleftrightarrow{\kappa}^{-1} \\
\begin{pmatrix} 2\lambda_{\mathrm{cov}} \kappa_{\delta a} \dot{u}_1 - \delta_a + \phi_{\mathrm{app}} \\ -2\lambda_{\mathrm{cov}} \kappa_{\delta b} \dot{u}_1 - \delta_b + \phi_{\mathrm{app}} \end{pmatrix} &
\end{aligned} \tag{4.41}$$

where the second equation is the dimensionless form, with $u_1 = 2\pi V_1/(\Phi_0 \omega_{\rm geo})$, and $\overleftrightarrow{L} = L_{\rm geo}\overleftrightarrow{\kappa} = \begin{pmatrix} L_{\rm geo} & M \\ M & L_{\rm geo} \end{pmatrix}$. We can then substitute the time derivative of Eq. (4.41) into Faraday's laws, Eq. (4.2) and obtain the expression for $\ddot{u}_1(\dot{\delta}_a, \dot{\delta}_b, u_1)$:

$$\begin{aligned}
\ddot{u}_1 = [\dot{\phi}^{\rm app}_{\rm cen} - \dot{\phi}^{\rm app}(M_{{\rm cen},a} + M_{{\rm cen},b})/(L+M) \\
+\dot{\delta}_a(LM_{{\rm cen},a} - MM_{{\rm cen},b})/(L^2 - M^2) + \\
\dot{\delta}_b((LM_{{\rm cen},b} - MM_{{\rm cen},a})/(L^2 - M^2) - 1) + 2u_1] \\
(2\lambda_{\rm cov}/L[(M_{{\rm cen},b1} - L_{{\rm cen},a1}) + \\
((LM_{{\rm cen},b} - MM_{{\rm cen},a})(M_{b,a1} - L_{b,b1}) \\
+(LM_{{\rm cen},a} - MM_{{\rm cen},b})(L_{a,a1} - M_{a,b1}))/(L^2 - M^2)])^{-1}
\end{aligned}$$

where $M_{{\rm cen},a} = L_{{\rm cen},a1} + M_{{\rm cen},a0}$, $M_{{\rm cen},b} = L_{{\rm cen},b0} + M_{{\rm cen},b1}$, and $L_{\rm geo}$ is abbreviated as L. Consequently, the equation of motion can be fully expressed in terms of a new set of six variables, $\delta_{a,b},\ \dot{\delta}_{a,b},\ u_1,$ and $\dot{u}_1$. One can therefore set up the six first-order initial value problems for the numerical solver in the following manner:

$$\frac{d\delta_a}{d\tau} = \dot{\delta}_a \tag{4.42a}$$

$$\frac{d\delta_b}{d\tau} = \dot{\delta}_b \tag{4.42b}$$

$$\frac{d\dot{\delta}_a}{d\tau} = \iota_{a0}(\delta_a, \delta_b, \dot{u}_1) - \beta_{\rm rf}\sin\delta_a - \gamma\dot{\delta}_a \tag{4.42c}$$

$$\frac{d\dot{\delta}_b}{d\tau} = \iota_{b0}(\delta_a, \delta_b, \dot{u}_1) - \beta_{\rm rf}\sin\delta_b - \gamma\dot{\delta}_b \tag{4.42d}$$

$$\frac{du_1}{d\tau} = \dot{u}_1 \tag{4.42e}$$

$$\frac{d\dot{u}_1}{d\tau} = \ddot{u}_1(\dot{\delta}_a, \dot{\delta}_b, u_1) \tag{4.42f}$$

We can appreciate immediately the simplicity of the voltage formalism. By introducing the nodal voltage V_1 as a variable, we eliminate the need for the constraint on the currents, and the symmetry between the two loops a and b is restored.

Let's now examine the linear limit approximation for this problem. Consider the solutions in the following form $\vec{\delta} = \vec{\delta}_{\rm rf}(t) + \vec{\delta}_{\rm dc}$, $\vec{\delta}_{\rm rf}(t) = \hat{\vec{\delta}}_{\rm rf} \exp(i\Omega\tau)$, and $u_1(t) = \hat{u}_1 \exp(i\Omega\tau)$, where $\hat{\vec{\delta}}_{\rm rf} = (\hat{\delta}_a, \hat{\delta}_b)$. Substituting these expressions in the equation of motion Eq. (4.8) and Faraday's law, Eq. (4.2), and rearranging the excitation to the left hand side of the equations, one can obtain a linear system in $(\hat{\delta}_a, \hat{\delta}_b, \hat{u}_1)$:

$$\begin{gathered}
\vec{\phi}_{\rm dc} = \vec{\delta}_{\rm dc} + \beta_{\rm rf} \overleftrightarrow{\kappa} \sin \vec{\delta}_{\rm dc} \\
\begin{pmatrix} \phi_{\rm rf} \\ \phi_{\rm rf} \\ \dot{\phi}_{\rm rf,cen} \end{pmatrix} = \overleftrightarrow{\chi} \cdot \begin{pmatrix} \hat{\delta}_a \\ \hat{\delta}_b \\ \hat{u}_1 \end{pmatrix}
\end{gathered} \tag{4.43}$$

where

$$\overleftrightarrow{\chi} = \begin{pmatrix} 1 + \hat{\iota}_{{\rm rf},a0} & \kappa_1 \hat{\iota}_{{\rm rf},a0} & i\Omega \frac{M_{{\rm cen},a0} + L_{{\rm cen},a1}}{L_{\rm geo}} \hat{\iota}_{{\rm rf},a0} \\ \kappa_1 \hat{\iota}_{{\rm rf},b0} & 1 + \hat{\iota}_{{\rm rf},a0} & i\Omega (\frac{L_{{\rm cen},b0} + M_{{\rm cen},b1}}{L_{\rm geo}} \hat{\iota}_{{\rm rf},b0} + 1) \\ -2i\lambda_{\rm cov}\kappa_{\delta a}\Omega & 2i\lambda_{\rm cov}\kappa_{\delta b}\Omega & -2 + 2\lambda_{\rm cov} \frac{L_{{\rm cen},a1} - M_{{\rm cen},b1}}{L_{\rm geo}} \Omega^2 \end{pmatrix}^T$$

and $\hat{\vec{\iota}}_{\rm rf} = \beta_{\rm rf} \cos \vec{\delta}_{\rm dc} + i\gamma\Omega - \Omega^2$. The resonance condition for the system is $\det(\overleftrightarrow{\chi} = 0)$, which can be solved for Ω to obtain the eigen solutions to the two corner-coupled SQUIDs.

4.2.5 The general strategy for modelling a system of overlapping SQUIDs

As discussed in Sec. 4.2.3, the voltage formalism can be applied to any size of corner-coupled overlapping SQUIDs array. Here, we outline the procedure for setting up the equations of motion for a system of corner-coupled SQUIDs in any general geometry. The first step in studying the dynamics is to identify the independent variables, which are $\vec{\delta}$ from the junctions, $\vec{V}$ from the overlapping capacitors, and their time derivatives. We can then express the induced fluxes in the system as

$$\begin{pmatrix} \vec{\Phi}^{\text{ind}}_{\text{SQUID}} \\ \\ \vec{\Phi}^{\text{ind}}_{\text{non-SQUID}} \end{pmatrix} = \overleftrightarrow{L}\overleftrightarrow{I}_{\text{con}} \begin{pmatrix} \vec{I}_{\text{JJ}} \\ \\ c\dot{\vec{V}} \end{pmatrix} \tag{4.44}$$

where $\overleftrightarrow{L}$ is the inductance matrix whose i, j the element describes the flux on the loop i induced by the segment j, and $\overleftrightarrow{I}_{\text{con}}$ is the matrix that expresses the currents in each branch in terms of junction currents $\vec{I}_{\text{JJ}}$ and the displacement currents through the capacitor nodes $c\dot{\vec{V}}$. Next, the same flux relations in the conventional RCSJ model (Sec. 3.1) are invoked here for each SQUID

$$\vec{\Phi}^{\text{app}}_{\text{SQUID}} - \vec{\Phi}^{\text{ind}}_{\text{SQUID}} = \frac{\Phi_0}{2\pi}\vec{\delta} \tag{4.45}$$

which can be solved for junction currents $\vec{I}_{\text{JJ}}(\vec{\delta}, \dot{\vec{V}})$. The non-SQUID loops, on the other hand, are described by Faraday's law in the following form

$$\dot{\vec{\Phi}}^{\text{app}}_{\text{non-SQUID}} - \dot{\vec{\Phi}}^{\text{ind}}_{\text{non-SQUID}} = \overleftrightarrow{V}_{\text{con}} \begin{pmatrix} \Phi_0/(2\pi)\dot{\vec{\delta}} \\ \\ \vec{V} \end{pmatrix} \tag{4.46}$$

where $\overleftrightarrow{V}_{\text{con}}$ is the matrix that associates the junction voltages $\Phi_0/(2\pi)\dot{\vec{\delta}}$ and voltages across the capacitor nodes $\vec{V}$ to each Faraday loop. After substituting the expression for $\vec{I}_{\text{JJ}}(\vec{\delta}, \dot{\vec{V}})$ into Eq. (4.46), the second time derivatives of the capacitor voltages, $\ddot{\vec{V}}(\dot{\vec{\delta}}, \vec{V})$ are obtained. Consequently, we can formulate the final dimensionless equations of motion in terms of $(\vec{\delta}, \dot{\vec{\delta}}, \vec{V}, \dot{\vec{V}})$:

$$\frac{d\vec{\delta}}{d\tau} = \dot{\vec{\delta}} \tag{4.47a}$$

$$\frac{d\dot{\vec{\delta}}}{d\tau} = \ddot{\vec{\delta}} = \vec{\iota}_{\text{JJ}}(\vec{\delta}, \dot{\vec{u}}) - \beta_{\text{rf}} \sin(\vec{\delta}) - \gamma\dot{\vec{\delta}} \tag{4.47b}$$

$$\frac{d\vec{u}}{d\tau} = \dot{\vec{u}} \tag{4.47c}$$

$$\frac{d\dot{\vec{u}}}{d\tau} = \ddot{\vec{u}}(\dot{\vec{\delta}}, \vec{u}) \tag{4.47d}$$

4.2.6 Four corner-coupled SQUIDs

With reference to the system shown in Fig. 4.15 (a), the dynamics of the system is now described by the 4 gauge-invariant phase differences $\delta_{a,b,c,d}$ and their time derivatives, as well as 5 independent capacitor nodal voltages $V_{1,2,3,4,5}$ and their time derivatives. The voltages across the rest of the capacitor nodes can be expressed in terms of $V_{1,2,3,4,5}$ through the current conservation laws inside each continuous SQUID loop. Applying Faraday's law to the non-SQUID loops and flux quantization conditions to the SQUID loops, we obtain the following system of

equations of motion.

$$\begin{pmatrix} \Phi_a^{\text{app}} \\ \Phi_b^{\text{app}} \\ \Phi_c^{\text{app}} \\ \Phi_d^{\text{app}} \\ \dot{\Phi}_{ac}^{\text{app}} \\ \dot{\Phi}_{ad}^{\text{app}} \\ \dot{\Phi}_{bc}^{\text{app}} \\ \dot{\Phi}_{bd}^{\text{app}} \\ \dot{\Phi}_{abcd}^{\text{app}} \end{pmatrix} = \begin{pmatrix} \Phi_0\delta_a/(2\pi) + \Phi_a^{\text{ind}}(\vec{I}, \dot{\vec{V}}) \\ \Phi_0\delta_b/(2\pi) + \Phi_b^{\text{ind}}(\vec{I}, \dot{\vec{V}}) \\ \Phi_0\delta_c/(2\pi) + \Phi_c^{\text{ind}}(\vec{I}, \dot{\vec{V}}) \\ \Phi_0\delta_d/(2\pi) + \Phi_d^{\text{ind}}(\vec{I}, \dot{\vec{V}}) \\ -V_1 + V_2 + \dot{\Phi}_{ac}^{\text{ind}}(\dot{\vec{I}}, \ddot{\vec{V}}) \\ V_d - V_3 - (V_1 + V_2 + V_3) + \dot{\Phi}_{ad}^{\text{ind}}(\dot{\vec{I}}, \ddot{\vec{V}}) \\ V_b - (V_1 + V_2 + V_5) - V_5 + \dot{\Phi}_{bc}^{\text{ind}}(\dot{\vec{I}}, \ddot{\vec{V}}) \\ (V_1 + V_2 - V_4) - V_4 + \dot{\Phi}_{bd}^{\text{ind}}(\dot{\vec{I}}, \ddot{\vec{V}}) \\ V_5 - V_2 - (V_1 + V_2 - V_4) + V_3 + \dot{\Phi}_{abcd}^{\text{ind}}(\dot{\vec{I}}, \ddot{\vec{V}}) \end{pmatrix} \tag{4.48}$$

where $\vec{I} = (I_a, I_b, I_c, I_d)$ and $\vec{V} = (V_1, V_2, V_3, V_4, V_5)$. The top 4 rows are from the flux quantization conditions on the 4 SQUID loops, and the bottom 5 rows from application of Faraday's law to the non-SQUID loops. The non-SQUID loops are

labeled by the SQUID loops involved in forming their circuit. For example, the top left partial loop in Fig. 4.15 (a) is labelled as *ac*. The voltages in the parentheses, e.g. $(V_1 + V_2 + V_3)$ in the sixth row, are dependent nodal voltages obtained from applying current conservation laws to the continuous SQUID loops. The induced flux Φ_{xx}^{ind} is calculated from the partial inductances from the individual branches just as in Sec.4.2.1, which is a function of junction currents $\vec{I}$ and node voltages $\vec{V}$.

The low rf flux amplitude linear limit solution can then be obtained by expressing $I_{a,b,c,d}$ in terms of $\delta_{a,b,c,d}$ and their time derivatives using the RCSJ model in Eq. (3.3), and replacing time derivatives with $i\Omega$ under Fourier transform. The resulting system has a size 9×9 with the 9 variables: $\delta_{a,b,c,d}$ and $V_{1,2,3,4,5}$. The eigenfrequencies for this linear system can be calculated and are plotted in Fig. 4.16 as a function of dc flux. As discussed in section 4.2.1.5, and illustrated in Figs. 4.4 and 4.6, the high frequency modes are dominated by the smaller loops, which contribute to smaller effective inductances, explaining their higher resonance frequency and weaker tunability, as explained through Eq. (4.15). The same loop-resonance correspondence can be established for the system of four corner-coupled SQUIDs containing 4 SQUID loops, 4 partial loops and 1 extra-SQUID loop, as labeled in Fig. 4.16. As expected, the much smaller extra-SQUID loop brings about a very high resonance at $\Omega \approx 12$, as shown in Fig. 4.16.

Similar to the two corner-coupled SQUIDs discussed in Sec.4.2.1.6, the full nonlinear solution is obtained numerically. The details for setting up the numerical solver can be found in Sec 4.2.5. Fig. 4.17 shows the resulting transmission S_{21} as a function of driving frequency Ω and applied dc flux Φ_{dc} in the low rf flux amplitude

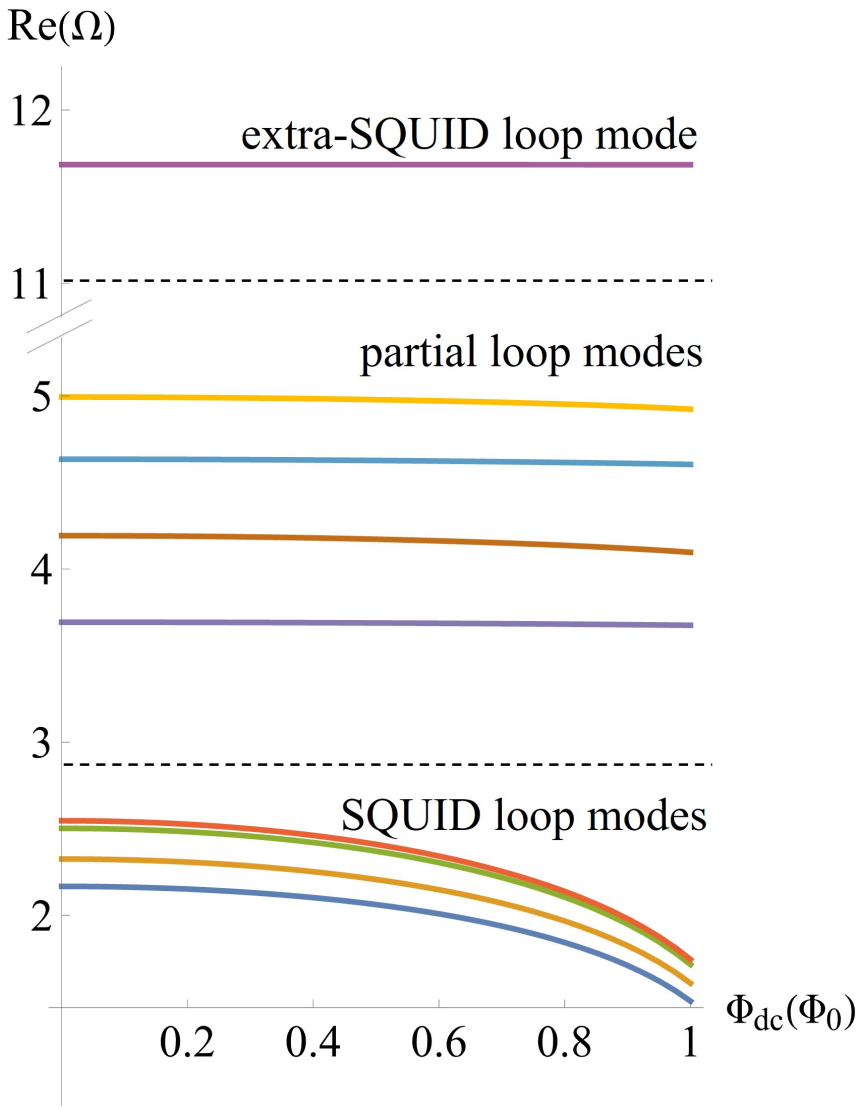

Figure 4.16: Real part of eigenfrequency solutions Re(Ω) from the characteristic equation $\det(\overleftrightarrow{\chi}) = 0$ in the linear limit for the four corner-coupled SQUIDs shown in Fig. 4.15 (a), as a function of dc magnetic flux Φ_{dc} in units of Φ_0. In this case 9 distinct resonance modes can be resolved. The two black horizontal dashed lines delineate the three types of resonant modes, as labeled.

linear limit, $\Phi_{\rm rf} \sim 10^{-3}\Phi_0$. The numerical solution has good agreement with the linear limit solutions, as illustrated with the coincidence of the dark (absorbing) features with the red dotted curves. A separate calculation is performed around $\Omega = 12$ which resolves the extra-SQUID loop modes that can not be captured in the frequency range in Fig.4.17.

4.2.7 $2 \times 2 \times 2$ corner-coupled overlapping SQUIDs

A full numerical solution, or even an analytical solution in the linear limit, is very computationally expensive to obtain for the large $N \times N \times 2$ system studied experimentally. However, the case of $N = 2$ (Fig. 4.15 (b)) can be tackled easily and should illustrate the general properties of the model. For the $2 \times 2 \times 2$ system, there are 8 SQUID loops, 9 partial loops, and 2 extra-SQUID loops. In the absence of any symmetries, we would thus expect a total of 19 resonant modes, comprised of 8 lower frequency modes near the single SQUID resonance, 9 partial loop modes at about twice the single-SQUID resonance frequency, and 2 extra-SQUID loop modes near $\Omega = 12$.

Following the same treatment as in Sec. 4.2.6, the eigenfrequencies in the low rf flux amplitude linear limit, and the full nonlinear numerical solution, can be obtained, and are shown in Figs. 4.18 and 4.19, respectively. Indeed, 19 eigenfrequencies fall in the expected range for their corresponding loop modes as depicted in Fig. 4.18. We note once again that the lowest-frequency ($2 < \Omega < 3$) SQUID-like modes with large effective inductance $|L_{\rm eff}| \gtrsim L_{\rm geo}$ show strong tuning with dc flux,

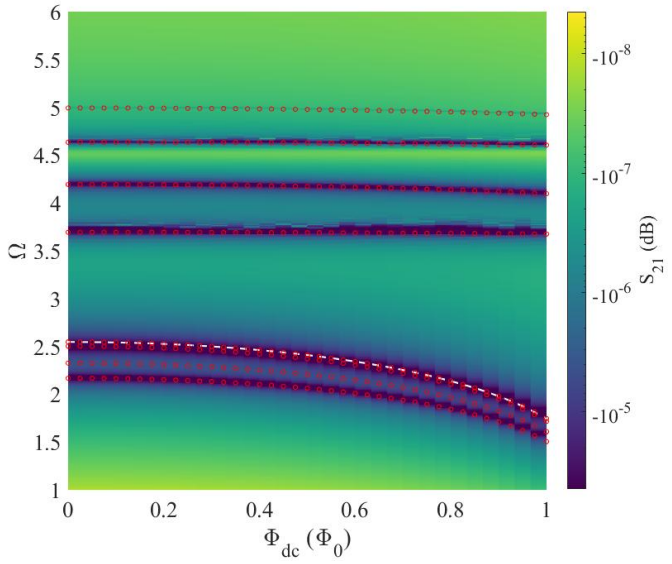

Figure 4.17: Nonlinear solutions to the four corner-coupled SQUIDs shown in Fig. 4.15(a) at $\Phi_{\rm rf} \sim 10^{-3}\Phi_0$. The quantity plotted is the magnitude of transmission $S_{21}(dB)$ on a logarithmic color scale, as a function of dimensionless frequency $\Omega = \omega/\omega_{\rm geo}$ and applied dc magnetic flux in units of the flux quantum Φ_0. The red dotted curves are the eigenfrequencies from the linear limit solution, and are closely matching to the resonances from the numerical solution. The dashed white curve is the eigenfrequency of the single SQUID with the same design parameter. The calculation cuts off at $\Omega = 6$ below the extra-SQUID loop modes.

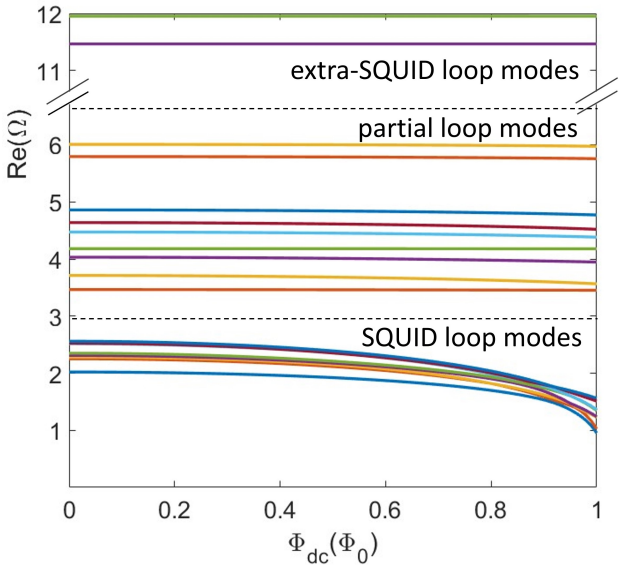

Figure 4.18: Real part of eigenfrequency solutions Re(Ω) from the characteristic equation $\det(\overleftrightarrow{\chi}) = 0$ in the linear limit for the $2 \times 2 \times 2$ corner-coupled SQUIDs shown in Fig. 4.15(b), as a function of dc magnetic flux $\Phi_{\rm dc}$ in units of Φ_0. A total of 19 distinct resonance modes can be resolved. The two black horizontal dashed lines delineate the three types of resonant modes, as labeled.

as expected for individual hysteretic ($\beta_{\rm rf} > 1$) rf SQUIDs. The intermediate frequency ($3 < \Omega < 6$) partial loop modes have much more modest dc flux tunability. The highest frequency modes ($11 < \Omega < 12$) arising from the two extra-SQUID loops are almost entirely insensitive to dc flux. One can note a general increasing insensitivity to dc flux with increasing frequency of the modes.

The full numerical solution in the low rf flux amplitude limit in Fig. 4.19 shows resonances coincident with the eigenfrequencies obtained from the linear-limit solution.

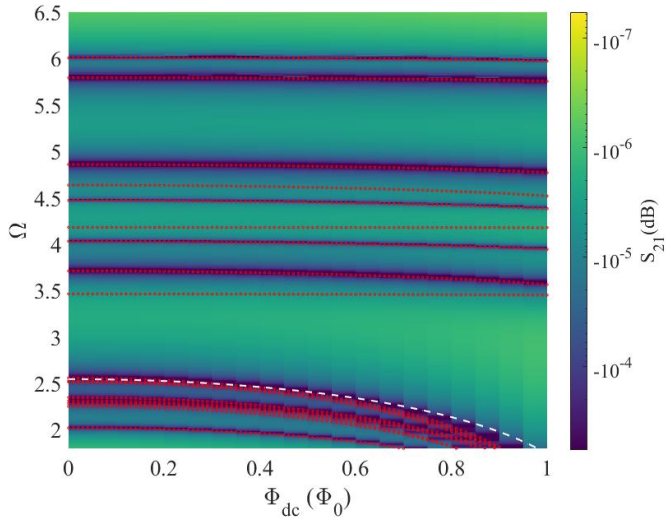

Figure 4.19: Nonlinear solutions to the $2 \times 2 \times 2$ system shown in Fig. 4.15(b) at $\Phi_{\mathrm{rf}} \sim 10^{-3}\Phi_0$. The quantity plotted is the magnitude of transmission $S_{21}(dB)$ on a logarithmic color scale, as a function of dimensionless frequency $\Omega = \omega/\omega_{\mathrm{geo}}$ and applied dc magnetic flux in units of the flux quantum Φ_0. The red dotted curves are the eigenfrequencies from the linear-limit solution matching the resonances from the numerical solution. The dashed white curve is the eigenfrequency of the single SQUID with the same design parameter.

4.2.8 $N \times N \times 2$ corner-coupled overlapping SQUIDs

Equipped with the loop-mode correspondence established in the analysis for the model systems discussed in section 4.2, we can extrapolate to the prediction for a larger system, where many partial loop modes should be visible between $\Omega = 3$ and 6, with very weak dc flux tunability, while the SQUID loop modes occur at lower frequency range with high dc flux tunability. The extra-SQUID loop modes around $\Omega = 12$ is almost invariant in dc flux and is beyond the frequency range of our measurement capability.

In the general case of an $N \times N \times 2$ SQUID array, there are $2N^2$ SQUID loops, $(2N-1)^2$ partial loops, and $2(N-1)^2$ extra-SQUID loops, resulting in a total number of $8N^2 - 8N + 3$ distinct loops. As illustrated above, each loop corresponds to an equation of motion in the voltage formalism. Thus, one would expect $8N^2 - 8N + 3$ equations for an $N \times N \times 2$ SQUID array. There are two capacitor nodes for each partial loop. However, the current conservation law from the SQUID loops will constrain the number of independent nodal voltages to $2 \times$ # of partial loops $-$ (# of SQUID loops $- 1$) $= 6N^2 - 8N + 3$. Together with the $2N^2$ gauge-invariant phase differences δ for each SQUID, the dynamics is described by a total of $8N^2 - 8N+3$ variables. The resulting $(8N^2-8N+3)\times(8N^2-8N+3)$ system can be solved exactly and will generate $8N^2 - 8N + 3$ modes in the absence of any symmetry.

4.3 Measurement results on the overlapping hysteretic SQUID metamaterials

The measurement was performed in the same setup as in Sec.3.3.2, with only the sample replaced by the overlapping SQUID array. The details of the experiment will not be reproduced here.

4.3.1 Frequency and dc flux dependence of the transmission

The rf SQUID response is typically very small in the transmission measurement due to its weak coupling to the waveguide mode. To better resolve the SQUID resonances, the data has been processed through a series of techniques as described in Sec.3.4. The resulting ΔS_{21} as a function of applied dc flux $\Phi_{\rm dc}$ and microwave frequency f is plotted in Fig. 4.20 for eight different values of the rf flux amplitude $\Phi_{\rm rf}$.

The yellow color represents nearly complete transmission of the microwaves (i.e. $\Delta S_{21} \lesssim 0$ dB), while the darker green features show conditions where the metamaterial interacts strongly with the passing electromagnetic fields and dissipates power. The green features trace out the resonant response as a function of applied dc magnetic flux with a typical $1\Phi_0$ periodicity. The red dashed curves mark the single-SQUID resonance and roughly corresponds to the expected boundary between the low-frequency and highly-tunable SQUID modes, and the high-frequency partial loop modes with lower-tunability introduced in Sec. 4.2.6. It should be noted that the third kind of mode, the extra-SQUID loops modes, with frequencies

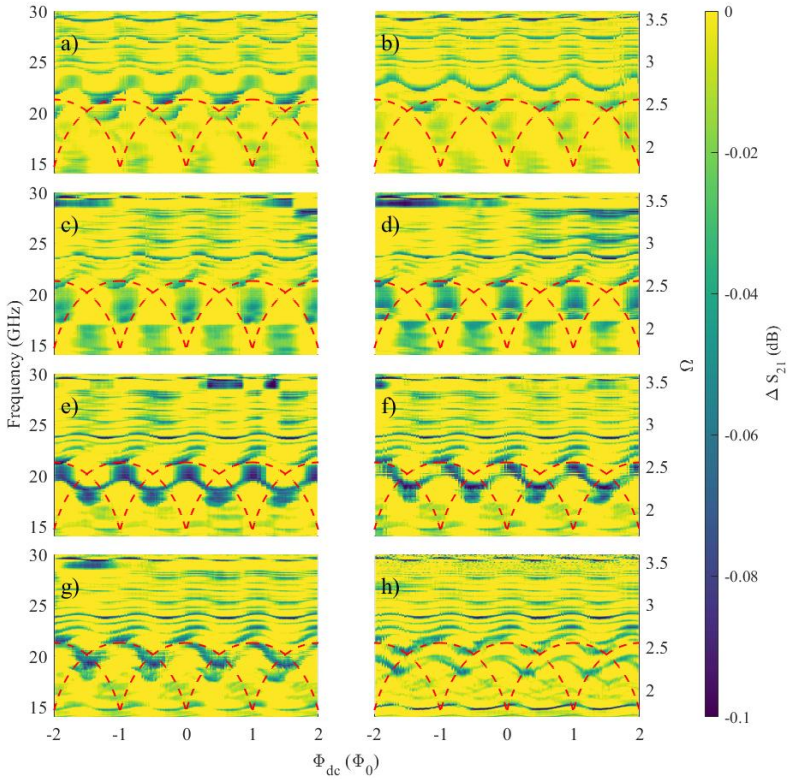

Figure 4.20: The measured magnitude of transmission ΔS_{21} (blue to yellow color) of the $12 \times 12 \times 2$ overlapping corner-coupled SQUID array as a function of dc flux swept from -2 to $+2$ Φ_0, and as a function of rf driving frequency f from 15 to 30 GHz ($\Omega = \frac{f}{f_{\text{geo}}} = 1.8 - 3.6$), at a temperature of 4.6 K. Results are presented at eight different applied rf flux amplitudes: [0.033, 0.023, 0.013, 0.01, 0.007, 0.006, 0.005, 0.0006] Φ_0 in panels a) through h). The red dashed curves denote the single-SQUID eigenfrequency.

around $12f_{\text{geo}} \approx 100$ GHz, are beyond the measurement range of our apparatus.

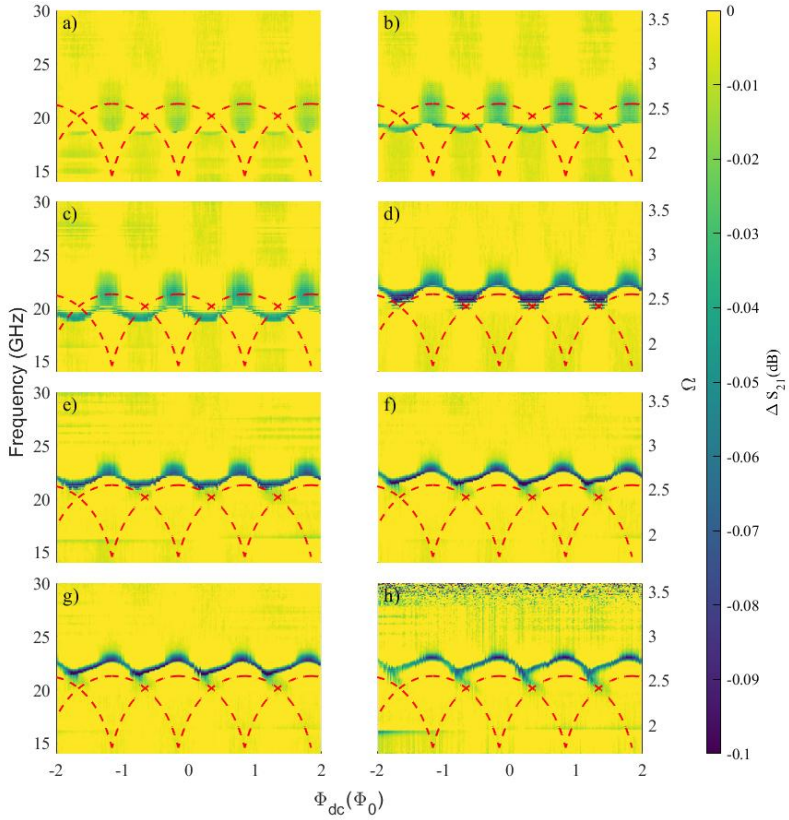

Figure 4.21: The measured magnitude of transmission ΔS_{21} (blue to yellow color) of the $12 \times 12 \times 1$ single-layer SQUID array as a function of dc flux swept from -2 to $+2$ Φ_0, and as a function of rf driving frequency f from 15 to 30 GHz ($\Omega = 1.8 - 3.6$), at a temperature of 4.6 K. Results are presented at eight different applied rf flux amplitudes: [0.042, 0.03, 0.026, 0.017, 0.015, 0.011, 0.009, 0.0003] Φ_0 in panels a) through h). The red dashed curves denote the single-SQUID eigenfrequency.

The response from the overlapping SQUID array SNAP161A is in clear contrast to the measurement on a single layer $12 \times 12 \times 1$ SQUID array (SNAP161D) with the same design parameters shown in Fig. 4.21. The SNAP161A sample is identical

to this $12 \times 12 \times 1$ array after removing the top overlapping layer of SQUIDs. Unlike the overlapping corner-coupled SQUID array, the single layer SQUID array has only one resonance band tuned with the applied dc flux Φ_{dc}, which is consistent with the coherent response seen in earlier measurements of single-layer SQUID metamaterials [44, 176, 178, 25] as well as shown in Chapter 3. The resonant frequency is close to that of a single-SQUID resonance shown as the red dashed curves. At low applied rf flux amplitude, the resonance is above that of the single SQUID since the collective antiferromagnetic coupling reduces the induced flux on each SQUID and thus the effective inductance. According to Eq. 4.15, a low $L_{\mathrm{eff}} < L_{\mathrm{geo}}$ corresponds to a resonance higher than that of the single SQUID as observed experimentally in Fig. 4.21. As expected for the SQUID modes, their tunability in Φ_{dc} also diminishes with increasing Φ_{rf}, again observed in earlier work on single-layer SQUID metamaterials [44, 176, 178, 25].

There are several other interesting features of Fig. 4.21 worth mentioning. First, note that green blobs appear around the turning points where the resonance tuning curves in applied dc flux from the two adjacent periods meet. These can be attributed to the fact that the meta-atom SQUID is strongly hysteretic ($\beta_{rf} > 1$), resulting in multiple stable solutions. At points where multiple solutions cross in the frequency-dc-flux space, there can be enhanced resonant responses over a range of frequencies, accounting for these blobs. We also note that the tuning curves are noticeably asymmetric as a function of dc flux at low rf flux amplitudes, and become increasingly symmetric as the rf flux amplitude increases. The asymmetry in the dc tuning curve is related to the hysteresis in dc flux sweep of the rf SQUID

metamaterial. For a measurement with decreasing dc flux, the asymmetric tilt of the tuning curve points to the opposite direction. This hysteresis is suppressed at higher applied rf flux amplitude because the strong oscillatory drive can overcome the barriers between local potential minima, preventing the system from becoming stuck in metastable states that are responsible for the hysteresis.

4.3.2 Frequency and rf flux dependence of the transmission

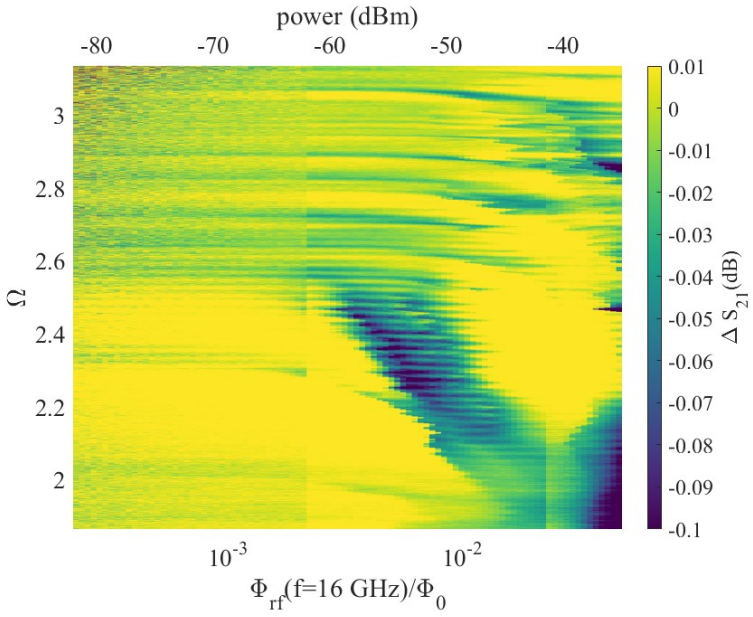

Figure 4.22: The measured magnitude of transmission ΔS_{21} (green to yellow color) of the $12 \times 12 \times 2$ overlapping corner-coupled SQUID array as a function of applied rf magnetic flux amplitude from $2 \times 10^{-4}\Phi_0$ to $5 \times 10^{-2}\Phi_0$ (and the corresponding microwave power incident on the sample in dBm), and rf driving frequency f from 15 to 26.5 GHz ($\Omega = 1.8$ to 3.2), at a temperature of 4.6 K. The measurement was taken at $\Phi_{dc} = -0.3\Phi_0$ with two separate power sweeps due to the limited 40 dB dynamic range in the VNA power sweep function. The two vertical lines around -62 and -42 dBm are the artifacts from stitching the two sweeps together.

Figure 4.22 shows the effects of increasing the driving rf flux amplitude beyond linear response on the spectrum of modes in the overlapping $12 \times 12 \times 2$ sample. The measurement was performed at zero current in the magnet but $\Phi_{\rm dc} = -0.3\Phi_0$ on the SQUIDs, based on their dc flux tunability curves. The result in Fig. 4.22 is

obtained from two separate power sweeps on the VNA due to its limited dynamic range. The first power sweep was performed from -82 to -42 dBm, while the second from -62 to -35 dBm. In the range where both power sweeps overlap, the average response is shown in Fig. 4.22 leading to the two vertical lines at the limits of the two power sweeps.

One notes strong tuning of the modes below $\Omega = 2.5$ and relatively small tuning for the higher frequency modes. This behavior is in qualitative agreement with that shown in Fig. 4.8 for the two corner-coupled SQUIDs. The low-frequency SQUID loop modes are strongly tuned, whereas the partial-loop modes only show modest tuning with rf flux. The experiment appears to just reach the high-power linear limit that is clearly seen in the model results in Fig. 4.8. However, these large rf flux amplitudes bring about the dangers of sample heating and amplifier saturation.

4.4 Discussion

We have so far explored the capacitively and inductively coupled overlapping SQUIDs in four different geometries so far: two edge-coupled SQUIDs, two and four corner-coupled SQUIDs and the two by two by two array of overlapping SQUIDs. More generally, for a system of many overlapping corner-coupled SQUIDs, the total number of elementary loops can be determined as follows. If we treat the SQUID loops as vertices and partial loops as edges connecting the corresponding vertices, we can represent the geometry of overlapping SQUIDs as a planar graph, as illustrated

in Fig.4.23. The most general system could be represented by a disconnected graph

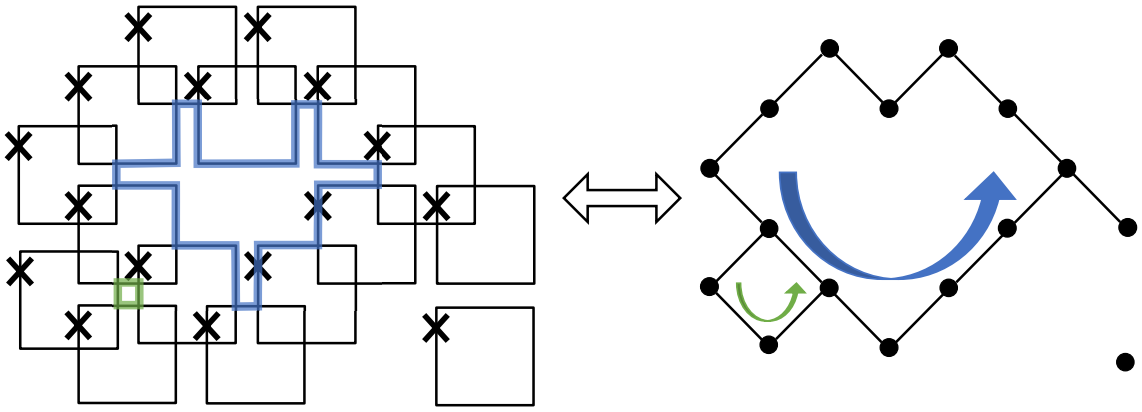

Figure 4.23: The correspondence between a general system of overlapping SQUIDs and its graph representation. The SQUID loops are represented by the vertices, and the partial loops connecting the neighboring SQUIDs by the bonds. The simple cycles in the graph correspond to extra-SQUID loops in the SQUID array, as highlighted by green and blue arrows in the graph, and corresponding closed loops in the SQUID array.

as shown in Fig.4.23 where a single SQUID in the lower right corner does not overlap with any other SQUIDs. Without loss of generality, we can examine each connected sub-graph individually and sum up the number of elementary loops. For each connected planar sub-graph with n vertices (SQUID loops) and m edges (partial loops), the extra-SQUID loops are just the simple cycles of the graph, the number of which is given by $m - n + 1$, bringing the total number of elementary loops to $m+n+m-n+1 = 2m+1$ in the sub-graph. The number of unknowns in the voltage formalism for the sub-graph can be obtained as in Sec. 4.2.8, where $2m - n + 1$ unknown voltages and the n phase differences from n junctions, give rise to $2m + 1$

unknowns, equal to the number of elementary loops. Tallying up all the sub-graphs, we have shown that for any general system of overlapping SQUIDs, the voltage formalism can result in an exactly determined system that describes the dynamics of the SQUIDs. For example, a single SQUID by itself is a planar connected graph with 1 vertex and 0 edges. The dynamics are described by 1 unknown, the phase difference, and 1 equation of motion, the flux quantization condition for a single SQUID (Eq. (3.5)). The $N \times N \times 2$ system in Sec. 4.2.8 is another special case of a system consisting of one planar connected graph.

Although, the extra-SQUID loops studied in the examples above are the smallest circuits corresponding to the very high frequency modes $12 f_{\text{geo}} \approx 100$ GHz, they can take on larger sizes in a more general geometry as shown in Fig.4.23. In fact, the extra-SQUID loop highlighted in blue in Fig.4.15 is the smallest realization permitted in our overlapping SQUID design.

The frequency and the tunability in applied dc magnetic flux of the resonance modes can be obtained from Eq.(4.15), where the effective inductance depends on the current distribution in the corresponding resonance modes. The modes with very small $|L_{\text{eff}}| \ll L_{\text{geo}}$ will have a high resonant frequency $\Omega_{\text{res}} \approx \sqrt{L_{\text{geo}}/L_{a,\text{eff}}}$, and be largely independent of dc flux applied to the metamaterial. On the other hand, the modes with large effective inductance $|L_{\text{eff}}| \gg L_{\text{geo}}$ will have a low resonant frequency $\Omega_{\text{res}} \approx \sqrt{\beta_{\text{rf}} \cos\delta}$, even lower than the single SQUID resonance, and will be strongly tunable with dc flux (through δ_{dc}). The experimental data on dc-flux tuning of the $12 \times 12 \times 2$ metamaterial is consistent with these expectations.

It should be noted that the only source of loss treated in this work arises from

quasiparticle tunneling, which appears as the resistance R in the RCSJ model, and is incorporated into the fully nonlinear equations of motion through the parameter γ. An extension of this treatment would be inclusion of other sources of loss. One candidate source of loss arises from dielectric losses in the Josephson junction tunnel barrier, the coupling capacitors between SQUIDs, as well as dielectrics surrounding the superconducting wiring. These dielectrics are known hosts for electric-dipole two-level systems [77, 78].

The treatment presented here assumes that all of the rf SQUIDs making up the metamaterial are nominally identical, having the same values of geometrical inductance, shunt capacitance, overlap capacitance, critical current, and junction resistance. We also assume that every SQUID experiences the same values of the externally-applied dc and rf flux, and that the driving rf flux is at a single frequency. It would be interesting to see how the results of this work depend on variations in these quantities due to either statistical or systematic variation in space.

In our treatment, we assume that the SQUIDs respond to external fields with a combination of dc currents and rf currents. However, the response rf currents are assumed to flow only at the same frequency as the driving flux. The latter assumption is expected to break down as the rf flux amplitude increases and activates the $\sin\delta_{rf}$ nonlinearity. This response is included in the solutions to the full nonlinear equations of motion, of course. Because of the broad frequency range over which the overlapping SQUID metamaterial responds, one can employ them for broadband parametric amplification or intermodulation generation.

Now that capacitive coupling between flux-based superconducting meta-atoms

has been established, one can ask whether the capacitive coupling can be varied? For example, there exist many nonlinear dielectric materials whose dielectric properties can be tuned with dc electric field, rf electric field, or with temperature at cryogenic temperatures [222, 223]. In addition, charge qubits can enjoy variable capacitive coupling through a small Josephson junction [205]. Thus a certain degree of tunability of capacitive coupling should be possible.

Chapter 5

Conclusions and future directions

This work started with the goal of building quantum metamaterials utilizing flux qubits as meta-atoms. The first generation of the quantum metamaterial with three-junction flux qubits embedded in a coplanar waveguide (CPW) resonator was designed and fabricated as shown in Fig.5.1. However, due to the lack of control in the junction tunneling currents in the fabrication, the ratios of the three junctions cannot be maintained to produce the double well potential required in these persistent current flux qubits. With a more mature fabrication recipe, we hope to finally realize a large array of similar qubits, approaching the limit of a quantum metamaterial in the future.

On the other hand, the rf SQUID metamaterials are fabricated by reliable commercial Niobium processes for relatively large Josephson junctions. In addition, the simple architecture of the rf SQUID, requiring only one junction in a meta-atom, imposes a much more relaxed constraint on the reproducibility of the process. The rf SQUID arrays are characterized by measuring the transmission through a rectangular waveguide loaded with the rf SQUID metamaterials. Although many multistability-induced features can be observed from the transmission signal, the measured response still effectively averages over all of the SQUID meta-atoms and lacks single-SQUID resolution. To address this limitation, laser scanning microscopy,

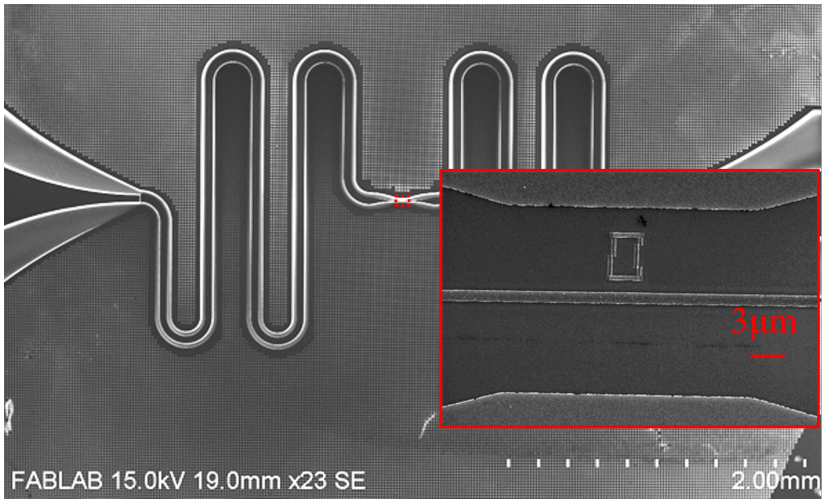

Figure 5.1: Scanning electron microscopy of the three junction flux qubit at the center of a CPW resonator.

able to spatially resolve the current distribution in a resonant superconducting meta-atom or device, has been employed to study non-hysteretic SQUID metamaterials [178]. We expect that the interesting nonlinear dynamics in the strongly coupled hysteretic SQUID arrays, as well as the overlapping SQUID arrays, can be better understood through this technique.

A brief summary of the key results from the works presented in the thesis is presented here. In chapter 2, we have discussed our work on characterizing a coplanar waveguide resonator intended for housing quantum metamaterials. The capacitively-coupled half wavelength superconducting aluminum microwave resonators is designed and fabricated with minimum critical dimension of 1 μm in the center conducting line of the CPW. The temperature and power dependence of the resonator Q_i deviate from the classical standard tunneling model for two level systems (TLS). At high applied powers, the internal loss shows logarithmic power

dependence, a signature of the generalized tunneling model with fluctuators. At powers below TLS saturation, the internal loss decreases from 50 mK down to the fridge base temperature. We attribute this behavior to the detuning between TLS and the CPW resonance frequency in a discrete TLS ensemble. Upon cooling, the single TLS response bandwidth, proportional to $\Gamma_2 \propto T^{1.3}$, decreases. When the bandwidth drops below the detuning between TLS and the resonance frequency defined by the CPW resonator, the resonant TLS response decreases and contributes less to the internal loss. The generalized tunneling model is revisited and modified with the discrete TLS formalism resulting in a comprehensive fit to the measured loss in the entire low temperature and low power range, with a reasonable set of parameters.

The work on hysteretic rf SQUID metamaterials is summarized in chapter 3. A series of rf SQUID metamaterials with high $\beta_{\mathrm{rf}} = L_{\mathrm{geo}}/L_{\mathrm{JJ}}$ values has been designed, fabricated and characterized. The multistability in the meta-atoms has been demonstrated analytically and numerically in the RCSJ model. Combined with the strong inductive coupling among the SQUIDs, the system presents a spread of resonance frequencies around the single SQUID resonance in our calculation. The multistable response is observed experimentally in the forms of hysteresis in dc flux sweep and coexistence of multiple resonances at one given applied dc flux. A large strongly-coupled hysteretic SQUID array also possess $2\Phi_0$ dc flux tuning period, as opposed to the common Φ_0 periodicity. This change in dc flux tuning pattern can be phenomenologically explained. In a strongly coupled system of hysteretic SQUIDs, the curve of resonance tuning with applied dc flux can skip one period to the next

curve centered $2\Phi_0$ away. The sample is under a large range of different dc flux biases, which leads to a spread of the tuning curves in applied dc flux creating the experimentally observed transmission spectrum.

Chapter 4 discusses the work on overlapping SQUID metamaterials, where we consider three-dimensional rf SQUID metamaterials with strong capacitive coupling between rf SQUID loops for the first time. Strong displacement currents can flow through the capacitors created by the overlap of the SQUID loops, creating new closed paths for the rf current through the rf SQUID network. The RCSJ model is extended to incorporate the capacitive coupling and the new current paths, leading to the prediction of a large range of resonances from frequencies below the single SQUID resonance to more than ten times of the single SQUID resonance. The number of distinct resonating loops in our three-dimensional $N \times N \times 2$ rf SQUID metamaterial design scales as $8N^2 - 8N + 3$. A large $N = 12$ three-dimensional rf SQUID metamaterial is measured, and is found to behave in a qualitatively different manner from the corresponding single-layer $12 \times 12 \times 1$ metamaterial. The observed multiplicity of resonances are in good agreement with our theory of capacitively-coupled overlapping SQUIDs.

Appendix A

Parameters for the two corner-coupled SQUIDs

To simplify the discussion in the main text, the definitions and numerical values of the parameters used in Sec.4.2.1 are summarized below.

$$\kappa_1 = M/L_{\rm geo} = 0.0335$$

$$\overleftrightarrow{\kappa} = \begin{pmatrix} 1 & \kappa_1 \\ \kappa_1 & 1 \end{pmatrix}$$

$$L_{\delta a} = L_{a,a1} - M_{a,b1} = 39.21\text{pH}$$

$$L_{\delta b} = L_{b,b1} - M_{b,a1} = 207.39\text{pH}$$

$$\kappa_{\delta a} = L_{\delta a}/L_{\rm geo} = 0.154$$

$$\kappa_{\delta b} = L_{\delta b}/L_{\rm geo} = 0.813$$

$$\kappa_a = \frac{L_{\rm geo}}{L_{\delta a}} + \frac{M}{L_{\delta b}} = 6.55$$

$$\kappa_b = \frac{M}{L_{\delta a}} + \frac{L_{\rm geo}}{L_{\delta b}} = 1.45$$

$$\text{CD} = \det \begin{pmatrix} L_{a,a1} & M_{a,b1} \\ M_{b,a1} & L_{b,b1} \end{pmatrix}$$

$$\kappa_{\rm va} = \det \begin{pmatrix} M_{\rm cen,b1} & L_{\rm cen,a1} \\ L_{b,b1} & M_{b,a1} \end{pmatrix} /\text{CD} = -0.714$$

$$\kappa_{\mathrm{v}b} = \det \begin{pmatrix} M_{a,b1} & L_{a,a1} \\ M_{\mathrm{cen},b1} & L_{\mathrm{cen},a1} \end{pmatrix} / \mathrm{CD} = -0.0085$$

$$L_{\mathrm{I}a} = \det \begin{pmatrix} M_{\mathrm{cen},a0} & L_{\mathrm{cen},a1} & M_{\mathrm{cen},b1} \\ L_{a,a0} & L_{a,a1} & M_{a,b1} \\ M_{b,a0} & M_{b,a1} & L_{b,b1} \end{pmatrix} / \mathrm{CD} = -134.4\mathrm{pH}$$

$$L_{\mathrm{I}b} = \det \begin{pmatrix} L_{\mathrm{cen},b0} & L_{\mathrm{cen},a1} & M_{\mathrm{cen},b1} \\ M_{a,b0} & L_{a,a1} & M_{a,b1} \\ L_{b,b0} & M_{b,a1} & L_{b,b1} \end{pmatrix} / \mathrm{CD} = 39.5\mathrm{pH}$$

$$\kappa_{\mathrm{I}a} = L_{\mathrm{I}a}/L_{\mathrm{geo}} = -0.527$$

$$\kappa_{\mathrm{I}b} = L_{\mathrm{I}b}/L_{\mathrm{geo}} = 0.155$$

$$\overleftrightarrow{\kappa}_{\mathrm{I}} = \begin{pmatrix} \kappa_{\mathrm{I}a} & \kappa_{\mathrm{I}b} \\ \kappa_{\mathrm{I}a} & \kappa_{\mathrm{I}b} \end{pmatrix}$$

$$\lambda_{\mathrm{cov}} = C_{\mathrm{ov}}/(2C) = 0.23$$

$$\overleftrightarrow{\kappa}_{\delta} = \begin{pmatrix} \kappa_{\mathrm{v}a} & 1+\kappa_{\mathrm{v}b} \\ \kappa_{\mathrm{v}a} & 1+\kappa_{\mathrm{v}b} \end{pmatrix}$$

$$\overleftrightarrow{\kappa}_{\mathrm{loop}} = \begin{pmatrix} -\kappa_{\delta a} & 0 \\ 0 & \kappa_{\delta b} \end{pmatrix}$$

$$\alpha = \kappa_b \Phi^{\mathrm{app}}_{\mathrm{cen}}/\Phi^{\mathrm{app}} + \kappa_b\kappa_{\mathrm{v}a} - \frac{L_{\mathrm{I}b}}{L_{\delta a}} + \kappa_b\kappa_{\mathrm{v}b} - \frac{L_{\mathrm{I}b}}{L_{\delta b}} = -2.00$$

The partial inductance matrix for the 2 corner-coupled SQUIDs (as shown in Fig. 4.3(a)) has the following numerical values

$$\begin{pmatrix} L_{a,a0} & M_{a,b0} & L_{a,a1} & M_{a,b1} \\ M_{b,a0} & L_{b,b0} & M_{b,a1} & L_{b,b1} \\ M_{\mathrm{cen},a0} & L_{\mathrm{cen},a1} & L_{\mathrm{cen},b0} & M_{\mathrm{cen},b1} \end{pmatrix} = \begin{pmatrix} 203.27 & -4.12 & 51.89 & 12.68 \\ 12.68 & 51.89 & -4.12 & 203.27 \\ 10.77 & 37 & 37 & 10.77 \end{pmatrix} \mathrm{pH} \tag{A.1}$$

Bibliography

[1] James Clerk Maxwell. *A Treatise on Electricity and Magnetism*, volume 1 of *Cambridge Library Collection - Physical Sciences*. Cambridge University Press, Cambridge, 1873.

[2] V. G. Veselago. The electrodynamics of substances with simultaneously negative values of ϵ and μ. *Soviet Physics Uspekhi*, 10(4):509–514, 1968.

[3] J. B. Pendry, A. J. Holden, W. J. Stewart, and I. Youngs. Extremely low frequency plasmons in metallic mesostructures. *Physical Review Letters*, 76(25):4773–4776, 1996.

[4] J. B. Pendry, A. J. Holden, D. J. Robbins, and W. J. Stewart. Magnetism from conductors and enhanced nonlinear phenomena. *IEEE Transactions on Microwave Theory and Techniques*, 47(11):2075–2084, 1999.

[5] Stefan Enoch, Gérard Tayeb, Pierre Sabouroux, Nicolas Guérin, and Patrick Vincent. A Metamaterial for Directive Emission. *Physical Review Letters*, 89(21):213902, November 2002. Publisher: American Physical Society.

[6] N. Garcia, E. V. Ponizovskaya, and John Q. Xiao. Zero permittivity materials: Band gaps at the visible. *Applied Physics Letters*, 80(7):1120–1122, February 2002.

[7] Brian T. Schwartz and Rafael Piestun. Total external reflection from metamaterials with ultralow refractive index. *JOSA B*, 20(12):2448–2453, December 2003. Publisher: Optica Publishing Group.

[8] Richard W. Ziolkowski. Propagation in and scattering from a matched metamaterial having a zero index of refraction. *Physical Review E*, 70(4):046608, October 2004. Publisher: American Physical Society.

[9] Mário Silveirinha and Nader Engheta. Tunneling of Electromagnetic Energy through Subwavelength Channels and Bends using $\ensuremath{\epsilon}$-Near-Zero Materials. *Physical Review Letters*, 97(15):157403, October 2006. Publisher: American Physical Society.

[10] Nader Engheta. Pursuing Near-Zero Response. *Science*, 340(6130):286–287, April 2013.

[11] J. Bardeen, L. N. Cooper, and J. R. Schrieffer. Theory of Superconductivity. *Phys. Rev.*, 108(5):1175–1204, December 1957.

[12] C. Kurter, T. Lan, L. Sarytchev, and Steven M. Anlage. Tunable negative permeability in a three-dimensional superconducting metamaterial. *Physical Review Applied*, 3(5), 2015.

[13] W. Rotman. Plasma simulation by artificial dielectrics and parallel-plate media. *IRE Transactions on Antennas and Propagation*, 10(1):82–95, January 1962. Conference Name: IRE Transactions on Antennas and Propagation.

[14] M. Ricci, N. Orloff, and S. M. Anlage. Superconducting metamaterials. *Applied Physics Letters*, 87(3):034102, 2005.

[15] R. A. Shelby, D. R. Smith, and S. Schultz. Experimental Verification of a Negative Index of Refraction. *Science*, 292(5514):77–79, April 2001. Publisher: American Association for the Advancement of Science.

[16] Mehmet Bayindir, K. Aydin, E. Ozbay, P. Markoš, and C. M. Soukoulis. Transmission properties of composite metamaterials in free space. *Applied Physics Letters*, 81(1):120–122, July 2002.

[17] Andrew A. Houck, Jeffrey B. Brock, and Isaac L. Chuang. Experimental Observations of a Left-Handed Material That Obeys Snell's Law. *Physical Review Letters*, 90(13):137401, April 2003. Publisher: American Physical Society.

[18] M. C. Ricci and S. M. Anlage. Single superconducting split-ring resonator electrodynamics. *Applied Physics Letters*, 88(26):264102, 2006.

[19] Steven M. Anlage. The physics and applications of superconducting metamaterials. *Journal of Optics*, 13(2):024001, 2011.

[20] M. C. Ricci, H. Xu, R. Prozorov, A. P. Zhuravel, A. V. Ustinov, and S. M. Anlage. Tunability of superconducting metamaterials. *IEEE Transactions on Applied Superconductivity*, 17(2):918–921, 2007.

[21] M. Tinkham. *Introduction to Superconductivity*. McGraw-Hill, New York, 2nd edition, 1996.

[22] Chunguang Du, Hongyi Chen, and Shiqun Li. Quantum left-handed metamaterial from superconducting quantum-interference devices. *Physical Review B*, 74(11):113105, 2006.

[23] P. Jung, S. Butz, S. V. Shitov, and A. V. Ustinov. Low-loss tunable metamaterials using superconducting circuits with josephson junctions. *Applied Physics Letters*, 102(6):062601–4, 2013.

[24] Daimeng Zhang, Melissa Trepanier, Thomas Antonsen, Edward Ott, and Steven M. Anlage. Intermodulation in nonlinear SQUID metamaterials: Experiment and theory. *Physical Review B*, 94(17):174507, 2016.

[25] Ethan Zack, Daimeng Zhang, Melissa Trepanier, Jingnan Cai, Tamin Tai, Nikos Lazarides, Johanne Hizanidis, and Steven M. Anlage. Tuning of strong nonlinearity in radio-frequency superconducting-quantum-interference-device meta-atoms. *Physical Review E*, 105(4):044202, 2022.

[26] N. Lazarides and G. P. Tsironis. Multistability and self-organization in disordered SQUID metamaterials. *Superconductor Science and Technology*, 26(8):084006, 2013.

[27] M. M. Müller, B. Maier, C. Rockstuhl, and M. Hochbruck. Analytical and numerical analysis of linear and nonlinear properties of an rf-SQUID based metasurface. *Physical Review B*, 99(7):075401, 2019.

[28] P. Jung, S. Butz, M. Marthaler, M. V. Fistul, J. Leppäkangas, V. P. Koshelets, and A. V. Ustinov. Multistability and switching in a superconducting metamaterial. *Nature Communications*, 5:3730, 2014.

[29] G. P. Tsironis, N. Lazarides, and I. Margaris. Wide-band tuneability, nonlinear transmission, and dynamic multistability in SQUID metamaterials. *Applied Physics A*, 117(2):579–588, 2014.

[30] Daimeng Zhang, Melissa Trepanier, Oleg Mukhanov, and Steven M. Anlage. Tunable broadband transparency of macroscopic quantum superconducting metamaterials. *Physical Review X*, 5(4):041045, 2015.

[31] Ting Zhou, Frank Moss, and Adi Bulsara. Observation of a strange nonchaotic attractor in a multistable potential. *Physical Review A*, 45(8):5394–5400, 1992.

[32] J. Hizanidis, N. Lazarides, and G. P. Tsironis. Flux bias-controlled chaos and extreme multistability in SQUID oscillators. *Chaos: An Interdisciplinary Journal of Nonlinear Science*, 28(6):063117, 2018.

[33] J. Shena, N. Lazarides, and J. Hizanidis. Multi-branched resonances, chaos through quasiperiodicity, and asymmetric states in a superconducting dimer. *Chaos: An Interdisciplinary Journal of Nonlinear Science*, 30(12), 2020.

[34] M. A. Castellanos-Beltran and K. W. Lehnert. Widely tunable parametric amplifier based on a superconducting quantum interference device array resonator. *Applied Physics Letters*, 91(8):083509, 2007.

[35] M. A. Castellanos-Beltran, K. D. Irwin, G. C. Hilton, L. R. Vale, and K. W. Lehnert. Amplification and squeezing of quantum noise with a tunable Josephson metamaterial. *Nature Physics*, 4(12):928–931, 2008.

[36] C. Macklin, K. O'Brien, D. Hover, M. E. Schwartz, V. Bolkhovsky, X. Zhang, W. D. Oliver, and I. Siddiqi. A near–quantum-limited Josephson traveling-wave parametric amplifier. *Science*, 350(6258):307–310, 2015.

[37] A. B Zorin. Josephson traveling-wave parametric amplifier with three-wave mixing. *Physical Review Applied*, 6(3):034006, 2016.

[38] Ananda Roy and Michel Devoret. Introduction to parametric amplification of quantum signals with josephson circuits. *Comptes Rendus Physique*, 17(7):740–755, 2016.

[39] EI Kiselev, AS Averkin, MV Fistul, VP Koshelets, and AV Ustinov. Two-tone spectroscopy of a SQUID metamaterial in the nonlinear regime. *Physical Review Research*, 1(3):033096, 2019.

[40] J. Aumentado. Superconducting parametric amplifiers: The state of the art in Josephson parametric amplifiers. *IEEE Microwave Magazine*, 21(8):45–59, 2020.

[41] S. Butz, P. Jung, L. V. Filippenko, V. P. Koshelets, and A. V. Ustinov. A one-dimensional tunable magnetic metamaterial. *Opt Express*, 21(19):22540–22548, 2013.

[42] Pascal Macha, Gregor Oelsner, Jan-Michael Reiner, Michael Marthaler, Stephan André, Gerd Schön, Uwe Hübner, Hans-Georg Meyer, Evgeni Il'ichev, and Alexey V. Ustinov. Implementation of a quantum metamaterial using superconducting qubits. *Nat Commun*, 5:5146, 2014.

[43] Ilya S. Besedin, Maxim A. Gorlach, Nikolay N. Abramov, Ivan Tsitsilin, Ilya N. Moskalenko, Alina A. Dobronosova, Dmitry O. Moskalev, Alexey R. Matanin, Nikita S. Smirnov, Ilya A. Rodionov, Alexander N. Poddubny, and Alexey V. Ustinov. Topological excitations and bound photon pairs in a superconducting quantum metamaterial. *Physical Review B*, 103(22):224520, 2021.

[44] M. Trepanier, Daimeng Zhang, Oleg Mukhanov, and Steven M. Anlage. Realization and modeling of metamaterials made of rf superconducting quantum-interference devices. *Physical Review X*, 3(4):041029, 2013.

[45] M. T. Bell, I. A. Sadovskyy, L. B. Ioffe, A. Yu Kitaev, and M. E. Gershenson. Quantum superinductor with tunable nonlinearity. *Physical Review Letters*, 109(13):137003, 2012.

[46] D. J. Durand, J. Carpenter, E. Ladizinsky, L. Lee, C. M. Jackson, A. Silver, and A. D. Smith. The distributed josephson inductance phase shifter. *IEEE Transactions on Applied Superconductivity*, 2(1):33–38, 1992.

[47] R. Kuzmin, R. Mencia, N. Grabon, N. Mehta, Y. H. Lin, and V. E. Manucharyan. Quantum electrodynamics of a superconductor–insulator phase transition. *Nature Physics*, 15(9):930–934, 2019.

[48] M. Trepanier, Daimeng Zhang, L. V. Filippenko, V. P. Koshelets, and Steven M. Anlage. Tunable superconducting Josephson dielectric metamaterial. *AIP Advances*, 9(10):105320, 2019.

[49] J. E. Mooij, T. P. Orlando, L. Levitov, Lin Tian, Caspar H. van der Wal, and Seth Lloyd. Josephson Persistent-Current Qubit. *Science*, 285(5430):1036–1039, August 1999.

[50] V. Bouchiat, D. Vion, P. Joyez, D. Esteve, and M. H. Devoret. Quantum coherence with a single Cooper pair. *Physica Scripta*, 1998(T76):165, January 1998. Publisher: IOP Publishing.

[51] R.C. Ramos, M.A. Gubrud, A.J. Berkley, J.R. Anderson, C.J. Lobb, and F.C. Wellstood. Design for effective thermalization of junctions for quantum coherence. *IEEE Transactions on Applied Superconductivity*, 11(1):998–1001, March 2001. Conference Name: IEEE Transactions on Applied Superconductivity.

[52] John M. Martinis, S. Nam, J. Aumentado, and C. Urbina. Rabi Oscillations in a Large Josephson-Junction Qubit. *Physical Review Letters*, 89(11):117901, August 2002. Publisher: American Physical Society.

[53] A. L. Rakhmanov, A. M. Zagoskin, S. Savel'ev, and F. Nori. Quantum metamaterials: Electromagnetic waves in a josephson qubit line. *Physical Review B*, 77(14):144507, 2008.

[54] S. Filipp, M. Göppl, J. M. Fink, M. Baur, R. Bianchetti, L. Steffen, and A. Wallraff. Multimode mediated qubit-qubit coupling and dark-state symmetries in circuit quantum electrodynamics. *Physical Review A*, 83(6):063827, June 2011. Publisher: American Physical Society.

[55] Arjan F. van Loo, Arkady Fedorov, Kevin Lalumière, Barry C. Sanders, Alexandre Blais, and Andreas Wallraff. Photon-Mediated Interactions Between Distant Artificial Atoms. *Science*, 342(6165):1494–1496, December 2013. Publisher: American Association for the Advancement of Science.

[56] J. A. Mlynek, A. A. Abdumalikov, C. Eichler, and A. Wallraff. Observation of Dicke superradiance for two artificial atoms in a cavity with high decay rate. *Nature Communications*, 5(1):5186, November 2014. Publisher: Nature Publishing Group.

[57] Neill Lambert, Yuichiro Matsuzaki, Kosuke Kakuyanagi, Natsuko Ishida, Shiro Saito, and Franco Nori. Superradiance with an ensemble of superconducting flux qubits. *Physical Review B*, 94(22):224510, December 2016.

[58] Andrew A. Houck, Hakan E. Türeci, and Jens Koch. On-chip quantum simulation with superconducting circuits. *Nature Physics*, 8(4):292–299, April 2012. Publisher: Nature Publishing Group.

[59] G. S. Paraoanu. Recent Progress in Quantum Simulation Using Superconducting Circuits. *Journal of Low Temperature Physics*, 175(5):633–654, June 2014.

[60] Philip Krantz, M. Kjaergaard, F. Yan, T. Orlando, Simon Gustavsson, and W. Oliver. A quantum engineer's guide to superconducting qubits. *Applied Physics Reviews*, 6:021318, 2019.

[61] Morten Kjaergaard, Mollie E. Schwartz, Jochen Braumüller, Philip Krantz, Joel I.-J. Wang, Simon Gustavsson, and William D. Oliver. Superconducting qubits: Current state of play. *Annual Review of Condensed Matter Physics*, 11(1):369–395, 2020.

[62] M. D. Hutchings and et al. Tunable superconducting qubits with flux-independent coherence. *Phys. Rev. Appl.*, 8:1, 2017.

[63] Tamin Tai, Jingnan Cai, and Steven M. Anlage. Anomalous Loss Reduction Below Two-Level System Saturation in Aluminum Superconducting Resonators. *Advanced Quantum Technologies*, 7(2):2200145, 2024. _eprint: https://onlinelibrary.wiley.com/doi/pdf/10.1002/qute.202200145.

[64] Jingnan Cai, Robin Cantor, Johanne Hizanidis, Nikos Lazarides, and Steven M. Anlage. Effects of strong capacitive coupling between meta-atoms in rf SQUID metamaterials. *Superconductor Science and Technology*, 37(7):075023, June 2024. Publisher: IOP Publishing.

[65] Jonas Zmuidzinas. Superconducting microresonators: Physics and applications. *Annual Review of Condensed Matter Physics*, 3(1):169–214, 2012.

[66] J. J. A. Baselmans and S. J. C. Yates. Long quasiparticle lifetime in aluminum microwave kinetic inductance detectors using coaxial stray light filters. *AIP Conference Proceedings*, 1185(1):160–163, 2009.

[67] Pascal Macha. *A path towards quantum metamaterials = Ein Weg zu Quantenmetamaterialien*. Ph.D. thesis, Karlsruher Instituts f ur Technologie, 2013.

[68] Jhy-Jiun Chang and D. J. Scalapino. Kinetic-equation approach to nonequilibrium superconductivity. *Physical Review B*, 15(5):2651–2670, 1977.

[69] D J Goldie and S Withington. Non-equilibrium supercondcutivity in quantum-sensing superconducting resonators. *Superconductor Science and Technology*, 26:015004, 2013.

[70] P. J. de Visser, D. J. Goldie, P. Diener, S. Withington, J. J. A. Baselmans, and T. M. Klapwijk. Evidence of a nonequilibrium distribution of quasiparticles in the microwave response of a superconducting aluminum resonator. *Physical Review Letters*, 112(4):047004, 2014.

[71] R. P. Budoyo. *EFFECTS OF OPTICAL ILLUMINATION ON SUPERCONDUCTING QUANTUM DEVICES*. Ph.D. thesis, University of Maryland, College Park, USA, 2015.

[72] Antti P. Vepsäläinen, Amir H. Karamlou, John L. Orrell, Akshunna S. Dogra, Ben Loer, Francisca Vasconcelos, David K. Kim, Alexander J. Melville, Bethany M. Niedzielski, Jonilyn L. Yoder, Simon Gustavsson, Joseph A. Formaggio, Brent A. VanDevender, and William D. Oliver. Impact of ionizing

radiation on superconducting qubit coherence. *Nature*, 584(7822):551–556, 2020.

[73] P. J. de Visser, J. J. A. Baselmans, P. Diener, S. J. C. Yates, A. Endo, and T. M. Klapwijk. Number fluctuations of sparse quasiparticles in a superconductor. *Physical Review Letters*, 106(16):167004, 2011.

[74] R. Barends, J. Wenner, M. Lenander, Y. Chen, R. C. Bialczak, J. Kelly, E. Lucero, P. O'Malley, M. Mariantoni, D. Sank, H. Wang, T. C. White, Y. Yin, J. Zhao, A. N. Cleland, John M. Martinis, and J. J. A. Baselmans. Minimizing quasiparticle generation from stray infrared light in superconducting quantum circuits. *Applied Physics Letters*, 99(11):113507–3, 2011.

[75] R. P. Budoyo, J. B. Hertzberg, C. J. Ballard, K. D. Voigt, J. R. Anderson Z. Kim, C. J. Lobb, and F. C. Wellstood. Effects of nonequilibrium quasiparticles in a thin-film superconducting microwave resonator under optical illumination. *Phys. Rev. B*, 93:024514, 2016.

[76] Nathalie P. de Leon, Kohei M. Itoh, Dohun Kim, Karan K. Mehta, Tracy E. Northup, Hanhee Paik, B. S. Palmer, N. Samarth, Sorawis Sangtawesin, and D. W. Steuerman. Materials challenges and opportunities for quantum computing hardware. *Science*, 372(6539):eabb2823, 2021.

[77] P. W Anderson, B. I. Halperin, and c M. Varma. Anomalous low-temperature thermal properties of glasses and spin glasses. *The Philosophical Magazine: A Journal of Theoretical Experimental and Applied Physics*, 25(1):1–9, 1972.

[78] W. A. Phillips. Tunneling states in amorphous solids. *Journal of Low Temperature Physics*, 7(3):351–360, 1972.

[79] M. Von Schickfus and S. Hunklinger. Saturation of the dielectric absorption of vitreous silica at low temperatures. *Physics Letters A*, 64(1):144–146, 1977.

[80] J. L. Black and B. I. Halperin. Spectral diffusion, phonon echoes, and saturation recovery in glasses at low temperatures. *Physical Review B*, 16(6):2879–2895, 1977.

[81] J. L. Black. Relationship between the time-dependent specific heat and the ultrasonic properties of glasses at low temperatures. *Physical Review B*, 17(6):2740–2761, 1978.

[82] W. A. Phillips. Two-level states in glasses. *Reports on Progress in Physics*, 50(12):1657, 1987.

[83] John M. Martinis, K. B. Cooper, R. McDermott, Matthias Steffen, Markus Ansmann, K. D. Osborn, K. Cicak, Seongshik Oh, D. P. Pappas, R. W. Simmonds, and Clare C. Yu. Decoherence in josephson qubits from dielectric loss. *Physical Review Letters*, 95(21):210503, 2005.

[84] Jiansong Gao, Jonas Zmuidzinas, Benjamin A. Mazin, Henry G. LeDuc, and Peter K. Day. Noise properties of superconducting coplanar waveguide microwave resonators. *Applied Physics Letters*, 90(10):102507, 2007.

[85] Jiansong Gao, Miguel Daal, Anastasios Vayonakis, Shwetank Kumar, Jonas Zmuidzinas, Bernard Sadoulet, Benjamin A. Mazin, Peter K. Day, and

Henry G. Leduc. Experimental evidence for a surface distribution of two-level systems in superconducting lithographed microwave resonators. *Applied Physics Letters*, 92(15):152505, 2008.

[86] A. D. O'Connell, M. Ansmann, R. C. Bialczak, M. Hofheinz, N. Katz, E. Lucero, C. McKenney, M. Neeley, H. Wang, E. M. Weig, A. N. Cleland, and J. M. Martinis. Microwave dielectric loss at single photon energies and millikelvin temperatures. *Applied Physics Letters*, 92(11):112903, 2008.

[87] Shwetank Kumar, Jiansong Gao, Jonas Zmuidzinas, Benjamin A. Mazin, Henry G. LeDuc, and Peter K. Day. Temperature dependence of the frequency and noise of superconducting coplanar waveguide resonators. *Applied Physics Letters*, 92(12):123503, 2008.

[88] R. Barends, H. L. Hortensius, T. Zijlstra, J. J. A. Baselmans, S. J. C. Yates, J. R. Gao, and T. M. Klapwijk. Contribution of dielectrics to frequency and noise of nbtin superconducting resonators. *Applied Physics Letters*, 92(22):223502, 2008.

[89] P. Macha, S. H. W. van der Ploeg, G. Oelsner, E. Il'ichev, H.-G. Meyer, S. Wünsch, and M. Siegel. Losses in coplanar waveguide resonators at millikelvin temperatures. *Applied Physics Letters*, 96(6):062503, 2010.

[90] Alexander L. Burin and Andrii O. Maksymov. Theory of nonlinear microwave absorption by interacting two-level systems. *Physical Review B*, 97(21):214208, 2018.

[91] Clare C. Yu and Hervé M. Carruzzo. Two-Level Systems and the Tunneling Model: A Critical View. In Miguel A. Romas, editor, *Low-Temperature Thermal and Vibrational Properties of Disordered Solids*, chapter 4, pages 113–139. World Scientific (Europe), 2022.

[92] Aaron M. Holder, Kevin D. Osborn, C. J. Lobb, and Charles B. Musgrave. Bulk and surface tunneling hydrogen defects in alumina. *Physical Review Letters*, 111(6):065901, 2013.

[93] Luke Gordon, Hazem Abu-Farsakh, Anderson Janotti, and Chris G. Van de Walle. Hydrogen bonds in al2o3 as dissipative two-level systems in superconducting qubits. *Scientific Reports*, 4(1):7590, 2014.

[94] William D. Oliver and Paul B. Welander. Materials in superconducting quantum bits. *MRS Bulletin*, 38(10):816–825, 2013.

[95] A. Bruno, G. de Lange, S. Asaad, K. L. van der Enden, N. K. Langford, and L. DiCarlo. Reducing intrinsic loss in superconducting resonators by surface treatment and deep etching of silicon substrates. *Appl. Phys, Lett.*, 106:182601, 2015.

[96] G. Calusine, A. Melville, W. Woods, R. Das, C. Stull, V. Bolkhovsky, D. Hover D. Braje1, D. K. Kim, X. Miloshi, D. Rosenberg, A. Sevi, J. L. Yoder, E. Dauler, and W. D. Oliver. Analysis and mitigation of interface losses in trenched superconducting coplanar waveguide resonators. *Appl. Phys. Lett.*, 112(6):1–7, 2018.

[97] A. Melville, G. Calusine, W. Woods, K. Serniak, E. Golden, B. M. Niedzielski, D. K. Kim, A. Sevi, J. L. Yoder, E. A. Dauler, and W. D. Oliver. Comparison of dielectric loss in titanium nitride and aluminum superconducting resonators. *Applied Physics Letters*, 117(12):124004, 2020.

[98] Jeremy M. Sage, Vladimir Bolkhovsky, William D. Oliver, Benjamin Turek, and Paul B. Welander. Study of loss in superconducting coplanar waveguide resonators. *J. Appl. Phys.*, 109(12):063915, 2011.

[99] B Chiaro, A Megrant, A Dunsworth, Z Chen, R Barends, B Campbell, Y Chen, A Fowler, I C Hoi, E Jeffrey, J Kelly, J Mutus, C Neill, P J J O'Malley, C Quintana, P Roushan, D Sank, A Vainsencher, J Wenner, T C White1, and John M Martinis. Dielectric surface loss in superconducting resonators with flux-trapping holes. *Supercond. Sci. Technol.*, 29(12):104006, 2016.

[100] C.J.K. Richardson, A. Alexander, C. G. Weddle, B. Arey, and M. Olszta. Low-loss superconducting titanium nitride grown using plasma-assisted molecular beam epitaxy. *J. Appl. Phys.*, 127:235302, 2020.

[101] A. Romanenko, R. Pilipenko, S. Zorzetti, D. Frolov, M. Awida, S. Belomestnykh, S. Posen, and A. Grassellino. Three-dimensional superconducting resonators at t¡20 mk with photon lifetimes up to τ=2 s. *Phys. Rev. Appl.*, 13:034032, 2020.

[102] S. E. de Graaf, L. Faoro, L. B. Ioffe, S. Mahashabde, J. J. Burnett, T. Lindström, S. E. Kubatkin, A. V. Danilov, and A. Ya. Tzalenchuk. Two-level

systems in superconducting quantum devices due to trapped quasiparticles. *Science Advances*, 6(51):eabc5055, 2020.

[103] J. Jäckle. On the ultrasonic attenuation in glasses at low temperatures. *Zeitschrift für Physik A Hadrons and nuclei*, 257(3):212–223, 1972.

[104] S. Hunklinger and W. Arnold. 3 - ultrasonic properties of glasses at low temperatures. In Warren P. Mason and R. N. Thurston, editors, *Physical Acoustics*, volume 12, pages 155–215. Academic Press, 1976.

[105] Chunguang Du, Hongyi Chen, and Shiqun Li. Quantum left-handed metamaterial from superconducting quantum-interference devices. *Physical Review B*, 74(11):113105, 2006.

[106] Philipp Jung, Alexey V. Ustinov, and Steven M. Anlage. Progress in superconducting metamaterials. *Superconductor Science and Technology*, 27(7):073001, 2014.

[107] Alexandre M. Zagoskin, Didier Felbacq, and Emmanuel Rousseau. Quantum metamaterials in the microwave and optical ranges. *EPJ Quantum Technology*, 3:2(1), 2016.

[108] N. Lazarides and G. P. Tsironis. Superconducting metamaterials. *Physics Reports*, 752:1–67, 2018.

[109] J. Q. You and F. Nori. Atomic physics and quantum optics using superconducting circuits. *Nature*, 474(7353):589, 2011.

[110] K. V. Shulga, E. Il'ichev, M. V. Fistul, I. S. Besedin, S. Butz, O. V. Astafiev, U. Hübner, and A. V. Ustinov. Magnetically induced transparency of a quantum metamaterial composed of twin flux qubits. *Nature Communications*, 9(1):150, 2018.

[111] Z. L. Xiang, S. Ashhab, J. Q. You, and F. Nori. Hybrid quantum circuits: Superconducting circuits interacting with other quantum systems. *Rev. Mod. Phys*, 85(2):623, 2013.

[112] S. I. Mukhin and M. V. Fistul. Generation of non-classical photon states in superconducting quantum metamaterials. *Superconductor Science and Technology*, 26(8):084003, 2013.

[113] P. A. Volkov and M. V. Fistul. Collective quantum coherent oscillations in a globally coupled array of superconducting qubits. *Physical Review B*, 89(5):054507, 2014.

[114] P. J. Petersan and S. M. Anlage. Measurement of resonant frequency and quality factor of microwave resonators: Comparison of methods. *Journal of Applied Physics*, 84(6):3392–3402, 1998.

[115] S. J. Weber, K. W. Murch, D. H. Slichter, R. Vijay, and I. Siddiqi. Single crystal silicon capacitors with low microwave loss in the single photon regime. *Applied Physics Letters*, 98(17):172510, 2011.

[116] J. Gao. *The Physics of Superconducting Microwave Resonators*. PhD dissertation, Caltech, Department of Physics, Caltech, 2008.

[117] C. R. H. McRae, H. Wang, J. Gao, M. R. Vissers, T. Brecht, A. Dunsworth, D. P. Pappas, and J. Mutus. Materials loss measurements using superconducting microwave resonators. *Review of Scientific Instruments*, 91(9):091101, 2020.

[118] Kevin D. Crowley, Russell A. McLellan, Aveek Dutta, Nana Shumiya, Alexander P.M. Place, Xuan Hoang Le, Youqi Gang, Trisha Madhavan, Matthew P. Bland, Ray Chang, Nishaad Khedkar, Yiming Cady Feng, Esha A. Umbarkar, Xin Gui, Lila V.H. Rodgers, Yichen Jia, Mayer M. Feldman, Stephen A. Lyon, Mingzhao Liu, Robert J. Cava, Andrew A. Houck, and Nathalie P. de Leon. Disentangling Losses in Tantalum Superconducting Circuits. *Physical Review X*, 13:041005, October 2023.

[119] J Burnett, L Faoro, and T Lindstrom. Analysis of high quality superconductor resonators: consequences for tls properties in amphorphous oxides. *Superconductivity Science and Technology*, 29:044008, 2016.

[120] J. Gao, J. Zmuidzinas, A. Vayonakis, P. Day, B. Mazin, and H. Leduc. Equivalence of the Effects on the Complex Conductivity of Superconductor due to Temperature Change and External Pair Breaking. *J Low Temp Phys*, 151(1):557–563, April 2008.

[121] D. P. Pappas, M. R. Vissers, D. S. Wisbey, J. S. Kline, and J. Gao. Two level system loss in superconducting microwave resonators. *IEEE Transactions on Applied Superconductivity*, 21(3):871–874, 2011.

[122] R. C. Zeller and R. O. Pohl. Thermal Conductivity and Specific Heat of Noncrystalline Solids. *Physical Review B*, 4(6):2029–2041, September 1971. Publisher: American Physical Society.

[123] E. Cuevas, R. Chicón, and M. Ortuño. Density of states for a disordered system of interacting dipoles. *Physica B: Condensed Matter*, 160(3):293–296, December 1989.

[124] Lara Faoro and Lev B. Ioffe. Interacting tunneling model for two-level systems in amorphous materials and its predictions for their dephasing and noise in superconducting microresonators. *Physical Review B*, 91(1):014201, January 2015.

[125] Alexander Churkin, Shlomi Matityahu, Andrii O. Maksymov, Alexander L. Burin, and Moshe Schechter. Anomalous low-energy properties in amorphous solids and the interplay of electric and elastic interactions of tunneling two-level systems. *Physical Review B*, 103(5):054202, 2021.

[126] Lara Faoro and Lev B. Ioffe. Internal Loss of Superconducting Resonators Induced by Interacting Two-Level Systems. *Physical Review Letters*, 109(15):157005, October 2012.

[127] R. Jankowiak and G. J. Small. Origin of the T1.3 power law of pure dephasing for impurity electronic transitions in amorphous solids. *Chemical Physics Letters*, 207(4):436–442, May 1993.

[128] H. Wang, M. Hofheinz, J. Wenner, M. Ansmann, R. C. Bialczak, M. Lenander, Erik Lucero, M. Neeley, A. D. O'Connell, D. Sank, M. Weides, A. N. Cleland, and John M. Martinis. Improving the coherence time of superconducting coplanar resonators. *Applied Physics Letters*, 95(23):233508, December 2009.

[129] Moe S. Khalil, F. C. Wellstood, and Kevin D. Osborn. Loss dependence on geometry and applied power in superconducting coplanar resonators. *IEEE Transactions on Applied Superconductivity*, 21(3):879–882, 2011.

[130] B. Sarabi, A. N. Ramanayaka, A. L. Burin, F. C. Wellstood, and K. D. Osborn. Projected dipole moments of individual two-level defects extracted using circuit quantum electrodynamics. *Physical Review Letters*, 116(16):167002, 2016.

[131] Chih-Chiao Hung, Liuqi Yu, Neda Foroozani, Stefan Fritz, Dagmar Gerthsen, and Kevin D. Osborn. Probing hundreds of individual quantum defects in polycrystalline and amorphous alumina. *Phys. Rev. Applied*, 17:034025, Mar 2022.

[132] M. Schechter and P. C. E. Stamp. What are the interactions in quantum glasses? *Journal of Physics: Condensed Matter*, 20(24):244136, May 2008.

[133] M. S. Khalil, M. J. A. Stoutimore, S. Gladchenko, A. M. Holder, C. B. Musgrave, A. C. Kozen, G. Rubloff, Y. Q. Liu, R. G. Gordon, J. H. Yum, S. K. Banerjee, C. J. Lobb, and K. D. Osborn. Evidence for hydrogen two-level systems in atomic layer deposition oxides. *Applied Physics Letters*, 103(16):162601, October 2013.

[134] M. Schechter and P. C. E. Stamp. Inversion symmetric two-level systems and the low-temperature universality in disordered solids. *Physical Review B*, 88(17):174202, November 2013.

[135] M. Schechter, P. Nalbach, and A. L. Burin. Nonuniversality and strongly interacting two-level systems in glasses at low temperatures. *New Journal of Physics*, 20(6):063048, June 2018.

[136] Liuqi Yu, Shlomi Matityahu, Yaniv J. Rosen, Chih-Chiao Hung, Andrii Maksymov, Alexander L. Burin, Moshe Schechter, and Kevin D. Osborn. Experimentally revealing anomalously large dipoles in the dielectric of a quantum circuit. *Scientific Reports*, 12(1):16960, October 2022.

[137] J. Burnett, L. Faoro, I. Wisby, V. L. Gurtovoi, A. V. Chernykh, G. M. Mikhailov, V. A. Tulin, R. Shaikhaidarov, V. Antonov, P. J. Meeson, A. Ya Tzalenchuk, and T. Lindström. Evidence for interacting two-level systems from the 1/f noise of a superconducting resonator. *Nature Communications*, 5:4119, 2014.

[138] Jiansong Gao, Miguel Daal, John M. Martinis, Anastasios Vayonakis, Jonas Zmuidzinas, Bernard Sadoulet, Benjamin A. Mazin, Peter K. Day, and Henry G. Leduc. A semiempirical model for two-level system noise in superconducting microresonators. *Applied Physics Letters*, 92(21):212504, May 2008.

[139] Shwetank Kumar, Jiansong Gao, Jonas Zmuidzinas, Benjamin A. Mazin, Henry G. LeDuc, and Peter K. Day. Temperature dependence of the frequency and noise of superconducting coplanar waveguide resonators. *Applied Physics Letters*, 92(12):123503, March 2008.

[140] S. E. de Graaf, S. Mahashabde, S. E. Kubatkin, A. Ya. Tzalenchuk, and A. V. Danilov. Quantifying dynamics and interactions of individual spurious low-energy fluctuators in superconducting circuits. *Physical Review B*, 103(17):174103, May 2021.

[141] Bahman Sarabi. *CAVITY QUANTUM ELECTRODYNAMICS OF NANOSCALE TWO-LEVEL SYSTEMS*. Ph.D. thesis, University of Maryland, College Park, 2014.

[142] J. Lisenfeld, C. Müller, J. H. Cole, P. Bushev, A. Lukashenko, A. Shnirman, and A. V. Ustinov. Measuring the temperature dependence of individual two-level systems by direct coherent control. *Physical Review Letters*, 105(23):230504, 2010.

[143] Grigorij J. Grabovskij, Torben Peichl, Jürgen Lisenfeld, Georg Weiss, and Alexey V. Ustinov. Strain tuning of individual atomic tunneling systems detected by a superconducting qubit. *Science*, 338(6104):232–234, 2012.

[144] M. Bhattacharya, K. D. Osborn, and Ari Mizel. Jaynes-Cummings treatment of superconducting resonators with dielectric loss due to two-level systems. *Physical Review B*, 84(10):104517, September 2011.

[145] CC Yu and AJ Leggett. Low temperature properties of amorphous materials: Through a glass darkly. *Comments Cond. Mat. Phys*, 14(4):231, 1988.

[146] Jürgen Lisenfeld, Grigorij J. Grabovskij, Clemens Müller, Jared H. Cole, Georg Weiss, and Alexey V. Ustinov. Observation of directly interacting coherent two-level systems in an amorphous material. *Nature Communications*, 6(1):6182, 2015.

[147] S. N. Coppersmith. Frustrated Interactions and Tunneling: Two-Level Systems in Glasses. *Physical Review Letters*, 67(17):2315–2318, October 1991.

[148] A. L. Burin and Yu. Kagan. The low energy collective excitations in dielectric glasses. The attenuation of sound waves at ultra low temperatures. *Physica B: Condensed Matter*, 194-196:393–394, February 1994.

[149] Dervis C. Vural and Anthony J. Leggett. Universal sound absorption in amorphous solids: A theory of elastically coupled generic blocks. *Journal of Non-Crystalline Solids*, 357(19):3528–3537, October 2011.

[150] D. C. Mattis and J. Bardeen. Theory of the anomalous skin effect in normal and superconducting metals. *Physical Review*, 111(2):412–417, 1958.

[151] J. P. Turneaure, J. Halbritter, and H. A. Schwettman. The surface impedance of superconductors and normal conductors - the mattis-bardeen theory. *Journal of Superconductivity*, 4(5):341–355, 1991.

[152] W. H. Parker. Modified heating theory of non-equilibrium superconductor. *Physical Review B*, 12:3667, 1975.

[153] Allen Rothwarf and B. N. Taylor. Measurement of recombination lifetimes in superconductors. *Physical Review Letters*, 19(1):27–30, 1967.

[154] T. Guruswamy, D. J. Goldie, and S. Withington. Nonequilibrium superconducting thin films with sub-gap and pair-breaking photon illumination. *Superconductor Science and Technology*, 28(5):054002, 2015.

[155] Lukas Grünhaupt, Nataliya Maleeva, Sebastian T. Skacel, Martino Calvo, Florence Levy-Bertrand, Alexey V. Ustinov, Hannes Rotzinger, Alessandro Monfardini, Gianluigi Catelani, and Ioan M. Pop. Loss mechanisms and quasiparticle dynamics in superconducting microwave resonators made of thin-film granular aluminum. *Physical Review Letters*, 121(11):117001, 2018.

[156] A. H. Silver and J. E. Zimmerman. Quantum states and transitions in weakly connected superconducting rings. *Physical Review*, 157:317–341, 1967.

[157] Michael Mück, Boris Chesca, and Yi Zhang. Radio frequency squids and their applications. In Harold Weinstock and Martin Nisenoff, editors, *Microwave Superconductivity*, pages 505–540. Springer Netherlands, Dordrecht, 2001.

[158] R. K. Ritala and M. M. Salomaa. Odd and even subharmonics and chaos in RF SQUIDS. *Journal of Physics C: Solid State Physics*, 16(14):L477, May 1983.

[159] K. Fesser, A. R. Bishop, and P. Kumar. Chaos in rf SQUID's. *Applied Physics Letters*, 43(1):123–124, July 1983.

[160] R. K. Ritala and M. M. Salomaa. Chaotic dynamics of periodically driven rf superconducting quantum interference devices. *Physical Review B*, 29(11):6143–6154, June 1984. Publisher: American Physical Society.

[161] M. P. Soerensen, M. Bartuccelli, P. L. Christiansen, and A. R. Bishop. On low-dimensional chaos in RF SQUIDs. *Physics Letters A*, 109(7):347–351, June 1985.

[162] Adi R. Bulsara. Subthreshold response of rf SQUIDs to a general external perturbation. *Journal of Applied Physics*, 60(7):2462–2476, October 1986.

[163] W. C. Schieve, A. R. Bulsara, and E. W. Jacobs. Homoclinic chaos in the rf superconducting quantum-interference device. *Physical Review A*, 37(9):3541–3552, May 1988. Publisher: American Physical Society.

[164] E. W. Jacobs, A. R. Bulsara, and W. C. Schieve. Homoclinic and chaotic transitions in the rf squid. *Physica D: Nonlinear Phenomena*, 34(3):439–448, March 1989.

[165] S. A. Bulgakov, V. B. Ryabov, V. I. Shnyrkov, and D. M. Vavriv. Effect of the magnetic-flux variations on SQUID stability. *Journal of Low Temperature Physics*, 83(5):241–255, June 1991.

[166] Luca Gammaitoni, Peter Hänggi, Peter Jung, and Fabio Marchesoni. Stochastic resonance. *Reviews of Modern Physics*, 70(1):223–287, January 1998. Publisher: American Physical Society.

[167] N. Lazarides, G. Neofotistos, and G. P. Tsironis. Chimeras in SQUID metamaterials. *Physical Review B*, 91(5):054303, 2015.

[168] J. Hizanidis, N. Lazarides, and G. P. Tsironis. Robust chimera states in SQUID metamaterials with local interactions. *Physical Review E*, 94(3):032219, 2016.

[169] J. Hizanidis, N. Lazarides, G. Neofotistos, and G.P. Tsironis. Chimera states and synchronization in magnetically driven SQUID metamaterials. *The European Physical Journal Special Topics*, 225(6):1231–1243, 2016.

[170] Amitava Banerjee and Debopriya Sikder. Transient chaos generates small chimeras. *Physical Review E*, 98(3):032220, 2018.

[171] Johanne Hizanidis, Nikos Lazarides, and Giorgos P. Tsironis. Chimera states in networks of locally and non-locally coupled squids. *Frontiers in Applied Mathematics and Statistics*, 5, 2019.

[172] J. Hizanidis, N. Lazarides, and G. P. Tsironis. Pattern formation and chimera states in 2D SQUID metamaterials. *Chaos: An Interdisciplinary Journal of Nonlinear Science*, 30(1):013115, 2020.

[173] N. Lazarides, J. Hizanidis, and G. P. Tsironis. Controlled generation of chimera states in SQUID metasurfaces using dc flux gradients. *Chaos, Solitons & Fractals*, 130:109413, 2020.

[174] N. Lazarides and G. P. Tsironis. SQUID metamaterials on a Lieb lattice: From flat-band to nonlinear localization. *Physical Review B*, 96(5):054305, 2017.

[175] N. Lazarides and G. P. Tsironis. Multistable dissipative breathers and collective states in SQUID Lieb metamaterials. *Physical Review E*, 98(1):012207, 2018.

[176] Melissa Trepanier, Daimeng Zhang, Oleg Mukhanov, V. P. Koshelets, Philipp Jung, Susanne Butz, Edward Ott, Thomas M. Antonsen, Alexey V. Ustinov, and Steven M. Anlage. Coherent oscillations of driven rf SQUID metamaterials. *Physical Review E*, 95(5):050201, 2017.

[177] P. Jung, R. Kosarev, A. Zhuravel, S. Butz, V. P. Koshelets, L. V. Filippenko, A. Karpov, and A. V. Ustinov. Imaging the electromagnetic response of superconducting metasurfaces. In *Advanced Electromagnetic Materials in Microwaves and Optics (METAMATERIALS), 2013 7th International Congress on*, pages 283–285, 2013.

[178] Alexander P. Zhuravel, Seokjin Bae, Alexander V. Lukashenko, Alexander S. Averkin, Alexey V. Ustinov, and Steven M. Anlage. Imaging collective behavior in an rf-SQUID metamaterial tuned by dc and rf magnetic fields. *Applied Physics Letters*, 114(8):082601, 2019.

[179] Daimeng Zhang. *Radio Frequency Superconducting Quantum Interference Device Meta-atoms and Metamaterials: Experiment, Theory, and Analysis*. Ph.D. thesis, University of Maryland, 2016.

[180] Paul K. Hansma. Superconducting single-junction interferometers with small critical currents. *Journal of Applied Physics*, 44(9):4191–4194, 1973.

[181] Paul K. Hansma. Observability of josephson pair-quasiparticle interference in superconducting interferometers. *Physical Review B*, 12(5):1707–1711, 1975.

[182] J. C. Booth, D. H. Wu, S. B. Qadri, E. F. Skelton, M. S. Osofsky, A. Pique, and S. M. Anlage. Large dynamical fluctuations in the microwave conductivity of $YBa_2Cu_3O_{7-\delta}$ above T_c. *Physical Review Letters*, 77(21):4438–4441, 1996.

[183] R. Rifkin, D. A. Vincent, B. S. Deaver, and P. K. Hansma. RF squids in non-hysteretic mode - detailed comparison of theory and experiment. *Journal of Applied Physics*, 47(6):2645–2650, 1976.

[184] R. Rifkin and B. S. Deaver. Current-phase relation and phase-dependent conductance of superconducting point contacts from RF impedance measurements. *Physical Review B*, 13(9):3894–3901, 1976.

[185] Antonio Barone and Gianfranco Paternò. *Physics and applications of the Josephson effect*. Wiley, New York, 1982.

[186] Jonathan R. Friedman, Vijay Patel, W. Chen, S. K. Tolpygo, and J. E. Lukens. Quantum superposition of distinct macroscopic states. *Nature*, 406(6791):43–46, July 2000. Publisher: Nature Publishing Group.

[187] Robert Schmidt. *The Early Theory of Equations: On Their Nature and Constitution : Translations of Three Treatises*. Golden Hind Press, 1986. Google-Books-ID: _FmqAAAAIAAJ.

[188] Mark B. Ketchen, W. J. Gallagher, A. W. Kleinsasser, S. Murphy, and John R. Clem. DC SQUID FLUX FOCUSER. In *SQUID '85 Superconducting Quan-*

tum Interference Devices and their Applications, pages 865–872. De Gruyter, 1986.

[189] Ali A. Babaei Brojeny and John R. Clem. Four coplanar superconducting strips: flux-focusing effects and inductance. *Superconductor Science and Technology*, 17(11):1275, August 2004.

[190] Juan A. Acebrón, L. L. Bonilla, Conrad J. Pérez Vicente, Félix Ritort, and Renato Spigler. The Kuramoto model: A simple paradigm for synchronization phenomena. *Reviews of Modern Physics*, 77(1):137–185, April 2005. Publisher: American Physical Society.

[191] R. Cantor and J. Hall. Six-layer process for the fabrication of Nb/Al-AlO_x/Nb josephson junction devices. *IEEE Transactions on Applied Superconductivity*, 15(2):82–85, 2005.

[192] S. Basavaiah and J. H. Greiner. Capacitance and ellipsometrically determined oxide thickness of nb-oxide-pb josephson tunnel junctions. *Journal of Applied Physics*, 47(9):4201–4202, 1976.

[193] W. Henkels and C. Kircher. Penetration depth measurements on type ii superconducting films. *Magnetics, IEEE Transactions on*, 13(1):63–66, 1977.

[194] Philipp Jung. *Nonlinear Effects in Superconducting Quantum Interference Meta-Atoms*. Ph.D. thesis, Karlsruher Instituts f ur Technologie, 2014.

[195] A. M. Zagoskin. Superconducting quantum metamaterials in 3d: possible realizations. *Journal of Optics*, 14(11):114011, 2012.

[196] K. K. Likharev and V. K. Semenov. Rsfq logic/memory family: a new josephson-junction technology for sub-terahertz-clock-frequency digital systems. *Applied Superconductivity, IEEE Transactions on*, 1(1):3–28, 1991.

[197] Sergey K. Tolpygo. Superconductor digital electronics: Scalability and energy efficiency issues (review article). *Low Temperature Physics*, 42(5):361–379, 2016.

[198] Takumi Ando, Shuichi Nagasawa, Naoki Takeuchi, Naoki Tsuji, Fumihiro China, Mutsuo Hidaka, Yuki Yamanashi, and Nobuyuki Yoshikawa. Three-dimensional adiabatic quantum-flux-parametron fabricated using a double-active-layered niobium process. *Superconductor Science and Technology*, 30(7):075003, 2017.

[199] Yuriy Makhlin, Gerd Scöhn, and Alexander Shnirman. Josephson-junction qubits with controlled couplings. *Nature*, 398(6725):305–307, 1999.

[200] L. F. Wei, Yu-xi Liu, and Franco Nori. Quantum computation with josephson qubits using a current-biased information bus. *Physical Review B*, 71(13):134506, 2005.

[201] J. Clarke and F. K. Wilhelm. Superconducting quantum bits. *Nature*, 453(7198):1031–1042, 2008.

[202] R. Harris, T. Lanting, A. J. Berkley, J. Johansson, M. W. Johnson, P. Bunyk, E. Ladizinsky, N. Ladizinsky, T. Oh, and S. Han. Compound josephson-

junction coupler for flux qubits with minimal crosstalk. *Physical Review B*, 80(5):052506, 2009.

[203] A. J. Berkley, H. Xu, R. C. Ramos, M. A. Gubrud, F. W. Strauch, P. R. Johnson, J. R. Anderson, A. J. Dragt, C. J. Lobb, and F. C. Wellstood. Entangled macroscopic quantum states in two superconducting qubits. *Science*, 300(5625):1548–1550, 2003.

[204] Yu A. Pashkin, T. Yamamoto, O. Astafiev, Y. Nakamura, D. V. Averin, and J. S. Tsai. Quantum oscillations in two coupled charge qubits. *Nature*, 421(6925):823–826, 2003.

[205] D. V. Averin and C. Bruder. Variable electrostatic transformer: Controllable coupling of two charge qubits. *Physical Review Letters*, 91(5):057003, 2003.

[206] R. McDermott, R. W. Simmonds, Matthias Steffen, K. B. Cooper, K. Cicak, K. D. Osborn, Seongshik Oh, D. P. Pappas, and John M. Martinis. Simultaneous state measurement of coupled josephson phase qubits. *Science*, 307(5713):1299–1302, 2005.

[207] Michele C. Collodo, Johannes Herrmann, Nathan Lacroix, Christian Kraglund Andersen, Ants Remm, Stefania Lazar, Jean-Claude Besse, Theo Walter, Andreas Wallraff, and Christopher Eichler. Implementation of Conditional Phase Gates Based on Tunable ZZ Interactions. *Physical Review Letters*, 125(24):240502, December 2020.

[208] Yuan Xu, Ji Chu, Jiahao Yuan, Jiawei Qiu, Yuxuan Zhou, Libo Zhang, Xinsheng Tan, Yang Yu, Song Liu, Jian Li, Fei Yan, and Dapeng Yu. High-Fidelity, High-Scalability Two-Qubit Gate Scheme for Superconducting Qubits. *Physical Review Letters*, 125(24):240503, December 2020.

[209] J. Stehlik, D. M. Zajac, D. L. Underwood, T. Phung, J. Blair, S. Carnevale, D. Klaus, G. A. Keefe, A. Carniol, M. Kumph, Matthias Steffen, and O. E. Dial. Tunable Coupling Architecture for Fixed-Frequency Transmon Superconducting Qubits. *Physical Review Letters*, 127(8):080505, August 2021.

[210] Youngkyu Sung, Leon Ding, Jochen Braumüller, Antti Vepsäläinen, Bharath Kannan, Morten Kjaergaard, Ami Greene, Gabriel O. Samach, Chris McNally, David Kim, Alexander Melville, Bethany M. Niedzielski, Mollie E. Schwartz, Jonilyn L. Yoder, Terry P. Orlando, Simon Gustavsson, and William D. Oliver. Realization of High-Fidelity CZ and ZZ-Free iSWAP Gates with a Tunable Coupler. *Physical Review X*, 11(2):021058, June 2021.

[211] Gioele Consani and Paul A. Warburton. Effective hamiltonians for interacting superconducting qubits: local basis reduction and the schrieffer–wolff transformation. *New Journal of Physics*, 22(5):053040, 2020.

[212] Sai Pavan Chitta, Tianpu Zhao, Ziwen Huang, Ian Mondragon-Shem, and Jens Koch. Computer-aided quantization and numerical analysis of superconducting circuits. *New Journal of Physics*, 24(10):103020, 2022.

[213] T. V. Filippov, S. K. Tolpygo, J. Mannik, and J. E. Lukens. Tunable transformer for qubits based on flux states. *Ieee Transactions on Applied Superconductivity*, 13(2):1005–1008, 2003.

[214] B. L. T. Plourde, J. Zhang, K. B. Whaley, F. K. Wilhelm, T. L. Robertson, T. Hime, S. Linzen, P. A. Reichardt, C. E. Wu, and John Clarke. Entangling flux qubits with a bipolar dynamic inductance. *Physical Review B*, 70(14):140501, 2004.

[215] A. O. Niskanen, K. Harrabi, F. Yoshihara, Y. Nakamura, S. Lloyd, and J. S. Tsai. Quantum coherent tunable coupling of superconducting qubits. *Science*, 316(5825):723–726, 2007.

[216] S. H. W. van der Ploeg, A. Izmalkov, Alec Maassen van den Brink, U. Hübner, M. Grajcar, E. Il'ichev, H. G. Meyer, and A. M. Zagoskin. Controllable coupling of superconducting flux qubits. *Physical Review Letters*, 98(5):057004, 2007.

[217] J. B. Majer, F. G. Paauw, A. C. J. ter Haar, C. J. P. M. Harmans, and J. E. Mooij. Spectroscopy on two coupled superconducting flux qubits. *Physical Review Letters*, 94(9):090501, 2005.

[218] M. Grajcar, A. Izmalkov, S. H. W. van der Ploeg, S. Linzen, E. Il'ichev, T. Wagner, U. Hubner, H. G. Meyer, A. M. van den Brink, S. Uchaikin, and A. M. Zagoskin. Direct Josephson coupling between superconducting flux qubits. *Physical Review B*, 72(2):020503, 2005.

[219] M. Grajcar, A. Izmalkov, S. H. W. van der Ploeg, S. Linzen, T. Plecenik, T. Wagner, U. Hubner, E. Il'ichev, H. G. Meyer, A. Y. Smirnov, P. J. Love, A. M. van den Brink, M. H. S. Amin, S. Uchaikin, and A. M. Zagoskin. Four-qubit device with mixed couplings. *Physical Review Letters*, 96(4):047006, 2006.

[220] Edward Bennett Rosa. The self and mutual inductances of linear conductors. *Bulletin of the Bureau of Standards*, 4(2):301, 1908.

[221] C. R. Paul. *The Concept of "Partial" Inductance*, chapter 5, pages 195–245. John Wiley & Sons, Ltd, 2009.

[222] L. B. Kong, S. Li, T. S. Zhang, J. W. Zhai, F. Y. C. Boey, and J. Ma. Electrically tunable dielectric materials and strategies to improve their performances. *Progress in Materials Science*, 55(8):840–893, 2010.

[223] A. T. Findikoglu, C. Doughty, S. M. Anlage, Q. Li, X. X. Xi, and T. Venkatesan. DC Electric-Field Effect on the Microwave Properties of $YBa_2Cu_3O_7/SrTiO_3$ Layered Structures. *Journal of Applied Physics*, 76(5):2937–2950, 1994.